Flame Stability and Emissions in Methane/Hydrogen Combustion

Designing for Fuel Flexibility

Link, S.J.

DOI
10.4233/uuid:e91f07f6-a580-4d1a-876b-4c8cc30738f8

Publication date
2025

Document Version
Final published version

Citation (APA)
Link, S. J. (2025). *Flame Stability and Emissions in Methane/Hydrogen Combustion: Designing for Fuel Flexibility* . [Dissertation (TU Delft), Delft University of Technology]. https://doi.org/10.4233/uuid:e91f07f6-a580-4d1a-876b-4c8cc30738f8

Flame Stability and Emissions in Methane/Hydrogen Combustion

Designing for Fuel Flexibility

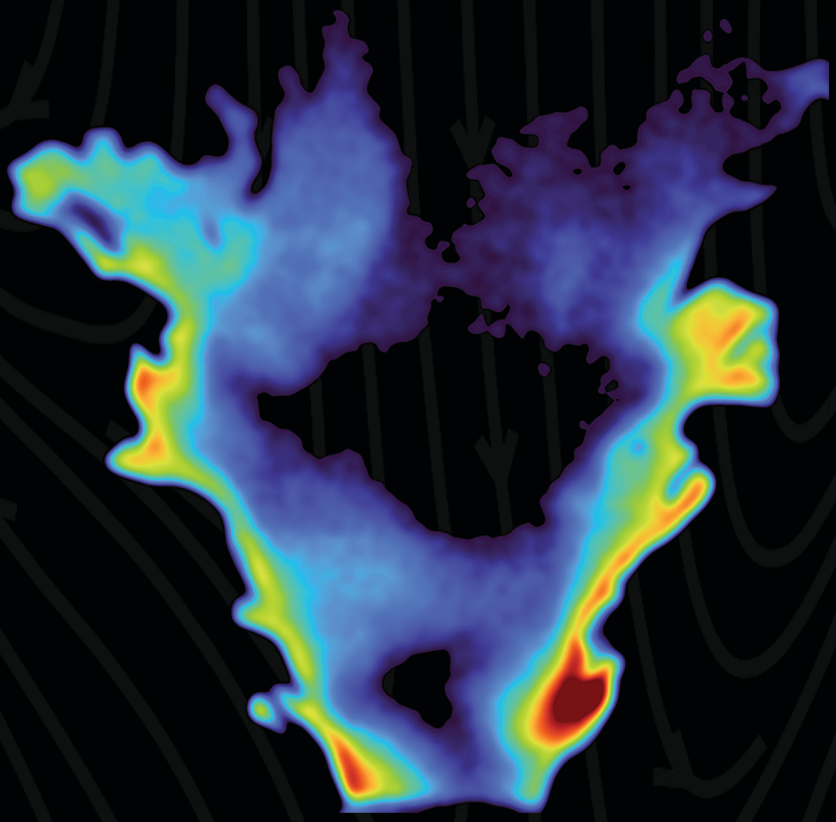

Sarah Jacqueline Link

Flame Stability and Emissions in Methane/Hydrogen Combustion

Designing for Fuel Flexibility

FLAME STABILITY AND EMISSIONS IN METHANE/HYDROGEN COMBUSTION

DESIGNING FOR FUEL FLEXIBILITY

Dissertation

for the purpose of obtaining the degree of doctor
at Delft University of Technology
by the authority of the Rector Magnificus, prof. dr. ir. H. Bijl,
chair of the Board for Doctorates
to be defended publicly on
Wednesday 21 January 2026 at 12:30 o'clock

by

Sarah Jacqueline LINK

Master of Science in Aerospace Engineering, University of Stuttgart, Germany
born in Tuttlingen, Germany

This dissertation has been approved by the promotors.

Composition of the doctoral committee:

Rector Magnificus	chairperson
Prof. Dr.-Ing. G. Eitelberg	Delft University of Technology, promotor
Prof. dr. A. Gangoli Rao	Delft University of Technology, promotor
Dr. F. De Domenico	Delft University of Technology, copromotor
Independent members:	
Prof. Dr.-Ing. C. O. Paschereit	TU Berlin, Germany
Prof. dr. B. Renou	INSA Rouen Normandie, France
Dr. N. Treleaven	Safran Tech, France
Prof. dr. ir. S. A. Klein,	Delft University of Technology
Prof. Dr.-Ing.habil S. Hickel	Delft University of Technology, reserve member

This work is part of the APPU project, which has been financed by the Dutch Ministry of Economic Affairs and Climate under the TKIscheme (Grant number TKI HTSM/18.0170) along with SAFRAN TECH.

Keywords: Methane-hydrogen combustion, Swirl-stabilized combustion, Fuel-flexibility, Jet in cross-flow, Fuel-air mixing, Laser diagnostics, Flame stabilization, NO emissions, Operational range

Printed by: Ridderprint

Cover by: Sarah Link & Carmine Varriale. Front: OH-PLIF image of a methane-hydrogen flame. Back: Artistic representation of the laser set-up for PIV and PLIF measurements.

ISBN 978-94-6518-211-7

An electronic copy of this dissertation is available at
https://repository.tudelft.nl/.

Science is more than a body of knowledge;
it is a way of thinking,
a process of questioning the universe with scepticism
and an understanding of human fallibility.

Wissenschaft ist mehr als eine Ansammlung von Wissen;
sie ist eine Denkweise,
ein Prozess, das Universum mit Skepsis
und dem Bewusstsein menschlicher Fehlbarkeit zu hinterfragen.
- Carl Sagan

SUMMARY

Human civilization must transition to more sustainable energy sources to meet the goals of the Paris Agreement, which aims to limit the global temperature increase to well below 2 °C above pre-industrial levels. However, hard to abate sectors such as aviation and heavy industries will continue to rely on combustion for the foreseeable future. For these industries, the development and deployment of alternative fuels are essential. One of the most promising alternative fuels is hydrogen (H_2), primarily because it enables carbon-free combustion. Nevertheless, significant challenges remain regarding its production, storage, and transportation, leading to uncertainties in its large-scale availability. As a result, there is growing interest in fuel-flexible combustion systems that can operate efficiently on traditional carbon-based fuels, hydrogen, or any mixture of the two, while maintaining combustion stability and low emissions across the full fuel range. Hydrogen differs significantly from carbon-based fuels such as methane (CH_4) in its combustion characteristics. It has a much higher flame speed and higher adiabatic flame temperature at the same equivalence ratio. These properties can pose serious design challenges such as increased risk of flashback and elevated NO_x emissions.

In swirl-stabilized combustion, injecting non-swirled air axially on the centreline can be a very efficient way to stabilize flames with high hydrogen content. This work investigates the emissions and flame stability of a fuel flexible swirl-stabilized combustor that can operate on fuel mixtures ranging from 100 % CH_4 to 100 % H_2. In this set-up, fuel is injected in a jet in cross-flow configuration just downstream of the swirler exit. A mixing tube is placed between the injection point and the combustion chamber to allow for fuel-air mixing. The objective of this thesis is to identify the dominant parameters that govern emissions and stability in fuel-flexible combustion systems. To support this aim, several research questions are formulated and addressed in dedicated chapters.

The first part of the thesis examines the non-reacting flow field within the mixing tube and combustion chamber. Geometric and operating parameters are systematically varied to assess their influence on the time-averaged and unsteady flow field. This analysis provides insight into which parameters significantly affect the flow under non-reacting conditions. Such understanding is essential for interpreting observations under reacting conditions, as it enables a distinction between changes induced by flow field alterations and those caused purely by combustion processes. The results show that the level of confinement, the outlet boundary condition, and the degree of Axial Air Injection (AAI) strongly influence the overall flow structure — primarily by altering the size of the recirculation zones, the type of vortex breakdown, and the velocity distributions. In contrast, operational parameters such as fuel composition and the momentum flux ratio between fuel and air mainly affect the velocity distribution, while the overall flow topology and unsteady features remain largely unchanged.

In partially premixed configurations, where fuel and air are not perfectly premixed and the fuel is injected just upstream of the combustion chamber, the quality of mix-

ing has a critical impact on flame stability and emissions. To assess mixing under non-reacting conditions, the second part of this thesis uses helium/air mixtures as surrogates for various CH_4/H_2 blends, using tracer droplets to visualize the mixing process without combustion interference. The effects of fuel composition, inlet velocity, and swirl intensity on mixing are systematically analysed. Results show that mixing quality is primarily governed by fuel composition, with lighter fuels, such as hydrogen, enhancing mixing. For a given composition, mixing improves with increasing momentum flux ratio between fuel and air up to a critical threshold, beyond which no further improvement is observed. Although AAI reduces mixing near the injection point, this effect can be offset by sufficiently high swirl. These findings establish a baseline for interpreting emission trends in the reacting flow experiments.

The third part of this thesis investigates the fuel flexibility of the partially premixed combustor with AAI. This includes an assessment of the operational range, by identifying the conditions for flashback and blowout across varying equivalence ratios (φ) and hydrogen contents, as well as the influence of AAI on these limits. Flame stabilization mechanisms derived from OH Planar Laser-Induced Fluorescence (PLIF) images and flow fields are also analysed to explain the observed changes in operational range. Finally, an emission analysis investigates how fuel composition and the degree of AAI influence emission performance, and whether these effects can be attributed to changes in mixing quality. The results show that AAI effectively extends the operational range and increases the flashback limit for high hydrogen-content fuels. This improvement is attributed to a shift in flame stabilization mechanism compared to cases without AAI. However, higher levels of AAI also lead to increased NO emissions, likely due to reduced fuel-air mixing.

NO_x emissions are strongly influenced by local fuel-air mixing, the flow field and the dominant NO formation pathways. The relative importance of these pathways changes significantly when transitioning from methane to hydrogen, complicating the prediction of NO distribution and total NO emissions in partially premixed, fuel-flexible combustion. The fourth part of this thesis presents a detailed investigation of NO emissions in partially premixed swirl-stabilized flames with AAI. Using NO planar laser-induced fluorescence (NO-PLIF), the spatial distribution of NO within the combustion chamber is characterized alongside measurements of total NO concentration in the exhaust. These data are analysed in relation to flame location and the flow field, providing insights into the causes of NO emission trends and strategies for their reduction. Results show that NO distribution is strongly affected by the level of AAI, which is linked to the changes in the flow field and flame stabilization. Moreover, the flame lift-off height plays a critical role in local fuel-air mixing and NO emissions, as well as in shifting the balance between different NO formation mechanisms contributing to total NO production.

The fifth and final part builds on the insights from the previous chapters, which identified the momentum flux ratio as a key factor in fuel-air mixing. Accordingly, in this chapter the effect of variations in the momentum flux ratio between fuel and air on combustor stability and emissions is investigated. This ratio is adjusted by changing the fuel inlet diameter. Emission analysis, including exhaust gas measurements and spatial NO distribution, is performed to assess the effects on the NO emissions. These results are interpreted in the context of fuel and air mixing behaviour, building on insights from the

second part of this thesis. The findings reveal that increasing the momentum flux ratio enhances mixing and reduces NO emissions. While the flame stabilization mechanism remains unchanged, the flame position shifts closer to the injector at higher momentum flux ratios, which lowers the flashback limits of the system.

In conclusion, this thesis delivers a fundamental understanding of the processes and parameters that govern stability and emissions in a partially premixed, fuel-flexible swirl-stabilized combustor. The findings provide valuable insights into the interplay between injector design, fuel composition, and flow field characteristics, and how these factors influence stability limits, emissions, and overall combustor performance. Through systematic investigation within a well-characterized geometry, clear trends and underlying mechanisms were identified, laying a solid foundation for the future design and optimization of fuel-flexible combustors. The insights gained are broadly applicable and highly relevant for the development of next-generation combustion systems.

SAMENVATTING

Om de doelstellingen van de Overeenkomst van Parijs te behalen, die gericht is op het beperken van de mondiale temperatuurstijging tot ruim onder de 2°C ten opzichte van het pre-industriële tijdperk, moet de mensheid overstappen op duurzamere energiebronnen. Sommige sectoren, zoals de luchtvaart, zijn echter moeilijk te verduurzamen en blijven voorlopig afhankelijk van verbrandingsmotoren. Voor deze sectoren is de ontwikkeling en toepassing van alternatieve brandstoffen van essentieel belang. Een van de veelbelovendste alternatieve brandstoffen is waterstof (H_2), voornamelijk omdat de verbranding ervan koolstofvrij is. Desondanks bestaan er aanzienlijke uitdagingen rondom de productie, opslag en het transport ervan, wat leidt tot onzekerheid over de grootschalige beschikbaarheid. Daarom groeit de belangstelling voor brandstofflexibele verbrandingssystemen die efficiënt en schoon kunnen functioneren op zowel conventionele koolstofhoudende brandstoffen als waterstof, of mengsels daarvan, met als doel de verbrandingsstabiliteit en lage emissies over het volledige brandstofbereik te behouden. Waterstof verschilt echter aanzienlijk van methaan (CH_4) in zijn verbrandingseigenschappen. Bij eenzelfde equivalentie-verhouding heeft het een beduidend hogere vlamsnelheid en een hogere adiabatische vlamtemperatuur. Deze eigenschappen kunnen serieuze ontwerpuitdagingen met zich meebrengen, zoals een verhoogd risico op *flashback* en verhoogde NO_x-emissies.

Bij *swirl-stabilized* verbranding kan het axiaal en zonder werveling injecteren van lucht op de middellijn van de verbrandingskamer een zeer effectieve methode zijn om vlammen met een hoog waterstofgehalte te stabiliseren. In dit werk worden daarom de emissies en vlamstabiliteit onderzocht van een *swirl-stabilized* verbrandingssysteem dat kan functioneren op brandstofmengsels variërend van 100 % CH_4 tot 100 % H_2. In deze configuratie wordt de brandstof vlak na de uitgang van de *swirl-generator* geïnjecteerd in een straal dwars op de hoofdstroom. Tussen het injectiepunt en de verbrandingskamer is een mengbuis geplaatst die zorgt voor een menging van brandstof en lucht. Het doel van het onderzoek is om de dominante parameters te identificeren die de emissies en stabiliteit bepalen in brandstofflexibele *swirl-stabilized* verbrandingssystemen. Ter ondersteuning van dit doel worden vijf onderzoeksvragen geformuleerd, die elk worden behandeld in een afzonderlijk hoofdstuk.

Het eerste deel van dit proefschrift richt zich op het niet-reagerende stromingsveld binnen de mengbuis en de verbrandingskamer. Geometrische en operationele parameters worden systematisch gevarieerd om hun invloed op het tijdsgemiddelde en fluctuerende stromingsveld te bepalen. Deze analyse verschaft inzicht in welke parameters het stromingsgedrag onder niet-reagerende omstandigheden significant beïnvloeden. Dergelijke inzichten zijn essentieel voor het interpreteren van waarnemingen onder reagerende omstandigheden, omdat ze een onderscheid mogelijk maken tussen veranderingen die voortkomen uit aanpassingen in het stromingsveld en veranderingen die veroorzaakt worden door verbrandingsprocessen. De resultaten tonen aan dat de dia-

meter van de verbrandingskamer, de randvoorwaarde van de uitlaat en de hoeveelheid axiale luchtinjectie (Axial Air Injection, AAI) een sterke invloed hebben op de algemene stromingsstructuur; voornamelijk door veranderingen in de grootte van de recirculatiezones, het type *vortex breakdown* en de snelheidsverdeling. Daarentegen beïnvloeden operationele parameters zoals de brandstofsamenstelling en de momentumfluxverhouding tussen de brandstof en lucht met name de snelheidsverdeling, terwijl de algemene stromingstopologie en fluctuerende stroming grotendeels onveranderd blijven.

In gedeeltelijk voorgemengde configuraties, waarbij brandstof en lucht niet perfect zijn voorgemengd en de brandstof vlak vóór de verbrandingskamer wordt geïnjecteerd, heeft de mengkwaliteit een cruciale invloed op de vlamstabiliteit en emissies. Om het mengproces onder niet-reagerende omstandigheden te beoordelen, maakt het tweede deel van deze studie gebruik van helium/luchtmengsels als substituut voor verschillende CH_4/H_2-mengsels, waarbij tracer-druppels worden ingezet om het mengproces te visualiseren zonder verstoring door verbranding. De effecten van de brandstofsamenstelling, inlaatsnelheid en *swirl*intensiteit op het mengproces worden systematisch geanalyseerd. De resultaten tonen aan dat de mengkwaliteit vooral wordt bepaald door de brandstofsamenstelling, waarbij lichtere brandstoffen het mengen bevorderen. Voor een gegeven samenstelling verbetert de mengkwaliteit met toenemende momentumfluxverhouding tussen brandstof en lucht tot een kritisch niveau, waarna geen verdere verbetering wordt waargenomen. Hoewel AAI het mengen nabij het injectiepunt vermindert, kan dit effect worden gecompenseerd door voldoende hoge *swirl*. Deze bevindingen vormen de basis voor het interpreteren van emissietrends onder reagerende omstandigheden.

Het derde deel van dit proefschrift onderzoekt de brandstofflexibiliteit van het gedeeltelijk voorgemengde verbrandingssysteem met AAI. Dit omvat een beoordeling van het operationele bereik, waarbij de condities voor *flashback* en *blowout* worden vastgesteld bij verschillende equivalentie-verhoudingen en waterstofgehalten, evenals de invloed van AAI op deze grenzen. Mechanismen voor vlamstabilisatie, afgeleid uit beelden en stromingsvelden van *OH Planar Laser-Induced Fluorescence* (PLIF), worden geanalyseerd om de waargenomen veranderingen in het operationele bereik te verklaren. Ten slotte wordt in een emissie-analyse onderzocht hoe de brandstofsamenstelling en de mate van AAI de emissieprestaties beïnvloeden en of deze effecten samenhangen met veranderingen in de mengkwaliteit. De resultaten tonen aan dat AAI het operationele bereik effectief vergroot en de *flashback*grens verhoogt voor brandstoffen met een hoog waterstofgehalte. Deze verbetering wordt toegeschreven aan een verschuiving in het mechanisme van vlamstabiliteit ten opzichte van situaties zonder AAI. Hogere niveaus van AAI leiden echter ook tot verhoogde NO-emissies, waarschijnlijk als gevolg van een verminderde menging van de brandstof en lucht.

NO_x-emissies worden sterk beïnvloed door de lokale brandstof-luchtmenging, het stromingsveld en de dominante NO-vormingsmechanismen. De relatieve bijdrage van deze mechanismen verandert aanzienlijk bij de overgang van methaan naar waterstof, wat de voorspelbaarheid van zowel de ruimtelijke NO-verdeling als de totale emissies in gedeeltelijk voorgemengde, brandstofflexibele verbranding bemoeilijkt. Het vierde deel van dit proefschrift presenteert daarom een gedetailleerd onderzoek naar NO-emissies in gedeeltelijk voorgemengde vlammen met AAI. Met behulp van PLIF wordt de ruimte-

lijke verdeling van NO in de verbrandingskamer in kaart gebracht, naast metingen van de totale NO-concentratie in de uitlaat. Deze gegevens worden geanalyseerd in relatie tot de vlamlocatie en het omliggende stromingsveld, wat inzicht biedt in de oorzaken van trends in NO-emissie en mogelijke reductiestrategieën. De resultaten tonen aan dat de NO-verdeling sterk afhankelijk is van de mate van AAI, die zowel het stromingsveld als de vlamstabilisatie beïnvloedt. Bovendien speelt de *lift-off* hoogte van de vlam een cruciale rol in de lokale brandstof-luchtmenging en NO-vorming, en verschuift deze de balans tussen NO-vormingsmechanismen die bijdragen aan de totale NO-productie.

Het vijfde en laatste deel bouwt voort op de inzichten uit de voorgaande hoofdstukken, waarin de momentumfluxverhouding werd geïdentificeerd als een belangrijke factor in de brandstof-luchtmenging. Dit hoofdstuk onderzoekt daarom hoe variaties in de momentumfluxverhouding tussen brandstof en lucht de stabiliteit van de verbrandingskamer en de emissies beïnvloeden. Deze verhouding wordt aangepast door de diameter van de brandstofinlaat te wijzigen. De studie beoordeelt hoe deze aanpassingen de vlamstabilisatie en het operationele bereik van het verbrandingssysteem beïnvloeden. De emissie-analyse, gebaseerd op uitlaatgasmetingen en de ruimtelijke verdeling van NO, beoordeelt de effecten op de NO-emissies. De resultaten worden geïnterpreteerd in de context van het menggedrag van de brandstof en lucht, wat voortbouwt op de inzichten uit het tweede deel van dit proefschrift. De bevindingen tonen aan dat een hogere momentumfluxverhouding het mengen bevordert en de NO-emissies verlaagt. Hoewel het mechanisme van vlamstabilisatie onveranderd blijft, verschuift de vlampositie bij hogere verhoudingen dichter naar de injector, wat leidt tot een verlaging van de *flashback*-limieten van het systeem.

Dit proefschrift biedt een fundamenteel inzicht in de processen en parameters die de stabiliteit en emissies bepalen in een gedeeltelijk voorgemengde, brandstofflexibele swirl-gestabiliseerde verbrandingskamer. De bevindingen verschaffen waardevolle inzichten in de wisselwerking tussen brandstofsamenstelling, injectorontwerp en stromingsveldkarakteristieken, en hoe deze factoren de stabiliteitslimieten, emissies en de algehele prestaties van de verbrandingskamer beïnvloeden. Door een systematisch onderzoek binnen een goed gekarakteriseerde geometrie konden duidelijke trends en onderliggende mechanismen worden geïdentificeerd, wat een solide basis legt voor het toekomstige ontwerp en de optimalisatie van brandstofflexibele verbrandingskamers. De verkregen inzichten zijn breed toepasbaar en van groot belang voor de ontwikkeling van verbrandingssystemen van de volgende generatie.

CONTENTS

LIST OF ACRONYMS

AAI	Axial Air Injection
CIVB	Combustion Induced Vortex Breakdown
CRZ	Central Recirculation Zone
FB	Flashback
FFT	Fast Fourier Transform
FoV	Field of View
ISL	Inner Shear Layer
JICF	Jet in Cross-flow
LBO	Lean Blowout
LES	Large Eddy Simulation
LHV	Lower Heating Value
LIF	Laser-Induced Fluorescence
ORZ	Outer Recirculation Zone
OSL	Outer Shear Layer
P&ID	Piping and Instrumentation Diagram
PIV	Particle Image Velocimetry
PLIF	Planar Laser-Induced Fluorescence
POD	Proper Orthogonal Decomposition
PVC	Precessing Vortex Core
SAF	Sustainable Aviation Fuel
SNR	Signal to Noise Ratio
SPOD	Spectral Proper Orthogonal Decomposition
TKE	Turbulent Kinetic Energy
TRL	Technology Readiness Level

LIST OF SYMBOLS

Roman letters

A	Area, m^2
c	Confinement Ratio
D	Mass Diffusivity, m^2/s
d	Diameter, mm
Da	Damköhler Number
δ	Length Scale, mm
f	Frequency, Hz
G_θ	Axial Flux of Tangential Momentum, $kg \cdot m^2/s$
G_x	Axial Thrust, $kg \cdot m/s$
J	Momentum Flux Ratio
l	Length, mm
Le	Lewis Number
$\dot{m}$	Mass Flow Rate, kg/s
P	Power, kW
p	Pressure, bar
$\dot{Q}$	Volumetric flow rate, L/min
r	Radius, mm
Re	Reynolds Number
s	Stoichiometric Ratio
s_l	Laminar Flame Speed, m/s
Sr	Strouhal Number
St	Stokes Number
s_t	Turbulent Flame Speed, m/s
Sw	Swirl Number
T	Temperature, K
T_ad	Adiabatic Flame Temperature, K
U	Axial Velocity, m/s
u	Velocity, m/s
V	Radial Velocity, m/s
W	Tangential Velocity, m/s
W	Molar Mass, mol
X	Mole Fraction
Y	Mass Fraction

Greek letters

α	Thermal Diffusivity, m^2/s
χ	Axial Air Injection, %
η	Azimuthal Vorticity, 1/s
ν	Kinematic Viscosity, $N \cdot s/m^2$
ω	Vorticity, 1/s
φ	Equivalence Ratio
ρ	Density, kg/m^3
τ	Time Scale, s
ξ	Axial Vorticity, 1/s
ζ	Radial Vorticity, 1/s

I

BACKGROUND & METHODOLOGY

1

INTRODUCTION

The urgency of transitioning to sustainable practices has never been greater due to the escalating effects of climate change. The Paris Agreement from 2015 represents a global commitment to keep the temperature increase below 2°C above pre-industrial levels, with the ambition to limit the increase to 1.5°C. Achieving this goal would have required global greenhouse gas emissions to peak by 2025, followed by a 43 % reduction by 2050 [1]. However, with emissions still on the rise, reaching this target is becoming highly unlikely. Carbon dioxide (CO_2) emissions contribute approximately 76 % of global greenhouse gas emissions, largely driven by the energy and transportation sectors [2]. While efforts to decarbonize these sectors are ongoing, progress varies across applications. Battery technology offers a promising solution for road transport, where electrification is rapidly advancing. In contrast, sectors such as aviation and large-scale power generation continue to rely on combustion engines due to their high energy density requirements.

At the same time, the aviation sector is growing fast, and is expected to continue to grow around 4 % annually over the next 20 years [3]. Additionally, global power demand is expected to rise sharply, driven by widespread electrification and the rapid growth of renewable energy. A notable share of this increase will come from data centres, with artificial intelligence emerging as the primary driver of their growing energy consumption [4]. In this evolving energy landscape, high-efficiency gas turbine power plants will play an increasingly important role. Their ability to provide flexible, dispatchable power makes them essential for stabilizing grids that rely on intermittent renewables. Modern gas turbines are a critical component of the transition toward a low-carbon energy future, ensuring reliability while supporting the shift to sustainable energy sources, with fuel efficiencies now reaching up to 63 % [5].

To meet the increasing energy demand while striving to meet the goals of the Paris Agreement, there is a need for more sustainable fuels than conventional carbon-based options. One of the most promising alternatives to carbon-based fuels is hydrogen (H_2), primarily because it burns without producing carbon emissions. Its combustion results in water as the main by-product, making it a cleaner and more sustainable fuel option. Hydrogen can be produced from various sources, each categorized by a colour code that

reflects their production method (see Figure 1.1). Most hydrogen production methods, except of green and pink hydrogen, rely on fossil fuels as energy source. As a result, significant amounts of CO_2 and methane (CH_4) are emitted during the production process. Green hydrogen, produced via electrolysis of water using renewable energy, is the most sustainable production option. However, its production costs remain significantly high, and it heavily depends on the availability of renewable energies. Currently, green hydrogen accounts for only about 1% of total hydrogen production, whereas coal-based hydrogen represents roughly 62%. By 2045, green hydrogen is projected to contribute approximately 45% of production [6]. In addition to production challenges, the low density of hydrogen makes its storage and transport a significant technical hurdle [7, 8]. These factors hinder the large-scale adoption of hydrogen production and introduce uncertainty about its availability in the near future.

As a result, it is essential to develop combustion systems that can operate in a fuel-flexible manner, capable of using a wide range of fuel mixtures, from conventional fossil fuels to pure hydrogen.

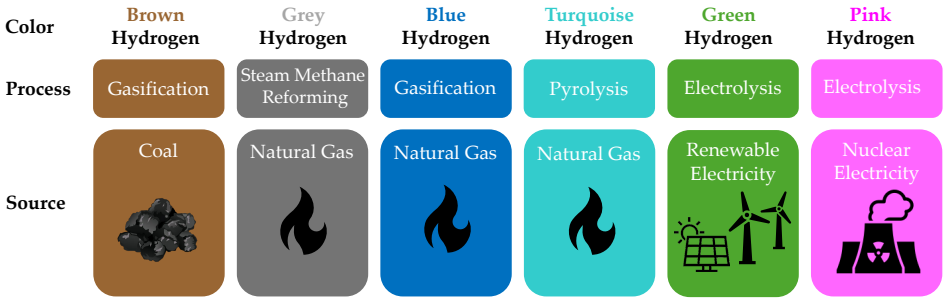

Figure 1.1: Colours of hydrogen (H_2) based on the production method.

1.1. MOTIVATION

Hydrogen has significantly different combustion characteristics than carbon-based fuels, making the design of fuel-flexible combustion chambers challenging. At the same equivalence ratio, the higher adiabatic flame temperature for hydrogen compared to carbon-based fuels leads to increased Nitrogen oxide (NO_x) emissions. NO_x emissions are formed during combustion when nitrogen (N_2) and oxygen (O_2) in the air react. Although the contribution of NO_x emissions to global warming is considerably smaller than that of CO_2 [2], NO_x still acts as an indirect greenhouse gas and contributes to climate change [9]. In order to minimize NO_x, it has become standard in many power generation processes using hydrocarbon fuels to fully premix the fuel and oxidizer before the combustion process. This guarantees a uniform temperature distribution in the flame and consequently controls NO_x emissions, which are strongly temperature dependent. However, the high reactivity and flame speed of hydrogen can shift the position of the flame in the combustion chamber, increasing the risk of flashback in fully premixed cases, where the flame can move upstream into the premixing zone [10, 11]. Flashback poses a serious safety risk by imposing a high thermal load on solid components.

To avoid flashback, a more suitable option for hydrogen combustion compared to fully premixing involves partial premixing of the fuel and the oxidizer by injecting the fuel as late as possible upstream of the combustion chamber, while still ensuring a high degree of fuel-air mixing. This is a widely used approach to keep the NO_x emissions low while minimizing the flashback risk. New combustion concepts or modifications to existing geometries are essential to enable partial premixing in fuel-flexible combustion systems. One example of a new approach is the micro-mix concept, which shows great potential for maintaining low NO_x emissions for both methane and hydrogen flames [12], while avoiding the risk of flashback, as the fuel enters the combustion chamber in a non-premixed manner. This combustion concept is based on a cross-flow mixing of gaseous fuel with air, which reacts in multiple small diffusion flames. By creating those micro flames with a short residence time of the products in the flame region, this results in a low NO_x formation. Implementing the micro-mix concept requires substantial modifications to the combustion chamber geometry and introduces a high pressure drop across the injector, which negatively impacts the gas turbine performance. This causes adoption in short term not to be feasible. As a stopgap solution, existing geometries can be modified to enable the accommodation of a range of fuel mixtures of conventional fuel to hydrogen.

Swirl-stabilized combustion is the most conventional form of flame stabilization in modern gas turbines and aero-engines. If the swirl number is high enough, a Central Recirculation Zone (CRZ) forms in the combustion chamber (see Figure 1.2), which aerodynamically anchors the flame away from the solid components [13]. This recirculation of hot combustion products back into the reaction zone, combined with low velocity regions in the Inner Shear Layer (ISL) and Outer Shear Layer (OSL), allows flames to stabilize even under very fuel-lean conditions. Apart from the CRZ, the flow field features a Outer Recirculation Zone (ORZ). The ORZ forms due to the sudden expansion of the cross-section between the premixing section and the combustion chamber.

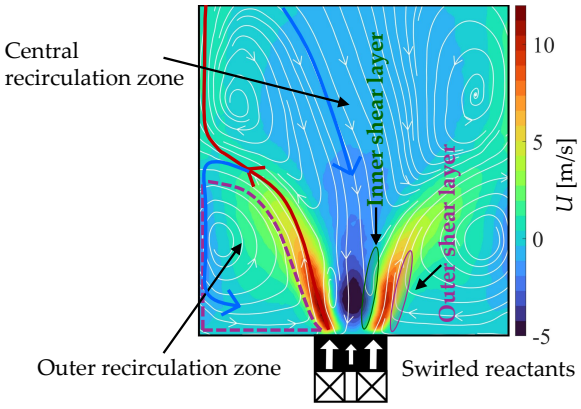

Figure 1.2: Flow field of the high-swirl burner investigated in this thesis. The illustration highlights key features such as the central and outer recirculation zones and the shear layers.

Stationary gas turbines are well-suited for fuel flexibility with hydrogen because they operate in controlled environments and can be gradually adapted to burn hydrogen or

hydrogen blends. Some modern heavy-duty gas turbines, like the GE B/E series [14], are already capable of burning the full range from 100 % natural gas (or methane) to 100 % H_2 in a diffusion mode. Additionally, the Ansaldo GT36 can achieve 100 % H_2 combustion with a unique sequential combustion concept, one premix stage followed by an auto-ignited second stage, overcoming the limits of traditional premixed combustion systems [15]. For traditional (partially) premixed swirl-stabilized configurations, the GE Vernova's 9HA [16] (see Figure 1.3a) and the Siemens SGT5-9000HL [17] (see Figure 1.3b) have demonstrated the capability to operate with hydrogen content up to 50 % in volume in the fuel mixture while maintaining low NO_x emissions. However, no gas turbine on the current market is capable of operating entirely fuel flexible up to 100 % H_2 in a premixed mode. Therefore, further research is needed to understand the flame stabilization mechanisms as well as pollutant formation in swirl-stabilized combustion chambers.

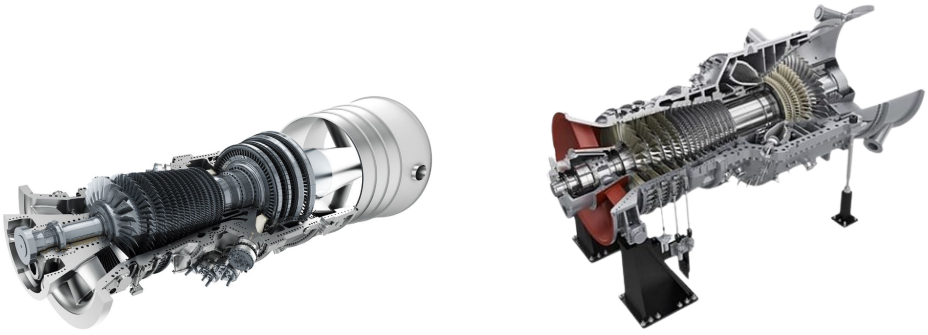

a) b)

Figure 1.3: Modern gas turbines operating designed for fuel-flexible up to 50 % H_2 content in the fuel mixture in premixed configuration. (a) GE 9HA gas turbine [16] (b) Siemens SGT5-9000HL gas turbine [17].

While much of the current development focuses on stationary gas turbines, also interest in fuel-flexible combustion systems for aviation has grown in recent years. Several projects, like the Clean Aviation CAVENDISH project [18], the APPU project [19], and the HOPE HORIZON project [20] are looking into the feasibility of dual-fuel combustor systems (capable of operating on 100 % H_2 and 100 % Sustainable Aviation Fuel (SAF)). However, testing dual-fuel combustion with hydrogen and SAF introduces challenges due to their different combustion properties. While hydrogen burns in gaseous phase and is therefore easier to inject, kerosene requires atomization and evaporation. Testing dual-fuel combustion in real flight scenarios adds further complexity, since significant changes to the aircraft are required, which raises the concern of safety and high costs. In contrast, stationary gas turbines provide a more immediate and controlled platform for advancing hydrogen combustion technologies, particularly with dual gaseous fuels such as methane and hydrogen.

Exploring the extensive parameter space necessary to identify the effective combustor design changes to achieve fuel flexibility, together with the need to understand fundamental phenomena like NO_x formation and flashback mechanisms, presents a significant challenge. Real-scale gas turbine combustion chambers are often not suitable for

such detailed investigations due to limited optical access, high costs, and safety constraints when handling hydrogen-rich mixtures. This makes laboratory-scale experiments an essential and practical alternative. Laboratory-scale setups provide a cost-effective and flexible platform for investigating fuel-flexible (CH_4/H_2) swirl-stabilized flames under well-controlled conditions. They allow optical access to the combustion chamber for detailed measurements and enable the safe exploration of innovative combustion concepts, delivering fundamental insights at a low Technology Readiness Level (TRL) before advancing to higher TRLs.

1.2. KNOWLEDGE GAP

Most laboratory studies investigating the effect of hydrogen enrichment in CH_4/H_2 swirl-stabilized flames have not investigated hydrogen contents above 80 % H_2 by volume [21]. Given the low molecular weight of hydrogen, transitioning from 80 % to 100 % H_2 represents a significant change in fuel composition in terms of both mass and energy content. This alteration affects both the chemical and the physical processes occurring in the reacting flow, thereby posing considerable challenges for the combustor operation. To stabilize 100 % H_2 flames, a suitable approach identified in the literature is Axial Air Injection (AAI), where a portion of the total combustion air is injected as non-swirling jets along the centreline of the swirling flow. Reichel et al. [22] demonstrated that AAI can stabilize hydrogen flames up to stoichiometric conditions, while maintaining low NO_x emissions. Although bluff-body stabilization also can support stable combustion of 100 % H_2 flames [23], AAI offers the additional benefit of aerodynamically stabilizing the flame, which in turn reduces the thermal load on surrounding solid components.

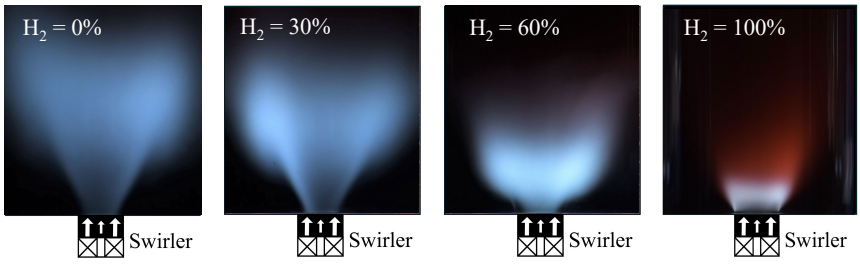

Figure 1.4: Flame shapes of the dual-fuel (CH_4/H_2) swirl-stabilized combustor investigated in this thesis for different volumetric hydrogen contents at a constant thermal power.

Figure 1.4 presents several flames with varying hydrogen content in the fuel at constant power, measured in the TU Delft swirl-stabilized burner studied in this thesis, which deploys the concept of AAI [24, 25]. As the hydrogen content increases, the overall characteristics of the flame change noticeably. The flame becomes more compact and stabilizes further upstream. Additionally, its shape transitions from a V-shape to a shorter, wider structure. These differences highlight the distinct combustion properties of H_2 compared to CH_4 and the challenges of designing a combustor capable of operating efficiently with both fuels.

Ensuring rapid mixing of fuel and oxidizer in partially premixed swirl-stabilized ge-

ometries before entering the combustion chamber remains a significant challenge. The most common ways to inject the fuel into the air are perpendicular to the swirling flow (*jet in cross-flow configuration*) or parallel to the swirling flow (*jet in co-flow configuration*). The jet in cross-flow configuration possesses a high potential to mix the fluid streams more efficiently and faster than other configurations like the jet in co-flow configuration [26]. Therefore, this injection concept is used in the injectors of many gas turbines [27]. However, the mixing process in jet in cross-flow is complex, as it is significantly influenced by a diversity of parameters, like the fuel jet momentum, the fuel Reynolds number, and the fuel density [28]. This makes it challenging to predict the degree of mixing in systems designed for fuel flexibility, where fuel properties can vary significantly. Additionally, while mixing of a jet in cross-flow configuration with an axial cross-flow has been studied comprehensively, the effect of a swirling cross-flow on the mixing process remains largely unexplored.

Many aspects of the mixing behaviour, flow field, and combustion processes in partially premixed swirl-stabilized combustion are not yet fully understood, particularly regarding their complex interactions. While certain individual features have been studied in detail, a comprehensive understanding of how they interact is still lacking. Swirl-stabilized combustion using jet in cross-flow in combination with flow features like AAI and a varying fuel composition of the fuel jets is inherently complex, requiring an examination of how various parameters interact. To date, the key design and operating parameters that determine combustor performance in a dual-fuel (CH_4/ H_2) swirl-stabilized burner have not been fully established. In order to operate on both carbon-based fuels and hydrogen within the same combustion chamber, it is essential to identify the key design and operating parameters that influence flame stability and emissions. These parameters provide essential input for developing design and operational considerations when retrofitting existing combustor geometries.

1.3. RESEARCH AIM AND METHODOLOGY

In order to uncover the underlying parameters that determine combustor performance in CH_4/H_2 fuel-flexible combustion chambers

Main research goal

This work aims to identify the governing parameters for flame stability and emissions in partially premixed swirl-stabilized CH_4/H_2 flames with Axial Air Injection

The key design and operating variables that are hypothesized to influence flame stability and emissions based on the literature survey are outlined in Figure 1.5. These include the fuel injection strategy (the fuel density ρ and the momentum flux ratio J), operating conditions (equivalence ratio φ, thermal power P_{th}, and the volumetric hydrogen content in the fuel XH_2), and the geometric design parameters, including the swirl number and the level of AAI. Throughout this thesis, the impact of these variables on flame stability (flashback and blowout) and emissions is evaluated. To achieve this, their influence on stability and emission indicators—such as the degree of fuel-air mixing and the flame front location—is assessed. These indicators are then compared with

the measured emissions and stability limits of the combustor to identify correlations between the indicator values and the measured flame stability and emission levels.

From this analysis, the dominant design and operating variables that govern flame stability and emissions are identified. These relationships provide insight into the fundamental causes of variations in combustor performance, thereby revealing the key mechanisms driving stability and emissions in a partially premixed swirl-stabilized combustor. This understanding can contribute to the development of design considertations for achieving flashback-free operation with low emissions.

The following specific sub-research questions are answered in this work:

Subquestion 1

What are the effects of the geometric parameters and the operating conditions on the flow field in a non-reacting swirl-stabilized combustor with AAI and jet in cross-flow fuel injection?

Subquestion 2

How do the momentum flux ratio, the density ratio, and AAI affect fuel-air mixing in a jet in swirling cross-flow configuration?

Subquestion 3

What is the effect of AAI on the emissions and operational range of CH_4/H_2 swirl-stabilized flames?

Subquestion 4

What is the effect of the flow field (AAI, fuel injection, CRZ) on the NO emissions?

Subquestion 5

What is the effect of the momentum flux ratio on the emissions and operational range of CH_4/H_2 swirl-stabilized flames?

This research was conducted experimentally in a laboratory scale dual-fuel swirl-stabilized burner that incorporates the concept of AAI for stabilizing hydrogen flames. Given the extensive parameter space needed to isolate the dominant design and operating parameters and the large domain, computational studies employing Direct Numerical Simulation (DNS) or Large Eddy Simulation (LES) would require long simulation times. Experimental studies at a lab scale, on the other hand, allow for the exploration of a wide range of conditions. This study relies on the application of several optical and non-optical measurement techniques to measure the relevant parameters determining emissions and flame stability. To address the knowledge gap identified in Section 1.1, this study deploys Particle Image Velocimetry (PIV) and planar laser imaging to visual-

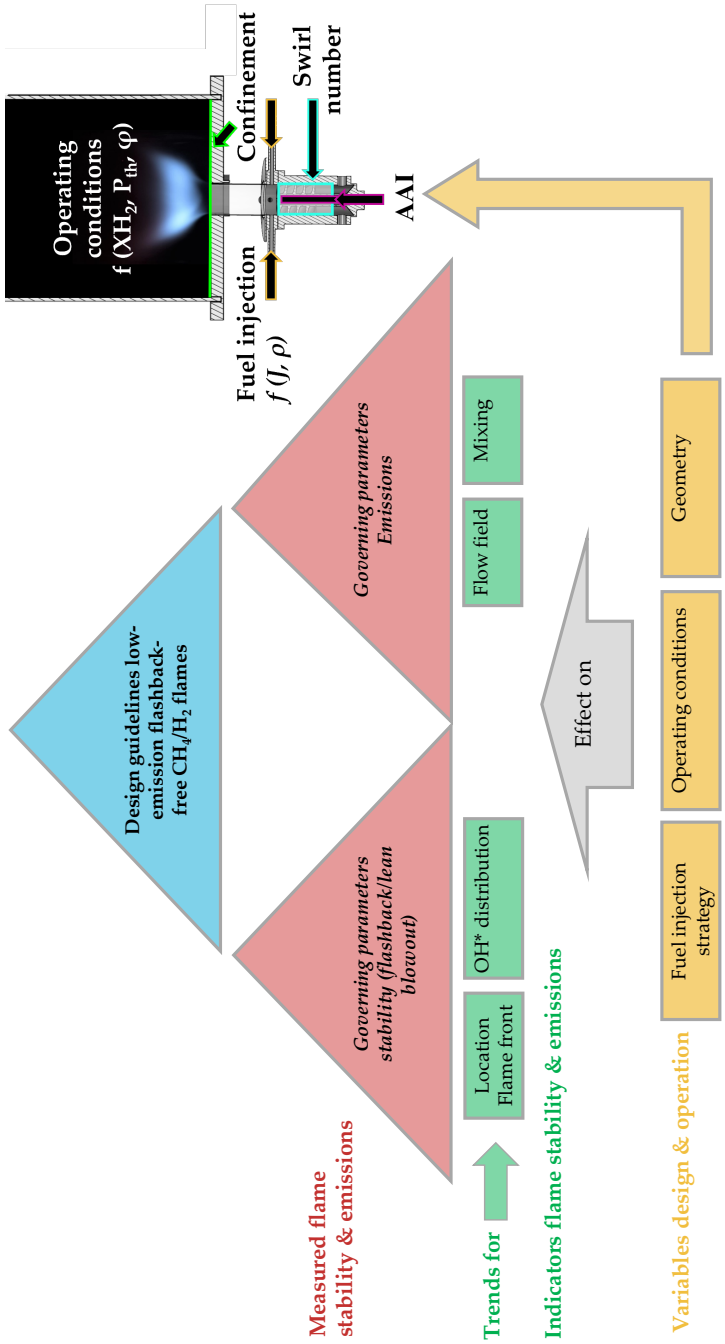

Figure 1.5: Illustration of the research conducted to identify the dominant parameters affecting flame stability and flashback, aimed at deriving design rules and an overview of the investigated variables.

ize the flow field in the combustion chamber in reacting and non-reacting conditions, as well as the mixing process in the non-reacting conditions. Additionally, the flame shapes and spatially resolved concentration of minor species (OH & NO) are obtained by PLIF and OH* chemiluminescence. Moreover, probe measurements are used to measure the exhaust gas composition after combustion.

1.4. DISSERTATION OUTLINE

The dissertation structure can be seen in Figure 1.6 and is as follows:

CHAPTER 2 provides the theoretical background for this dissertation. It includes a review of the relevant literature on swirl-stabilized CH_4/H_2 combustion, mixing in a jet in cross-flow, NO_x formation mechanisms, and flashback phenomena in swirling flames. Furthermore, it presents research on the effects of hydrogen enrichment on methane flames, focusing on emission characteristics and flame stability. The chapter concludes with an overview of state-of-the-art burner geometries for swirl-stabilized H_2 combustion.

CHAPTER 3 gives an overview of the methodology used in this work. This chapter describes in detail the geometry and operating conditions of the experimental set-up for the reacting and non-reacting studies. Additionally, it provides an overview of the measurement techniques and post-processing methods used in this work.

CHAPTER 4 answers Subquestion 1, by examining the non-reacting flow field within the combustion chamber under varying geometric parameters (AAI, swirl number, and confinement ratio) and different fuel compositions as well as the momentum flux ratio between fuel and air. This chapter presents an analysis of the time-averaged flow field and explores the characteristics of the unsteady flow using Spectral Proper Orthogonal Decomposition (SPOD). The primary focus is on the dynamics of the Precessing Vortex Core (PVC).

CHAPTER 5 answers Subquestion 2 by assessing how the mixing in a jet in cross-flow configuration is affected by different parameters. The focus lies on the effects of the momentum flux ratio and the density ratio of fuel and air, as well as the role of AAI and the swirl number. The mixing is experimentally evaluated in non-reacting conditions, by seeding a surrogate fuel stream with DEHS droplets and measuring the droplet concentration in the premixing section by means of Mie scattering of the particles. The mixing process for different fuel compositions is analysed for varying levels of AAI and fuel jet compositions at two different swirl numbers.

CHAPTER 6 answers Subquestion 3 by examining how AAI affects the combustor performance for two different swirl numbers across different levels of hydrogen in the fuel mixture. This includes an analysis of the exhaust gas emissions at varying levels of AAI. Additionally, the operational range of the combustor is evaluated to determine the effect of AAI on the flashback resistance and blowout limits of the combustor. A flow field analysis and a comparison of the flame shapes and stabilization mechanisms give insights into how the flames are anchored in the

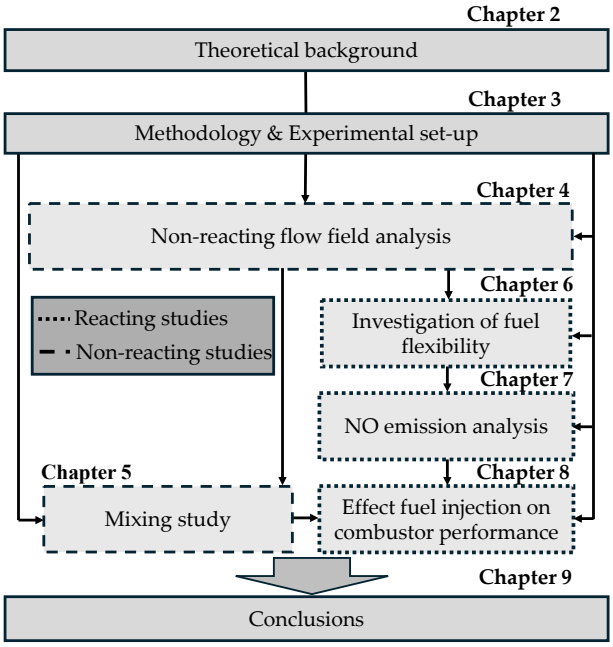

Figure 1.6: Layout of the dissertation.

combustion chamber and how the flame and flow field interact for the varying operating conditions.

CHAPTER 7 answers Subquestion 4 by exploring how the flow field in the combustion chamber relates to the NO emissions. The planar NO distribution within the combustion chamber is compared with the planar flow field and the location of the flames in the combustion chamber, to identify where NO is formed and to understand the role of different flow features in this process. Additionally, the NO distribution inside the combustion chamber is compared with measured exhaust gas values to assess how NO distribution impacts overall NO emissions in the exhaust. This is assessed for varying levels of AAI and hydrogen content.

CHAPTER 8 answers Subquestion 5 by investigating the effect of the fuel injection strategy (varying momentum flux ratio in jet in cross-flow configuration) on the emissions and operational range of the dual-fuel combustor by means of an exhaust gas analysis and OH and NO PLIF. This analysis aims to determine what the effect of the momentum flux ratio on the NO emissions is and whether the flashback resistance is affected across the full range of hydrogen concentrations.

CHAPTER 9 presents the overall conclusions, summarizing the findings of the previous chapters into design recommendations based on the identified dominant parameters. They also highlight the key contributions of this work, discusses the limitations, and provides an outlook for future work.

2

THEORETICAL BACKGROUND

This chapter provides the necessary background for the following chapters of this dissertation. It begins with an exploration of swirling flows, outlining methods for quantifying swirl strength and describing the swirling flow aerodynamics. Next, it reviews literature on swirl-stabilized combustion, focusing on the effect of the swirl number on the flame characteristics as well as the effect of combustion on the PVC dynamics. The chapter also summarizes the different NO formation mechanisms. This is followed by a discussion of key mixing mechanisms in jet in cross-flow configurations. Subsequently, the combustion characteristics and fuel properties of hydrogen as an alternative fuel are discussed. Furthermore, the operational range of gas turbines is described, with particular emphasis on the mechanisms of flashback and blowout. Finally, the chapter concludes with a review of relevant studies on the effects of hydrogen enrichment in methane flames, particularly regarding emissions and stability, and presents geometries that can be found in literature for partially-premixed hydrogen swirl-stabilized flames.

2.1. SWIRLING FLOWS

Swirling flows play a crucial role in a wide variety of industrial applications. In non-reacting scenarios, they are utilized in devices such as vortex amplifiers and heat exchangers. In reacting systems, swirlers are extensively employed in combustion applications, including gas turbines and industrial furnaces.

QUANTIFICATION OF SWIRL

The intensity of swirl can be defined with the non-dimensional swirl number proposed by Beér et al. [29]. The swirl number given in Equation 2.1 is defined as the axial flux of tangential momentum G_θ (Equation 2.2) divided by the axial thrust G_x (Equation 2.3) times the outer radius of the swirl r_0

$$Sw = \frac{G_\theta}{r_0 \cdot G_x} \tag{2.1}$$

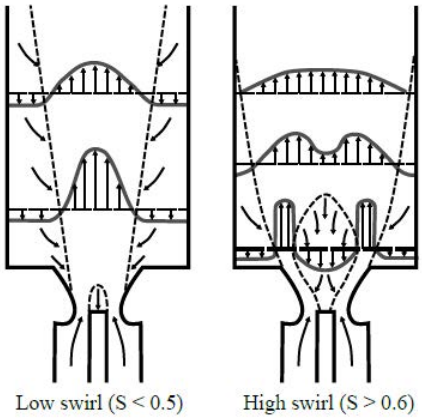

Figure 2.1: Left: High swirl flow field featuring a CRZ, Right: Low swirl flow field, figure taken from [30].

$$G_\theta = \int_0^R (\rho W r)(U 2\pi r) dr \tag{2.2}$$

$$G_x = \int_0^R (\rho U)(U 2\pi r) dr + \int_0^R p 2\pi r dr \tag{2.3}$$

In these equations, U denotes the axial velocity component, W the tangential velocity component, ρ the fluid density, and p the static pressure within any cross-section of the swirling flow. Accurately determining the pressure distribution and precise velocity components is complex. To circumvent this difficulty, Beér and Chigier [29] proposed to disregard the pressure term in Equation 2.3, provided the outlet flow conditions of the swirler are used to define the swirl number. Consequently, Equation 2.3 remains solely reliant on the axial velocity profile at the swirler outlet.

Based on the swirl number, the swirling flow can be classified as high swirl (Sw >0.6) and as low swirl (Sw < 0.5). Both regimes are shown in Figure 2.1. Introducing swirl to a previously non-swirling jet generates a radial pressure gradient that significantly influences the flow dynamics. As the jet expands downstream, the tangential velocity diminishes, reducing the radial pressure gradient. Upstream, a stronger radial pressure gradient induces a negative axial pressure gradient near the centreline, slowing the axial velocity along the jet core. With increasing swirl intensity (and above Sw = 0.6), this velocity reduction becomes more pronounced, eventually reversing the flow and forming a CRZ. Two main types of vortex breakdown have been observed. The bubble type vortex breakdown is characterized by the presence of an approximately axisymmetric, spheroidal recirculation zone (bubble) of size the same order as that of the vortex core. The flow field surrounding the bubble closely resembles that of a spherical rigid body, resulting in a shift from a jet-like profile upstream to a wake-like pattern downstream. The cone type vortex breakdown is characterized by a CRZ with a conical shape, where the swirling jet undergoes significant radial expansion downstream of the stagnation point. This forms a thin conical sheet with a wide opening angle. This sheet extends over a

considerable distance before eventually contracting again, which results in a large recirculation zone [31]. The size and position of the CRZ is dependent on the level of swirl [29, 32], with an increased entrained mass flow, increased jet opening angle with increased swirl number and more upstream location of the CRZ. A detailed review of the vortex breakdown mechanisms can be found in [13, 33]. Between $0.5 < Sw < 0.6$ there is a transition swirl regime. During this transition phase, the swirl intensity is not high enough for vortex breakdown to occur, but can still occur with the support of the chamber geometry and turbulence levels.

AERODYNAMICS OF SWIRLING FLOWS

The vortex breakdown pattern for aerodynamic flame stabilization in swirl burners without a centre body is strongly governed by the vorticity transport equation. The inviscid vorticity transport equation is given by:

$$\frac{D\omega}{Dt} = \frac{\delta}{\delta t}(\omega) + (u \cdot \nabla)\omega = (\omega \cdot \nabla)u - \omega(\nabla \cdot u) + \frac{1}{\rho^2}(\nabla \rho \mathrm{x} \nabla p) \tag{2.4}$$

Where ω is the vorticity, u the velocity vector ρ the density and p the pressure. The first term on the right-hand side of the equation represents the effect of stretching and tilting of vortices, which is the only transport term present in isothermal conditions. The second describes the vorticity transport term due to volume expansion due to heat release, and the third term accounts for the vorticity generation due to baroclinic torque. In a steady, inviscid, and axisymmetric flow, the vorticity components are given by [34]:

$$\zeta = \frac{1}{r}\frac{\delta(rV)}{\delta r}, \xi = -\frac{\delta U}{\delta z}, \eta = \frac{\delta U}{\delta z} - \frac{\delta W}{\delta z} \tag{2.5}$$

Where ζ, ξ and η are the radial, axial and azimuthal vorticity components, respectively. U, V and W are the axial, radial and azimuthal velocity components, respectively. The azimuthal vorticity induces in the case of rotational symmetry an axial velocity component according to the law of Biot-Savart, which is given as follows [35]:

$$U_{\mathrm{ind}}(z) = \frac{1}{2}\int_{-\infty}^{\infty}\int_{0}^{\infty} \frac{r*^2 \eta(r*, z*)}{[r*^2 + (z - z*)^2]^{3/2}} dr* dz* \tag{2.6}$$

If a swirling flow passes through a diverging section, such as a combustion chamber, the radii of the stream surfaces increase. This effect is driven by centrifugal forces resulting from the swirling motion of the flow. Due to the conservation of angular momentum, the azimuthal velocity decreases in the axial direction, leading to a reduction in azimuthal vorticity. If this decrease in azimuthal velocity is significant enough to cause the azimuthal vorticity η to become negative, the stagnating core flow ejects fluid outward, further increasing streamline divergence. As a result, the additional decrease in azimuthal velocity generates more negative azimuthal vorticity, initiating a feedback loop that ultimately leads to abrupt vortex breakdown. In both the non-reacting case and all reacting cases where the flame stabilizes within the combustor, the position of the upstream end of the recirculation bubble is determined by the balance between axial flow and the induced velocity opposing the main flow.

2.2. SWIRL-STABILIZED COMBUSTION

Swirl-stabilized combustion is state-of-the-art in most gas turbines. As explained in the previous section, if the level of swirl is high enough, a toroidal CRZ forms, due to the generation of a positive pressure gradient along the axial axis. This recirculation zone plays a crucial in the flame stabilization process, by recirculating heat and active radicals back into the reaction zone. Additionally, the low velocity region in the CRZ serves as an aerodynamic flame holder, stabilizing the flame away from solid components, where the local flow speed match the flame speed.

Finally, recirculating hot gases into the reaction zone and promoting rapid mixing near the exit nozzle reduces the flame length, potentially reducing it to as little as one-fifth of that observed in a non-swirling flame [29, 36]. The qualitative representation of a swirl-stabilized flow field with the recirculation zones and shear layers, as shown in Figure 1.2, applies to a wide range of Sw and Re numbers, including those typical of gas turbine operating conditions [37].

EFFECT OF COMBUSTION IN SWIRLING FLOWS

The central recirculation zone (CRZ) is the most relevant flow feature for the flame stabilization, by recirculating hot combustion products and radicals back to the unburnt mixture, sustaining continuous flame ignition. The outer recirculation zone (ORZ) is significantly influenced by high heat transfer rates to the combustion chamber walls, making it less effective at sustaining the flame. The presence of combustion can have a dominant effect on the swirling flow field. Under reacting conditions, both the size and strength of the CRZ typically decrease [36, 38]. Here, the strength of the CRZ refers to the ratio of reverse flow to inlet flow at a certain streamwise location, whereas the size denotes the extent of the region exhibiting negative axial velocity within the flow field. This reduction occurs because heat release causes thermal expansion of the gas, increasing the axial velocity more than the tangential velocity. The change in axial velocity depends on both the overall amount of heat released and the location of heat release. When the flame stabilizes close to the upstream end of the recirculation zone, it can strongly influence the velocity field. In contrast, if the flame stabilizes much further downstream its impact on the velocity field becomes minimal [39]. The strength of the CRZ during combustion is related to the effective swirl number, which accounts for combustion induced changes in tangential and axial velocities [38]. In reacting cases, the negative axial velocities within the CRZ can be overall higher than in non-reacting cases. As a result, vortex breakdown can appear in some reacting cases, whereas no vortex breakdown occurs in the corresponding non-reacting case. This can be explained with the adverse pressure gradient present in swirling flows

$$\frac{\delta p}{\delta z} = \frac{\delta}{\delta z} \int_0^R \rho [W^2/r] dr \tag{2.7}$$

This equation demonstrates, that when the gas density ρ decreases due to combustion while the tangential velocity W remains relatively constant, the adverse pressure gradient $\delta p/\delta z$ will increase [39]. This adverse pressure gradient acts as a force in the negative z-direction. Additionally, the previously mentioned baroclinic torque, which

produced negative η in swirl-stabilized flames contributes to the generation of negative axial velocity.

Figure 2.2 presents the non-reacting and corresponding reacting flow fields for a CH_4 flame in the TU Delft swirl-stabilized burner with a swirl number Sw = 0.7, obtained using PIV. In the reacting case (Figure 2.2b), the axial velocities within the swirling jet are significantly higher compared to the non-reacting case (Figure 2.2a). Additionally, the size of the CRZ is reduced in the reacting case, as indicated by the contour of zero axial velocity. Furthermore, the regions of high negative velocity within the CRZ (dark blue areas) extend further downstream in the reacting case, suggesting either an increased generation of negative velocity due to baroclinic torque or the presence of a stronger adverse pressure gradient.

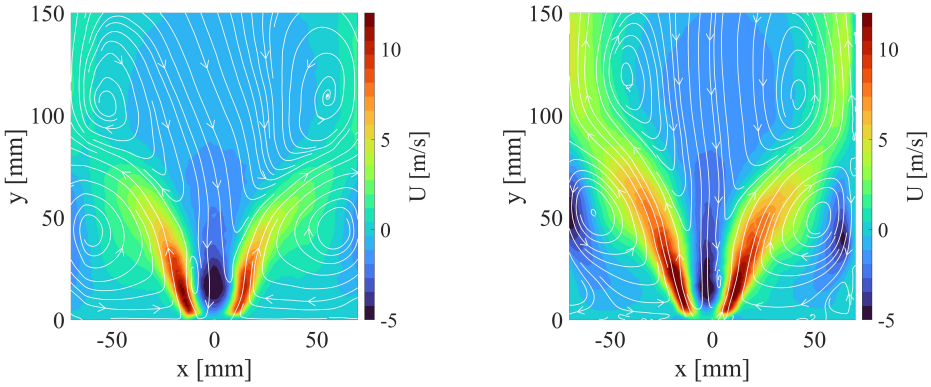

Figure 2.2: Average streamwise velocity fields of the swirl-stabilized burner investigated in this thesis for the (a) non-reacting condition and (b) the corresponding reacting condition.

EFFECT OF SWIRL NUMBER

Many studies focused on the effect of the swirl number on the flame characteristics. Increasing the swirl number in the reacting case leads to a more upstream position of the flame in the flow field, which significantly increases the flashback risk. This is caused by an increase in adverse pressure gradient $\delta p/\delta z$ due to higher tangential velocities, which serves as a force acting in the negative z-direction. Additionally, increasing the swirl number decreases the height of flame [39, 40]. Increasing Sw to $Sw > 1$ has shown to not significantly influence the height any more [39]. Beyond the flame structure, many studies also focussed on the effect of the swirl number on the emissions. Generally it has been observed, that a higher swirl number reduces CO and unburned hydrocarbon emissions, as higher swirl numbers prolongs the residence time in the reaction zone, helps to achieve complete combustion [41, 42]. Regarding NO_x emissions, different trends have been observed. Several studies report a decrease in NO_x emissions with an increase in Sw, attributed to stronger mixing as the turbulence intensity increases [41, 43]. However, other studies observe an increase in NO_x emissions, resulting from longer residence times in the reaction zone [44]. As a result, the effect on NO_x emissions reflects

the balance between enhanced mixing, which tends to reduce emissions, and increased residence time, which tends to promote them.

In summary, the impact of heat release on swirling flow fields is strongly dependent on the specific flow and flame characteristics, and often requires case-by-case analysis for each geometry. Combustion has a significant influence on the flow field, making it insufficient to base combustor design solely on non-reacting studies. Nevertheless, non-reacting flow field investigations can still offer valuable insights into the effects of operating and geometrical parameters, without the added complexity introduced by heat release.

PRECESSING VORTEX CORE

The formation of a CRZ is often accompanied by a precessing vortex core (PVC). The PVC is a self-excited single helical (azimuthal wave number $m = 1$) vortex structure that precesses around the central axis of the flow. Figure 2.3 shows the PVC structure illustrated with the $p = 101\,200$ Pa isoline in the TU Delft swirl stabilized burner for $Sw = 1.1$. The PVC is wrapped around the central vortex breakdown bubble and the windings are directed opposite to the swirl direction. The PVC originates from a region of absolute instability in the ISL, then grows to the OSL, and finally might impose its frequency on the whole flow field [45] in the combustion chamber.

The PVC can significantly influence the combustor performance. It can affect the flame-vortex interaction, which can lead to global heat release oscillations, potentially inducing thermoacoustic instabilities [46]. It also can enhance mixing by promoting large-scale coherent structures. Early research showed that the PVC can improve flame stability and reduce NO_x emissions, by enhancing the vortex-induced fuel-air mixing close to the combustion chamber inlet [47, 48]. Later research however, has shown that the presence of the PVC might also increase NO_x emissions, due to an increase in flame surface in the ISL, which locally increases the residence time of hot products [49].

The presence and characteristics of the PVC in the non-reacting conditions depend on various factors, including the swirl number and operating conditions. The PVC frequency follows a linear trend with increasing mass flow rate [50], and the frequency increases with increased swirl number [51].

For turbulent flows, at a constant swirl number, the Strouhal number is independent of the Re number. The Strouhal number is defined as $Sr_{\mathrm{PVC}} = \frac{f d_{\mathrm{MT}}}{U_\infty}$, where f is the frequency of the PVC, d_{MT} is the diameter of the tube and U_∞ is the velocity of the incoming flow. Sr increases linearly with increasing swirl number [51, 52]. The presence and type of PVC is also dependent on the swirl number and the type of vortex breakdown. If the swirl number is too low, e.g. $Sw < 0.6$, no vortex breakdown occurs, and consequently no PVC is formed. If the swirl number is high enough, and a bubble type vortex breakdown occurs, the flow field typically exhibits a strong PVC at a distinct frequency. For a cone type vortex breakdown the PVC is much less consistent, which can be seen in much noisier shapes in the coherent structures of the flow field and varying PVC frequencies [53].

In the reacting case, the PVC presence is strongly dependent on the flame shape. For flames lifted off the injector (M-flames), the PVC is typically sustained in the reacting case. For flames attached to the injector (V-flame), the PVC is suppressed [50]. If the

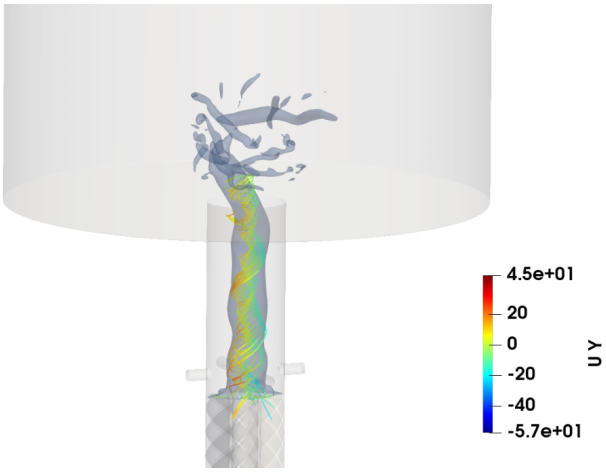

Figure 2.3: PVC illustrated with the p = 101200 Pa isoline. Visualization from in-house LES simulations, Courtesy of G. Ferrante [24].

flame is attached, there is a strong density gradient between the high densities in the swirling jet of unburnt gas, and low densities in the burnt gas in the CRZ and ORZ. This density gradient introduces a baroclinic torque, which crucially affects the growth rate of the instability, which eventually leads to the suppression of the PVC instability [50]. The frequency of the PVC in reacting conditions is slightly higher than in non-reacting conditions, but still follows a linear trend with increasing mass flow rate $\dot{Q}$ [50, 54]. Understanding the dynamics of the PVC is crucial because it can strongly influence flame stability, mixing, and pressure oscillations in swirl-stabilized combustors.

2.3. NO_x FORMATION

Nitrogen oxides (NO_x) are produced during combustion through the reaction of nitrogen N_2 and oxygen O_2 in the air, significantly contributing to global warming as an indirect greenhouse gas [9]. Additionally, it significantly impacts human health and biological ecosystems, causing effects such as acid rain and ozone depletion [55]. NO_x emissions are mostly composed of nitric oxide (NO) emissions, with smaller contributions from nitrogen dioxide (NO_2) and nitrous oxide (N_2O). The formation of NO_x in combustion systems is primarily influenced by the flame temperature, the residence time of the reactants in the high-temperature zone, and the availability of oxygen. In the combustion of fuels that do not contain nitrogen compounds, nitrogen oxides (NO) are produced from molecular nitrogen N_2 in the air through the breaking of the nitrogen-nitrogen triple bond. This process occurs through four distinct pathways, each involving a different mechanism for breaking the N_2 bond. In the next subsections, those mechanisms are briefly described.

ZELDOVICH OR THERMAL NO MECHANISM

Thermal NO_x is formed through the high-temperature reaction of N_2 and O_2 in the combustion air. This mechanism is described by the extended Zeldovich mechanism [56], which includes the two following main reactions [57]:

$$N_2 + O \rightleftharpoons NO + N^- \tag{2.8}$$

$$N^- + O_2 \rightleftharpoons NO + O \tag{2.9}$$

The reaction between OH and N is important in fuel-rich combustion zones, where the [OH]>>[O] ratio is high. This reaction is described by the following equation:

$$N^- + OH \rightleftharpoons NO + H \tag{2.10}$$

The rate of thermal NO_x formation increases exponentially with temperature, making it a significant concern in high-temperature combustion systems. The first reaction (Equation 2.8) is considered to be the rate determining reaction, and it is the one that requires the most activation energy. This allows the reaction to proceed only at high temperatures ($T > 1800$ K), therefore the name thermal NO formation mechanism. This makes fuels with a higher adiabatic flame temperature, such as hydrogen, more susceptible to thermal NO formation compared to hydrocarbon fuels.

If assuming that the initial concentration of NO is low, the overall rate of thermal NO formation can be expressed as

$$\frac{d[NO]_{\text{zeldovich}}}{dt} = 2k_{f1}(T)[O][N_2] \tag{2.11}$$

Where k_{f1} is the rate constant for the first reaction $k_{f1} = 1.8 \cdot 10^{14}$ exp(-318kJmol^{-1}/RT), [O] and [N_2] are the concentrations of oxygen and nitrogen, respectively. In most air-fed combustion cases, the molecular nitrogen concentration remains relatively constant. As a result, the formation rate of thermal NO primarily depends on temperature, through the reaction rate k_{f1}, and the concentration of atomic oxygen.

PROMPT MECHANISM

NO_x formation through the prompt or Fenimore mechanism [58] is most prominent in fuel-rich flames, where the concentration of hydrocarbon radicals is high, and flame temperatures are low. It is produced by the reaction of hydrocarbon radicals with nitrogen in the combustion air.

The rate determining reaction for this NO formation mechanism [59]

$$CH + N_2 \rightleftharpoons HCN + N \tag{2.12}$$

Once the hydrogen cyanide (HCN) and nitrogen N are produced they react rapidly to form NO. The actual formation involves a complex series of reactions and many possible intermediate species. The route now accepted is as follows [57]:

$$HCN + O \rightleftharpoons NCO + H \tag{2.13}$$

$$NCO + H \rightleftharpoons NH + CO \tag{2.14}$$

$$NH + H \rightleftharpoons N + H_2 \tag{2.15}$$

$$OH + N \rightleftharpoons NO + H \tag{2.16}$$

Since the prompt mechanism is dependent on the concentration of CH radicals and is fast compared to the main combustion reactions, the NO via this pathway is mainly produced in the reaction zone [60].

N_2O MECHANISM

NO can also be formed through the N_2O mechanism via the following reaction [57]:

$$N_2 + O \rightleftharpoons N_2O \tag{2.17}$$

The N_2O then reacts with atomic oxygen or hydrogen to form NO:

$$N_2O + O \rightleftharpoons 2\,NO \tag{2.18}$$

$$N_2O + H \rightleftharpoons NO + NH \tag{2.19}$$

The N_2O mechanism is particularly relevant in low temperatures and lean conditions. Therefore, apart from lean-premixed combustion applications, it only plays a minor role compared to the Zeldovich mechanism and the prompt mechanism.

NNH MECHANISM

In this mechanism, NO is formed through the reaction of nitrogen and hydrogen atoms [61]

$$N_2 + H \rightleftharpoons NNH \tag{2.20}$$

Afterwards, the NNH oxidizes with oxygen to form NO and NH:

$$NNH + O \rightleftharpoons NO + NH \tag{2.21}$$

The NNH mechanism has been proposed to be the dominant mechanism in fuel-rich hydrogen flames [62], where the temperature is too low for NO formation via the Zeldovich mechanism, and no carbon atoms are present for the formation of prompt NO.

2.4. MIXING OF JET IN CROSS-FLOW

A high degree of fuel-air mixing reduces NO_x emissions by creating a more uniform temperature profile in the flame, which limits the NO_x formation via the thermal pathway. Rapid mixing of fuel and oxidizer is especially important in partially premixed combustion, where there is limited time to achieve complete mixing. Jets injected perpendicular to the cross-flow (*jet in cross-flow*) have strong potential for achieving rapid mixing. As a result, this technique is widely used in applications where efficient fuel–air mixing must occur within a short time, such as in scramjets [63]. The mixing process is highly complex due to various vortical structures forming in the flow field and depends on a wide range of parameters.

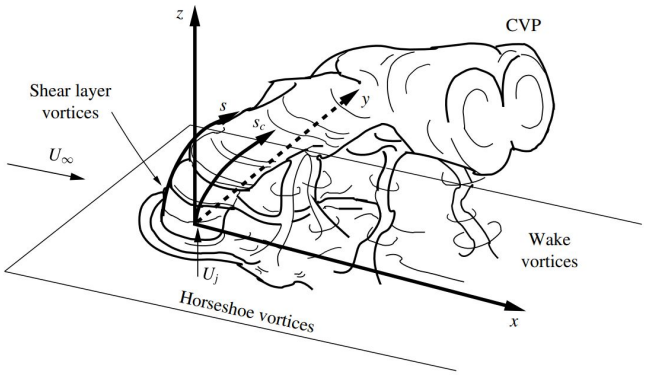

Figure 2.4: Illustration of jet in cross-flow vortices [64].

2.4.1. AXIAL CROSS-FLOW

Figure 2.4 shows an example of the flow and vortex structure of a jet in axial cross-flow configuration [64]. The jet is injected perpendicular to the cross-flow, resulting in the formation of a horseshoe vortex, a counter-rotating vortex pair (CVP), and a vortex pair in the wake of the jet. The horseshoe vortex is formed by the interaction between the jet and the cross-flow. The counter-rotating vortex pair in the jet wake is formed by the shear layer between the jet and the cross-flow. The vortex pair in the wake of the jet is formed by the jet shear layer. The interaction of these vortices significantly influences the mixing process in the jet in cross-flow configuration. The horseshoe vortex and the counter-rotating vortex pair enhance the mixing process by entraining the cross-flow fluid into the jet, whereas the vortex pair in the wake of the jet enhances the mixing by entraining the jet into the cross-flow. Additionally, the interaction of the vortices with the wall can lead to the formation of secondary vortices and the entrainment of the wall boundary layer into the flow, further improving the mixing process [64].

The mixing of the jet with the cross-flow is depending on many parameters, namely the jet to cross-flow velocity ratio $R = U_{\text{jet}}/U_{\text{crossflow}}$, the jet to cross-flow density ratio $S = \rho_{\text{jet}}/\rho_{\text{crossflow}}$, the jet to cross-flow momentum flux ratio $J = SR^2$, the jet Reynolds number $Re_{\text{jet}} = U_{\text{jet}}D/\nu$ and the jet kinematic viscosity ν. The level of mixing has been linked to the jet penetration depth into the cross-flow [65], where a greater jet penetration depth is associated with a higher degree of mixing. For a high degree of mixing, J needs to exceed $J > 20$, in some cases it even $J > 100$ [66]. Several studies concluded that J is the most dominant parameter in determining the degree of mixing [28, 65]. Figure 2.4 shows the instantaneous mixing field visualized with acetone PLIF imaging of a jet in cross-flow configuration for J= 41 (right) and J = 5 (left) [64]. As observed, the jet with a higher J (J = 41) penetrates much deeper into the cross-flow, indicating enhanced mixing. Additionally, the case with J = 41 shows weaker shear layer instabilities, resulting in delayed and less coherent vortices, which causes the jet to spread less near the inlet. In contrast, the case with J = 5 exhibits a significantly more distorted jet with stronger shear layer instabilities. However, for mixing applications, the penetration depth remains the key parameter for determining mixing efficiency. At constant jet

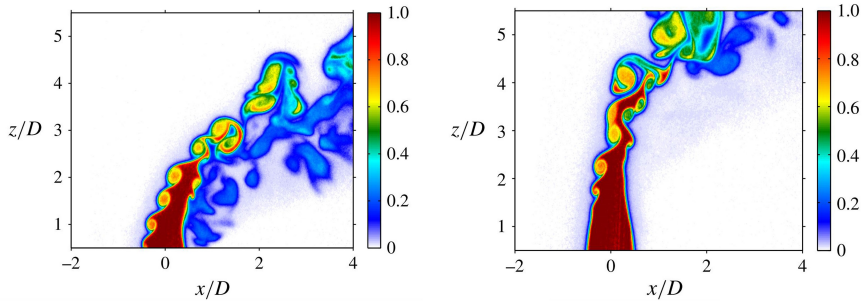

Figure 2.5: Instantaneous mixing field visualized with acetone PLIF imaging of a jet in cross-flow configuration for $J = 5$ (left) $J = 41$ (right) [64].

Reynolds number (Re_{jet}) and momentum ratio (J), decreasing the density ratio S—and thus increasing the velocity ratio R—reduces the jet penetration depth. This effect is especially pronounced at high J values. To maintain a fixed Re_{jet}, both the jet and cross-flow velocities must increase as S decreases, leading to a thinner boundary layer. A thinner boundary layer allows the cross-flow to act more immediately on the jet, causing it to turn earlier and reducing its penetration depth.

2.4.2. SWIRLING CROSS-FLOW

While the behaviour of jets in cross-flow configurations with axial cross-flows is well understood, there is a gap in research concerning the mixing of transverse jets in swirling flows. Given that swirling flows are commonly used in gas turbines and jet in cross-flow configurations are promising for achieving a high degree of mixing, understanding the mixing characteristics of this configuration is crucial. When the cross-flow is a swirling flow, the velocity of the cross-flow is composed of an axial and a tangential component, adding further complexities to the flow field. The momentum flux ratio J between the jets and the swirling flow has been proposed as [67]

$$J_{\text{swirl}} = \frac{\rho_{\text{jet}} u_{\text{jet}}^2}{\rho_{\text{swirl}} u_{\text{swirl,xo}}^2} \cdot \frac{1}{(1+4Sw^2)} \tag{2.22}$$

Where ρ_{jet} and ρ_{swirl} are the density of jet and swirling flow stream respectively, $u_{\text{swirl,xo}}$ is the initial axial velocity of the swirling stream, and Sw the initial swirl number. Early studies have shown that swirl decreases the jet penetration depth of the jet compared to an axial cross-flow (air jet into an air cross-flow). For a swirl number of $Sw = 2.25$ this reduction of the jet penetration depth was around 5 times with respect to the axial cross-flow, for values between $0.05 < J_{\text{swirl}} < 9.27$ [68]. A similar study has been conducted with a helium jet into an air cross-flow, for values up to $J_{\text{swirl}} = 1$ [69]. It has been concluded that that swirl has a negative effect on the penetration depth, consequently reduces the level of mixing. However, this can be offset by a low density ratio of the jet to the cross-flow $\rho_{\text{jet}}/\rho_{\text{crossflow}} \ll 1$. This favourable density gradient was shown to push the light jet fluid into the centre of the swirling flow. It was also shown that the density effect could overcome the negative effect of swirl, achieving the same degree of mixing

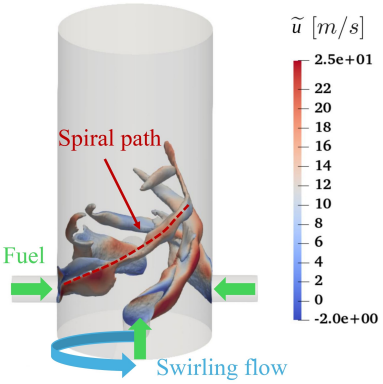

Figure 2.6: Visualization of helium jets in swirling cross-flow in the mixing tube, shown with iso surface of a helium mass fraction $Y_{\mathrm{He}} = 0.2$, coloured by the axial velocity U. Courtesy of G. Ferrante [70].

compared to an axial cross-flow [69]. Both studies concluded that even at high J_{swirl}, the jets follow a spiral path and advance in the same direction as the swirling cross-flow. This is illustrated in Figure 2.6, which shows the jet-swirling flow interaction visualized with in-house LES simulations by the isoline of a helium mass fraction of $Y_{\mathrm{He}} = 0.2$. As shown, the fuel enters the swirling flow perpendicularly but is deflected immediately after entering the mixing tube, and then follows the swirling flow in a spiral path.

The mixing of hydrogen jets into a swirling cross-flow also has been investigated by Tan et al. [67]. Figure 2.7 shows the spreading areas experimentally determined for different J_{swirl} (left) and different swirl numbers Sw (right). The inserts show the RMS values of schlieren intensity, which quantify temporal fluctuations in refractive index gradients. The values are normalized to allow comparison between operating conditions. An increase in spreading area indicates an increase in mixing. As it can be seen, the jet spreading area increases with increasing swirl number, This is especially pronounced for higher levels of J_{swirl} ($J_{\mathrm{swirl}} > 5$). For lower values of J_{swirl}, the effect of change on spreading area is relatively slight. It also can be seen that the degree of mixing increases for increasing J_{swirl} for a fixed swirl number.

2.5. OPERATIONAL RANGE OF GAS TURBINES

The operational range of gas turbines is defined by static stability limits, which include flashback and blowout phenomena. Flashback is defined as the uncontrolled upstream movement of the flame front into the premixing section, as a consequence of a local imbalance between the flow speed and the flame speed. Blowout, on the other hand, occurs when the flow speed exceeds the flame speed, causing the flame to lift off and be extinguished as it is carried out of the combustion chamber. In addition to static stability limits, certain operating points may also exhibit combustion instabilities caused by thermoacoustic coupling. Thermoacoustic instabilities are self-excited pressure oscillations that arise from a feedback loop between flow perturbations, unsteady heat re-

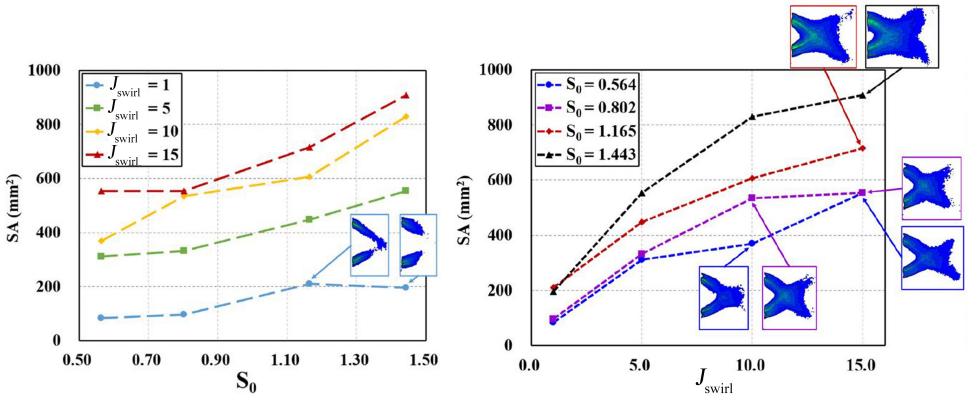

Figure 2.7: Spreading areas measured from experiments for different J_{swirl} (left) and different swirl numbers S_0 (right), inserts show the normalized RMS schlieren intensities [67].

lease, and acoustic waves [71]. These instabilities can lead to mechanical damage and reduced combustion efficiency. However, the focus of this work is on the static stability limits, therefore the following sections will only focus on the mechanisms of flashback and blowout.

2.5.1. FLASHBACK

The mechanisms for flashback in (partially) premixed swirl stabilized systems has been extensively discussed in literature [30, 72, 73]. Five different types of flashback were identified, which will be discussed in the following subsections.

FLASHBACK IN THE CORE FLOW

The first type of flashback, driven by flame propagation in the core flow, occurs when the turbulent flame speed s_t exceeds the local flow velocity u_0, allowing the flame to propagate upstream into the injector due to the resulting velocity imbalance. This type of flashback can occur in swirling as well as non-swirling flows. This mechanism is relatively straightforward and can typically be mitigated through injector designs that maintain sufficiently high bulk flow velocities. When taking a conservative estimate of turbulence intensity u_{rms} in a gas turbine combustor of around 20 % of u_0, the criterion for flame propagation is then [30]

$$s_t / u_{rms} > 5 \tag{2.23}$$

Typical velocity fluctuations u_{rms} in a swirl-stabilized burner are between u_{rms} = 9–18 m/s. Lieuwen et al. [30] derived an estimation for the turbulent flame speed by using the Damköhler relationship between the turbulent and the laminar flame speed $s_t \approx s_l + u_{rms}$. In the worst-case scenario ($s_l \approx 2.5$ m/s for H_2 flames) this leads to $s_t / u_{rms} < 1.5$, which is significantly lower than the $s_t / u_{rms} = 5$ required for flame propagation, indicating that flashback against the bulk flow is not the most critical type of flashback for swirling flows if the bulk velocity is sufficiently high. However, it still might be relevant

in poorly designed flow field (e.g. combustors where vortex breakdown occurs in the mixing tube, or the existence of strong wake regions with low velocities, for example the wake of swirler vanes). A well-designed flow field with uniform and high axial velocities and free of strong wakes provides flashback resistance against this type of flashback.

WALL BOUNDARY LAYER FLASHBACK

Boundary layer flashback occurs when the flame propagates into the boundary layer along the wall of the premixing section. This type of flashback is driven by the interaction between the flame and the low-velocity region near the wall. When the local flame speed exceeds the local flow velocity within the boundary layer, the flame can propagate upstream along the wall, leading to flashback. This mechanism is particularly critical in systems with high wall temperatures or low flow velocities near the wall. Flame propagation along the wall is hindered by quenching, a process where chemical reactions cease within a certain distance from the wall due to heat losses and third-body recombination reactions. This region, where the flame cannot sustain itself, is defined as the quenching distance δ_q. The flashback limit in a laminar flow can be expressed with a critical velocity gradient [74], defined as the ratio of the quenching distance δ_q to the turbulent flame speed s_l:

$$g_f = s_l / \delta_q \tag{2.24}$$

In turbulent boundary layers, whether g_f is higher than in laminar flow depends on the ratio between the laminar sublayer thickness and the quenching distance δ_q [75]. For hydrogen, the risk of boundary layer flashback is significantly higher due to its high laminar flame speed and thermal diffusivity α, which result in a much smaller quenching distance compared to carbon-based fuels.

FLASHBACK DUE TO AUTOIGNITION

Autoignition refers to the spontaneous ignition of a combustible mixture without an external ignition source. It can occur when the mixture is at or above its autoignition temperature, which may be reached, for example, by preheating the mixture. If, under these conditions, the residence time in the premixing section exceeds the ignition delay time, the mixture ignites within the premixing section, resulting in flashback. The ignition delay time is defined as the time interval between the start of injection and the start of combustion. The ignition delay time decreases with an increase in temperature and an increase in pressure [76]. Figure 2.8 shows the ignition delay times for methane and hydrogen at $p = 15$ bar at different φ, while varying the mixture temperature [77]. It can be seen that for mixture temperatures below 800 K the ignition delay time for hydrogen is significantly higher than that for methane at the same φ. These temperatures are relevant for laboratory scale applications, where real engine conditions might not be achieved. At temperatures above 900 K, this trend is reversed, and the ignition delay time of hydrogen is slightly lower than that of methane. This is explained with the fact that for temperatures lower than $T < 1000$ K, $C\dot{H}_3$ radicals are more active than the $\dot{H}_2$ radicals, which results in methane being more reactive than hydrogen [77]. At lower temperatures, the reactivity of hydrogen is inhibited due to the formation of HO_2 radicals, which can recombine to produce H_2O_2. This pathway favours chain propagation

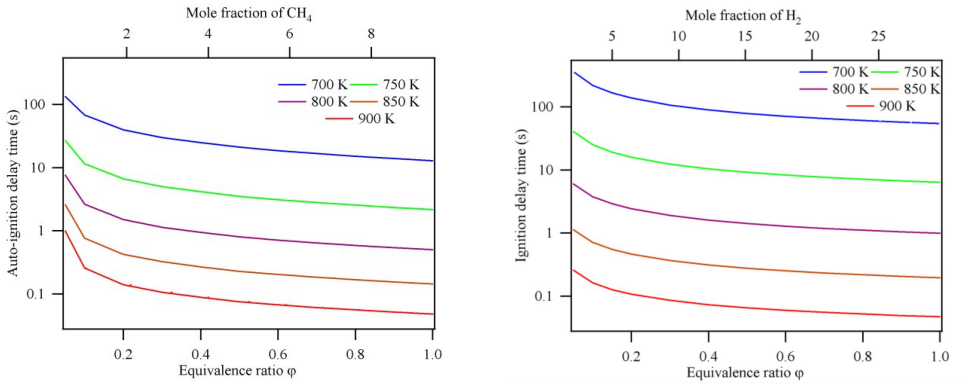

Figure 2.8: Ignition delay times for CH_4 (a) and H_2 (b) at different temperatures and p = 15 bar [77].

rather than branching, thereby slowing down the overall reactivity of hydrogen. In contrast, methane undergoes chain branching reactions, resulting in a comparatively higher reactivity. However, at temperatures above 1000 K ($T > 1000$ K), this trend reverses. The chain-branching reaction H + O_2 <=> OH becomes dominant in the case of H_2, significantly accelerating its reactivity beyond that of methane [78].

At engine relevant conditions ($T > 1000$ K) the addition of hydrogen to methane results in a decrease of ignition delay time [79, 80], which has been attributed to enhanced kinetic production of active species and preferential diffusion of hydrogen into the hot oxidizer region [81].

FLASHBACK DUE TO COMBUSTION INDUCED VORTEX BREAKDOWN

Flashback due to Combustion Induced Vortex Breakdown (CIVB) significantly differs from the other types of flashback mechanisms, as it is caused by the alteration of the flow field due to heat release. CIVB occurs when the swirling flow undergoes a sudden change in structure due to the interaction between the flame and the vortex breakdown bubble. To explain this interaction, the vorticity transport equation (Equation 2.4) can be used to describe the interaction between the flame and the vortex breakdown bubble.

A negative axial velocity can be generated by azimuthal vorticity via the law of Biot-Sarvat (Equation 2.6), in the case of rotational axis symmetry. The baroclinic torque is the main driver for the vortex breakdown. Due to a misalignment of pressure and density gradient, negative azimuthal vorticity gets generated, which in turn generates additional negative velocity. The effects leading to CIVB can be summarized as follows [82].

The heat release from combustion causes the flow to expand, which leads to a misalignment between the pressure and density gradients and generation of negative vorticity in the vortex breakdown bubble. This allows the flame to travel upstream with the recirculation bubble, leading to flashback. If the flame is able to pass the stagnation point of the recirculation bubble towards the upstream direction, the volume expansion upstream of the recirculation zone generates positive vorticity and thereby it stabilizes the flame and prevents flashback. The flow field inside the premixing section can be

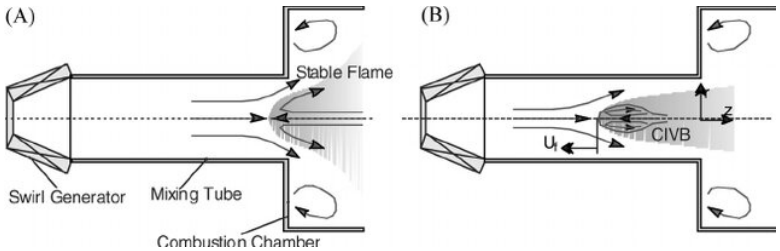

Figure 2.9: Flashback due to combustion induced vortex breakdown, stable flame (a) and flame moving upstream with the breakdown bubble (b), figure taken from [30].

tailored to improve the resistance against this type of flashback. Here, the gradient of azimuthal vorticity ($\delta\omega_\theta/\delta z$) can be used as a measure of the resistance against flashback. A positive gradient of azimuthal vorticity works against the destabilizing negative gradient caused by the baroclinic torque. Furthermore, for the flow field to be stable, the azimuthal vorticity should be positive upstream of the combustion chamber. This can be achieved with a converging nozzle upstream of the combustion chamber, with leads to an increasing circumferential velocity, which creates a positive azimuthal vorticity gradient [83]. A positive gradient of $\delta\omega_\theta/\delta z$ can also be achieved with introducing a non-swirling axial air jet (AAI) [84, 85]. For a swirling flow without AAI, the value of ω_z decreases in streamwise direction, leading to a divergence of the streamlines due to a decrease in axial velocity on the centreline. For a swirler with AAI instead, this streamwise divergence is delayed, which moves the location of vortex breakdown further downstream and consequently increases the resistance against flashback [84].

FLASHBACK DUE TO THERMOACOUSTIC INSTABILITIES

In premixed combustion systems, thermoacoustic instabilities arise due to a feedback loop between flow perturbations, heat release and acoustic oscillations, as illustrated in Figure 2.10. If the energy from the driving mechanism (for example the energy addition to the acoustic field by the flame) is higher than the energy dampening mechanism (for example the energy dissipation due to viscosity) this results in an unstable feedback cycle. This means that the oscillations grow, which leads to large amplitude pressure and velocity oscillations. A detailed description of different driving and damping mechanisms can be found in [71]. Those oscillations lead to a periodic drop of the flow velocity below the time average, accompanied by the generation of large scale vortices. When the frequency is sufficiently low so that the timescale of oscillations exceeds the chemical timescale, the flame can propagate upstream. High reactive fuels like hydrogen have a higher critical frequency than methane to trigger flashback [30].

2.5.2. BLOWOUT

Blowout occurs when the flow moves faster than the flame, causing flame lift-off and extinguishing it. Methods to develop correlations for the blowout limit for premixed flames have been extensively studies in literature [86, 87], and most agree to relate the blowout limit to a critical Damköhler number Da [73]. The Da number is defined as the ratio of the residence time of the reactants in the high-temperature zone to the chemical

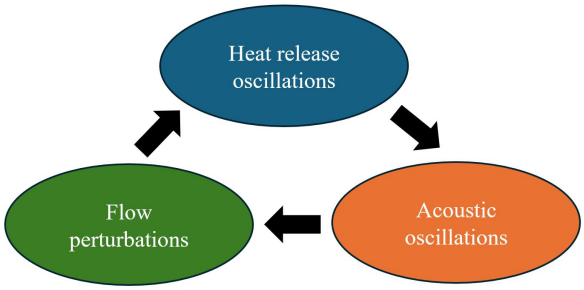

Figure 2.10: Feedback process which is responsible for combustion instabilities in premixed conditions.

timescale. The Da number can be expressed as follows:

$$Da = \frac{\tau_{res}}{\tau_{chem}} = \frac{{s_l}^2 d}{\alpha u_{ref}} \tag{2.25}$$

Where τ_{res} is the residence time, defined as the ratio of a characteristic length scale d and a characteristic velocity scale u_{ref} and τ_{chem} is the chemical timescale, defined as the ratio of the thermal conductivity α and the square of the laminar flame speed s_l [88]. For τ_{chem}, also the blowout residence time from a well-stirred reactor model can be used to calculate the Da number. The appropriate choice of the reference velocity u_{ref} and the length scale d are less clear. For swirl stabilized flames, u_{ref} is often chosen as the velocity downstream of the flame front, as $U_{ref} = f(T_0, T_b/T_0)$, where u_0 is the bulk flow velocity upstream of the flame front and T_b/T_0 the temperature change across the flame front. For d, the diameter of the combustion chamber can be chosen. Although this model has limitations, it still offers useful insights into how blowout limits change with fuel composition. The Damköhler scaling has successfully captured the blowout trends across a wide range of fuel composition for lean-premixed swirl-stabilized combustors, if the local equivalence ratio is known [89].

2.6. FUEL PROPERTIES OF HYDROGEN

Hydrogen burns completely carbon-free due to its lack of carbon atoms, making it an attractive fuel for eliminating carbon dioxide (CO_2) emissions in combustion systems. The combustion of hydrogen primarily produces water vapour (H_2O) as a by-product. However, hydrogen has significantly different fuel characteristics compared to carbon-based fuels like methane.

Table 2.1 provides a summary of relevant fuel properties of hydrogen compared to methane. Due to its low density, hydrogen poses challenges for storage and transport, requiring either large volumes or high pressures. Additionally, the low density results in a significant increase in volumetric flow rate compared to carbon-based fuels, which in turn leads to higher velocities, an important consideration for injector design. The table also highlights that the Lower Heating Value (LHV) of hydrogen per unit mass is around 2.5 times greater than that of methane. However, due to the low density of hydrogen the volumetric LHV is significantly lower than the one for methane. The stoichiomet-

ric air-to-fuel ratio is around twice as large for hydrogen, meaning that it requires twice the amount of air to burn 1 kg of hydrogen. The wide range of flammability of hydrogen in air (4–75 %) increases the likelihood of a fire in the event of an accidental leakage [90]. The autoignition temperature, where the fuel can spontaneously ignite without any external ignition sources is similar for both fuels. Additionally, the quenching distance δ_q, which is defined as the minimum separation between two parallel surfaces that allows the propagation of a laminar flame in the space between them, is much smaller for hydrogen with respect to hydrocarbons. This reduction in quenching distance has implications for flashback phenomena, such as boundary layer flashback.

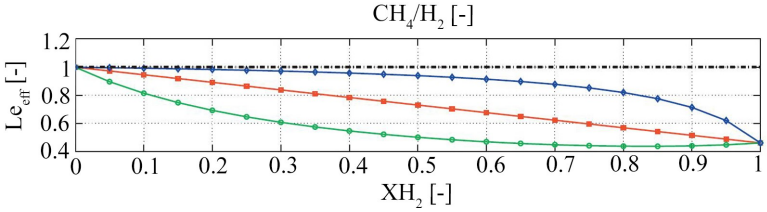

Figure 2.11: Effective Lewis number calculated using different formulations, heat released based (—), volume based (—) and diffusion based (—), figure adapted from [11].

Property	Unit	H_2	CH_4
Density ρ	kg/m^3	0.084	0.65
LHV (mass basis)	MJ/kg	120	50
LHV (molar basis)	kJ/mol	241	802
Stoichiometric air-to-fuel ratio	-	34.33	17.23
Flammability limits in air	vol%	4.0–75.0	5.3–15.0
Autoignition temperature	K	858	813
Quenching distance δ_q	mm	0.64	2.5
Mass diffusivity D	1×10^{-5} m/s^2	77.9	22.4
Thermal diffusivity α	1×10^{-5} m/s^2	159.4	24.6

Table 2.1: Fuel characteristics of H_2 compared to CH_4, values taken from [11, 22, 91].

The mass diffusivity, which is defined as the amount of fuel that diffuses across a unit area in 1 s at a concentration gradient of unity, is roughly three times higher for hydrogen. This makes hydrogen susceptible to leakages. The characteristics of the combustion process and flame properties are significantly determined by the Lewis number (Le), defined as the ratio of the mass diffusivity D and the thermal diffusivity α. The thermal diffusivity, in turn, is defined as the ratio of the thermal conductivity divided by the density and specific heat capacity at constant pressure. Thermal-diffusive instabilities occur when $Le \neq 1$. While for methane the Lewis number is $Le \approx 1$, the one for hydrogen is $Le \approx 0.3$. For fuel mixtures, the mixture Le number can be derived based on volume, heat release or diffusion of the components within the mixture. Figure 2.11 presents the effective Le number for the three different formulations. For $Le < 1$, preferential diffusion of hydrogen to heat conduction causes an increase in flame temperature.

This leads to a local increase in flame speed, amplifying the flame perturbations and as a result leading to thermal-diffusion instabilities [11, 92].

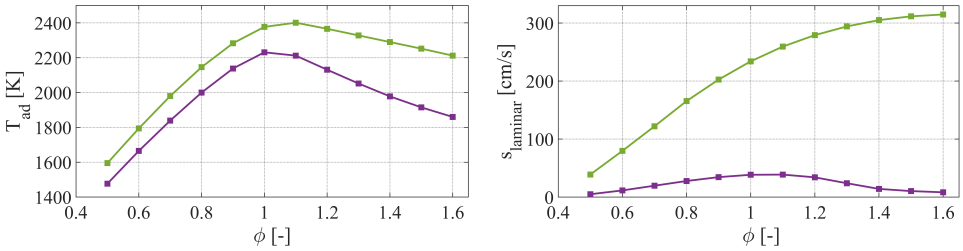

a) **b)**

Figure 2.12: (a) Adiabatic flame temperature and (b) laminar flame speed for CH_4 (—) and H_2 (—) at different φ, calculated with CANTERA using GRI3.0 mechanism [93].

The main factors affecting emissions and flame stability (flashback and blowout) are the laminar flame speed (s_l) and the adiabatic flame temperature (T_{ad}), respectively. Figure 2.12 compares T_{ad} and s_l for methane (purple line) and hydrogen (green line) across different equivalence ratios (φ), calculated using CANTERA with the GRI3.0 mechanism [93]. As shown, T_{ad} of hydrogen is significantly higher than that of methane at the same φ. This elevated temperature can lead to increased NO_x emissions through the thermal pathway, as discussed earlier in Section 2.3. Moreover, s_l of hydrogen is approximately five times that of methane at stoichiometric conditions, significantly increasing the risk of flashback. Notably, s_l continues to increase beyond stoichiometric conditions for hydrogen, only decreasing at around $\varphi = 2$.

2.7. HYDROGEN-ENRICHMENT EFFECT ON METHANE FLAMES

2.7.1. STATIC STABILITY LIMITS

As previously discussed, both blowout and flashback limits are influenced by the fuel properties. Variations in the hydrogen content notably affect these limits due to changes in fuel characteristics such as laminar flame speed and quenching distance, as shown in Table 2.1. Commonly, it has been observed that an increase in hydrogen content of the fuel lowers the φ at which lean blowout occurs. Schefer et al. [94] demonstrated that in premixed-swirl stabilized flames with a centre body, the addition of hydrogen increases the peak concentrations of OH, O, and H in the flame. They also observed an increase in strain resistance, which is thought to contribute to enhanced lean flame stability. Similarly, Strakey et al. [95] found that increasing the hydrogen content in the fuel from 0 % to 80 % reduced the blowout limit from $\varphi = 0.46$ to $\varphi = 0.30$. The lean blowout limits were effectively modelled using the perfectly stirred reactor (PSR) method, which assumes that turbulent and molecular mixing occur much faster than the chemical reactions. In this approach, flame anchoring depends on the residence time in the recirculation zone being sufficiently long for combustion to occur. A critical Damköhler number can be defined, and Equation 2.25 can be used to determine whether a given fuel composition lies above or below this threshold.

Flashback is a more complex phenomenon because it can occur in a wide range of mechanisms, as described in Section 2.5 and is for most types a function of the ratio of turbulent flame speed to the flow velocity. Since predicting turbulent flame speed is challenging, forecasting flashback limits is also difficult. Due to the significantly lower quenching distance compared to methane, hydrogen enrichment greatly increases the likelihood of boundary layer flashback [96]. Additionally, the higher flame speeds of hydrogen increase the risk of flashback in the core flow and flashback due to combustion-induced vortex breakdown [97]. Compared to its impact on blowout limits, hydrogen has a much stronger effect on lowering the flashback limits, which narrows the overall static operational range [89] compared to the one of CH_4 flames.

2.7.2. FLAME STABILIZATION

Several studies have observed that increasing the hydrogen content in the fuel leads to a more compact heat release distribution compared to a pure CH_4 flame. [44, 94] This is accompanied by a higher OH concentration [44], with increased intensity levels at upstream locations of the flame. For confined swirl-stabilized CH_4/H_2 flames with swirl numbers higher than $Sw > 0.6$, four different flame shapes were commonly observed, which are summarized in Figure 2.13 [98]. Their exact shape can depend on the combustor geometry and the operating conditions. The first type is a V-flame shape, where the flame trailing edge points towards the exhaust. The V-flame is commonly located along the inner shear layer bounding the CRZ. An M-flame occurs if the trailing edge of the flame points to the combustor dump plane, as combustion also takes place between the outer shear layer and the outer recirculation zone. An M-flame can be either attached or not attached to the exit rim of the premixing tube. For swirl-stabilized flames with a high level of swirl, also a gradual propagation of the flame front into the outer shear layer has been observed for increased hydrogen content, which reflects the transition from a V-flame to an M-flame [21, 99]. This transition has been primarily attributed to the higher strain extinction limit of flames with high hydrogen content. However, the flame shape is also significantly influenced by the temperature of the combustor dump plane. When the dump plane is cold, the V to M-flame transition probability is reduced compared to a situation with a hot dump plane [99]. The last type is a Π-flame [98, 100]. For a Π-flame, the flame front is stabilized within the OSL and anchors near the dump plane (entrance plane) of the combustion chamber, resembling the behaviour of an attached M-flame. However, the flame front on the centreline of the flow moves further downstream, which results in a Π-shaped flame. This is a result of a change in the CRZ location caused by the flame/flow interaction and the higher flame speeds due to hydrogen addition in the fuel [98]. It has been observed that hydrogen addition triggers a shape transition from M-flame to Π-flame. For methane flames, the flame stabilizes as an M-flame for all φ, and as φ increases, the flame moves further upstream due to an increase flame speed. For CH_4/H_2 mixtures at lower φ, the flame stabilizes as an M-flame, but transitions to a Π flame beyond a critical φ. This critical φ decreases as the hydrogen content in the fuel increases [98]. Consequently, the dominant flashback mechanism changes from flashback due to combustion induced vortex breakdown for an M-flame to boundary layer flashback for a Π-flame.

For a low swirl CH_4/H_2 burner different flame shapes have been observed, as shown

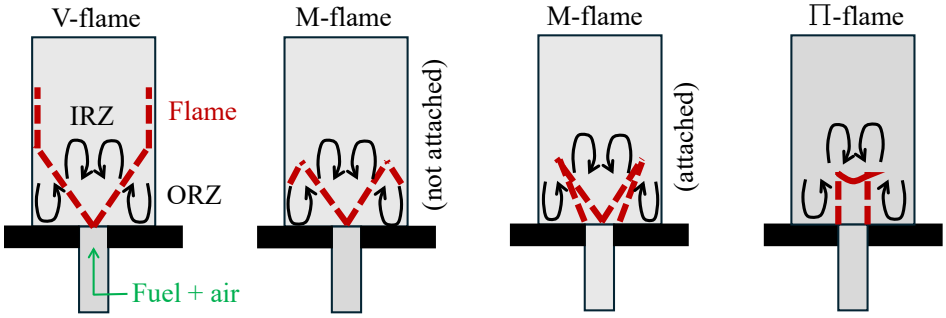

Figure 2.13: Illustration of different type of flame stabilization mechanisms typically observed in a swirl-stabilized combustor with high swirl ($Sw > 0.6$), figure adapted from [98].

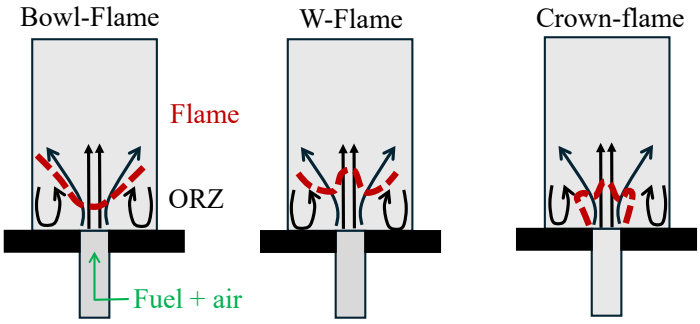

Figure 2.14: Illustration of different type of flame stabilization mechanisms typically observed in a swirl-stabilized combustor with low swirl ($Sw < 0.6$), figure adapted from [101].

in Figure 2.14 [101]. The bowl shape flame is enclosed by the ISL, with the flame stabilizing on the centreline, depending on the equilibrium of turbulent flame speed and local flow velocity. The W-flame exhibits a central bulge, which is also dependent on the velocity balance between flame speed and flow speed. The outer edges however are stabilized in the OSL. The Crown-flame shares a similar stabilization mechanism on the centreline, but attached to the injector in the OSL.

Figure 2.15 shows typical flame shapes of hydrogen-enriched methane flames at different hydrogen enrichments between $XH_2 = 0$ and $XH_2 = 1$ [102]. It can be seen that the flame shape changes significantly with increasing hydrogen content in the fuel. The OH-PLIF images in the same study revealed that the pure CH_4 flame is stabilized as a V-flame. For increasing hydrogen content the flame protrudes more into the OSL, but does not manage to attach to the rim below $XH_2 = 1$. This represents the previously defined unattached M-flame. For $XH_2 = 1$, the flame is stabilized as a Π-flame, which is attached in the OSL to the rim of the injector, which is in correspondence with other flame shape studies for pure H_2 flames [98, 103].

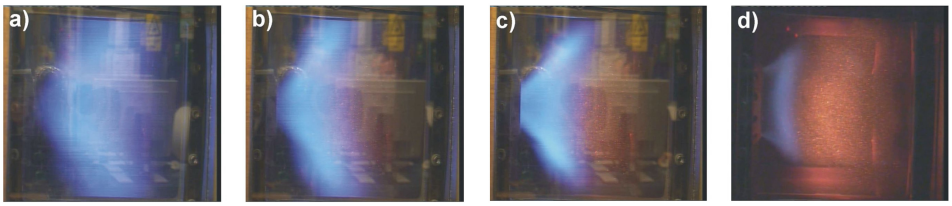

Figure 2.15: Flame shapes for different H_2 contents in an H_2 enriched natural gas flame, (a) $XH_2 = 0$, (b) $XH_2 = 0.3$, (c) $XH_2 = 0.6$, $XH_2 = 1$, images taken from [102].

2.7.3. NO_x EMISSIONS

Many studies investigated the effect of hydrogen enrichment on the NO_x formation in laboratory scale CH_4 flames. While the NO_x levels observed in these studies may not be fully representative of those in full-scale devices, the trends provide valuable insights into what can be expected in larger systems. Although NO_x emissions include both NO and NO_2, flame studies often focus solely on NO. This is because NO_2 primarily forms through the oxidation of NO in post-combustion regions [104]. Within the flame itself, the high temperatures typically cause NO_2 to decompose back into NO.

When hydrogen is burnt at the same φ as CH_4, the adiabatic flame temperatures are significantly higher, as previously discussed in Section 2.6. This leads to an increase in NO formation through the thermal pathway. However, this can be compensated, since the lean extinction limit is lowered for hydrogen enriched fuels. Increased NO_x emissions have been observed with higher hydrogen content in the fuel, despite operating at lower φ to reduce the adiabatic flame temperature compared to a methane flame [102]. Kim et al. [44, 105] observed opposite trends in NO emissions depending on the swirl number for low amounts of hydrogen in a perfectly premixed unconfined flame. For low swirl numbers (swirler vane angle 30°), an increase in hydrogen content in the fuel reduced the NO emissions. At stronger swirl strengths (swirler vane angle 45° and 60°), the NO concentration increases with increasing hydrogen content. This is based on the balance of the fact that hydrogen addition increases the local flame temperatures but also reduced the residence time in the high temperature zone.

Hydrogen addition also has shown to significantly influence the pathway of NO formation. For lean, freely-propagating flames at varying pressures and constant adiabatic flame temperature ($T_{ad} = 1870\,K$), overall NO emissions (in ppm) have been found to increase with rising hydrogen content, up to $XH_2 = 0.3$ [106]. The NO produced via the thermal NO pathway is the main contributor to the overall NO concentration in that study. However, the increase in NO_x formation in this configuration is primarily attributed to prompt NO, which forms in the reaction zones where heat is released. This increase in prompt NO is driven by an increase in the radical pool of OH and H for increasing hydrogen content. Additionally, the formation of NO via the NNH pathway also increases with higher hydrogen content, as it is highly sensitive to the presence of H-radicals, which react to form NH—an intermediate species in the NO formation process. On the other hand, NO formation via the N_2O pathway is reduced due to the lower O_2 concentration in the reactants.

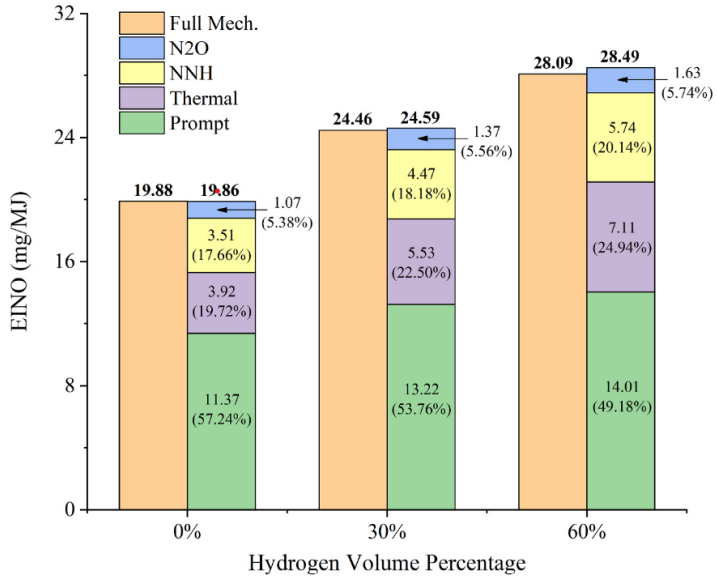

Figure 2.16: NO produced per unit power (EINO) for different hydrogen contents in volume, figure taken from [107].

In an unconfined CH_4/H_2 swirl burner, hydrogen addition up to $XH_2 = 0.6$ resulted in an increase in the total NO emissions (Y_{NO}) [107], when the thermal power was kept constant. For a hydrogen content of $XH_2 = 0.6$ the NO emissions increased by 40 % compared to a pure CH_4 flame. This has been shown with LES simulations with a novel prediction model, incorporating an efficient NO reaction source term and tabulation approach. The increase is partially due to a slight increase in adiabatic flame temperature, which increases the NO formation via the thermal pathway. Additionally, the contribution of NO formed through the prompt pathway also slightly increases with higher hydrogen content, as the mass fractions of H and OH increase in this configuration. This likely promotes the formation of CH, further contributing to the overall NO formation. However, the contribution of the prompt pathway to the total NO emissions decreases with increasing hydrogen content. Nevertheless, at $XH_2 = 0.6$ the prompt pathway still contributes around 50 % to the total NO emissions. Additionally, NO formation via the NNH route increases, due to a larger presence of H and O-radicals. For all hydrogen contents, the NO formed via the N_2O pathway is negligible, since it only contributes to less than 6 % to the overall NO emissions. This is summarized in Figure 2.16, which shows the mass of NO produced per unit power (EINO), for three different XH_2 at the same thermal power. They are separated by the contribution of the different NO formation pathways [107].

For partially premixed CH_4/H_2 flames, the formation of NO_x is highly dependent on both the fuel composition and the degree of fuel-air mixing. As previously discussed, the mechanism of NO formation varies with changes in fuel composition, making it particularly challenging to accurately predict NO_x emissions in these flames. Additionally, when

changing the fuel composition from methane to hydrogen to maintain the same power output, it is necessary to adjust the fuel flow rate to keep the volumetric heating value constant. This results in a significant change in velocity profiles in the premixing section, which can lead to a change in the mixing profile [11]. An increase in non-uniformity in the mixing tends to decrease the NO emissions, as local hot temperature regions in the flame will be formed. Consequently, a detailed emission analysis is typically required for each specific burner geometry in order to determine how operating parameters and fuel composition influence NO_x emissions.

2.8. STATE OF THE ART PARTIALLY PREMIXED SWIRL-STABILIZED HYDROGEN BURNERS

Several studies have focuses on the understanding of flashback and emissions in 100 % partially premixed swirl-stabilized hydrogen flames and have proposed suitable approaches to stabilize pure hydrogen flames. Figure 2.17 shows an overview of the proposed burner configurations identified from literature. While the HYLON and Ansaldo burners have been developed and extensively tested with both 100 % CH_4 and 100 % H_2 flames, the AHEAD burner was designed specifically to stabilize 100 % H_2 flames. The following section discusses the working principles of swirl-stabilized burners and summarizes the key findings:

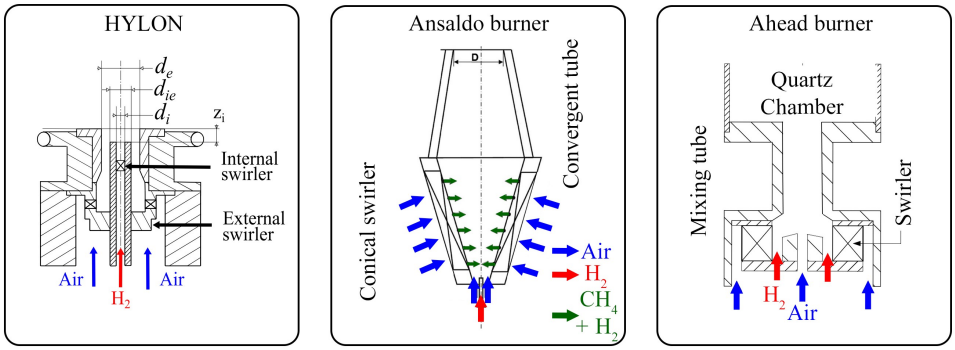

Figure 2.17: Overview of the partially premixed H_2 burners obtained from literature. HYLON burner [108] (left), Ansaldo conical burner [109] (middle) and AHEAD burner with AAI [85] (left).

HYLON BURNER

Recently, the HYLON injection system has demonstrated promising results in stabilizing 100 % CH_4 and 100 % H_2 flames for selected operating conditions [108, 110, 111]. The set-up consists of an internal and an external swirler (see Figure 2.17). The methane and air mixtures is sent through the external swirler. Hydrogen is injected either swirling or non-swirling through a central pipe just a few millimetres before the combustion chamber. Figure 2.18 shows the effect of hydrogen content on the flame stabilization mechanism in the HYLON burner for the case with swirling hydrogen injection ($Sw \neq 0$) and the case with non-swirling hydrogen injection ($Sw = 0$). Changing the fuel results in a change

of the momentum ratio J, defined as the ratio of momentum of the external (methane and air) and internal (hydrogen) flow. For the non-swirling fuel injection, all the flames are anchored to the central injector as a V-flame. Significant differences between the hydrogen contents are only observed close to the combustion chamber walls. For $XH_2 = 0$, the flame stabilizes in the OSL close to the chamber walls. This slowly disappears as the hydrogen content increases. For the case with swirling hydrogen injection, the flames look similar to the ones without swirling fuel injection for low hydrogen contents up to $XH_2 = 0.2$. Above that, the topology of the flame changes significantly. At $XH_2 = 0.6$, the flame is completely aerodynamically stabilized. For even higher hydrogen contents, the flame attaches again to the injector rim, but the CRZ is pushed downstream which can be seen by the reaction layer in the centre which is stabilized at the top of the CRZ.

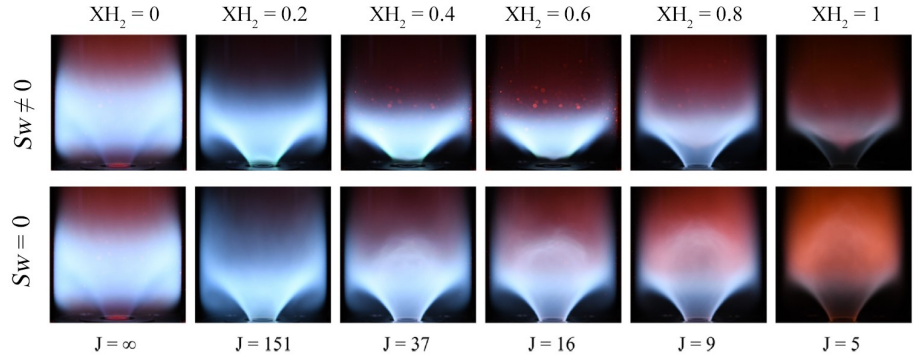

Figure 2.18: Effect of H_2 content on the flame stabilization mechanism in the HYLON burner [108].

NO_x emissions have shown to increase with increasing hydrogen content for both configurations, since φ is kept constant, which results in higher adiabatic flame temperatures. For the cases without inner swirl, the NO_x emissions increased much more rapidly with respect to the cases with inner swirl. Additionally, flames which are attached to the injector rim reached high NO_x levels, while the aerodynamically stabilized flames showed lower NO_x emissions. This is expected due to the fact that the attached flames possesses a diffusion flame front, while the lifted flames burn in a more premixed flame front. It is expected that the swirl of the hydrogen stream significantly improves fuel air mixing before combustion takes place, reducing the NO_x emissions by more than two times compared to a non-swirling fuel injection.

MODULAR CONICAL BURNER ALSTOM

The swirler in the modular conical Alstom burner features a thick-walled hollow cone with four symmetrically arranged tangential slots positioned around its circumference. These slots are oriented to direct the flow tangentially along the inner surface of the cone. The majority of the combustion air enters the cone through these tangential slots, promoting a predominantly tangential flow pattern. A part of the air enters on the centreline of the cone.

The swirler is attached to a converging mixing tube, as it can be seen in Figure 2.17. Fuel can either be injected through slots at the trailing edge of the swirler vanes, or ax-

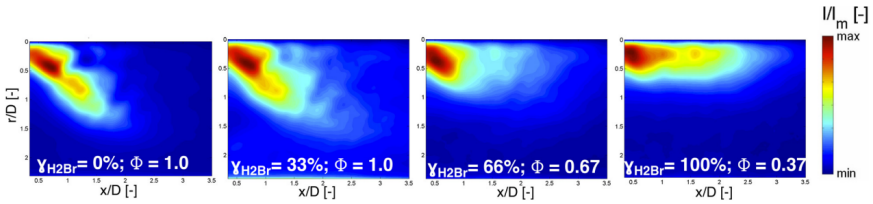

Figure 2.19: OH* images for varying H_2 content with axial H_2 injection in the Alstom burner [112].

ially through the centre of the swirler. For the pure hydrogen case, a part of the fuel is injected axially through the centre of the swirler, while the rest is injected through the vanes. Axial fuel injection changes the flame structure from the one of a classical vortex breakdown flame to a more compact flame shape with no vortex breakdown. This allows to operate the burner up to higher φ, before flashback occurs compared to the trailing edge injection [109], due a lower risk of boundary layer flashback. Figure 2.19 shows the Abel deconvoluted OH* images for axial hydrogen injection, for increasing hydrogen content in the fuel mixture. It can be seen that the higher the hydrogen content, the less the flame looks like the one of a swirl stabilized flame. Axial fuel injection also resulted in higher NO_x emissions [112]. This effect becomes stronger when the axial fuel injection ratio increases. This is because for axial fuel injection, the fuel is concentrated in the centre and consequently does not properly distribute over the entire mixing tube.

AHEAD BURNER (TU BERLIN)

One of the most promising solutions to stabilize hydrogen flames, while keeping the injector changes minimal is AAI, where a non-rotating air jet is injected on the centreline of the swirling flow, to increase the flow velocity and to delay the streamline divergence [84]. The AHEAD burner (TU Berlin) makes use of the concept of AAI. The hydrogen stream is injected as well in axial direction, a high radius (r/D = 0.5), where it can directly interfere with the swirling air (see Figure 2.17). Boundary layer flashback in this configuration is prevented by diluting the mixture close to the mixing tube wall with air.

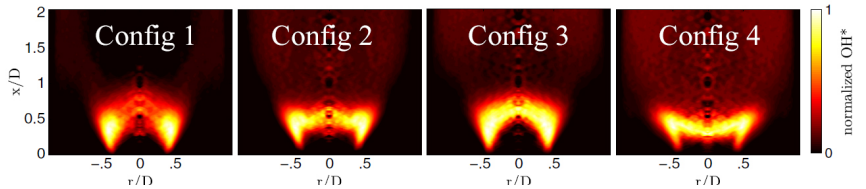

Figure 2.20: Abel deconvoluted OH* images for different mixing tube lengths and swirl numbers for XH_2 = 1, χ = 12.5 % and T_{preh} = 620 K [22].

With high amounts of AAI (12.5 %), no flashback was observed in the burner up to stoichiometric conditions, with preheating temperatures up to 620 K. Figure 2.20 shows the Abel deconvoluted OH* images for hydrogen flames at stoichiometric conditions with χ = 12.5 %. The images are shown for different geometric configurations. Configuration 1: Sw = 0.7, short mixing tube, configuration 2: Sw = 0.7, long mixing tube,

configuration 3: Sw = 1.0, short mixing tube and configuration 4: Sw = 1.0, long mixing tube. All the flames show the Π-shape, where the centre of the flame is lifted off the injector. It clearly can be seen that the long mixing tubes result in a more uniform OH* profile, which is due to the increase in mixing quality. For adiabatic flame temperatures up to ≈ 2000 K, the NO_x emissions stayed below 10ppm at 15 % O_2. However, a sufficiently high initial swirl number or mixing tube length is required to ensure a high level of fuel-air mixing and consequently keep NO_x emissions low. Summarizing, this concept has shown excellent flashback resistance for partially premixed hydrogen flames, while keeping the NO_x emissions low.

3

METHODOLOGY

This chapter outlines the methodology followed in this dissertation. While the research is primarily conducted experimentally, it is complemented by one-dimensional flame simulations using the open source software CANTERA [93] to assess how variations in fuel composition affect fundamental combustion properties. However, this chapter focuses solely on the experimental methodology of this work. The chapter begins with a description of the partially premixed swirl-stabilized burner geometry. The operating conditions for both reacting and non-reacting experiments are discussed afterwards, along with the modifications made to the set-up for non-reacting conditions. Next, the chapter provides an overview of the experimental techniques employed, including gas analyser, PIV, OH* chemiluminescence, and PLIF measurements. Each section covers the general working principle of the technique, along with the specific setup used in this study. Where applicable, the data processing methods used to analyse the experimental results are also discussed.

3.1. EXPERIMENTAL SET-UP

Experiments, both non-reacting and reacting, were conducted in a lab-scale partially premixed, swirl-stabilized combustor. The burner is equipped with a single-stage axial swirler, a design commonly used in gas turbines due to its lower pressure drop and more uniform radial velocity profile compared to radial swirlers [113, 114]. To enhance flashback resistance, the injector employs the concept of AAI, which, as discussed in Chapter 2, is one of the most effective strategies for stabilizing flames with high hydrogen content [85].

3.1.1. BURNER GEOMETRY REACTING STUDY

Reacting experiments were conducted in the partially-premixed TU Delft atmospheric laboratory scale combustor at the Sustainable Aircraft Propulsion laboratory of TU Delft [24, 115]. A schematic of the set-up is provided in Figure 3.1. The combustion air is supplied through four inlets, which direct the airflow through an axial swirler. The AAI

jet is positioned on the centreline of the swirling flow [85], and is injected through an 8 mm diameter port. The AAI flow rate is a part of the total air flow rate available for combustion and is therefore always given as the percentage of the total air mass flow rate

$$\chi = \dot{m}_{\mathrm{AAI}} / (\dot{m}_{\mathrm{swirl}} + \dot{m}_{\mathrm{AAI}}) \tag{3.1}$$

The axial swirler, made from stainless steel 316, is designed with geometric swirl numbers of 0.7 and 1.1 with straight vanes based on [29]

$$Sw = \frac{G_\theta}{R_\mathrm{n} \cdot G_x} = 0.5 \frac{1}{1-\psi} \frac{1-(R_\mathrm{h}/R_\mathrm{n})^4}{(R_\mathrm{h}/R_\mathrm{n})^2} tan(\phi_0) \tag{3.2}$$

Where G_θ is the axial flux of tangential momentum, G_x the axial thrust, ψ the blockage factor, Φ_0 the tip vane angle and R_n and R_h respectively the outer and hub radius of the swirler vanes (R_n = 12 mm and R_h = 5 mm). The blockage factor ψ is defined as

$$\psi = \frac{n \int_{R_n}^{R_h} \frac{t}{cos(\Phi)} dr}{(R_n^2 - R_h^2)\pi} \tag{3.3}$$

Where n is the number of vanes and t the thickness of the vanes. G_x and G_θ can be obtained by solving the Equation 2.2 and Equation 2.3.

The burner operates in a partially premixed configuration with different fuel mixtures (CH_4 and H_2) injected through four nozzles with a diameter of d_{fuel} = 3.5 mm in jet in cross-flow configuration into the swirling flow, 6 mm downstream of the swirler exit. The mixing process of fuel and oxidizer takes place in the mixing tube with a diameter d_{MT} = 24 mm and length l_{fuel} = 60 mm.

Downstream of the mixing tube, the fuel-air mixture enters the optically accessible quartz (ilmasil® PN) combustion chamber (d_{CC} = 148 mm and l_{CC} = 400 mm) with a wall thickness of t = 3.5 mm. The fused silica has the advantage of having a transmission efficiency of around 75 % close to 230 nm and 85 % above 280 nm, which makes it suitable for measurement techniques in the UV-range. The dimensions of the mixing tube and the combustion chamber result in a confinement ratio (ratio of combustion chamber area to mixing tube area) of c = 38. Compared to similar swirl-stabilized burners in literature [85, 108], this is a relatively large confinement ratio. However, it allows investigating the combustion process with fewer flame-wall interactions, which include heat loss to the wall. The main swirl-stabilized flame is locally ignited by a remotely controlled CH_4/air Honeywell ZMI series pilot burner at a power of 1 kW and φ = 0.65. The mass flow rates for all the fuel and air streams are controlled by Bronkhorst digital mass flow meters with an accuracy of ± 0.5 % RD plus ± 0.1 % FS. The Piping and Instrumentation Diagram (P&ID) diagram of the swirl-stabilized combustor can be found in Appendix A.

The combustion chamber is connected to flexible exhaust duct with a length of $l_{\mathrm{exh}} \approx$ 2 m and a diameter of $d_{\mathrm{exh}} \approx$ 200 mm, which connects the set-up to the fixed exhaust which is part of the infrastructure and directs the exhaust gases to a location outside the lab. Before entering the fixed exhaust, the exhaust gases get diluted with a constant flow of ambient air, to keep the exhaust temperature below 650 K. The combustor was operated with an open outlet, without an orifice. This was decided after evaluating the

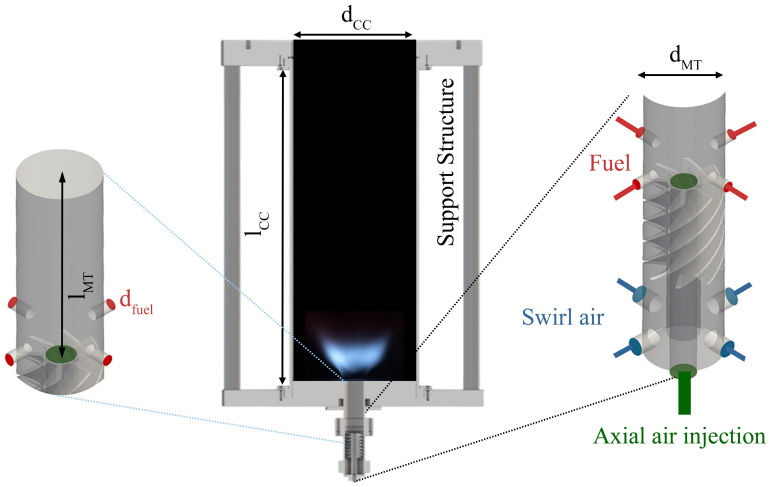

Figure 3.1: Schematic TU Delft swirl burner with dimensions and a detailed view of the swirler with the AAI port and the jet in cross-flow fuel inlets.

effect of the outlet contraction on the flow field in the combustion chamber. This will be further discussed in Chapter 4. The burner is controlled via LabView software, and the set-up temperatures and the location of the flame are monitored with K-type thermocouples and a Honeywell UV sensor.

3.1.2. OPERATING CONDITIONS IN REACTING STUDY

The burner is operated with mixtures ranging from pure CH_4 to pure H_2. Due to the flow rate limitations of the CH_4 mass flow controller, it was not possible to reach operating conditions between 85 % and 100 % H_2 at the design point of $P = 12$ kW. When H_2 is added to CH_4, the thermal power P and the total air mass flow rate $\dot{m}_{air}$ are kept constant. The overall equivalence ratio for the mixture is calculated with

$$\varphi = s\frac{\dot{m}_{CH_4} + \dot{m}_{H_2}}{\dot{m}_{air}} \tag{3.4}$$

The stoichiometric ratio s is defined as:

$$s = \frac{(2 - 1.5X_{H_2})(W_{O2} + 3.76W_{N_2})}{X_{CH_4}W_{CH_4} + X_{H_2}W_{H_2}} \tag{3.5}$$

Where XH_2 and XCH_4 represent the mole fractions of H_2 and CH_4 in the fuel mixture, and W the molar masses. At the design point the combustor operates with CH_4 at an equivalence ratio $\varphi = 0.75$ at a power of $P = 12$ kW (corresponding to a total air flow of $\dot{m}_{air} = 5.1 \times 10^{-3}$ kg/s and fuel flow $\dot{m}_{CH4} = 2.2 \times 10^{-4}$ kg/s). The Reynolds number with respect to the mixing tube diameter is around $Re = 16{,}000$ for the conditions at the reference case.

Table 3.1 shows an overview of the operating conditions at the design point of 12 kW for different hydrogen contents XH_2, including the equivalence ratio φ, the adiabatic

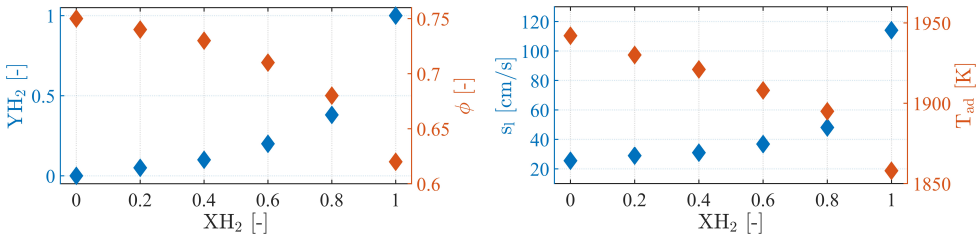

Figure 3.2: Fuel properties for different XH_2 in the fuel at the design point of P = 12 kW calculated for a freely-propagating flame with CANTERA [93] using GRI 3.0: (a) Mass-fraction YH_2 and equivalence ratio φ (b) laminar flame speed s_l and adiabatic flame temperature T_{ad} for different XH_2 in the CH_4/H_2 fuel mixture.

flame temperature T_{ad}, the momentum flux ratio J_{swirl} for Sw = 0.7 ($J_{swirl-0.7}$) and Sw = 1.1 ($J_{swirl-1.1}$), as well as the thermal expansion ratio. T_{ad} and the thermal expansion ratio ρ_{react}/ρ_{prod} were calculated for freely propagating laminar premixed flames with CANTERA [93] using GRI 3.0. Table 3.1 shows, that φ, T_{ad} and the thermal expansion ratio decrease for increasing XH_2. Due to the increased volumetric flow rate of the fuel for increasing XH_2, the bulk velocity in the mixing tube increases. The highest value for J_{swirl} is for XH_2 = 0.8. Due to a low J_{swirl} [69] and a short mixing tube, the mixture is anticipated to be partially premixed when entering the combustion chamber. Furthermore, as it is shown later in Chapter 4, the mixing process is influenced by the ratio ρ_{jet}/ρ_{air} as well as the level of AAI. Figure 3.2 shows the laminar flame speed s_l and the adiabatic flame temperature T_{ad} as well as the mass fraction YH_2 for different XH_2 in the fuel mixture at the design point.

The points were tested at three different levels of AAI, 0 %, 10 %, and 20 % for the two different swirl numbers. An overview of all the operating conditions in the set-up can be found in Appendix B.

Design points at P = 12 kW and $\dot{m}_{air}$ = 5.1 $\cdot 10^{-3}$ kg/s								
Tag	XH_2	U_{MT} [m/s]	U_{fuel} [m/s]	φ	T_{ad} [K]	$J_{swirl-0.7}$	$J_{swirl-1.1}$	ρ_{react}/ρ_{prod}
A	0	10.45	9.92	0.75	1942	0.17	0.09	6.40
B	0.25	10.62	10.69	0.74	1930	0.19	0.09	6.33
C	0.4	10.75	12.76	0.73	1921	0.21	0.11	6.26
D	0.6	11.01	15.82	0.71	1908	0.24	0.12	6.13
E	0.8	11.44	20.96	0.68	1895	0.26	0.13	5.94
F	1	12.26	30.42	0.62	1858	0.25	0.12	5.60

Table 3.1: Operating conditions for the design points at constant air flow rate, H_2 fraction XH_2, the bulk velocity in the mixing tube U_{MT}, equivalence ratio φ, adiabatic flame temperature T_{ad}, momentum flux ratio J_{swirl} for the swirl numbers Sw = 0.7 as well as Sw = 1.1 and thermal expansion ratio ρ_{react}/ρ_{prod}.

3.1.3. BURNER GEOMETRY NON-REACTING STUDY

Non-reacting experiments were performed in a 3D-printed duplicate of the TU Delft partially premixed CH_4/H_2 swirl-stabilized burner [24, 25]. The stainless steel axial swirler is reused from the reacting swirl-stabilized set-up to maintain consistency in the injector geometry. The combustion chamber and mixing tube were made from clear acrylic, to allow optical access. The diameter of the acrylic combustion chamber was d_{CC} = 152 mm, slightly larger than that in the reacting case. The diameter of the mixing tube was d_{MT} = 24 mm, consistent with the dimensions used in the reacting studies. The wall thickness of the combustion chamber is 3 mm, and that of the mixing tube is 0.9 mm. For the mixing tube such a thin diameter was chosen to reduce reflections and distortion close to the mixing tube wall. The non-reacting set-up with the optically accessible mixing tube can be seen in Figure 3.3. Due to the non-transparent baseplate of the combustion chamber, the range between -11 mm$< y <0$ mm is not optically accessible. During the experiments, the mass flow rates for both air and fuel were controlled by Bronkhorst digital mass flow meters with an accuracy of ±0.5 % RD plus ± 0.1 % FS.

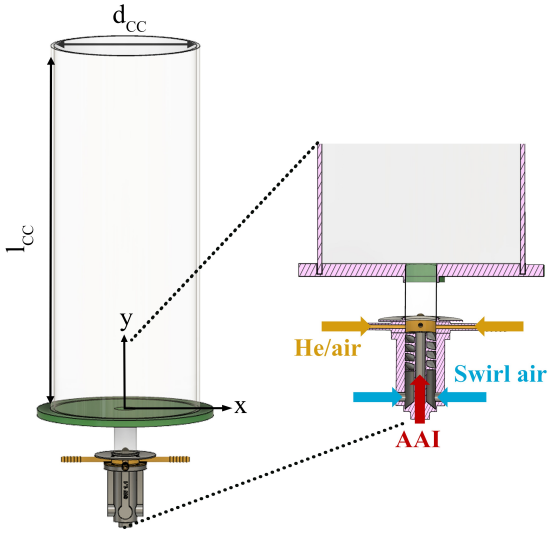

Figure 3.3: 3D printed duplicate of the TU Delft swirl-stabilized burner used for non-reacting experiments, with optically accessible mixing tube.

3.1.4. OPERATING CONDITIONS NON-REACTING STUDY

The mixing process in a jet in swirling cross-flow configuration is complex and influenced by many parameters, especially considering configurations which operate on various mixtures of CH_4 and H_2. When studying mixing, it is advantageous to use a non-reactive surrogate gas to avoid dealing with reactive fluids. Helium has been proposed previously as a surrogate for H_2. Although it does not replicate the micro-mixing characteristics of H_2 with oxidizers, it does exhibit a similar global mixing trend in a jet in

cross-flow configuration with axial cross-flow [116]. Following the parameters outlined in [117], it is desirable to match the jet velocity U_{jet}, density ρ_{jet}, and Reynolds number Re_{jet} in non-reactive scenarios with those of reacting cases.

As a surrogate for the CH_4/H_2 mixtures, a He/air mixture was used to match both the density ρ_{jet} and bulk fluid velocity U_{jet} of the jet with the same fuel inlet diameter. When the fuel composition changes, the thermal power of the reacting case and the air flow rate were kept constant, consequently only the fuel flow rate changes. For replacing the 100 % H_2 case, it is not possible to match the H_2 density with He since He has a density roughly twice as high. Consequently, it was decided to match the momentum flux ratio J_{swirl} between reacting and non-reacting case. To achieve this, the volumetric flow rate is kept constant when exchanging H_2 with He, and the diameter of the fuel inlet was increased.

Table 3.2 shows the fuel compositions for the reacting case (Tag A - D) for the design point at 12 kW and the corresponding fuel surrogates (Tag A_s - D_s) for the non-reacting experiment. The X_{He} in the surrogate fuel relates with the X_{H_2} in the CH_4/H_2 mixture as follows:

$$X_{He} = X_{H_2} \cdot \frac{W_{H_2} - W_{CH_4}}{W_{He} - W_{air}} + \frac{W_{H_2} - W_{CH_4}}{W_{He} - W_{air}} \tag{3.6}$$

where X is the mole fraction and W is the molar mass of the species. In addition to examining the effect of fuel composition on the mixing, this study also explores the impact of J_{swirl} (see Equation 2.22) on the mixing. To calculate J_{swirl}, U_{air} is taken as the mean mass axial velocity, due to the complex velocity distribution at the swirler outlet. Additionally, the swirl number was taken as the geometric swirl number. In addition to the conditions of the baseline case (J_{low}) representing the surrogate conditions of the reacting case, two higher momentum flux ratios were investigated (J_{mid} and J_{high}). This is achieved by increasing the jet velocity through a reduction in the diameter of the fuel inlet ports. The diameters for the different momentum flux ratios at the different fuel compositions are summarized in Table 3.3. Figure 3.4a shows the momentum flux ratios J_{swirl} for the reacting cases (CH_4/H_2) and its surrogate (He/air at J_{low}) for Sw = 1.1 and Sw = 0.7. It can be seen, that the curves of the two mixtures match, since the density is kept constant between the fuel mixture and the surrogate fuel. For both, the momentum flux ratio increases up to XH_2 = 0.8, and afterwards drops again slightly. Figure 3.4b shows the J_{swirl} for the two swirl numbers for all the diameters investigated (J_{low}, J_{mid} and J_{high}). Instead of maintaining a constant J_{swirl} across the different cases, the fuel inlet diameter was kept constant to better represent a realistic scenario. As mentioned before, for the surrogate case of XH_2 = 1, the diameter was increased. This adjustment was necessary because the differing densities of the fuel and its surrogate would otherwise result in a significantly higher momentum flux ratio. Figure 3.4c shows the Re numbers for the same cases. Due to the higher viscosity of Helium compared to H_2 and CH_4 some discrepancies are observed in the Re numbers between the reacting fuel and its surrogate at the same value of J_{swirl}. Additionally, as expected, decreasing the fuel injection diameter results in an increase in the Re number. However, for all investigated cases, the flow remains in the laminar or transition regime. Therefore, the change in Re number between the different cases is not anticipated to affect the mixing significantly.

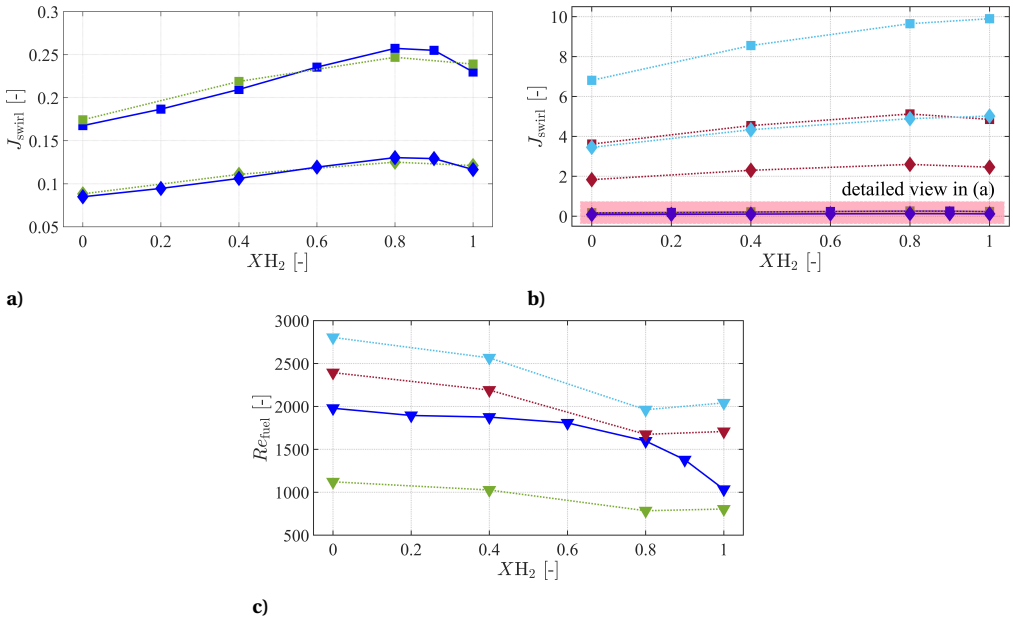

Figure 3.4: (a) & (b) Momentum flux ratio for CH_4/H_2 mixtures (—) and the surrogate conditions (····) for Sw = 1.1 (♦) and Sw = 0.7 (■). (c) Re numbers in the fuel nozzles for CH_4/H_2 mixtures (—) and the surrogate fuel at different momentum flux ratios J_{swirl}: low(····), mid (····) and high (····). (a) is a zoomed version of (b).

Table 3.2: Fuel mixtures for the reacting experiments and the corresponding surrogate fuel mixtures at p = 1 atm and T = 288.15 K

Fuel reacting case at P = 12 kW					Surrogate fuel			
Tag	XH_2	$\dot{Q}_{H2}$ [L/min]	$\dot{Q}_{CH4}$ [L/min]	ρ_{mix} [kg/m^3]	Tag	$\dot{Q}_{He}$ [L/min]	$\dot{Q}_{air}$ [L/min]	ρ_{mix} [kg/m^3]
A	0	0	21.21	0.678	A_s	11.01	10.58	0.684
B	0.4	11.17	16.76	0.441	B_s	22.27	7.82	0.442
C	0.8	39.2	9.13	0.204	C_s	42.87	2.25	0.222
D	1	71.8	0	0.085	D_s	71.80	0	0.169

Table 3.3: Diameter d_{fuel} of the fuel injection ports and bulk velocities in the fuel port U_{fuel} for the reacting case and the surrogate fuel for three different momentum flux ratios J_{swirl} (low, mid, and high). J_{low} represents the surrogate conditions for the reacting case.

Fuel reacting case				Surrogate fuel						
Tag	XH_2	d_{fuel} [mm]	U_{fuel} [m/s]	Tag	d_{J-low} [mm]	$U_{fuel,J-low}$ [m/s]	d_{J-mid} [mm]	$U_{fuel,J-mid}$ [m/s]	d_{J-high} [mm]	$U_{fuel,J-high}$ [m/s]
A	0	3.50	9.92	A_s	3.50	9.31	1.64	42.58	1.40	58.44
B	0.4	3.50	12.75	B_s	3.50	13.03	1.64	59.35	1.40	81.45
C	0.8	3.50	20.96	C_s	3.50	19.54	1.64	89.02	1.40	122.16
D	1	3.50	30.42	D_s	4.07	22.01	1.96	99.13	1.64	141.64

3.2. EXPERIMENTAL AND DATA PROCESSING TECHNIQUES

This dissertation uses a gas analyser probe to analyse the exhaust gas composition. Additionally, the work utilizes a range of laser-based diagnostics to investigate the flow field, mixing and the combustion process within the mixing tube and combustion chamber. The following section provides an overview of the fundamental principles behind the diagnostics used, along with the measurement set-up which is specific to this work.

3.2.1. GAS ANALYSER MEASUREMENTS

Probe measurements are intrusive measurement techniques as the probe interacts with the flow field and can influence both the flow dynamics and the flame chemistry. In this work, an exhaust gas analyser probe placed at the outlet of the combustion chamber is used to measure the gas composition of the combustion products. The exhaust gas is measured with an ABB gas analyser, which is equipped with the modules Limas21 HW (NO and NO_2 -accuracy 0.1 ppm), Uras26 (CH_4 - accuracy 0.1 %vol, CO - accuracy 1 ppm, CO_2 - accuracy 0.1 %vol), and Magnos28 (O_2- accuracy 0.1 %vol). Both the Uras and Limas units operate based on the UV photometry principle, where the sample gas is passed through a cuvette and the light is absorbed according to the Beer-Lambert law

$$I_1 = I_0 e^{-\epsilon(\lambda) p L} \tag{3.7}$$

Where I_0 is the intensity of the light, I_1 is the intensity of the light after passing through the sample, ϵ is the extinction coefficient, p is the pressure, L is the path length and λ is the wavelength of the light. The Limas unit uses the UV-RAS (Ultra Violet Resonant Absorption Spectroscopy) method to measure NO and NO_2. NO_x measurements are performed hot-wet, this means the water is not condensing. This is achieved by keeping the heated suction line at 180°C and the analyser itself at 80°C.

The remaining species are measured on a dry basis, meaning the water is removed from the sample gas using a cooler before it enters the analyser. The Magnos28 measures O_2 using its paramagnetic properties, with ABB's microwing technology.

A recalibration of the gas analyser with designated calibration gases was performed before each measurement day, in order to reduce uncertainties due to zero drift and sensitivity drift. For all three modules, the linear deviation is ≤ 2 % of the span and the repeatability is ≤ 1 %.

The gas composition measurements are corrected to a standard value of 15 % O_2 with the following equation

$$X_{\text{species,15\%O2}} = X_{\text{species,measured}} \left(\frac{0.2096 - 0.15}{0.2096 - X_{\text{O}_2\text{, measured}}} \right) \tag{3.8}$$

Where $X_{\text{species,15\%O2}}$ is the mole fraction of a certain species at 15 % O_2, $X_{\text{species,measured}}$ is the measured mole fraction of the species and $X_{\text{O2,measured}}$ is the measured mole fraction of O_2.

3.2.2. PARTICLE IMAGE VELOCIMETRY

WORKING PRINCIPLE

Particle Image Velocimetry (PIV) is a widely used, non-intrusive technique for measuring velocity fields by particle displacement. A typical 2D2C PIV setup is illustrated in

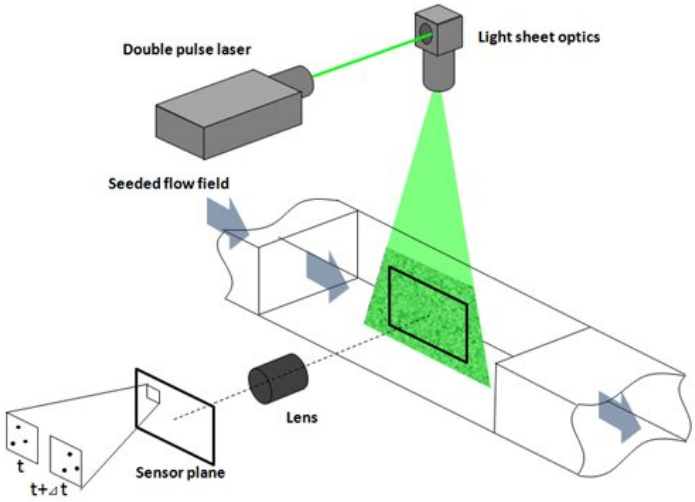

Figure 3.5: Example of a 2D2C PIV set-up taken from SEIKA Digital image corporation.

Figure 3.5. For this technique, the flow is seeded with tracer particles that closely follow the fluid motion, if the Stokes number, which is defined as the ratio of the characteristic time of the particle to a characteristic time of the flow, is below $St < 0.1$ [118]. A double-pulsed laser illuminates the test region, and particle images are captured using a camera in double-frame mode with a short time interval δt. For a 2D2C PIV set-up the sensor plane of the camera is oriented perpendicular to the laser sheet. A sufficiently high laser power and a uniform seeding density are critical for obtaining high-fidelity PIV data. This is because the scattering observed during PIV measurements generally falls within the Mie scattering regime, where the effective diameter of the seeding particles are much larger than the excitation wavelength of the laser $d_p \gg \lambda_{laser}$. In the Mie-scattering regime, the side scattering is significantly weaker than the forward scattering, making it challenging to collect a sufficiently high signal.

The acquired double-frame images are divided into interrogation windows, within which two-dimensional cross-correlation is applied to determine the particle displacement between the two frames. A multi-pass approach is employed, where the size of overlapping interrogation windows decreases with each pass. This ensures that large particle displacements are captured while maintaining the resolution of small-scale velocity structures.

PIV SET-UP

PIV measurements in this work were taken using a high-repetition-rate PIV set-up. Two laser systems were used: either a 527 nm Nd:YAG laser (Quantronix Darwin Duo 527-80-M) with a pulse energy of 30 mJ, pulse width < 200 ns, and a maximum repetition rate of 3 kHz, or a 532 nm laser (MESA PIV 532-80-M) with a pulse energy of 13 mJ, pulse width < 170 ns, and a maximum repetition rate of 30 kHz. Scattered light was recorded using a high-repetition-rate double-frame camera with a sensor resolution of either 1024×1024

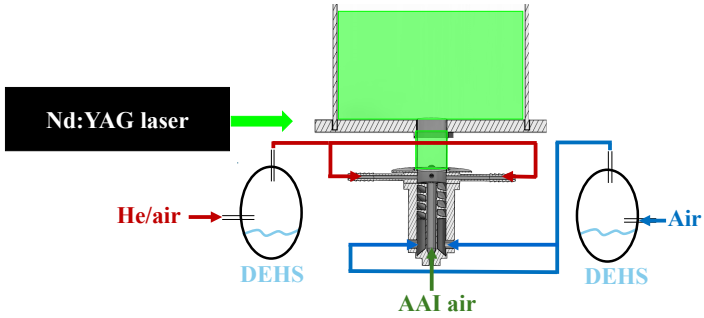

Figure 3.6: PIV set-up used in this work for the non-reacting studies, the laser sheet illuminates either the mixing tube or the combustion chamber. Depending on the study the surrogate stream (He/air) or the swirling air stream is seeded with DEHS particles. The laser sheet is oriented perpendicular to the camera sensor plane.

(Photron Mini AX 100) or 2016×2016 pixels (LaVision Imager Pro HS). The laser and camera were synchronized using a DaVis PTU X. As the specific laser and camera configuration varied between experimental campaigns, detailed descriptions are provided in the respective chapters. All image processing and velocity calculations were performed using the commercial software DaVis versions 8.4.0 and 10.0.8.

In the non-reacting studies, either the mixing tube or the combustion chamber was illuminated by the Nd:YAG laser (see Figure 3.6), depending on the specific experiment. The laser sheet was oriented perpendicular to the camera sensor plane. For the PIV measurements, the swirling air was seeded with DEHS droplets. Additionally, Mie scattering imaging was performed to investigate fuel-air mixing of the jet in cross-flow configuration within the mixing tube. For this purpose, the surrogate fuel stream (He/air) was seeded with DEHS particles, enabling the visualization of particle distribution as an indicator of the mixing quality. A deeper penetration of seeding particles into the centre of the mixing tube corresponds to a higher degree of mixing. The optical set-up for laser and camera was identical to that used in the PIV measurements, except that images are acquired in single-frame mode rather than double-frame mode. The post-processing procedure for the Mie scattering images is detailed in Chapter 5.

In the reacting studies, only the combustion chamber was illuminated by the Nd:YAG laser (see Figure 3.7), as the mixing tube is not optically accessible. The swirling air was seeded with TiO_2 particles, and the laser sheet remained oriented perpendicular to the camera sensor plane.

PIV SEEDING

To ensure the seeding follows the flow, the Stokes number (St) should generally be less than 0.1 [118]. The St number is defined as the ratio of the particle response time to the characteristic timescale of the flow:

$$St = \frac{\tau_p}{\tau_f} \tag{3.9}$$

where the particle response time τ_p is given by

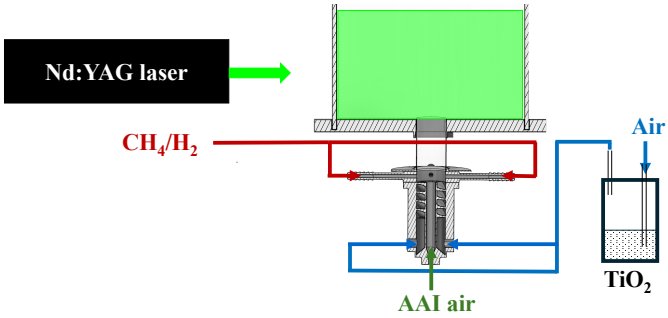

Figure 3.7: PIV set-up used in this work for the reacting studies, the laser sheet illuminates the combustion chamber, and the swirling air stream is seeded with TiO_2 particles. The laser sheet is oriented perpendicular to the camera sensor plane.

$$\tau_p = \frac{\rho_p d_p^2}{18\mu} \tag{3.10}$$

and the characteristic timescale of the flow τ_f is given by

$$\tau_f = \frac{\delta}{U_\infty} \tag{3.11}$$

Where ρ_p is the particle density, d_p the particle diameter, μ the dynamic viscosity of the fluid, δ the characteristic length scale of the flow and U_∞ the velocity of the flow.

For the non-reacting studies, DEHS droplets generated with a PIVTEC PIVpart45 oil seeder with a density of 912 kg/m^3 and a diameter of 0.9 µm were injected into the flow. For the case where the droplets were injected into the He/air stream, the diameter of the fuel inlet ports is used as δ, and the bulk fluid velocity in the fuel ports as U_∞. The exact calculation procedure for the Stokes number can be found in Appendix C. For the fuel surrogate case at P = 12 kW (see Table 3.2), DEHS particles were injected into the surrogate fuel (He/air) stream, resulting in a Stokes number $St < 0.1$. When the DEHS particles are injected into the swirling air stream, the Stokes number is calculated using the bulk velocity and the diameter of the mixing tube. As expected, this results in significantly lower St values compared to the case where the particles are introduced with the high-velocity surrogate fuel stream.

For the reacting studies TiO_2 seeding was used with a density of 4000 kg/m^3 and a diameter of 1 µm, distributed with an in-house manufactures cyclone seeder. The Stokes number is here calculated with the bulk velocity in the mixing tube and the mixing tube diameter, resulting in a Stokes number of $St << 0.1$ for all cases.

SPECTRAL PROPER ORTHOGONAL DECOMPOSITION

Studying the unsteady flow field involves the calculation of the coherent structure or modes from the flow field data. The most common method to extract coherent structures from the flow field is the Proper Orthogonal Decomposition (POD) [119]. The POD is a statistical method that decomposes the flow field into a set of orthogonal modes,

which are ordered by the amount of energy they contain. SPOD, first introduced by Lumley [119], is preferred over POD for analysing flows with dominant frequency-dependent structures, as it identifies modes that are coherent in both space and time and orthogonal under a space–time inner product, whereas POD modes are orthogonal only in space [120]. As a consequence, they are optimal at expressing spatiotemporal coherence in the data. This makes the technique ideal for studying periodic or oscillatory phenomena in the flow field, such as the PVC in swirling flows or combustion instabilities. A comprehensive overview of the SPOD methodology can be found in Schmidt et al. [121]. The methodology is summarized in the following part for completeness, and can be seen in Figure 3.8.

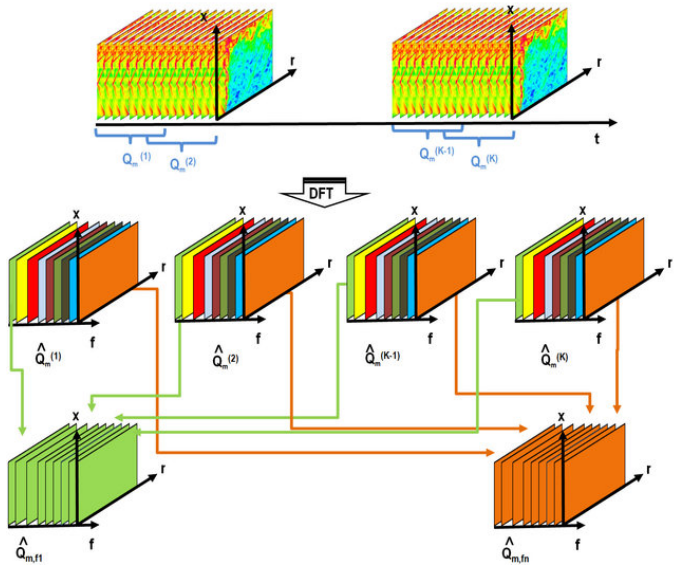

Figure 3.8: Schematic of spectral proper orthogonal decomposition SPOD modes using Welch's method (Colours represent discrete frequencies), figure taken from [122].

Considering a data matrix Q

$$Q = [q_1, q_2, ..., q_M] \in \mathbb{R}^{NxM} \tag{3.12}$$

Where N is the length of the single vector q and M is the number of snapshots. With Welch's method, the data matrix is divided into blocks of size n_s with a possible overlap.

The blocks can be written as follows

$$Q^{(n)} = [q_1^{(n)}, q_2^{(n)}, ..., q_M^{(n)}] \in \mathbb{R}^{NxN_f} \tag{3.13}$$

with the $k_t h$ entry in the $n_t h$ block given by $q_k^{(n)} = q_{k+(n-1)(N_f-N_o)}$. N_f is here the number of snapshots in each block, N_o is the overlap between the blocks and N_b is the total number of blocks. The blocks are then multiplied with a window function w to

reduce the leakage effect in the Fourier transform. The Fourier transform of the blocks is then calculated as follows:

$$\hat{q}_k^{(n)} = \sum_{j=1}^{N_f} w_j q_i^{(n)} e^{-i2\pi(k-1)[(j-1)/N_f]} \tag{3.14}$$

A new data matrix is formed at the k_{th} frequency by collecting all the Fourier realizations of the blocks, shown by the equally coloured blocks in Figure 3.8.

$$\hat{Q}_f k = [\hat{q}_f k^{(1)}, \hat{q}_f k^{(2)}, ..., \hat{q}_f k^{(N)}] \in \mathbb{C}^{NxM} \tag{3.15}$$

Each frequency now has a data matrix $\hat{Q}_f$ associated with it. For each $\hat{Q}_f$, the cross-spectral density matrix is calculated as follows:

$$\hat{C}_f = \frac{1}{N-1} \hat{Q}_f \hat{Q}_f^H \tag{3.16}$$

The Eigenvalues can be calculated via the method of snapshots based on the traditional POD approach, see for example [123].

3.2.3. OH* CHEMILUMINESCENCE

WORKING PRINCIPLE

OH* Chemiluminescence is the result of emissions of the OH when transitioning from the electronically excited state $A^2\sum^+$ to its ground state $X^2\Pi$. The electronically excited OH molecules are a short living intermediate species in the reaction zone of a flame, created via several possible mechanisms. For carbon fuels, the main OH* formation mechanism is [124]

$$CH + O_2 \longrightarrow OH^* + CO \tag{3.17}$$

For hydrogen flames, the main OH* formation mechanism is [125]

$$H + O + M \longrightarrow OH^* + M \tag{3.18}$$

where H-atoms combine with atomic oxygen involving a third collision partner M. Chemiluminescence appears, when OH* transitions to its ground state OH, while emitting light:

$$OH^* \longrightarrow OH + h\nu \tag{3.19}$$

The wavelength ($\lambda = \frac{c}{\nu}$) of the A-X transition lies in the near UV range, around 308 nm. Most of the molecules however release their energy not via emitting light, but via a collision with a third body partner. The amount of OH* which transitions to its ground state via emitting light is so small that it can be neglected in chemical kinetics studies [125]. However, the released light represents a simple form for qualitatively detecting the location and shape of the flame [126]. Figure 3.9 presents the emission spectrum of a premixed methane-air flame, highlighting the distinct emission peaks of OH* near 308 nm and CH* around 430 nm. A narrowband filter centred at the target wavelength

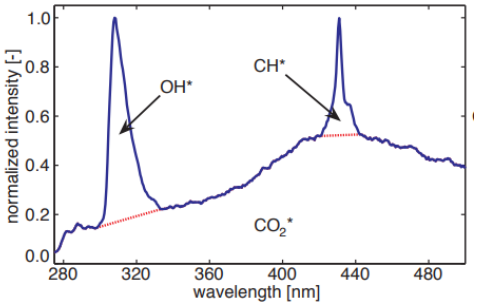

Figure 3.9: Spectrum of a premixed methane-air flame, OH* and CH* signal is superimposed by broadband CO_2* signal [132].

is mounted on the camera to isolate the emission from the species of interest. However, in hydrocarbon flames, the detected signals for OH* and CH* are always superimposed with broadband emissions from CO_2*, affecting the accuracy of species-specific measurements.

For laminar premixed flames, the spatially resolved OH* chemiluminescence is seen as a good approximation for the local heat release rate [127]. For turbulent flames however a spatially resolved heat release distribution can not be obtained by any direct signal from OH* and CH* due to the varying turbulence intensity in the reaction zone [128]. Although the OH* signal cannot be directly correlated with the heat release, it can still provide valuable insights into the flame shape and location in the combustion chamber.

Chemiluminescence is a line-of-sight technique that integrates the luminescence along the lines of sight viewed by the camera. A common way to approach the line-of-sight problem for axisymmetric intensity distributions is to reconstruct the spatial field with the so-called Abel transform [129]. This Abel inversion utilizes a Fourier-series-type expansion to map the radial pixel intensity distribution onto a theoretical 2-D plane through cosine expansions.

OH* IMAGING SET-UP

In this study OH* images where captured by an intensified sCMOS camera (LaVision IRO X and a VC-Imager M-lite 5M, with 1216x1024 pixel resolution) equipped with a band-pass filter centred around 310 nm (LaVision 1108760 VZ with 75 % average transmissivity). Images were acquired with the Davis 10.2.1 software and averaged over at least 200 images. Post-processing on the averaged images was initially carried out using the MATLAB code provided by Cardiff University [130], which is a modification of the MATLAB Abel transform open-source software developed by Killer [131]. After confirming that the Abel transform algorithm by Davis yielded identical results, the built-in algorithm was used to streamline the post-processing steps and save computational time.

3.2.4. PLANAR LASER INDUCED FLUORESCENCE

WORKING PRINCIPLE

Planar laser induced fluorescence (PLIF) is a technique used to detect the presence of minor species in a flame. The species relevant for this work are the hydroxyl radical (OH)

and the nitric oxide radical (NO). For this, a dye laser pumped by the second (OH-PLIF) or third (NO-PLIF) harmonics of a Nd:YAG laser is used to excite the molecules from the ground state to a high-energy state. In the linear regime, the Laser-Induced Fluorescence (LIF) signal is directly proportional to the target species number density and inverse proportional to the quenching rate [133]. A UV intensified camera with a filter mounted in front of the lens then captures fluorescence emitted when the molecules transition back to a lower energy state. A simplified schematic of the set-up can be seen in Figure 3.10.

OH is an intermediate species in the reaction zone and stays in the post-flame zone when the temperature is high enough. OH in CH_4/H_2 flames is formed by several reactions, but mainly via the two reactions [134]

$$H + O_2 \longrightarrow OH + O \tag{3.20}$$

and

$$H_2 + O \longrightarrow OH + H \tag{3.21}$$

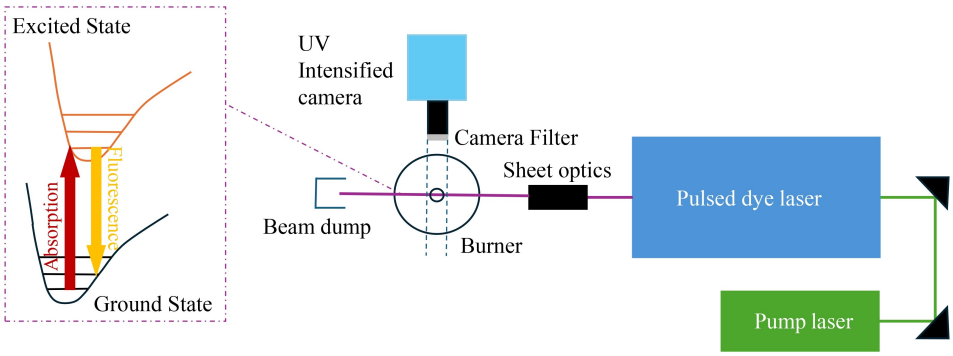

Figure 3.10: Working principle and laser-camera arrangement for laser-induced fluorescence (LIF) used in this work.

In the reaction zone, the formation rate of OH radicals significantly exceeds their reaction rate, leading to a super-equilibrium concentration. Downstream of the reaction zone, the OH concentration gradually declines in the post-flame region. As OH radicals are indicative of high-temperature regions, they serve as markers for both the reaction zone and the hot burnt gases. Due to the rapid increase in OH concentration within the reaction zone, they effectively distinguish between burnt and unburnt gases, making them a reliable indicator of the flame front [135].

Nitric oxide (NO) PLIF can be used as direct marker of the local NO concentration in the flame. NO is formed through one of the following reactions:

$$NO + O \rightarrow NO_2 \tag{3.22}$$

$$N + OH \rightarrow NO + H \tag{3.23}$$

$$N_2 + O \rightarrow NO + N \tag{3.24}$$

PLIF SET-UP

The PLIF laser system in this study consisted of a Nd:YAG laser (Q-smart 850) pumping a tunable dye laser (Sirah CobraStrech G 30) with a nanosecond pulse. The dyes used were Rhodamine 590 (OH-PLIF) or Coumarine 2 (NO-PLIF). The output beam of the dye laser was then steered into a collimator (LV 1108409), resulting in a 30 mm height usable laser sheet. The fluorescence was captured by an intensified sCMOS camera (LaVision IRO X and a VC-Imager M-lite 5M, with 1216x1024 px resolution). The intensifier was equipped with a bandpass filter, depending on the species investigated (for OH bandpass filter LaVision 1108760 VZ, with a width of 20 nm, centred at 308 nm with 75 % average transmissivity, for NO highpass filter LaVision 1108619 VZ (> 250 nm) with 92 % average transmissivity). Images were acquired with the software Davis 10.2.1.

To obtain a fluorescence signal representative of species concentration (OH and NO), the dye laser output wavelength has to be carefully selected to match energy transitions with minimal temperature dependence. The intensity of these transitions is linearly correlated with the molecular population of the initial state, which follows a Boltzmann distribution [133]. The excitation wavelength was chosen based on the temperature dependence and the intensity of the corresponding transition. Although collisional quenching is also temperature dependent [136], it was assumed to contribute uniformly across all excitation wavelengths, not influencing the line selection. Figure 3.11 shows the transition spectrum for the OH A-X(1,0) and the NO A-X(0,0) transition, including the temperature dependence of each excitation wavelength. The figure was generated with the open-source Matlab code *LIFTempDependence* [137]. The code is based on applying the Boltzmann distribution to the electronic, vibrational, and rotational states of OH and NO, assuming a harmonic oscillator and rigid rotator model, as described by Linne [138]. The code also makes use of the coefficients for each energetic state from the NIST database [139].

Excitation lines with relative intensities below 75 % for OH and 85 % for NO compared to their respective spectrum maxima were excluded for selection. For OH PLIF, the $A^2\Sigma^+$-$X^2\Pi$ transition (1,0) $Q_1(8)$ transition at 283.636 nm was chosen (see Figure 3.11, zoomed area in the top graph). This is a common wavelength selected for OH-PLIF [140]. For this wavelength the measured output energy was 26.5 mJ/pulse. For temperatures between 1300 K and 2000 K, which is the expected range of the temperatures in the combustor, the fluorescence intensity varies by 3.98 %. This is less than other transitions, while the signal remainings strong enough for OH-PLIF detection.

For the NO-PLIF, the $A^2\Sigma^+$-$X^2\Pi$ (0,0) $Q_2(20)$ transition line at 226.109 nm was selected, with an output energy of 6 mJ/pulse. This resulted in a sufficiently high intensity to detect NO, but came with the expense of an increase in temperature dependence of 12.32 %.

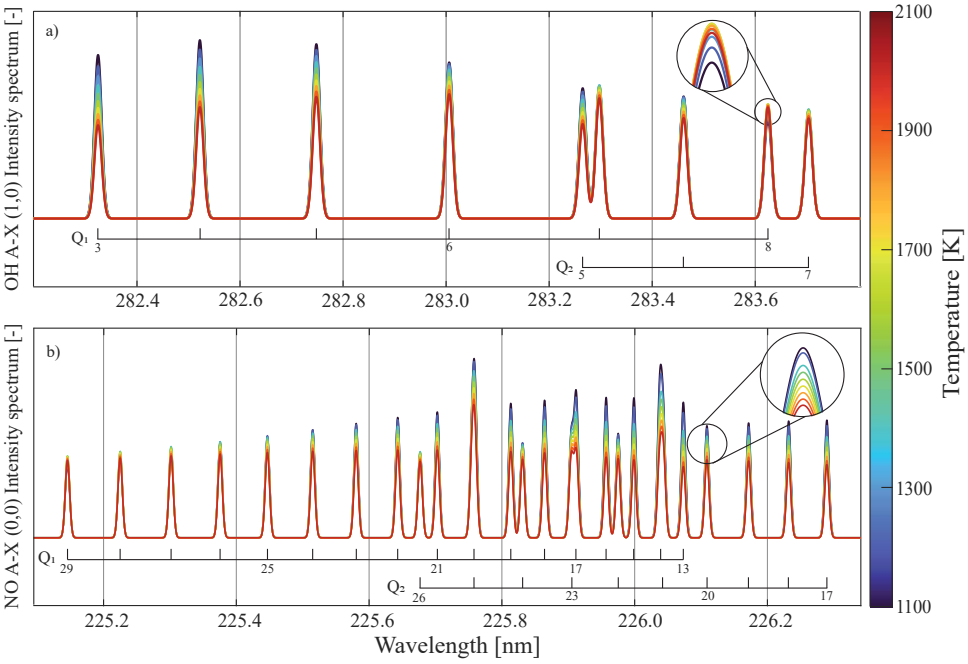

Figure 3.11: Effect of temperature in (a) OH A-X(1,0) transition spectrum and in (b) NO A-X(0,0) transition spectrum. Transitions with intensity lower than 75 % and 82.5 % were neglected for OH and NO, respectively.

II

Results & Discussion

4

NON-REACTING STUDIES IN A SWIRL-STABILIZED COMBUSTOR

A detailed investigation of the non-reacting flow field is essential to differentiate between changes in the flow field caused by inherent flow dynamics and those resulting from heat release in the reacting case. In fuel-flexible systems, changing the fuel from methane to hydrogen can significantly alter the flow field in the combustion chamber due to changes in density and injection velocities. However, geometric features, like the outlet boundary condition or the confinement ratio, can also influence the velocity profiles in the combustion chamber. In swirl-stabilized configurations, the flow is particularly sensitive to variations in velocity, as these influence key features like vortex breakdown and unsteady field features, like the PVC. Both of those flow field features are critical factors in determining the combustor performance, including flame stability and NO_x emission characteristics. This chapter investigates how several operational and geometric parameters influence the non-reacting flow field in a swirl-stabilized combustor, with jet in cross-flow fuel injection. The investigated parameters include outlet boundary conditions, confinement ratio, AAI, fuel composition, and the injection momentum of the fuel. The analysis focuses on how these parameters affect the mean flow field as well as and the dynamic behaviour associated with the PVC. Understanding these effects under non-reacting conditions provides a baseline for distinguishing flow-driven phenomena from combustion-induced changes in stability and emissions in subsequent chapters.

Parts of this chapter have been published in **S.Link et al.**, Proceedings of the ASME Turbo Expo, 2023, https://doi.org/10.1115/GT2023-101678

4.1. INTRODUCTION

Studying flow fields in a combustion chamber under non-reacting conditions provides essential insights into how geometric and operational parameters influence the flow, without the added complexity of combustion. In swirl-stabilized combustors, the flow field plays a critical role in determining flame stability and emission characteristics, as discussed in Chapter 2. Key features of swirling flows include the central and outer recirculation zones (CRZ and ORZ). The inlet conditions, such as the swirl number, along with the combustion chamber geometry, determine the type of vortex breakdown (see Section 2.1) and the location of the stagnation point. These factors also influence unsteady flow features, including the PVC, a helical (azimuthal wave number $m = 1$) self-induced hydrodynamic instability originating from the ISL. The PVC plays a major role in flame dynamics by influencing flame-vortex interactions [46] and potentially causing global heat release oscillations in asymmetric flow fields. Its interaction with thermoacoustic instabilities remains an open question, as contrasting behaviours have been observed. Steinberg et al. [141] demonstrated that the PVC can excite thermoacoustic instabilities in a fully premixed combustor. However, other studies suggest that actively generating a PVC in conditions where it does not naturally occur can suppress thermoacoustic instabilities [142, 143]. Furthermore, the PVC increases turbulent kinetic energy levels, enhancing fuel-oxidizer mixing in partially premixed configurations [144, 145]. The average flow field characteristics, such as the size and strength of the CRZ and the dynamics of the PVC, are influenced by a range of parameters. The following section discusses the factors that are likely to affect the flow field in the investigated swirl-stabilized burner.

One such factor is the outlet boundary condition of the combustion chamber. To suppress thermoacoustic instabilities in reacting conditions, it is common practice to modify the acoustic outlet boundary condition, typically by introducing an area contraction through an orifice or nozzle [146]. If the Mach number approximately matches the nozzle area contraction ratio, the outlet can act as an anechoic termination for frequencies below 1000 Hz [147]. However, such area contractions can significantly affect the upstream flow field under both non-reacting and reacting conditions, particularly when the flow is subcritical, where the mean flow field can sustain long inertia waves, therefore perturbations can move upstream in the flow field. When the swirl number is low, the impact of an outlet contraction is minimal, as the flow tends to recover to supercritical conditions downstream of the vortex breakdown [33]. In contrast, if the swirl number is sufficiently high, the flow remains subcritical, and the outlet contraction alters the flow field throughout much of the domain. Whether this influence persists when moving from non-reacting conditions to reacting conditions depends on the flow remaining subcritical after heat release, which is strongly influenced by the initial swirl number and the amount of heat release [38, 148]. Overall it has been concluded, that when the effective swirl number at the combustion chamber exceeds $Sw > 0.2$-0.3, the flow stays subcritical, and consequently the outlet contraction has a significant influence on the flow field [149].

Another key parameter affecting the flow field in the combustion chamber is the confinement ratio, defined as the ratio of the combustion chamber area to the premixing section area. Confinement strongly influences the behaviour of swirling flows, primarily

by promoting the formation of outer recirculation zones. A smaller combustion chamber diameter results in a more compact and shorter CRZ in the streamwise direction [150], which can shorten the flame and reduce stability. Higher confinement ratios enlarge the CRZ, enhancing the recirculation of hot combustion products into the reaction zone [36], thereby extending the blow-out limits of the flame [151]. Additionally, confinement significantly increases turbulent kinetic energy, up to double that of unconfined cases, with this effect becoming more pronounced as the chamber diameter decreases [151, 152].

Another important design parameter influencing the flow field in the investigated configuration is AAI [22], where part of the total air is injected along the centreline of the mixing tube without swirl. As the level of AAI increases, the effective swirl number decreases [53], thereby reducing the size and strength of the recirculation zone [85]. If the reduction of the swirl number is high enough, the swirl number may fall below the critical threshold for vortex breakdown or change the vortex breakdown mode from bubble-type to cone-type [53].

In fuel-flexible configurations, the fuel composition can also affect the flow field. For instance, injecting a lower-density fuel such as hydrogen, compared to methane, results in a significantly higher volumetric fuel flow rate to maintain the same thermal input. This results in higher bulk velocities and modified velocity profiles in the premixing section, potentially affecting the effective swirl number. Moreover, variations in fuel composition, and thus in flow rate and density, change the momentum flux ratio between fuel and air (J_{swirl}). When the fuel is injected radially or axially, these changes can impact the swirl number and, in turn, the overall flow field in the combustion chamber.

A clear understanding of how operational and geometric parameters affect the non-reacting flow field is essential before introducing combustion. It allows the separation of flow-driven effects from those induced by heat release. For this reason, this chapter focuses on the non-reacting flow field, exploring a wide range of operational and geometrical conditions, and identifying the parameters that cause significant changes in the flow field. This chapter is structured as follows: Section 4.2 describes the experimental set-up and operating conditions. Section 4.3 presents the results of the non-reacting studies, investigating the effects of the boundary condition, confinement ratio, level of AAI, momentum flux ratio J_{swirl}, and fuel composition variations on the flow field. Finally, Section 4.4 summarizes the key findings of this chapter.

4.2. CONFIGURATION SPECIFICATIONS

GEOMETRY & OPERATING CONDITIONS

Experiments were performed in the 3D printed duplicate of the TU Delft swirl-stabilized burner, as described in Section 3.1.3. The set-up can be seen in Figure 4.1, and it comprises an axial swirler with a swirl number Sw = 1.1. Only one swirl number was investigated, as it was shown in the reacting cases that the Sw = 1.1 outperforms the Sw = 0.7 swirler in terms of emissions and flashback resistance (see results in Chapter 6). The fuel gets injected downstream of the swirler through four fuel ports in jet in cross-flow configuration. Downstream of the optically accessible mixing tube with a diameter of d_{MT} = 24 mm, the mixture enters an optically accessible cylindrical combustion cham-

Fuel reacting		Surrogate				
Tag	XH_2	Tag	d_{J-low} [mm]	J_{low}	d_{J-high} [mm]	J_{high}
A	0	A_s	3.5	0.09	1.4	3.45
B	0.4	B_s	3.5	0.11	1.4	4.33
C	0.8	C_s	3.5	0.13	1.4	4.89
D	1	D_s	4.07	0.12	1.64	5.01

Table 4.1: Fuel mixture tags and hydrogen molar fractions for the reacting experiments and corresponding surrogate fuels and the diameters for the fuel inlets for the different momentum flux ratios J_{swirl} at $Sw = 1.1$.

ber. The combustion chamber has a length of 400 mm and a variable inner diameter d_{CC} (152 mm, 100 mm, 68 mm), which results in three different confinement ratios c (c = 40, 17 and 8), defined as the ratio of the combustion chamber area to the mixing tube area:

$$c = \frac{A_{CC}}{A_{MT}} \tag{4.1}$$

For the cases with AAI, the total mass flow is kept constant and the percentage of AAI is given with

$$\chi = \frac{\dot{m}_{AAI}}{\dot{m}_{total}} \quad \text{with} \quad \dot{m}_{total} = \dot{m}_{air} = 5.1 \times 10^{-3}\,\text{kg/s} = 264\,\text{L/min} \tag{4.2}$$

The CH_4/H_2 fuel mixtures are replaced with He/air mixtures according to the method described in Section 3.1.3, with maintaining a constant mixture density. Table 4.1 presents the tag nomenclature and corresponding hydrogen molar fractions used in this chapter, along with the diameters of the fuel injection holes and the resulting values of J_{swirl}. Throughout this chapter, any reference to a hydrogen fraction XH_2 denotes the surrogate case associated with that fuel composition, corresponding to cases A_s through D_s as defined in Table 4.1.

Replacing the 100 % H_2 case with helium does not allow for matching the density, as helium has approximately twice the density of hydrogen. As a result, the momentum flux ratio is maintained, which required an increase in the fuel inlet diameter when substituting hydrogen with helium.

This chapter presents data from two experimental campaigns. The first part investigates flow conditions without fuel injection, focusing on the influence of confinement ratio and outlet boundary conditions. The second part examines the flow field with fuel injection in jet in cross-flow configuration, addressing the effects of AAI, fuel composition, and momentum flux ratio. Two different PIV set-ups were used, each with seeding strategies adapted to the specific aims of each campaign. The specific experimental configurations for both campaigns are described in the following section.

MEASUREMENT TECHNIQUES

For the cases without fuel injection, time-resolved PIV measurements with two cameras were performed at the centre plane (see Figure 4.1a, dark red boxes). The field of

view of the cameras overlapped by 1.5 cm, and data where stitched together during post-processing of the data. The swirling air stream was seeded with DEHS droplets, which results in a Stokes number of $St \ll 0.1$, based on the diameter and bulk velocity of the mixing tube. The specifications of the PIV set-up can be found in Table 4.2.

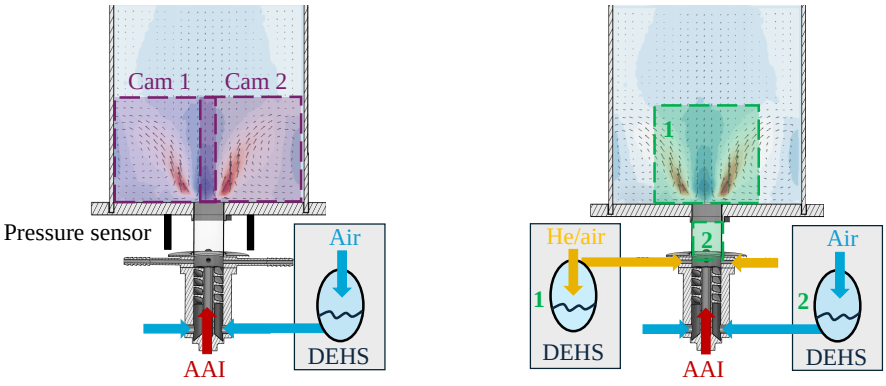

a) Set-up cases without fuel injection

b) Set-up cases with fuel injection

Figure 4.1: Measurement planes and seeding locations for the PIV measurements.

Laser	Nd:YAG Laser Continuum MESA (532 nm)
Camera	2 x Photron Fastcam SA-1
Lens	60 mm
Sensor size	1024× 1024 px
Interrogation window	24× 24 px, 50 % overlap
Spatial resolution	14.6 px/mm
Acquisition frequency	2 kHz
Seeding particles	DEHS droplets ($d \approx 0.9\,\mu$m)
δt	15 µs

Table 4.2: Specifications PIV set-up without fuel injection.

One of the cameras looked at an angle of 11° at the field of view, which caused a slight error of around 2 % in the absolute velocities. The velocity fields were averaged over N = 2000 image pairs and normalized with the bulk velocity U_{MT} in the mixing tube. The random error in the velocities is given by $U_{rms}/\sqrt{N}$, where U_{rms} is the root-mean-square of the velocity. With the sample size of 2000 images this resulted in a velocity uncertainty of around 2 % of U_{rms}. In addition to the PIV measurements, two differential pressure sensors were installed on the combustor baseplate at r = 2.7 mm and r = −2.7 mm (see Figure 4.1a). These pressure measurements provide insight into the PVC frequency and can be used to validate the findings of the PIV measurements. The pressure data were acquired with a HoneyWell TruStability differential pressure transducer (accuracy: 0.25 % FS, sampling frequency: 2 kHz, range ± 0.6 kPa).

Laser	Nd:YAG Quantronix Darwin Duo 527-80-M
Camera	1 x Photron Fastcam Mini AX 100
Lens	105 mm
Sensor size	1024× 1024 px
Final interrogation window	16× 12 px (CC), 12× 12 px (MT), 75 % overlap
Spatial resolution	19.1 px/mm (CC, MT)
Acquisition frequency	1 kHz
Seeding particles	DEHS droplets ($d \approx 0.9\,\mu$m)
δt	15 µs

Table 4.3: Specifications PIV set-up with fuel injection.

For the cases with fuel injection, the measurement plane was either in the combustion chamber (plane 1 in Figure 4.1b) or in the mixing tube (plane 2 in Figure 4.1b). For measurements in plane 1 the swirling air was seeded with DEHS droplets, while for measurements in plane 2 the surrogate fuel stream (He/air) was seeded. Since this chapter also investigates the effect of momentum flux ratio (for the definition refer back to Equation 2.22) on the flow field, the diameter of the fuel injection holes was varied to modify the inlet velocity. For the large diameter (see Table 4.1), indicated as J_{low}, the Stokes number, calculated using the fuel bulk velocity and fuel inlet diameter, remains below $St < 0.1$. For the smallest diameter (J_{high}), Stokes numbers up to $St < 0.2$ were reached due to the higher fuel inlet velocities. Nevertheless, since all values remain well below $St < 1$, the particles are expected to follow the flow accurately [118]. Since the velocities in the combustion chamber are significantly lower than the injection velocities it is assumed that $St < 0.1$ holds in the combustion chamber. In the figures of this chapter, all the length scales are normalized with the mixing tube diameter D_{MT}. For all results the systematic error was investigated with the correlation statistics method available in the LaVision Davis software, and they were lower than 5 %.

DATA PROCESSING AND ANALYSIS

A spectral proper orthogonal decomposition (SPOD) was applied separately on the x-component V (transverse) and y-component U (streamwise) of the velocity data obtained from both experiments. The SPOD modes are presented in V velocity since the helical (asymmetric) structure of the PVC can be identified easily by the axis-symmetric patterns in the modes [153]. As demonstrated in Terhaar et al. [154], a POD of the swirling flow field data in Cartesian coordinates results in a symmetric pattern when analysing the PVC modes of the transverse velocity V or the through-plane vorticity ω_z. If they are computed in cylindrical coordinates, the modes become skew-symmetric. The SPOD, derived from a space-time POD, has the advantage of capturing coherent evolution of the modes in space and time. While SPOD applied to a two-dimensional flow field can only provide an indication of the three-dimensional structure in the two-dimensional view, it does offer insights into the spatial and temporal correlations in 2D. Characteristic PVC patterns in two-dimensional planes have been clearly identified in previous studies [153]. Therefore, given the rotational symmetry of swirling flows, meaningful conclusions on the PVC structure can be drawn from an analysis of the two-

dimensional flow field.

The SPOD analysis was performed with the open-source MATLAB function SPOD [121]. The data matrix of the fluctuating velocity component V' consists of m (number of snapshots) columns and n_s rows, with the dimension of $n_s = N_x \cdot N_y = 29\,241$ (number of data points in x- and y-direction). The matrix V' of the fluctuating velocities gets determined by removing the average velocities of every column from their respective column in the velocity matrix.

$$V' = \begin{bmatrix} v'_{11} & \dots & v'_{1m} \\ v'_{21} & \dots & v'_{2m} \\ \dots & & \dots \\ v'_{n_s 1} & \dots & u'_{n_s m} \end{bmatrix} = [v'_1, v'_2, ..., v'_m] \in \mathbb{R}^{n_s \mathrm{x} m} \tag{4.3}$$

For the Discrete Fourier Transform (DFT) applied to the matrix V', the columns of V' got divided into blocks with a length of $l = 512$. Each n^{th} block (size $n_s \mathrm{x}\, l$) and its Fourier transform can be written as

$$\begin{aligned} V'^{(n)} &= [v'^{(n)}_1, v'^{(n)}_2, \dots, v'^{(n)}_l] \\ &\xrightarrow{\text{DFT}} \hat{V}'^{(n)} = [\hat{v}'^{(n)}_1, \hat{v}'^{(n)}_2, \dots, \hat{v}'^{(n)}_l] \end{aligned} \tag{4.4}$$

A 50 % overlap resulted in $n_b = 6$ blocks with a size of $n_s \mathrm{x}\, l$. A Hanning window filtering was applied to the data, which resulted in a frequency resolution of 4 Hz. After the DFT, the data are present at 257 discrete frequencies f. The Eigenvalue analysis is performed on one frequency at a time, with the data matrix written as following

$$\hat{V}'_f = [\hat{v}'^{(1)}_f, \hat{v}'^{(2)}_f, ..., \hat{v}'^{(n_b)}_f] \tag{4.5}$$

The cross-spectral density tensor is determined as

$$\hat{C} = \frac{1}{n_b - 1} \hat{V}'_f \hat{V}'^T_f \tag{4.6}$$

Finally, the eigenvalues and eigenvectors are computed following the traditional POD procedure [155]. For a more detailed description of the SPOD methodology, the reader is referred to the work of Schmidt et al. [156].

For the pressure measurements, a Fast Fourier Transform (FFT) of $\Delta p = p_2 - p_1$ provides the spectrum of the pressure fluctuations. Applying the FFT to the difference between the two pressure signals ensures that the pressure fluctuations are not caused by a symmetric structure, but by an asymmetric structure such as the PVC. The pressure signal recorded for 5 seconds was divided into blocks with a length of 4000 samples. A Hanning window filtering with 50 % overlap resulted in a final frequency resolution of 2 %. The difference on the frequency of the PVC obtained from the pressure measurements and the frequency obtained from the SPOD data is below 3 %.

4.3. RESULTS

In this section, first the effect of the outlet boundary condition and the confinement ratio on the average flow field and the PVC dynamics is evaluated. This analysis is performed without radial fuel injection. The subsequent sections investigate the effect of AAI, the surrogate fuel composition and the momentum flux ratio on the flow field and PVC dynamics.

4.3.1. EFFECT OF OUTLET CONTRACTION

To evaluate the effect of the outlet contraction on the flow field, measurements were conducted both with and without a nozzle at the largest confinement ratio, $c = 40$, and an air flow rate of $\dot{Q}_{\text{swirl}} = 264\,\text{L/min}$ without radial fuel injection and without AAI. In the case with the nozzle, the outlet diameter was set to $d_{\text{nozzle}} = 15\,\text{mm}$, to satisfy the condition that the area contraction ratio approximately matches the Mach number in the nozzle for the studied cases. This ensures the outlet contraction functions as an anechoic termination for frequencies below 1000 Hz. Figure 4.2 shows the time-averaged streamwise velocity field in the combustion chamber for the two outlet configurations: an open outlet (a) and a nozzle (b). The red dashed line in the figure indicates the zero axial velocity line. The figure highlights that the CRZ is notably influenced by the presence of an outlet contraction. Up to $y/D_{\text{MT}} = 1.5$, the velocities in the swirling jet and the negative axial velocities within the CRZ remain largely unchanged. However, beyond this axial location, the outlet contraction induces an accelerating centreline flow in the forward direction, leading to a reduction in both the size and strength of the CRZ. Moreover, downstream of $y/D_{\text{MT}} = 1.5$, the opening angle of the swirling jets decreases in the presence of the outlet contraction. The red dashed line in the figure indicates the zero axial velocity. According to the results of Terhaar et al. [149], the strong influence of the outlet contraction on the flow field indicates that the swirl number at the combustion chamber outlet exceeds the critical value of $Sw = 0.2$, meaning the flow remains subcritical downstream of the vortex breakdown. Under reacting conditions, the effective swirl number generally decreases, which can reduce or even eliminate the influence of the outlet contraction if it falls below a critical threshold. To ensure consistency and enable a direct comparison between reacting and non-reacting flow fields, an open outlet configuration was adopted for all subsequent experiments.

4.3.2. EFFECT OF THE CONFINEMENT RATIO

This section investigates the effect of the confinement ratio on the flow field by varying the combustion chamber diameter. Three different chamber diameters, along with an unconfined case, are examined. The experiments are done without radial fuel injection and without AAI. Figure 4.3 presents the time-averaged streamwise velocity fields at $\dot{Q}_{\text{swirl}} = 264\,\text{L/min}$ for different confinement ratios c, including the unconfined case ($c = \infty$). Adding confinement to the swirling flow (from $c = \infty$ to $c = 40$) leads to a significant increase in both the length and width of the CRZ, and also results in the formation of an ORZ. These effects are attributed to increased pressure recovery in confined geometries, which induces a stronger adverse axial pressure gradient. This, in turn, promotes earlier and more abrupt vortex breakdown, resulting a wider CRZ with significantly higher negative axial velocities in the CRZ, from around $-2.4\,\text{m/s}$ for $c = \infty$ to $-7\,\text{m/s}$ for $c = 40$.

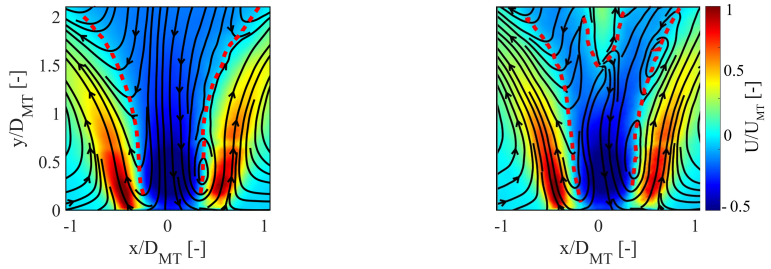

a) Open outlet **b)** Outlet contraction

Figure 4.2: Effect of orifice on the outlet of the combustion chamber on the non-reacting average flow field (a) open outlet, (b) outlet contraction, dashed line indicates the zero axial velocity line.

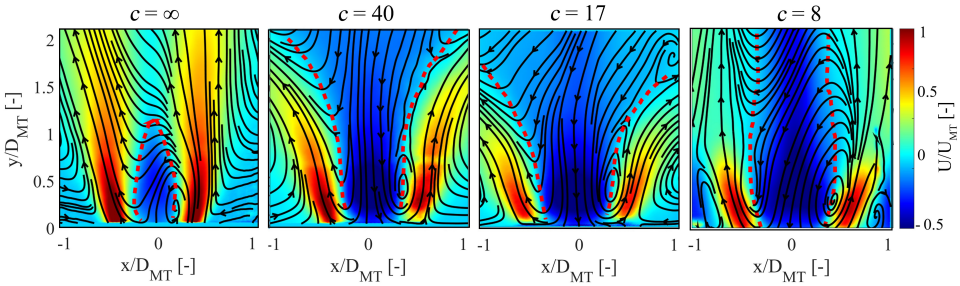

Figure 4.3: Average streamwise velocity fields for different c at $Sw = 1.1$ without AAI and without fuel injection, dashed lines indicate zero axial velocity line.

Confinement also influences the velocities within the swirling jet, causing it to spread more radially and reduce its axial velocity. While the jet velocity generally decreases with decreasing c, the lowest velocity is observed at $c = 17$ rather than at $c = 8$. This is attributed to the slightly wider spreading of the swirling jet at $c = 17$.

A smaller combustion chamber diameter initially results in a broader and longer region of strong negative axial velocities in the CRZ ($0 < y/D_{MT} < 0.5$). However, in the case of $c = 8$, the CRZ quickly reaches its maximum width further downstream. This is due to the swirling jets impinging on the combustion chamber walls at an angle close to 45°, leading to a strong deflection and a predominantly axial flow with minimal radial velocity further downstream. In contrast, at higher confinement ratios, the CRZ continues to expand radially downstream, extending beyond the field of view. While the magnitude and extent of negative axial velocities near the mixing tube outlet ($y/D_{MT} = 0$) are similar across all confined cases, further downstream the extent and intensity of the reverse flow increase with confinement ratio. Assuming rotational symmetry, the broader recirculation zones and stronger negative axial velocities suggest an increased recirculated mass flow. In the reacting case, this is expected to enhance flame stabilization by promoting the entrainment of hot combustion products into the reaction zone.

Figure 4.4 shows the real part of the SPOD mode 1 (most energetic SPOD mode) at $f = 320$ Hz for the normalized transverse velocity component for the different confine-

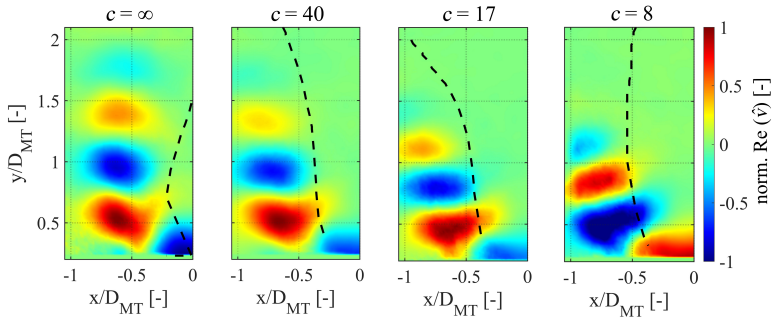

Figure 4.4: Normalized transverse velocity component $\hat{v}$ (real part) from the SPOD mode 1 at f = 320 Hz, dashed lines indicates zero U line.

ment configurations at $\dot{Q}_{\text{swirl}}$ = 264 L/min. The frequency corresponds to the highest amplitude in the energy spectrum of the strongest SPOD mode. The alternating high and low values of the normalized real part of the transverse SPOD mode component ($Re(\hat{v})$) reveal coherent helical structures along the streamwise direction, characteristic of the PVC. This pattern provides insight into the size and shape of the structure. The opening angle of the helix, indicating the PVC radius, increases with decreasing confinement, consistent with the behaviour of the swirling jet shown in Figure 4.3. This correlation is expected, as the PVC wraps around the CRZ, therefore reflects its shape. The streamwise extent of the PVC is greatest in the unconfined case and shortest for the lowest value of confinement c = 8. This is likely due to a wider helix radius at a moderate confinement ratio c = 17, which, by conservation of angular momentum, reduces the angular velocity in the axial direction and shortens the region where the CRZ can influence the flow field. For c = 8, the PVC interacts with the combustion chamber wall already at around y/D_{MT} = 0.75, leading to a rapid decay of the coherent structures in streamwise direction. Additionally, the helix pitch decreases with decreasing confinement, which is consistent with the findings of Favrel et al. [157]: at constant swirl number, a larger helix radius leads to a smaller pitch. The PVC at c = 8 exhibits both a smaller radius and smaller pitch than at c = 17, suggesting a reduction in swirl number due to strong wall interaction. These observations suggest that reducing confinement initially increases the PVC radius and lowers the pitch. However, below a critical confinement ratio (c_{critical}), wall interaction becomes the dominant effect, suppressing the PVC and further reducing the effective swirl number downstream.

In Figure 4.5 the PVC frequencies f are presented for different confinement ratios with varying swirling air flow rates $\dot{Q}_{\text{swirl}}$, to evaluate how the frequency scales with the air flow rate. The frequencies are obtained from the pressure measurements in the combustion chamber. In addition, a line with constant Strouhal number $Sr_{\text{PVC}} = \frac{f \cdot d_{\text{MT}}}{U_{\text{MT}}}$ of 0.78 is shown, calculated by fitting to the observed frequency trends. The unconfined configuration follows this constant Strouhal number line almost perfectly. In the confined cases, the frequencies slightly deviate below the theoretical predictions as $\dot{Q}_{\text{swirl}}$ increases. This shows that the frequency of the PVC is only marginally affected by the level of confinement. This scaling aligns well with previous studies conducted under

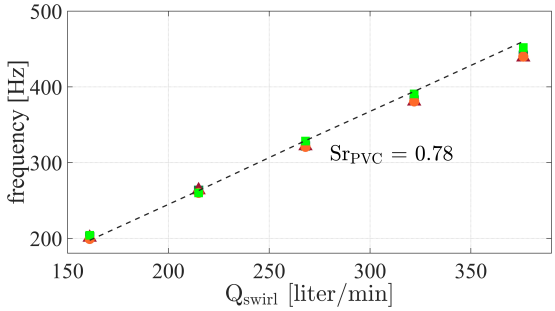

Figure 4.5: PVC frequencies obtained from pressure measurements at different swirling air flow rates $\dot{Q}_{swirl}$ and different c, ■ c = 40, ▲ c = 17, ● = c = 8, ■ c = unconfined, dashed line indicates constant Strouhal number line Sr = 0.78.

non-reacting conditions at a swirl number of Sw = 1.1, where a Strouhal number Sr_{PVC} of around 0.75 was reported [50, 158]. The observed constant Strouhal number with increasing flow rate reflects Reynolds' law of similarity, which states independence of the Strouhal number from the flow rate at a given Swirl number for high enough Reynolds numbers [158].

The large-diameter combustion chamber is particularly well-suited for the objectives of the present study, which looks into the flame stabilization and emissions of lean flames. The wider geometry helps reduce wall heat losses during combustion and promotes the formation of a broader and stronger CRZ, which enhances flame stability. This is especially advantageous for stabilizing lean CH_4 flames, which are more prone to blowout due to their lower reactivity compared to H_2 flames. Additionally, the large diameter enables the swirling jet and the development of the PVC with minimal interference from the walls. Since this work heavily relies on laser diagnostics, a larger combustion chamber diameter also helps to minimize laser sheet reflections in the flame region, which would otherwise complicate result interpretation. However, increasing the diameter also introduces certain drawbacks. The expanded area of interest makes it more difficult to obtain measurements at larger radial positions. Moreover, the reduced bulk flow velocities resulting from the increased cross-sectional area lead to significantly longer and more computationally expensive numerical simulations.

4.3.3. EFFECT OF AAI ON THE FLOW FIELD

This section examines the impact of AAI on the flow field. The measurements were conducted at c = 40 and at a total air flow rate of $\dot{Q}$ = 264 L/min. Furthermore, unlike the previous sections, the measurements were performed using a helium-based surrogate fuel mixture, as detailed in Table 4.1. Figure 4.6 presents the average streamwise velocity fields in the combustion chamber and the mixing tube for the surrogate case A_s (XH_2 = 0) at varying levels of AAI. The AAI fraction is varied according to Equation 4.2. At χ = 0 %, a low-velocity core and secondary flow structures are observed in the mixing tube, including a wake region with reduced axial velocity near y/D_{MT} = -2, just downstream of the AAI duct. This pattern arises as high-velocity flow from the swirler vanes moves inward to fill the low-momentum core, creating alternating regions of high and low axial velocity

due to swirl-induced centrifugal effects and radial flow interactions, as explained more in detail in Chapter 5. At χ = 10 %, the central low-velocity region is replaced by a high-velocity jet upstream of y/D_{MT} = -1.5, although a slight velocity deficit remains further downstream compared to the velocity in the swirling flow. For χ = 20 %, the centreline velocity increases significantly, surpassing the axial velocity of the surrounding swirling flow. However, it can also be observed that the high-velocity region is slightly tilted to the left, rather than perfectly aligned with the centreline of the mixing tube. Based on the instantaneous images (not shown), this tilt appears to be a steady feature rather than a fluctuating phenomenon. A likely cause is asymmetry in the swirler geometry resulting from the chosen printing method or an inaccuracy in the injector alignment.

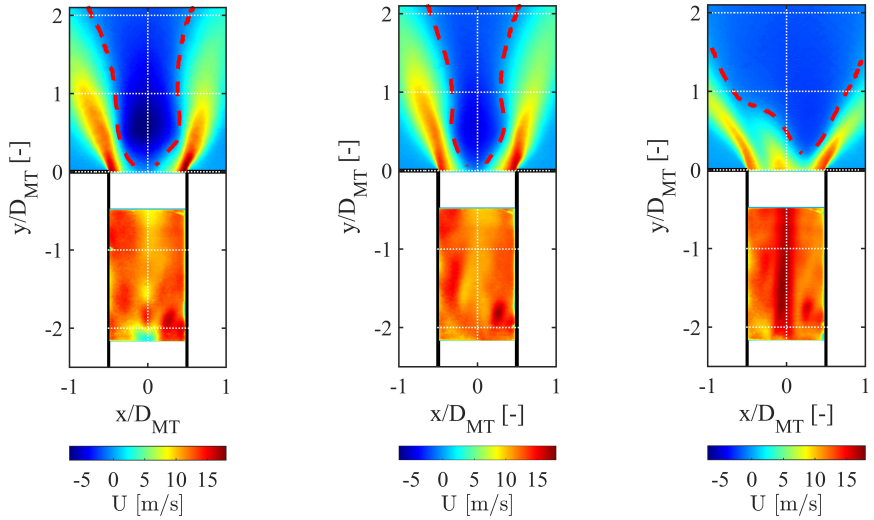

a) χ = 0 % **b)** χ = 10 % **c)** χ = 20 %

Figure 4.6: Average streamwise velocity fields in the combustion chamber and the mixing tube for surrogate case A_S (XH_2 = 0) and different levels of χ. Dashed line indicates the zero-axial velocity lines.

For the flow field in the combustion chamber, as the level of AAI increases from 0 % to 10 %, the negative axial velocities within the CRZ decrease. This reduction is attributed to a lower effective swirl number, as described by Equation 2.1, due to the addition of axial velocity and a reduction in tangential velocity. The decrease in tangential velocity leads to a narrower CRZ opening angle, which is consistent with a lower swirl number. Both the 0 % and 10 % AAI cases exhibit a bubble-type vortex breakdown, where the swirling jet initially contracts downstream of the bubble and then re-expands. For χ = 20 %, the shape of the CRZ changes from a bubble type to a cone type, characterized by the CRZ undergoing a significant radial expansion downstream of the stagnation point (point of zero axial and zero radial velocity), leading to higher opening angles of the CRZ compared to the other two cases. This configuration further reduces the negative axial velocities in the CRZ. These observations align with Terhaar et al. [53], who reported that cone-type breakdown occurs below a critical swirl number, which can be achieved by

increasing the level of AAI. At χ = 20 %, the AAI jet is clearly visible along the centreline, forming a bulge of positive axial velocity near the mixing tube outlet. For this high level of χ, the flow field exhibits a clear asymmetry in the CRZ. The bulge of high axial velocity is consistently tilted to the left-hand side, leading to an asymmetric velocity distribution in the central CRZ. In contrast, the cases with χ = 0 % and χ = 10 % do not display significant asymmetry, suggesting that the deviation observed at χ = 20 % originates from the AAI jet itself and is independent of the fuel injection. The pronounced change in flow field characteristics from χ = 10 % to 20 % highlight the nonlinear influence of AAI on the swirl number, where higher AAI levels lead to stronger reductions of the swirl number [53].

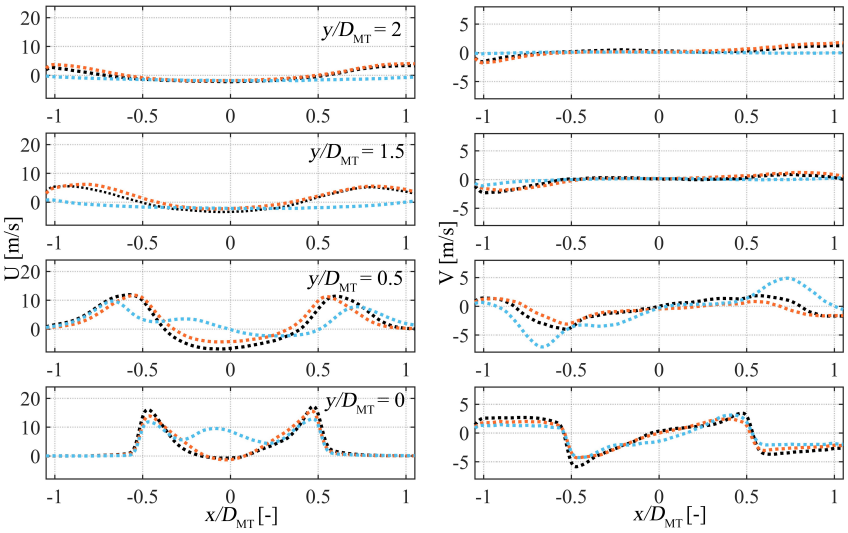

Figure 4.7: Axial U and transverse velocity V profiles at different streamwise locations y/D_{MT} forsurrogate case A_S (XH_2 = 0) at different levels of AAI: χ = 0 % (▪▪▪), χ = 10 % (▪▪▪), χ = 20 % (▪▪▪).

Additional insight is provided in Figure 4.7, which shows axial and transverse velocity profiles of the flow fields shown in Figure 4.6 at various streamwise positions for varying χ. Near the mixing tube outlet (y/D_{MT} = 0), the peak axial velocity at x/D_{MT} = 0.5 significantly decreases as AAI increases, from 15.9 m/s at χ = 0 % to 11.8 m/s at χ = 20 %. The negative axial velocities associated with the CRZ reduce between χ = 0 % and 10 %, from −6.5 m/s to −4.2 m/s and at χ = 20 %, they appear only at y/D_{MT} = 0.5, indicating a significant downstream shift of the stagnation point. While transverse velocity near the outlet only slightly decreases with increasing AAI, it becomes noticeably higher for the χ = 20 % case further downstream, consistent with the significantly wider opening angle of the cone-type vortex breakdown.

Figure 4.8 shows the real part of the SPOD mode 1 for the normalized transverse velocity component ($\hat{v}$) for different levels of AAI. At χ = 0 % and 10 %, shown at the frequency corresponding to the highest peak in the respective energy spectrum, the mode exhibits the typical helical structure of the PVC. As AAI increases from 0 % to 10 %, the

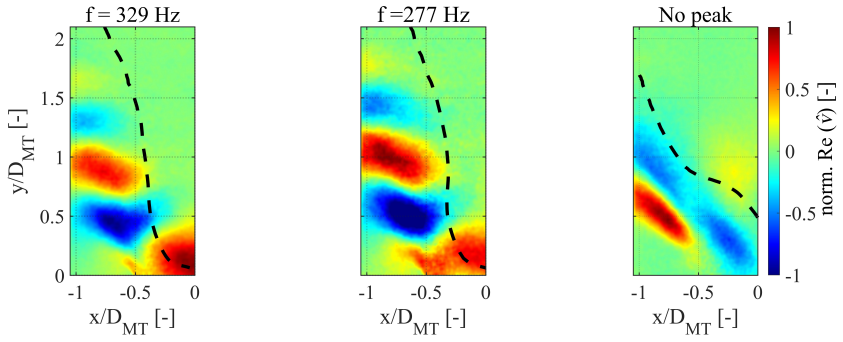

Figure 4.8: Normalized transverse velocity component $\hat{v}$ (real part) from the SPOD mode 1 at frequency f for surrogate case $A_s(XH_2 = 0)$ at different levels of χ, dashed lines indicates zero U line. Headers indicate the frequency of the peak of the corresponding mode in the energy spectrum of the SPOD.

PVC frequency decreases from 329 Hz to 277 Hz, consistent with a reduction in the swirl number [52]. For $\chi = 20\,\%$ (Figure 4.8c), no distinct peak is present in the energy spectrum of SPOD mode 1, indicative of the PVC frequency (see Figure 4.9). The mode shown corresponds to the SPOD mode that appears most frequently across the energy spectrum of the SPOD mode 1. No distinct PVC pattern is observed. Terhaar et al. [53] differentiate between two types of PVC. Type I is a strong, self-excited global mode, characterized by a distinct peak in the energy spectrum corresponding to a coherent PVC pattern, as observed for the cases $\chi = 0\,\%$ and $\chi = 10\,\%$ in Figure 4.9.

This mode typically occurs in flows exhibiting bubble-type vortex breakdown, as observed for $\chi = 0\,\%$ and $10\,\%$ (Figure 4.6a and Figure 4.6b). A type II PVC appears in flow fields with a cone-type vortex breakdown, as a large-scale coherent structure with a less defined, noisier signature. The mode shape shown in Figure 4.8c does not directly resemble typical type II PVC structures but instead reflects slow moving shear-layer dynamics in the ISL and OSL, as described by Terhaar et al. [53]. However, higher-order SPOD modes of the investigated flow field, which are not shown here, do exhibit type II PVC-like features, suggesting that these structures are present, though irregular, and contribute only minimally to the overall Turbulent Kinetic Energy (TKE).

4.3.4. EFFECT OF THE FUEL COMPOSITION ON THE FLOW FIELD

This section examines the impact of radial fuel injection on the mean flow field and PVC dynamics for different fuel compositions. Measurements are taken for $c = 40$, fuel inlet diameters for the lower investigated momentum flux ratio J_{low} (see Table 4.1) and a total air flow rate of $\dot{Q}_{swirl} = 264\,\mathrm{L/min}$. For this analysis, the CH_4/H_2 mixtures are represented by density-equivalent He/air mixtures, based on the set-points defined in Table 4.1. The volumetric flow rate increases substantially from $XH_2 = 0$ to $XH_2 = 1$, resulting in a higher bulk velocity in both the fuel inlet ports and in the mixing tube.

Figure 4.10 presents axial and transverse velocity profiles at various streamwise positions for different fuel compositions at $\chi = 0\,\%$. The corresponding contour plots of

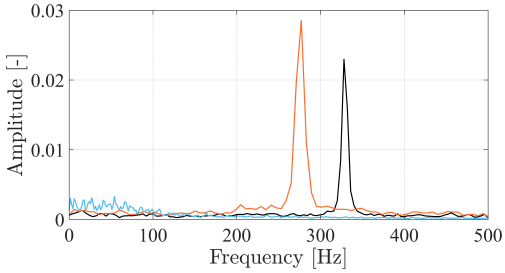

Figure 4.9: The amplitude of the most energetic SPOD mode at each frequency for surrogate case $XH_2 = 0$ at different levels of AAI: $\chi = 0\,\%$ (—), $\chi = 10\,\%$ (—), $\chi = 20\,\%$ (—).

the velocities are provided in Appendix D. From the velocity profiles it can be seen that the overall flow topology remains largely unaffected by changes in fuel composition: all cases exhibit swirling jets with comparable opening angles and a CRZ of similar width. However, the increased volumetric flow rate associated with higher hydrogen content leads to higher axial and radial velocity components. This effect is most pronounced in the swirling jets near the mixing tube outlet ($y/D_{MT} = 0$), at positions around $x/D_{MT} = -0.5$ and $x/D_{MT} = 0.5$, where both the axial and transverse velocity significantly increase for increasing XH_2. Specifically, the maximum axial velocity increases from 17.2 m/s for $XH_2 = 0$ to 19.2 m/s for $XH_2 = 1$, while the transverse velocity increases from 3.2 m/s to 5.1 m/s. Further downstream, these differences decrease as the velocity profiles flatten. Overall, the swirling jet opening angle remains relatively constant across all fuel compositions. Notably, the CRZ, which can be identified by the zero axial velocity line, appears slightly narrower for $XH_2 = 1$.

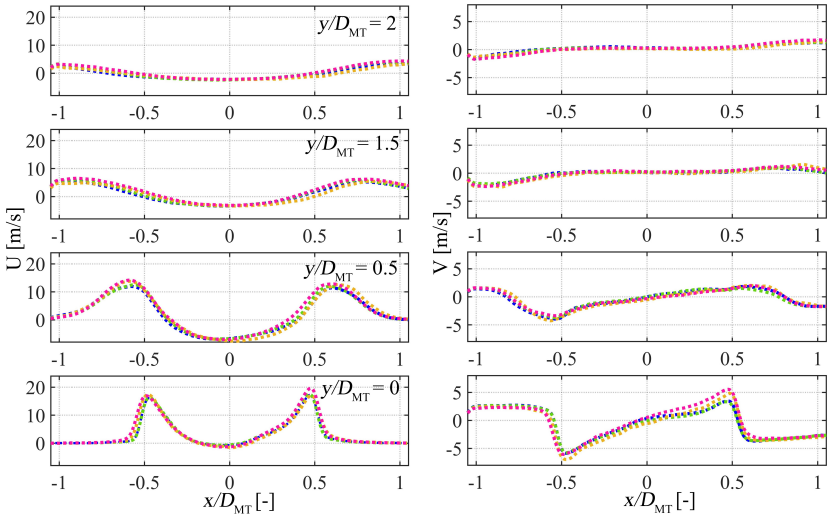

Figure 4.10: Axial U and transverse velocity V at different y/D_{MT} for different surrogate fuel compositions (case A_s - D_s) at $\chi = 0\,\%$ and J_{low}: XH_2= 0 (—), XH_2= 0.4 (—), XH_2 = 0.8 (—), XH_2 = 1 (—).

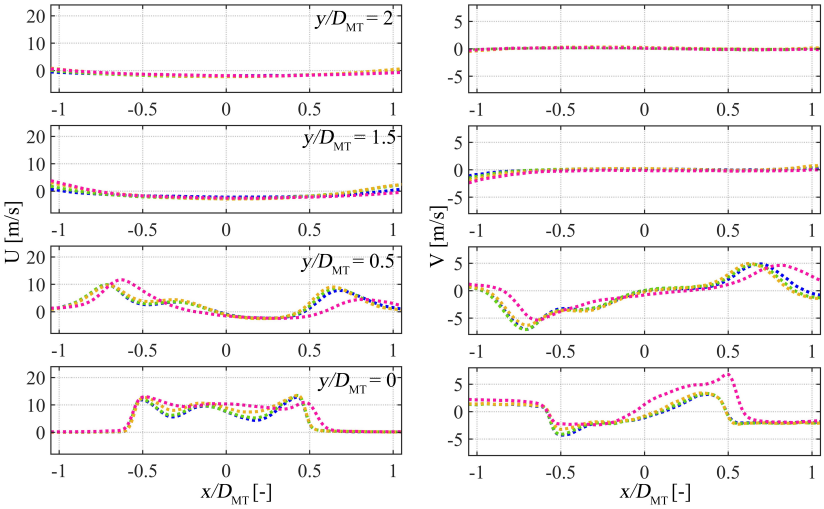

Figure 4.11: Axial U and transverse velocity V at different y/D_{MT} for different surrogate fuel compositions (case A_s - D_s) at $\chi = 20\,\%$ and J_{low}: XH_2= 0 (), XH_2= 0.4 (), XH_2 = 0.8 (), XH_2 = 1 ().

Figure 4.11 shows the axial and transverse velocity profiles at various streamwise positions for different fuel compositions at $\chi = 20\,\%$. For hydrogen fractions up to XH_2 = 0.8, both velocity components are only marginally affected by the change in fuel composition. In contrast, for $XH_2 = 1$, the axial velocity profile at the mixing tube outlet becomes noticeably flatter compared to the lower hydrogen content cases. Consequently, the bulge in axial velocity on the centreline due to AAI is less pronounced, therefore the overall streamwise velocity magnitude increases within the region $-0.25 < x/D_{MT} < 0.25$. Further downstream, at $y/D_{\mathrm{MT}} = 0.5$, the CRZ shows a wider and more asymmetric opening angle for the $XH_2 = 1$ case. Moreover, the bulge in the velocity profile due to AAI is no longer clearly distinguishable, while it remains visible for the other fuel compositions. These observations indicate that the flow field becomes significantly more sensitive to changes in fuel composition when AAI is present.

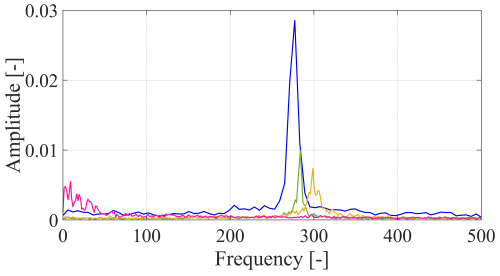

Figure 4.12: The amplitude of the most energetic SPOD mode at each frequency for cases A_s to cases D_s at AAI = 10 %: $XH_2 = 0$ (), $XH_2 = 0.4$ (), $XH_2 = 0.8$ (), $XH_2 = 1$ ().

Figure 4.13 shows the PVC frequencies at J_{low} for various surrogate fuel compositions at $\chi = 0\,\%$ and $\chi = 10\,\%$. At $\chi = 20\,\%$, no PVC was observed. Frequencies for the J_{high}

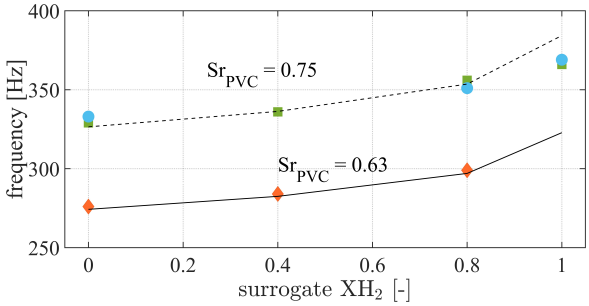

Figure 4.13: PVC frequencies obtained from SPOD for different surrogate fuel compositions for J_{low} at $\chi = 0\,\%$ (■) and $\chi = 10\,\%$ (♦), and for J_{high} at $\chi = 0\,\%$ (●), dashed lines indicate constant Strouhal number Sr_{PVC} lines.

cases at $\chi = 0\,\%$ are also included but will be discussed later. Lines of constant Strouhal number, $Sr_{PVC} = 0.75$ and $Sr_{PVC} = 0.63$, are included for reference. As observed, the PVC frequencies for J_{low} closely follow these constant Strouhal number lines, except of the case $XH_2 = 1$, where the PVC frequency is at $Sr = 0.71$, which is slightly lower than the $Sr = 0.75$ observed for the other hydrogen contents. Given that the Strouhal number typically correlates with the swirl number, and assuming this relationship remains valid despite changes in fuel composition, the observed deviation suggests a slight reduction in the effective swirl number for $XH_2 = 1$, while the other cases appear largely unaffected. The deviation in $XH_2 = 1$ is likely linked to the sharp increase in volumetric flow rate associated with the change from $XH_2 = 0.8$ to $XH_2 = 1$. This jump to $XH_2 = 1$ significantly increasing the velocity of the fuel jets and therefore also increasing the bulk velocity in the mixing tube, potentially affecting the swirl intensity despite the same injector geometry. The corresponding Strouhal number for cases with $XH_2 = 0$ to 0.8 is slightly lower than the value observed without fuel injection ($Sr_{PVC} = 0.78$, see Figure 4.5), further supporting the interpretation that radial fuel injection reduces the effective swirl number.

For $\chi = 10\,\%$, all cases align with the lower Sr number line ($Sr_{PVC} = 0.63$), consistent with a reduction in effective swirl number by injecting AAI. Notably, for $XH_2 = 1$ and $\chi = 10\,\%$, no distinct amplitude peak corresponding to the PVC frequency is observed in the energy spectrum of the strongest SPOD mode, as shown in Figure 4.12. In contrast, the remaining cases exhibit clear spectral peaks, although the peak amplitude decreases with increasing XH_2. The absence of a spectral peak for $XH_2 = 1$ suggests that the swirl number has fallen below the critical threshold necessary for the formation of a type I PVC.

4.3.5. EFFECT OF THE MOMENTUM FLUX RATIO J_{swirl} ON THE FLOW FIELD

This section examines how variations in the momentum flux ratio J_{swirl} affect the flow field. By adjusting the fuel inlet diameter, the fuel injection velocity and consequently J_{swirl} are varied. Measurements are taken for $c = 40$ and a total air flow rate of $\dot{Q}_{swirl} = 264$ L/min at different levels of AAI. Figure 4.14 presents the axial and transverse velocity profiles for $XH_2 = 0$ and $XH_2 = 1$ at the lowest ($J_{swirl} = 0.09$) and highest investigated momentum flux ratio ($J_{swirl} = 3.45$) without AAI, shown at various streamwise positions. For

$XH_2 = 0$, the momentum flux ratios are $J_{low} = 0.09$ and $J_{high} = 3.45$; for $XH_2 = 1$, they are 0.12 and 5.01 (see Table 4.1). Corresponding contour plots of the velocity fields are provided in Appendix D. While the velocity profiles indicate that the general flow structure remains consistent across cases, the magnitude of both axial swirling jet velocities and the negative velocities in the CRZ are strongly influenced by J_{swirl}. For $XH_2 = 0$, increasing J_{swirl} leads to a reduction in peak axial velocity of around 2 m/s. At the same time, the transverse velocities increase by almost 4 m/s, indicating a broader opening angle of the swirling jet. The negative axial velocities associated with the CRZ are also reduced at around 2 m/s at lower J_{swirl}, particularly near the injector outlet ($y/D_{MT} = 0$), suggesting a weaker recirculation. In contrast, for $XH_2 = 1$, the influence of J_{swirl} is less distinct. Around $x/D_{MT} = -0.5$, the axial jet velocity is higher for the J_{low} case by around 4 m/s, whereas this trend reverses downstream at $x/D_{MT} = 0.5$. This reversal is attributed to the flow asymmetry observed in the J_{low} condition. Additionally, the negative velocities in the CRZ show little sensitivity to the level of J_{swirl} for the surrogate case $XH_2 = 1$.

The influence of J_{swirl} becomes more pronounced with high levels of AAI, as shown in Figure 4.15, which presents the axial and transverse velocity profiles for $XH_2 = 0.8$ and $XH_2 = 1$ at different J_{swirl} levels and $\chi = 20\,\%$. The corresponding contour plots provided in Appendix D. In this analysis, the surrogate case with $XH_2 = 0.8$ (orange lines) is compared to $XH_2 = 1$ (pink lines), as elevated AAI levels are particularly relevant for mixtures with high hydrogen content. At $y/D_{MT} = 0$, no clear trend in velocity magnitude changes is observed. However, at $y/D_{MT} = 0.5$, the J_{high} cases show an increase in transverse velocities for both fuels. This indicates a wider opening angle of the CRZ than the cases with J_{low}. For $XH_2 = 0.8$, the streamwise velocity within the swirling jets close to $x/D_{MT} = \pm 0.5$ decreases significantly, by around 3.5 m/s compared to the J_{low} case. For XH_2 on the other hand the streamwise velocity component is not significantly affected. The central bulge of positive axial velocity appears especially sensitive to J_{swirl}, where the maximum velocities decrease up to 30 %. While the J_{low} cases exhibit negative axial velocities at $y/D_{MT} = 0.5$, indicating the presence of the CRZ, the J_{high} cases maintain positive axial velocities, suggesting the CRZ is pushed downstream.

The effect of J_{swirl} on PVC behaviour was examined by comparing the PVC frequencies at the highest and lowest investigated J_{swirl} levels, as shown in the previous discussed Figure 4.13. The frequency differences are no greater than 5 Hz, indicating that the PVC frequency is not significantly influenced by the level of J_{swirl}. This is notable given the significant impact of J_{swirl} on the velocity magnitudes in the mean flow field. However, it suggests that the overall swirl number remains largely unchanged, and that the variation in J_{swirl} primarily affects the internal velocity distribution within the mixing tube. This observation holds for the cases with $\chi = 0\,\%$ and $\chi = 10\,\%$. For $\chi = 20\,\%$, no PVC was detected, so a frequency comparison could not be made.

4.4. CONCLUSION

This chapter investigated how key geometric parameters (confinement ratio and outlet boundary conditions) and operating parameters (air axial injection level, fuel composition, and momentum flux ratio) influence the non-reacting flow field in a partially premixed, swirl-stabilized burner with jet in cross-flow fuel injection. The CH_4/H_2 fuel mixtures used in the reacting case were replaced by surrogate He/air mixtures matched for

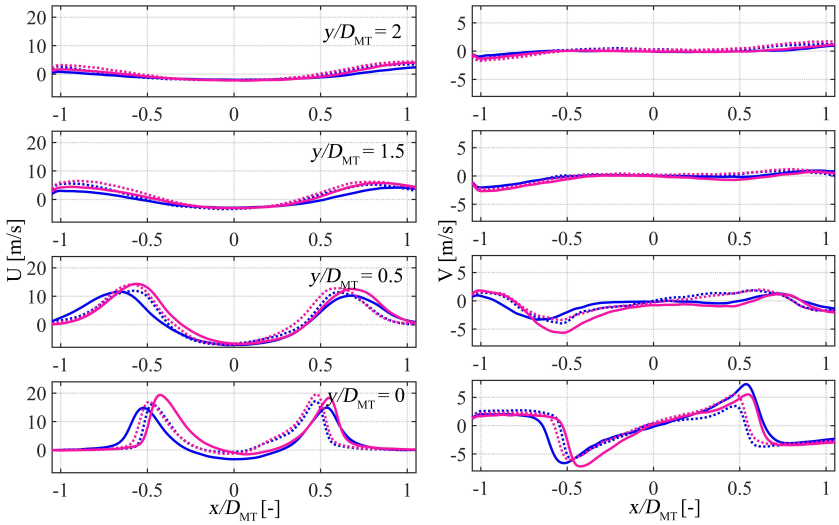

Figure 4.14: Axial U and transverse velocity V at different y/D_{MT} for different surrogate fuel compositions at $\chi = 0\,\%$: $XH_2 = 0$, J_{low} (····) $XH_2 = 0$, J_{high} (—) $XH_2 = 1$, J_{low} (····) $XH_2 = 1$, J_{high} (—).

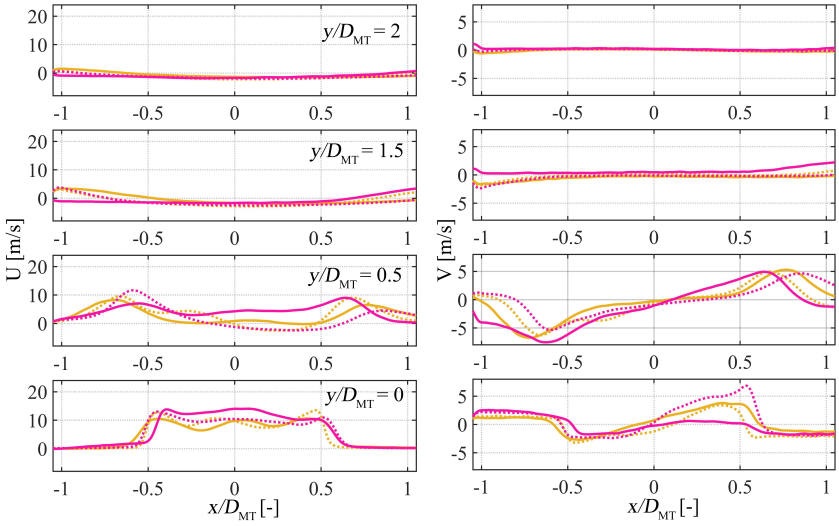

Figure 4.15: Axial U and transverse velocity V at different y/D_{MT} for different surrogate fuel compositions at $\chi = 20\,\%$: $XH_2 = 0.8$, J_{low} (····) $XH_2 = 0.8$, J_{high} (—) $XH_2 = 1$, J_{low} (····) $XH_2 = 1$, J_{high} (—).

density, as detailed in Chapter 3. High-frequency PIV measurements in the combustion chamber and mixing tube provided detailed flow field insights, while SPOD analysis of this data facilitates evaluation of the PVC dynamics. Both the time-averaged flow structures and the dynamic behaviour linked to the PVC were examined. These non-reacting studies establish a baseline for subsequent reacting studies, allowing differentiation between changes in emissions and stability caused by the flow field and those resulting from heat release effects. The main findings are summarized as follows:

- The presence of a contraction at the combustion chamber exit significantly alters the time-averaged flow field. Specifically, it promotes a region of positive axial velocity along the centreline, thereby reducing the strength and size of the CRZ. Due to this substantial influence on the flow field, all subsequent analyses, both non-reacting and reacting, are performed without an outlet contraction.

- A decrease in confinement ratio, achieved by increasing the combustion chamber diameter leads to a higher recirculated mass flow within the CRZ, which supports flame stabilization, as shown in the following chapters. The PVC frequency remains largely unaffected by changes in the confinement ratio, as it originates upstream inside the mixing tube. Additionally, a larger combustion chamber reduces interactions between the swirling jets and the chamber walls, thereby minimizing heat losses. For these reasons, subsequent reacting experiments were conducted using the largest investigated confinement ratio ($c = 40$), which proved to be well-suited for the study.

- AAI has a pronounced effect on both the shape and size of the CRZ and the overall velocity distribution within the combustion chamber. At $\chi = 20\,\%$, the flow undergoes a transition from a bubble-type to a cone-type vortex breakdown, significantly increasing the opening angle of the CRZ and simultaneously decreasing the strength of the CRZ. The PVC frequency decreases from $\chi = 0\,\%$ to $\chi = 10\,\%$, and at $\chi = 20\,\%$ the PVC becomes less coherent and contributes minimally to the total turbulent kinetic energy (TKE).

- When changing the fuel composition, the overall flow structure remains largely unchanged. However, the absolute velocity magnitudes increase with higher hydrogen content, consistent with the increase in bulk velocity in the mixing tube. The PVC frequency generally corresponds to a constant Strouhal number (Sr) scaling; however, the $XH_2 = 1$ case deviates from this trend. Since a constant swirl number typically implies a constant Strouhal number, this implies that the fuel composition influences the swirl number in the mixing tube.

- The momentum flux ratio (J_{swirl}) significantly impacts the mean flow field, especially for the cases with AAI. Lower J_{swirl} values are associated with reduced axial jet velocities and increased transverse velocities, indicating a broader jet spreading. Despite these changes in the mean flow, the PVC frequency remains largely unaffected for a given fuel composition, suggesting that the swirl number is preserved across different J_{swirl} levels.

In summary, this analysis offers a detailed understanding of how the non-reacting flow field responds to changes in geometry and operating conditions. These insights form an essential baseline for designing and interpreting the reacting cases, allowing for a clearer distinction between changes in flame stability and emission caused by heat release and those inherent to the non-reacting flow. Moreover, the results confirmed the selection of the configuration for the reacting studies, which will be conducted using the largest investigated diameter and an open outlet.

5

MIXING OF JET IN SWIRLING CROSS-FLOW

The mixing of fuel and air is a key factor in determining NO_x emissions and flame stability during combustion. For fuels such as hydrogen, the high flame speed makes full premixing impractical because of the increased risk of flashback. In partially premixed combustion, the fuel is injected further downstream, so it is important to achieve the best possible mixing within the limited available distance. In fuel-flexible combustion systems (e.g., CH_4/H_2), the mixing process is heavily influenced by the fuel mixture properties, requiring a thorough understanding of the mixing process to minimize NO_x emissions. This chapter investigates the mixing of fuel jets into a swirling cross-flow. Experimentally, the fuel is represented by a helium/air mixture matched in density to the methane-hydrogen mixtures, and the mixing process is visualized by seeding the fuel stream with DEHS droplets. The experimental results are compared with LES simulations. First helium is validated as a surrogate fuel for H_2 mixing. Then, the chapter explores how fuel composition and the momentum flux ratio J_{swirl} between the fuel jet and swirling cross-flow influence mixing performance, assessed using a spatial unmixedness parameter. The impact of varying levels of AAI at two different swirl numbers on mixing quality is also evaluated. Finally, conclusions are drawn regarding the key parameters that govern mixing in this jet in cross-flow configuration.

Parts of this chapter have been published in **S.Link et al.**, International Journal of Hydrogen Energy, 910, 2025, 10.1016/j.ijhydene.2025.05.070

5.1. INTRODUCTION

NO emissions in lean flames are mainly produced via the thermal pathway [106], making them sensitive to local flame temperatures. As shown in the burner geometries discussed in Section 2.8 in Chapter 2, the NO emissions are significantly influenced by design and operating conditions. The injector investigated in this thesis operates in a partially premixed configuration, with jet in cross-flow (JICF) fuel injection. This introduces the mixing level as a critical parameter affecting emission performance. Insufficient fuel-oxidizer mixing can lead to locally high-temperature zones, which in turn elevate NO formation. To improve emission performance, it is essential to identify the key parameters governing fuel-air mixing.

For a given geometry and a non-swirling cross-flow, the mixing is primarily determined by the jet to cross-flow density ratio $S = \rho_{\text{jet}}/\rho_{\text{crossflow}}$, the jet to cross-flow velocity ratio $R = U_{\text{jet}}/U_{\text{crossflow}}$, the jet to cross-flow momentum flux ratio $J = SR^2$ and the flow Reynolds numbers [28, 66, 117]. Many studies conclude that the momentum flux ratio J is the most significant parameter governing the degree of mixing [159, 160]. Effective mixing typically requires J to exceed 25, in some cases it even exceeds $J > 100$ [159]. At very high values ($J > 100$), the jet behaves more like a free jet in a static flow [161]. Conversely, for low values of J ($J < 1$), the jet adheres to the wall rather than penetrating into the cross-flow, a behaviour commonly used for film cooling in turbine blades [162].

More complex cross-flows are swirling flows, which are often used to stabilize flames in modern gas turbines. The mixing of transverse jets with a swirling cross-flow introduces new complexities, as the flow additionally has a tangential velocity component and a radial pressure gradient. Early research into this interaction focused on the mixing of helium jets discharged transversely into a swirling flow [68, 69].

It was concluded that swirl has a strong effect on the jet penetration depth, reducing it by a factor of 5 for a swirl number of $Sw = 2.25$ [68]. For momentum flux ratios $0.28 \leq J \leq 12.6$ the jets follow a spiral path and advance in the same direction as the swirling flow. Part of the reduced jet penetration depth is counteracted by the low density of helium ($\rho_{\text{He}}/\rho_{\text{air}}$), which pushes the helium towards the flow centre [69]. More recently, Tan et. al [67] explored the mixing mechanisms of hydrogen transverse jets in swirling cross-flows. Their findings suggest that increasing the swirl number enhances mixing by influencing the formation of a recirculation zone and altering the distribution of shear layers within the flow.

While swirling flows and jet in cross-flow configurations with axial cross-flow have been extensively studied individually, the combined influence of these parameters on mixing efficiency in swirling cross-flow systems remains less understood. This chapter presents an experimental investigation of the mixing characteristics of a fuel jet in swirling cross-flow configuration. By varying the momentum flux ratio J_{swirl} between the fuel and the swirling cross-flow as well as the fuel composition, this research aims to identify the key parameters for optimal mixing in fuel-flexible combustion systems that can operate with a range of fuels. Additionally, the effect of geometric parameters, which include the geometric swirl number and the level of AAI on the mixing quality is assessed.

Section 5.2 presents an overview of the experimental design, along with a description of the configuration specifications for this chapter. Section 5.3 describes the framework

Fuel reacting			Surrogate						
Tag	XH_2	d_{fuel} [mm]	Tag	$d_{\text{J-low}}$ [mm]	J_{low}	$d_{\text{J-mid}}$ [mm]	J_{mid}	$d_{\text{J-high}}$ [mm]	J_{high}
A	0	3.5	A_s	3.5	0.09	1.64	1.83	1.4	3.45
B	0.4	3.5	B_s	3.5	0.11	1.64	2.30	1.4	4.33
C	0.8	3.5	C_s	3.5	0.13	1.64	2.59	1.4	4.89
D	1	3.5	D_s	4.07	0.12	1.96	2.46	1.64	5.01

Table 5.1: Fuel mixture tags and hydrogen molar fractions for the reacting experiments and corresponding surrogate fuels and the diameters for the fuel inlets for the different momentum flux ratios J_{swirl} for $Sw = 1.1$.

of the study and Section 5.4 describes the procedure how the mixing quality is evaluated. Section 5.5 validates the usage of helium as a surrogate fuel for hydrogen to represent the macro-mixing in a jet in swirling cross-flow. It also examines the mixing behaviour under varying fuel densities and (J) at different swirl numbers and different levels of AAI. Finally, Section 5.6 summarizes the most important findings of this chapter.

5.2. CONFIGURATION SPECIFICATIONS

GEOMETRY & OPERATING CONDITIONS

Experiments were performed in the 3D printed duplicate of the TU Delft partially premixed swirl stabilized burner [24, 25], as described in Chapter 3. Downstream of the swirler exit, the He/air fuel surrogate mixtures, which aim at replicating the CH_4/H_2 fuel mixtures get injected perpendicular to the swirling flow through 4 injection ports. The investigated cases are summarized in Table 5.1, including the tag nomenclature used in this chapter. More details about the fuel compositions and its surrogates as well as the procedure can be found in Table 3.2 (Chapter 3). The size of the ports varies depending on the investigated momentum flux ratio J_{swirl} and the fuel composition. The diameters of the fuel injection ports as well as the resulting J_{swirl} are summarized in Table 5.1.

During the experiments, the mass flow rates for both air and helium were controlled by Bronkhorst digital mass flow meters with an accuracy of ± 0.5 % RD plus ± 0.1 % FS. To control the helium mass flow rate, a mass flow controller designed for air was used, applying a conversion factor provided by Bronkhorst, as no calibration curve was available for helium. This introduces some uncertainties in the mass flow rates of helium.

MEASUREMENT TECHNIQUES

The mixing process was analysed via Mie scattering images acquired in the mixing tube. The field of view in the optically accessible mixing tube can be seen in Figure 5.1, green box. For the analysis, the surrogate fuel stream (He/air) was seeded with DEHS droplets generated with a PIVTEC PIVpart45 seeder. Since the fuel stream is seeded, the Mie scattering of the particles is a good approximation of the level of mixing between the fuel and air stream. The DEHS particles in the surrogate He/air stream have a Stokes number of $St < 0.1$ for all J_{low} and J_{mid} cases based on the fuel inlet diameter and the fuel bulk velocity. For the J_{high} cases, due to the high velocities, the Stokes number is $St < 0.18$. The Stokes number indicates that the particle response time is sufficiently low to track large-

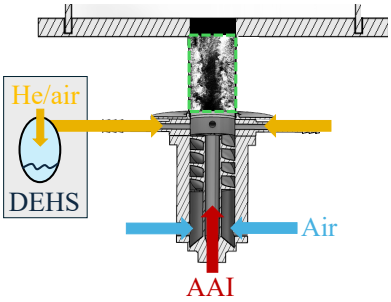

Figure 5.1: Field of view in the optically accessible mixing tube (green box) and seeding location.

scale flow structures, providing a reliable measure of the average macroscopic mixing [118]. However, since the local Stokes numbers might be locally higher in shear layers, small-scale turbulent mixing may not be accurately resolved. Additionally, the significantly higher density of DEHS droplets compared to helium, combined with centrifugal forces in swirling flows, may cause the DEHS droplets to move outward from the vortex core. Moreover, DEHS droplets do not replicate the molecular diffusion behaviour of helium, resulting in a significantly smaller Schmidt number for helium compared to the DEHS droplets, which implies that helium spreads more efficiently at small scales, while the droplets remain largely advected by the flow and do not capture fine-scale mixing.

The set-up parameters of the Mie scattering experiments are summarized in Table 5.2. The flow fields in the mixing tube and the combustion chamber for comparison with LES simulations were reused from Chapter 4, which were obtained using 2D2C PIV with the same laser and camera set-up and the same acquisition parameters. The velocity fields are averaged over 2000 images.

Laser	Nd:YAG Quantronix Darwin Duo 527-80-M
Camera	1 x Photron Fastcam Mini AX 100
Lens	105 mm
Sensor size	1024× 1024 px
Spatial resolution	19.1 px/mm
Acquisition frequency	1 kHz
Seeding particles	DEHS droplets ($d \approx 0.9\,\mu m$)
δt	10 µs

Table 5.2: Specifications Mie scattering imaging set-up.

5.3. COMBINATION OF EXPERIMENTAL AND NUMERICAL DESIGN

Figure 5.2 presents the flowchart of the combined numerical and experimental framework described in [70]. This framework validates the use of helium as a surrogate for studying hydrogen mixing and assesses the impact of various parameters on mixing performance. Although this chapter focuses primarily on the experimental component of

the framework, which represents the contribution of this dissertation to the combined numerical-experimental work, it also discusses the validation of helium as a surrogate fuel for hydrogen, carried out in collaboration with the numerical study. The results section concentrates on the suitability of helium as a hydrogen surrogate, the influence of surrogate fuel composition on mixing, and the effects of momentum flux ratio (J_{swirl}), level of AAI, and swirl number on the mixing process.

Within the framework, the experimental approach was selected to evaluate the influence of various parameters on mixing, due to the broad parameter space and the flexibility of the set-up, which enables straightforward adjustment of the swirl number and the fuel inlet diameters to achieve the desired momentum flux ratios. Some test cases were investigated numerically in-house using LES, performed by G. Ferrante [24], employing a multi-component mixture model to simulate turbulent mixing [70]. The LES was carried out in OpenFOAM v9 by solving the Favre-filtered Navier-Stokes equations. The numerical results provide quantitative details about the fuel mass fraction distribution in the mixing tube and combustion chamber. The 100 % He case (case D_s for J_{low} in Table 5.1) was simulated to validate the numerical model through the comparison of results with experimental measurements. Then, a comparison between case D (100 % H_2) and D_s (100 % He) allows assessing the suitability of helium as a surrogate tracer to represent the macroscopic mixing features of hydrogen.

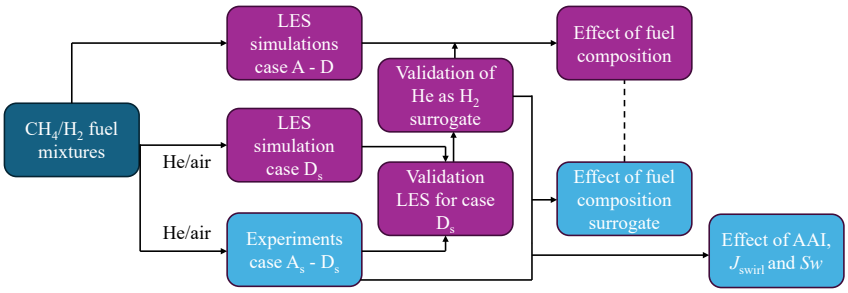

Figure 5.2: Flow chart of the experimental and numerical framework to study the mixing in the TU Delft swirl stabilized burner, purple boxes indicate the work performed by in-house LES [70] and blue boxes indicate the work performed by experiments presented in this dissertation.

5.4. EVALUATION OF MIXING QUALITY

Figure 5.3 shows the experimental methodology to determine the particle concentration from Mie scattering images acquired in the mixing tube. The raw images on the left show the single shot data acquired for case A_s, J_{low} (top) and case D_s, J_{high} (bottom). Since the fuel stream is seeded, the particle distribution within the mixing tube reflects the degree of mixing. Greater penetration of seeding particles into the centre of the mixing tube indicates a higher degree of mixing. It is evident that the raw image in the top row demonstrates worse mixing compared to the raw image in the bottom row, as the particles do not reach the centre of the mixing tube. After subtracting the minimum sliding background (filter length = 9 images), the noise floor was determined by the 10th percentile

of the pixel intensities. A Signal to Noise Ratio (SNR) of 2.5 was chosen, in order to guarantee a sufficiently high signal. The noise multiplied with the SNR gives the threshold. Pixel with an intensity below the threshold are set to 0, particles above this threshold are set to 1 (second column of the figure, step binarization). Afterwards, the particles per pixel were counted in a time-series of 200 statistically independent images. After calculating the average, the signal is normalized by its maximum value, and a smoothing filter with a filter size of 25x25 pixels is applied.

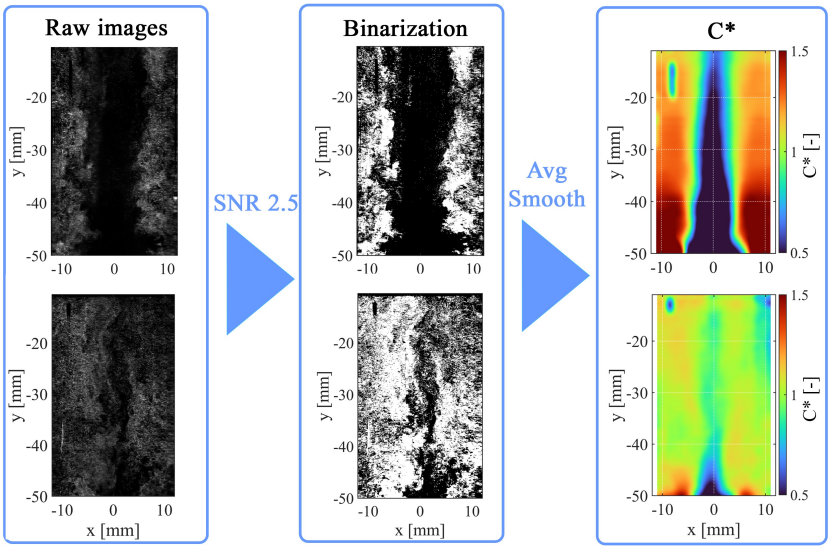

Figure 5.3: Experimental methodology to determine particle concentration from raw Mie scattering images. From left to right, the process involves identifying the noise floor on background-subtracted images (first column), binarizing the image based on a signal-to-noise ratio (SNR) threshold of 2.5 (second column), and after averaging over 200 images and applying a Gaussian smoothing calculating the normalized particle concentration C^*. Examples illustrating a lower degree of premixing (top, case A_s, J_{low}) and a higher degree of premixing (bottom, case D_s, J_{high}).

The mixing quality of the configuration is evaluated with the spatial unmixedness parameter U_s, which is the ratio of the spatial variance in fuel concentration in a given plane to the maximum spatial variance of the same quantity, and is defined as [163]

$$U_s(y) = \frac{\langle(\overline{C(x,y)} - \langle\overline{C(y)}\rangle)^2\rangle}{\langle\overline{C(y)}\rangle \cdot (1 - \langle\overline{C(y)}\rangle)} \tag{5.1}$$

$\overline{C}$ expresses the temporal average, and $\langle C\rangle$ expresses the spatial average of C. Consequently, $\langle(\overline{C(x,y)} - \langle\overline{C(y)}\rangle)^2\rangle$ refers to the variance of the fuel concentration C and $\langle\overline{C(y)}\rangle$ to the average of the concentration C at a given y-location. For the experiments, C refers to the particle concentration. Since no three-dimensional data are available, the degree of mixing is evaluated with planar data of the fuel distribution C.

U_s lays between 0 for a perfectly premixed system and 1 for totally unmixed system.

Besides this scalar parameter a spatial distribution of the normalized fuel concentration is used to show how the fuel distributes in the measurement plane

$$C^*(x,y) = \overline{C(x,y)} / \langle \overline{C(y)} \rangle \tag{5.2}$$

Since C^* represents the normalized fuel concentration, it is a useful parameter to compare cases with different fuel mass fractions. In a perfectly premixed configuration, C^* is equal to 1 throughout the region near the mixing tube outlet. An example plot of C^* for the experimental data can be seen in the right column of Figure 5.3, which shows the normalized particle distribution C^*, calculated after averaging the binarized images (second column) over 200 images and applying a Gaussian smoothing.

5.5. RESULTS

The results chapter begins by validating the methodology through a comparison of experimental results for the helium surrogate with in-house simulations for both helium and hydrogen. The second section explores how fuel composition influences the mixing process by analysing the fuel concentration in the mixing tube for various surrogate fuels. The third section examines the impact of the momentum flux ratio J_{swirl} on mixing. Finally, the chapter concludes by assessing how different levels of AAI and the swirl number affect the mixing process.

5.5.1. VALIDATION OF THE METHODOLOGY

To validate the use of helium as a surrogate for hydrogen, the experimental results of case D_s are compared with in-house LES simulations for both case D and case D_s, as listed in Table 3.2 (Chapter 3) [70]. Figure 5.4 shows contour plots of the axial and transverse velocity fields in the mixing tube and combustion chamber, obtained from both PIV and LES. The LES results show good agreement with the experimental data, accurately predicting vortex breakdown at the transition from the mixing tube to the combustion chamber. As the swirling flow enters the combustion chamber, it expands due to the sudden increase in cross-sectional area combined with centrifugal forces. This expansion, together with an adverse axial pressure gradient and a low-pressure region along the core, leads to the formation of a CRZ. At the current axial velocity and swirl number, the CRZ extends upstream into the final section of the mixing tube. The LES shows the stagnation point around $y \sim -5$ mm, while PIV measurements, although limited by optical access, suggest it lies between -10 mm and -5 mm, consistent with the LES predictions. A more detailed quantitative comparison of velocity profiles in the combustion chamber is provided in [70].

The LES also captures secondary flow structures within the mixing tube core (see Figure 5.4 LES), including a near-zero axial velocity wake and strong inward radial flow downstream of the central AAI duct at approximately $y \sim -60$ mm. These features result from high-velocity flows exiting the swirler and converging toward a low-momentum region at the centre. The combined action of radial inflow and centrifugal forces leads to alternating zones of high/low axial and inward/outward radial velocity, forming secondary recirculation structures. This behaviour is also qualitatively observed in the PIV data, particularly as a reduction in axial velocity near $y \sim -50$ mm.

Overall, the in-house LES successfully captures the main flow features including vortex breakdown and jet expansion angle despite minor underpredictions in peak velocity magnitudes.

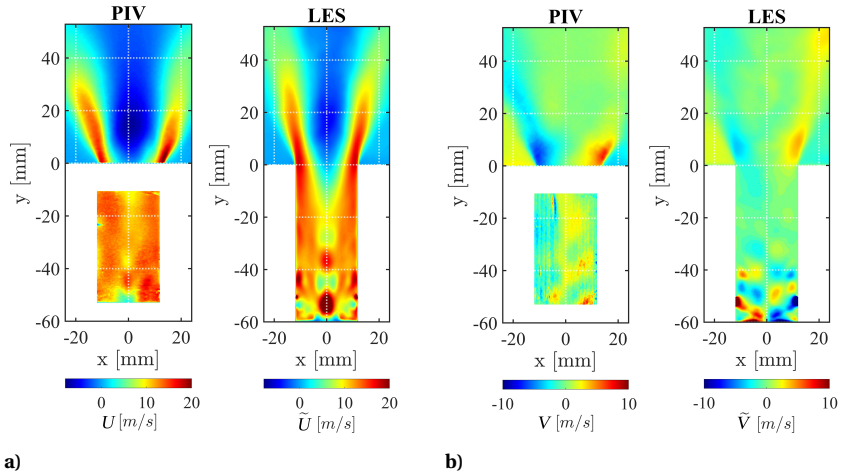

Figure 5.4: Average streamwise velocity flow field (a) and average transverse velocity flow field (b) in the mixing tube and combustion chamber obtained experimentally by PIV (left) and numerically (right) for case D_s at J_{low}, Table 3.2.

Figure 5.5a shows the normalized fuel concentration C^* for case D_s, derived from the Mie scattered images as described in Section 5.4. The highest particle count occurs near the fuel injection ports ($y \sim 50\,\text{mm}$), where radially injected helium penetrates the swirling flow toward the centreline.

Further downstream, both the magnitude and radial gradients of C^* decrease as mixing progresses. At the edge of the field of view ($y \sim -15\,\text{mm}$), C^* stays around 1.2 near the wall but remains around 0.5 at the core, indicating a stratified fuel distribution. This stratification results from the competing effects of inward convection caused by radial injection and jet in cross-flow dynamics and outward transport driven by centrifugal forces and radial flow components.

The time averaged helium mass fraction field Y_{He} predicted by the LES for case D_s is shown in Figure 5.5b. Consistent with the experiments, high helium concentrations are observed near the injection ports, decreasing downstream as the fuel mixes with swirling air. The LES also reveals isolated regions of high concentration near the fuel ports. This aligns with the sectional view of the LES results shown in Figure 5.6, which illustrates the development of the jet in swirling cross-flow through iso surfaces of helium mass fraction, highlighting the formation of helical structures. These structures are less evident in the experiments, likely due to limited spatial resolution or potential LES overprediction of coherent jet features, suggesting weaker turbulent mixing and a persistent memory effect extending to $y \sim -30\,\text{mm}$ [164]. Downstream, experimental results show more pronounced stratification than the LES, possibly due to centrifugal separation. While the LES treats helium as a passive scalar, the DEHS particles used in the experiments

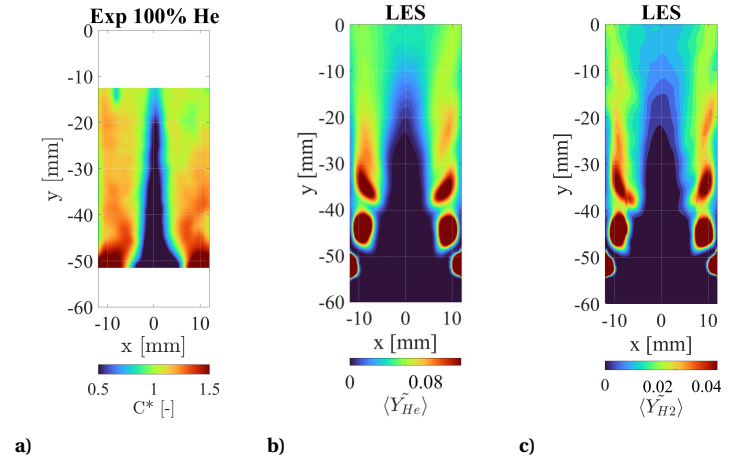

Figure 5.5: (a) Experimentally obtained C^* of case D_s at J_{low}, (b) He mass fraction of case D_s at J_{low} (c) H_2 mass fraction of the case D.

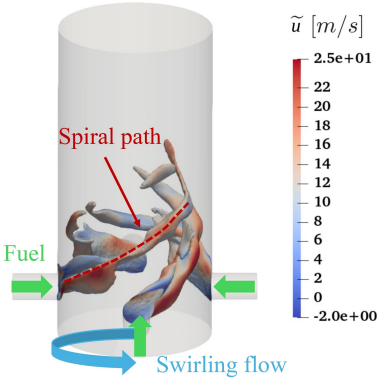

Figure 5.6: Visualization of He jets in swirling cross-flow structures in the mixing tube as predicted by LES of case D_s by instantaneous iso-surfaces of helium mass fraction $Y_{He} = 0.25$, coloured by axial velocity $\tilde{u}$. Courtesy of G. Ferrante [70].

have inertia, making them susceptible to centrifugal forces that can lead to increased accumulation near the walls. The lean core, largely free of fuel, is evident in both LES and experiments, though it appears wider in the LES up to the end of the field of view. At the mixing tube exit, LES predicts helium mass fractions of about $Y_{He} \sim 0.04$ near the wall and $Y_{He} \sim 0.0286$ at the core, roughly 10 percent higher and 21 percent lower than the nominal value 0.0362, respectively.

The LES prediction for case D (100 % H_2) is shown in Figure 5.5c and compared to the helium results from case D_s to evaluate the suitability of helium as a hydrogen surrogate. As shown in Table 5.1, the fuel inlet diameter for case D_s was increased to match the jet momentum of hydrogen in case D. Both cases exhibit similar mixing characteristics including fuel penetration and spreading, the extent of the lean core, and exit plane homogeneity. However, case D shows greater stratification near the exit, with higher wall concentrations $Y_{H_2} \sim 0.022$ and leaner core values $Y_{H_2} \sim 0.013$ compared to the nominal 0.0184. This indicates slightly less mixing than with helium. A more detailed quantitative comparison of mixing behaviour in cases D and D_s is provided in [70].

In conclusion, the LES results for case D_s show strong agreement with experimental data for both velocity and mixing fields validating the numerical model. Moreover, comparison between cases D and D_s confirms that helium is an effective surrogate for hydrogen under the present conditions. Based on this validation, the following section investigates how variations in fuel composition influence mixing characteristics using the experimental methodology described here.

5.5.2. EFFECT OF THE FUEL COMPOSITION ON GLOBAL MIXING

Figure 5.7 presents the spatial unmixedness U_s along the mixing tube for various fuel compositions, determined from post-processed Mie-scattered images of the J_{low} cases outlined in Table 5.1. The spatial unmixedness, calculated using Equation 5.1, is evaluated at multiple y-locations to assess mixture homogeneity and its streamwise evolution, which reflects the rate of mixing. For cases A_s, B_s, and C_s representing CH_4/H_2 fuel mixtures of increasing hydrogen content (0 %, 40 % and 80 % H_2 in volume, respectively), the unmixedness at the most upstream location ($y = -50$ mm) consistently measures approximately $U_s \sim 0.24$.

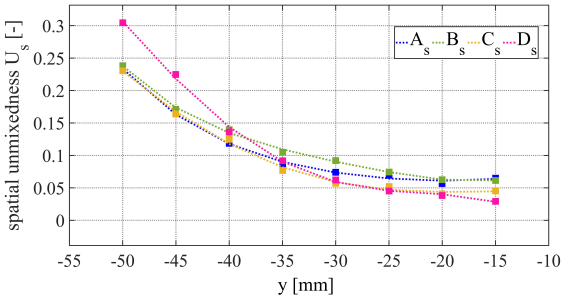

Figure 5.7: Spatial unmixedness U_s at different y-locations for different surrogate fuel compositions: $XH_2 = 0$ (▪▪▪), $XH_2 = 0.4$ (▪▪▪), $XH_2 = 0.8$ (▪▪▪) and $XH_2 = 1$ (▪▪▪) calculated with Equation 5.1.

At the mixing tube exit, a distinct correlation between higher helium content and better mixing quality is observed. Cases A_s and B_s, both representing similar methane mass fraction in the fuel stream, yield nearly identical unmixedness values of $U_s \sim 0.055$, while case C_s (representing 80 % H_2 by volume) achieves a slightly lower value of $U_s \sim 0.05$. In comparison, the full helium case (case D_s), which serves as a surrogate for pure hydrogen fuel stream, exhibits the highest initial unmixedness value of $U_s \sim 0.3$ and experiences a more rapid mixing, with respect to the other tested fuel compositions, reaching the lowest unmixedness value $U_s \sim 0.025$ at the tube exit. As it has been shown in the numerical part of the study on this set-up [70], the difference in mixing is a result of helium being less affected by outward radial convection at the mixing tube outlet than methane (or its surrogate gas) due to its lower density, resulting in reduced stratification. Additionally, helium exhibits higher inward diffusive transport due to its greater molecular diffusivity. However, since the DEHS droplets have a significantly different diffusivity than helium, it is expected that the change in mixing homogeneity in the surrogate cases is due to a change in convective transport.

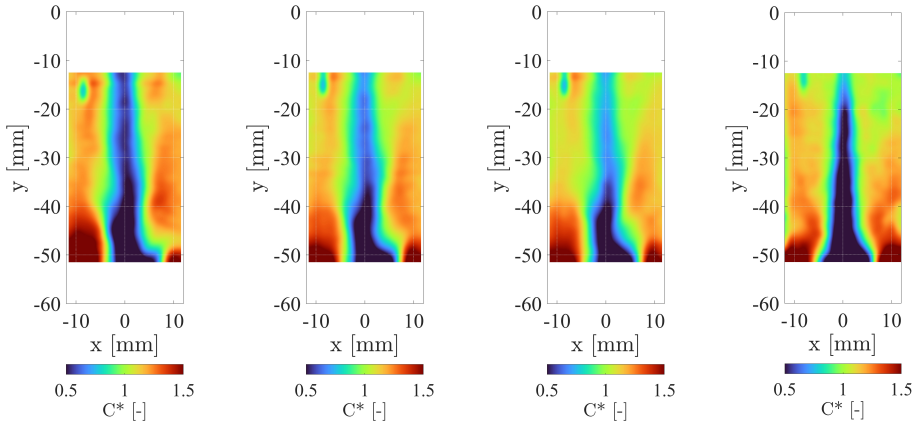

a) Case A_s, $\chi = 0\,\%$ **b)** Case B_s, $\chi = 0\,\%$ **c)** Case C_s, $\chi = 0\,\%$ **d)** Case D_s, $\chi = 0\,\%$

Figure 5.8: Normalized fuel concentration C^* for case A_s to D_s at J_{low} and $\chi = 0\,\%$.

Figure 5.8 illustrates the normalized particle distribution C^* for different fuel compositions at J_{low} and $\chi = 0\,\%$. As previously observed in the spatial unmixedness values near the mixing tube outlet, mixing homogeneity is higher for cases C_s and D_s than for cases A_s and B_s. The latter two cases exhibit more pronounced stratification, with a higher concentration of particles near the wall and a leaner core. The initial unmixedness is slightly higher for case D_s compared to the other cases, which can be attributed to the lower radial flux of convection near the fuel injection port in case D_s. This is likely because the lighter density jet is more deflected compared to the heavier density jet, as observed in other studies for axial cross-flows [64]. Downstream of y=−30 mm, case D_s shows a lower spatial unmixedness value (see Figure 5.7), despite a slightly more fuel-lean core compared to case B_s. This is probably due to the wider spreading angle of the fuel jet, which facilitates faster mixing with the cross-flow, as also demonstrated in axial cross-flow studies [64]. Furthermore, the lighter fuel jet is less influenced by centrifugal

forces, allowing it to mix more efficiently with the cross-flow.

5.5.3. EFFECT OF THE MOMENTUM FLUX RATIO J_{swirl} ON GLOBAL MIXING

Figure 5.9 shows, on the left-hand side, the spatial unmixedness (U_s) for various jet to cross-flow momentum ratios (J_{swirl}) at different streamwise locations for the 100 % H_2 surrogate (case D_s). The graph clearly shows that close to the fuel injection point the value for U_s decreases as J_{swirl} increases. This trend is intuitive because higher values of J_{swirl} correspond to deeper jet penetration into the swirling flow, allowing more helium to reach the centreline of the flow. This behaviour is also evident in the contour plot of normalized fuel distribution C^* (see Figure 5.9, right-hand side). At $y = -45$ mm, the dark blue region, representing areas with few or no particles, narrows significantly as J_{swirl} increases. For J_{high}, the value for U_s drops below 0.1 upstream of $y = -40$ mm, and remains nearly constant throughout the field of view. This is reflected in the contour plot, where the particle distribution for J_{high} appears nearly uniform by $y = -40$ mm. In contrast, for J_{mid}, U_s decreases more gradually, reaching a similar value to J_{high} around $y = -20$ mm. This behaviour suggests that, as expected, mixing near the injection point is primarily driven by convection, which is weaker at lower J_{swirl}. However, the mixing tube is long enough to ensure a low unmixedness value even if J_{swirl} is reduced to J_{mid}. For the lowest investigated J_{swirl}, the initial level of unmixedness is considerably higher compared to the higher J_{swirl} values. Nevertheless, as the flow progresses through the mixing tube, the unmixedness steadily decreases. While it approaches the levels observed for higher J_{swirl} values, it does not achieve the same degree of uniformity within the field of view. This suggests that for the lowest J_{swirl}, a longer mixing tube would be required to reach the same unmixedness level as for the higher J_{swirl} values.

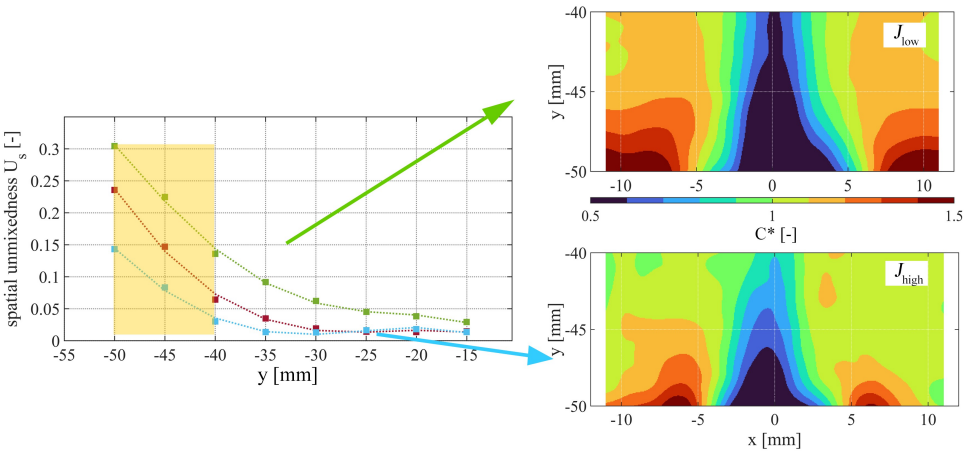

Figure 5.9: Left side: Spatial unmixedness obtained from normalized Mie scattering Images for $XH_2 = 1$ (case D_s) at different levels of J_{swirl}, $J_{low} = 0.12$ (····), $J_{mid} = 2.46$ (····) and $J_{high} = 5.01$ (····). Right side: Level of C^* for $J_{low} = 0.12$ and $J_{high} = 5.01$, field of view indicated in yellow in the graph.

Figure 5.10 shows the spatial distribution of unmixedness and fuel concentration (C^*) for the low hydrogen content case (B_s, $XH_2 = 0.4$). Notably, the case with the higher

momentum flux ratio (J_{high}) displays shows higher unmixedness in the upstream region (y = 50 mm) compared to J_{low}. This is likely due to a thinner mixing layer in the case with higher J_{swirl}, whereas the case with lower J_{swirl} exhibits a more gradual transition between regions of high and low C^*, as shown in the C^* contours on the right side of Figure 5.10. Similar trends have been reported in studies of axial cross-flows [64], where a higher J_{swirl} leads to deeper jet penetration into the cross-flow but reduced lateral spreading of the fuel jet, resulting in less effective mixing near the fuel inlets. However, this behaviour was not observed in the studies by Gevorkyan et al. [64], under conditions where the fuel jets had the same density as the cross-flow, and even high J_{swirl} resulted in broad jet spreading. This may explain why the observed increase in unmixedness near the fuel inlets with rising J_{swirl} is limited to case B_s in the present study. Due to its relatively low hydrogen content, the density difference with the swirling air jet is significantly smaller compared to that in case D_s.

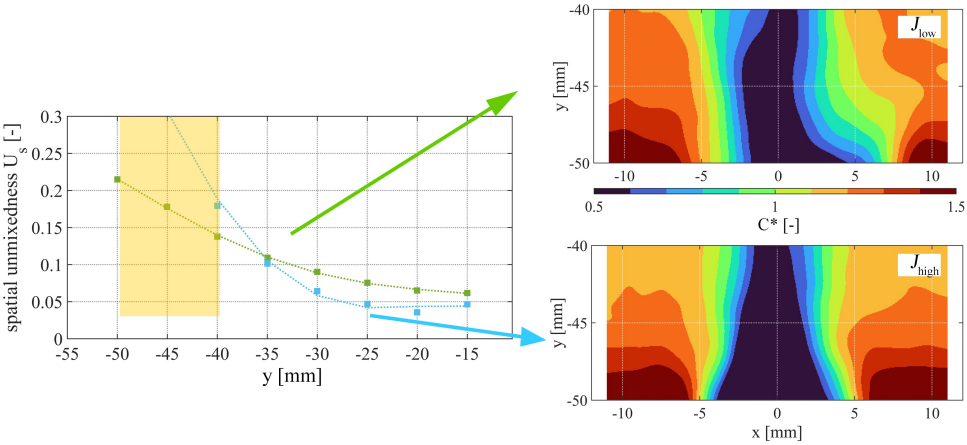

Figure 5.10: Left side: Spatial unmixedness obtained from normalized Mie scattering Images for XH_2 = 0.4 (case B_s) at different levels of J_{swirl}, J_{swirl} = 0.11 (····), and J_{swirl} = 4.3 (····). Right side: Level of C^* for J_{swirl} = 0.11 and J_{swirl} = 4.3, field of view indicated in yellow in the graph.

Focusing on the range $-11\,\text{mm} < x < 0\,\text{mm}$, the fuel concentration C^* for J_{high} shows a higher penetration depth compared to the case J_{low}, evident from the region of high particle density (dark red areas). Additionally, the length of these red regions in the streamwise direction is reduced for the case with higher J_{swirl}, suggesting that the mixing process occurs more rapidly after the fuel enters the mixing tube. Further downstream (beyond $y = -30\,\text{mm}$), the unmixedness value U_s shown on the left side of the figure is lower for the case with higher J_{swirl}, indicating that the mixture enters the combustion chamber at a higher degree of mixing. This observation aligns with the trends shown in Figure 5.9, where also a higher J_{swirl} resulted in a lower U_s close to the mixing tube outlet. Comparing Figure 5.9 and Figure 5.10 it is evident that unmixedness close to the mixing tube outlet is lower for all investigated J_{swirl} in case D_s compared to B_s. Close to the fuel injection ports ($y = -50\,\text{mm}$), it is clearly visible that the case B_s for the J_{high} case initially penetrates deeper into the cross-flow compared to case D_s for J_{low}, which

is to be expected due to the significantly higher J_{swirl}. However, faster fuel spreading is also observed for case D_s, as indicated by the more gradual gradient from the low fuel-concentration core region (dark blue) to the high-concentration region (dark red). This is, in part, likely due, to the significantly thicker mixing layer associated with the high hydrogen content, which enhances near-field mixing. Furthermore, as shown in [70], the lighter fuel stream experiences reduced centrifugal forces further downstream, and the helium-rich jet is less affected by outward radial convection. These effects combined suggest that fuel composition has a more pronounced influence on mixing performance than the momentum flux ratio J_{swirl}, particularly when comparing a case with low hydrogen content to a surrogate representing pure hydrogen fuel.

5.5.4. EFFECT OF AAI ON GLOBAL MIXING

Figure 5.11 shows the effect of AAI ($\chi = 0\,\%$ and $\chi = 20\,\%$) on the C^* distribution for case A_s ($XH_2 = 0$) and case D_s ($XH_2 = 1$) at J_{low}. For both cases A_s and D_s, the fuel jet near the injection ports ($y = -50\,mm$) is more strongly pushed towards the mixing tube wall in the absence of AAI. This behaviour is attributed to the higher mass flow rate of swirling air in the absence of AAI, which more strongly influences the trajectory of the fuel jets, pushing them toward the mixing tube wall.

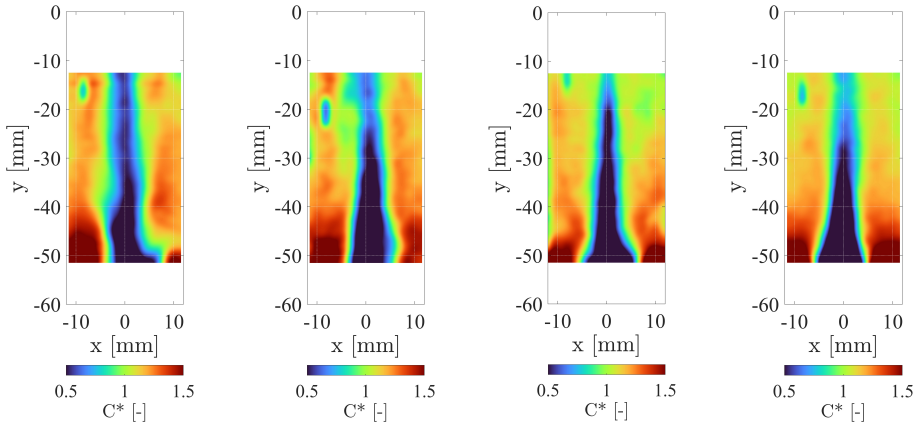

a) Case A_s, $\chi = 0\,\%$ **b)** Case A_s, $\chi = 20\,\%$ **c)** Case D_s, $\chi = 0\,\%$ **d)** Case D_s, $\chi = 20\,\%$

Figure 5.11: Normalized fuel concentration C^* of case A_s and case D_s at J_{low} for $\chi = 0\,\%$ and $\chi = 20\,\%$.

As previously shown in Figure 5.6, the fuel jets in the cases without AAI are deflected shortly after injection and follow the spiral trajectory of the swirling flow. In contrast, with AAI, the fuel jet penetrates the cross-flow with significantly less deflection. At approximately $y \sim -30\,mm$, cases without AAI still exhibit significantly higher unmixedness than those with AAI, as seen in the broader fuel-lean core along the centreline of the mixing tube. By the end of the field of view, the values and distribution of C^* still differ slightly between the cases with and without AAI, with higher levels of unmixedness for cases with AAI, but the differences are much lower. This observation aligns with the findings of Reichel [85], who reported that for sufficiently long mixing tubes and high

swirl numbers, spatial unmixedness does not increase significantly with higher AAI levels in coaxial fuel injection configurations. Nevertheless, in the present set-up, a relatively fuel-lean core persists in both cases, which could negatively impact emissions and flame stabilization, as discussed in Chapter 6. Overall, case D_s both with and without AAI shows a more uniform distribution of C^* than case A_s, which is consistent with the findings in Section 5.5 that higher hydrogen content leads to better mixing.

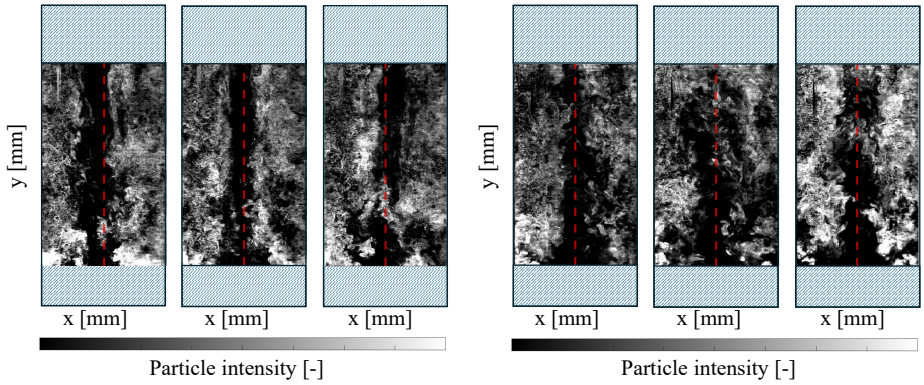

a) $\chi = 0\,\%$ **b)** $\chi = 20\,\%$

Figure 5.12: Instantaneous particle images for case D_s at $\chi = 0\,\%$ (a) and $\chi = 20\,\%$ (b) at J_{low} and J_{high}, respectively. The images show the particle distribution in the mixing tube, with the dashed line indicating the centreline of the mixing tube.

Moreover, as elaborated in Chapter 4, the cases without AAI show the presence of a PVC, whereas the cases with $\chi = 20\,\%$ do not. In the presence of a PVC, the centrifugal forces likely prevent particles from entering the vortex core, while the lighter helium, being less affected by these forces, may still be able to enter the core. Figure 5.12 shows instantaneous snapshots of the particle distribution in the mixing tube for $\chi = 0\,\%$ and $\chi = 20\,\%$. At $\chi = 0\,\%$, a particle-free core is observed oscillating around the centreline, which is expected to correspond to the PVC. In contrast, at $\chi = 20\,\%$, the core remains steady, resulting in a higher concentration of particles along the centreline, especially close to the mixing tube outlet, which indicates a more uniform mixing behaviour. This mechanism may lead to a slight underestimation of unmixedness in the case without AAI, suggesting that the actual unmixedness is higher in the case with AAI.

Figure 5.13 illustrates the effect of AAI ($\chi = 0\,\%$ and $20\,\%$) on the normalized fuel distribution C^* for cases A_s and D_s at J_{high}. For case A_s, the values of C^* in the mixing tube are comparable to those at lower J_{low} (Figure 5.11), indicating that the mixing level is similar. A comparison of Figure 5.11a and Figure 5.13a shows a steeper gradient between high fuel concentrations near the wall and lower concentrations in the core at J_{high}. This is likely due to reduced fuel jet spreading, leading to slower mixing near the injection points, despite the increased penetration depth.

For case D_s, significantly lower C^* values are observed throughout the field of view compared to the J_{low} case at both levels of AAI, attributed to deeper penetration into the cross-flow and more rapid spreading of the low-density fuel jet. Case D_s also exhibits

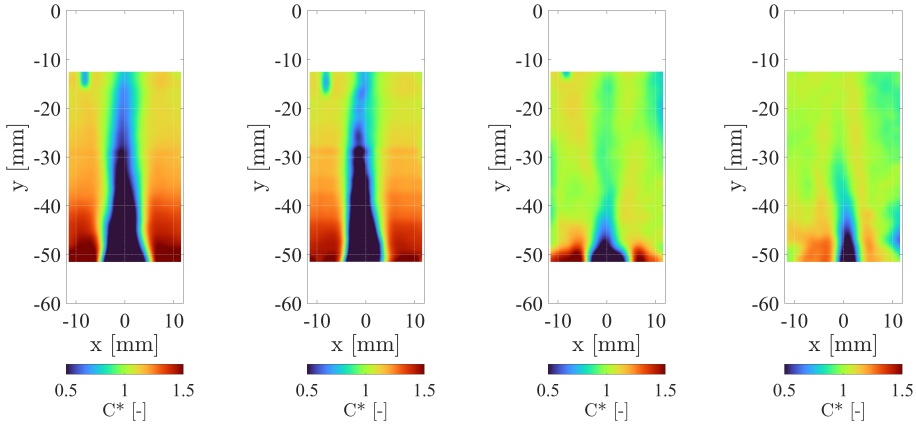

a) Case C_s, $\chi = 0\,\%$ **b)** Case C_s, $\chi = 20\,\%$ **c)** Case D_s, $\chi = 0\,\%$ **d)** Case D_s, $\chi = 20\,\%$

Figure 5.13: Normalized fuel concentration C^* of case A_s and case D_s at J_{high} for $\chi = 0\,\%$ and $\chi = 20\,\%$.

5

better mixing homogeneity than case A_s, consistent with trends noted in Figure 5.8. Additionally, case D_s has a higher J_{swirl} compared to case A_s at the maximum investigated momentum flux ratio (refer back to Table 5.1), which further enhances mixing. In the presence of AAI (Figure 5.13b), no fuel reaches the centreline for case A_s until $y = -30\,mm$. In contrast, for case D_s, fuel appears more upstream along the centreline, likely due to the lower-density fuel being less influenced by centrifugal forces and the wider jet angle. Interestingly, while case A_s with AAI shows more fuel near the periphery than the centre, this trend is reversed for case D_s. Downstream of $y = -30\,mm$, higher C^* values are observed in the core than in the outer regions, suggesting that the fuel jet penetrates deeply into the swirling flow. This implies that mixing predominantly occurs in the shear layer between the swirling flow and the AAI jet, with insufficient time for full mixing, leaving most of the fuel near the AAI jet.

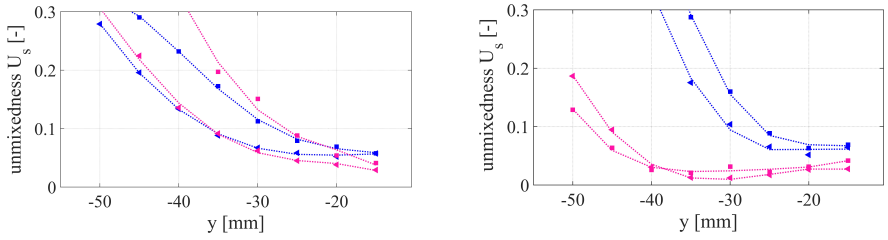

a) J_{low} **b)** J_{high}

Figure 5.14: Spatial unmixedness U_s at different y-locations for case A_s (▪▪▪) and case D_s (▪▪▪) for two different J, $\chi = 0\,\%$ (◂) and $\chi = 20\,\%$ (■).

The spatial unmixedness values U_s for J_{low} and J_{high} at various y-locations are shown in Figure 5.14. For case A_s, the unmixedness values close to the fuel inlet at J_{high} is increased, despite deeper fuel penetration into the cross-flow. This has been previously

observed in Figure 5.10, and has been attributed to the lower jet spreading of the fuel jet, and therefore a lower initial mixing. Further downstream, the unmixedness values for J_{high} reach similar values of the one for J_{low}. For all A_s and D_s cases, the initial unmixedness is higher with AAI than without. In cases A_s and D_s at J_{low}, this effect is observed despite the fuel jets being less deflected towards the mixing tube wall. This appears to result from the high-momentum AAI jet restricting the mixing of fuel with the air stream. Evidence for this includes a sharper gradient in fuel concentration between high and low concentration regions, indicating a thinner initial mixing layer, and a broader low-concentration region along the centreline (see Figure 5.11).

Nevertheless, as observed previously, the unmixedness values near the outlet are similar for $\chi = 0\,\%$ and $20\,\%$ across all cases. Interestingly, in case D_s at J_{low}, AAI initially reduces unmixedness by pushing the fuel closer to the centreline. Likely due to the high momentum of the fuel jets, the fuel penetrates far into the cross-flow and mixes within the shear layer between the swirling flow and the AAI jet. Although U_s at the outlet is similar with and without AAI, the fuel distribution shifts noticeably, from a slightly fuel-lean core to a slightly fuel-rich one, as the AAI level increases.

5.5.5. EFFECT OF SWIRL NUMBER ON GLOBAL MIXING

Figure 5.15 presents contour plots of the normalized fuel distribution C^* for case D_s at J_{low}, comparing two swirl numbers ($Sw = 0.7$ and $Sw = 1.1$) and two levels of AAI ($\chi = 0\,\%$ and $\chi = 20\,\%$). For $Sw = 0.7$ and $\chi = 0\,\%$ (Figure 5.15c), the fuel jet reaches far into the cross-flow and initially mixes rapidly, with C^* values around 1.2 near $y \sim -50$ mm. Under the same conditions, but with $Sw = 1.1$ (Figure 5.15a), C^* exceeds 1.5, indicating a more concentrated fuel distribution.

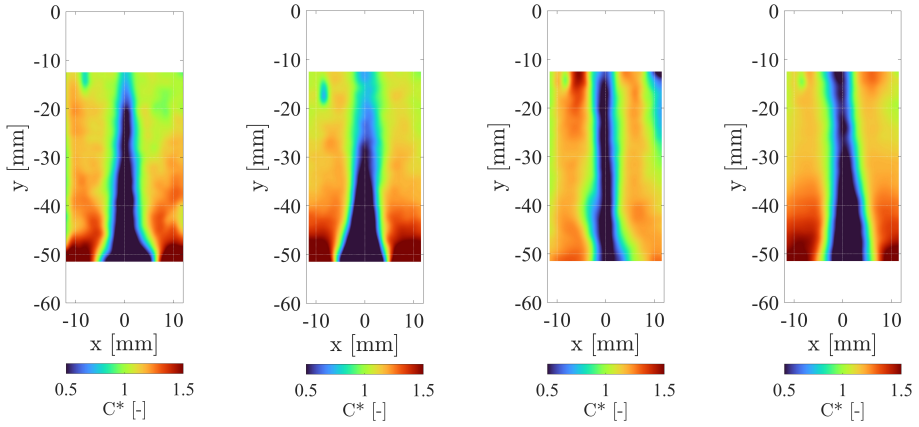

a) Case D_s, $Sw = 1.1$, $\chi = 0\,\%$ **b)** Case D_s, $Sw = 1.1$, $\chi = 20\,\%$ **c)** Case D_s, $Sw = 0.7$, $\chi = 0\,\%$ **d)** Case D_s, $Sw = 0.7$, $\chi = 20\,\%$

Figure 5.15: Normalized fuel concentration C^* of case D_s at J_{low} for two different swirl numbers for $\chi = 0\,\%$ and $\chi = 20\,\%$.

Further downstream, however, the fuel-lean core remains relatively wide. In contrast, for $Sw = 1.1$, the core narrows considerably in streamwise direction, indicating more ho-

mogeneous mixing with the cross-flow. A similar trend is observed at $\chi = 20\,\%$: near the fuel inlets, the C^* distribution is comparable between the two swirl numbers, but further downstream, the case with $Sw = 1.1$ exhibits significantly better mixing. Conversely, the fuel-lean core remains broader at the end of the field of view for $Sw = 0.7$.

These trends are also reflected in the profiles of spatial unmixedness U_s at various y-locations shown in Figure 5.16. Near the mixing tube outlet, unmixedness values are consistently higher for lower swirl numbers, regardless of the AAI level. As seen in the contour plots, unmixedness remains lower up to $y = -40\,\text{mm}$ for $Sw = 0.7$. This may be due to the higher J_{swirl} ($J_{\text{swirl}} = 0.23$ for $Sw = 0.7$ and $J_{\text{swirl}} = 0.12$ for $Sw = 1.1$), as defined in Equation 2.22, resulting from the lower swirl number, which allows the jet to reach more deeply into the cross-flow. However, further downstream, the case with $Sw = 1.1$ exhibits more homogeneous mixing. This agrees with previous findings that increased swirl enhances TKE, thereby promoting turbulent mixing [165].

In the presence of AAI, the unmixedness U_s is initially similar for both swirl numbers but diverges further downstream, likely due to increased levels of TKE at higher swirl. Notably, even the case with $Sw = 1.1$ and $\chi = 20\,\%$ shows lower unmixedness than the case with $Sw = 0.7$ and $\chi = 0\,\%$. This highlights the critical role of turbulence in the mixing process and suggests that the final mixing quality is not solely determined by the initial jet penetration depth.

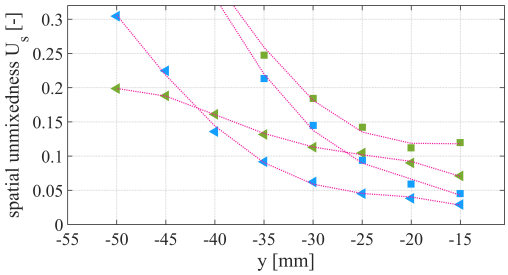

Figure 5.16: Spatial unmixedness U_s at different y-locations for case D_s, $Sw = 1.1$, $\chi = 0\,\%$ (◀) and $\chi = 20\,\%$ (■), $Sw = 0.7$, $\chi = 0\,\%$ (◀) and $\chi = 20\,\%$ (■).

5.6. CONCLUSIONS

This chapter investigated the mixing of a jet in swirling cross-flow configuration, representative of a lab-scale injector of a partially-premixed, swirl-stabilized burner. Mie scattering images of the seeded fuel stream enabled particle count techniques to evaluate the degree of mixing. The study focused on the influence of fuel composition, swirl number, level of AAI and jet to cross-flow momentum flux ratio J_{swirl} on the mixing process. Mixing performance is evaluated using a spatial unmixedness parameter U_s, and by examining the normalized fuel concentration C^*. To represent CH_4/H_2 fuel mixtures, He/air mixtures with varying helium concentrations were employed, where the use of helium as a surrogate for hydrogen was validated against LES simulations. The key conclusions are as follows:

- Helium is validated as a reliable surrogate for assessing macroscopic mixing trends

in swirl-stabilized configurations with hydrogen, when keeping the momentum flux ratio J_{swirl} constant. Due to the higher helium density, equal jet momentum (at constant mass flow rate) has to be achieved by adjusting the fuel inlet diameter.

- For similar values of J_{swirl}, reducing the density of the fuel stream enhances mixing. This improvement is attributed to the reduced influence of centrifugal forces on the lighter fuel, allowing deeper penetration into the cross-flow. Moreover, the lower-density fuel is expected to exhibit a wider jet spreading angle, further promoting mixing with the cross-flow.

- The fuel density has a more significant influence on the degree of mixing than the level of J_{swirl}. This is due to the fact that lighter fuels are less subject to outward convection, therefore less prone to stratification.

- A higher the J_{swirl} results in lower unmixedness at the outlet of the mixing tube. However, there is a critical J_{swirl} value beyond which, at any given mixing tube length, the final unmixedness level is insensitive to fuel injection momentum J_{swirl}.

- AAI significantly affects the degree of mixing near the fuel injection ports, as the cross-flow cannot easily mix with the high-momentum AAI jet. Further downstream this reduces, but the mixture generally enters the mixing tube with a higher level of unmixedness compared to the case with no AAI.

- Increasing the swirl number reduces the degree of mixing close to the fuel inlets. However, enhanced turbulence in the cross-flow results in higher mixing levels at the mixing tube outlet.

The non-reacting results show that increasing the hydrogen content improves mixing in fuel-flexible (CH_4/H_2) combustion systems with a jet in cross-flow configuration. This enhanced mixing with higher hydrogen content can contribute to lower NO_x emissions when the adiabatic flame temperature is held constant by reducing the operating equivalence ratio. Despite the reduction in φ, the significantly higher flame speed of hydrogen compared to methane can cause the flame to anchor significantly further upstream, in regions with less fuel-air premixing, potentially leading to increased local NO_x formation. Additionally, as shown in the results of this chapter, the level of AAI and the swirl number significantly influence the fuel-air mixing. Direct estimation of NO_x based on operating equivalence ratio and mixing information from non-reacting data alone are therefore challenging. An increase in J_{swirl} was found to improve mixing across all investigated hydrogen fractions, which would also favour reduced NO_x emissions. Nonetheless, a critical value of J_{swirl} was identified, beyond which further increases no longer significantly enhance mixing. This finding is particularly relevant for reacting conditions, as it implies the existence of an optimal mixing tube length for a given J_{swirl}. Beyond this point, additional length offers no mixing advantage and may increase the risk of flashback in H_2-rich flames, mainly due to the growth of the boundary layer.

While non-reacting studies may not fully capture the mixing behaviour under reacting conditions, they are still expected to provide indicative trends that reflect the mixing characteristics in the reacting case and can contribute to a better understanding of flame

anchoring behaviour and emission characteristics. Chapter 8 will focus on validating these non-reacting findings under reacting conditions. Specifically, the next steps will examine whether the expected changes in mixing degree are reflected in the NO_x emissions, and whether variations in fuel distribution within the mixing tube influence the flashback limits of the burner.

6

EXPERIMENTAL INVESTIGATION OF FUEL FLEXIBILITY

The distinct combustion characteristics of H_2, such as high flame speeds and elevated adiabatic flame temperatures, present challenges when designing fuel-flexible systems that can operate stably with low emissions across a wide range of CH_4/H_2 mixtures. To enhance flashback resistance, it is desirable to inject the fuel as close as possible upstream of the combustion chamber. Simultaneously, minimizing NO_x emissions requires achieving rapid and thorough mixing. This chapter investigates the fuel flexibility of an atmospheric laboratory-scale, partially premixed swirl-stabilized combustor. By injecting part of the combustion air as an axial air jet (AAI) along the centreline of the swirling flow, the flashback risk for fuels with high hydrogen content is reduced. The flashback and blow-off limits of the combustor are determined for the full range of fuel mixtures at various equivalence ratios (φ). Combined flow field and flame shape analyses provide insight into how the flame is stabilized within the flow and how this stabilization changes with varying hydrogen content and AAI levels. To investigate the influence of swirl on the flow field and flame stabilization, the analysis is conducted at two swirl numbers, Sw = 0.7 and Sw = 1.1. Additionally, to study the effect of H_2 enrichment, AAI and the swirl number on the emissions, an exhaust gas analysis is performed.

Parts of this chapter have been published in **S.Link et al.**, International Journal of Hydrogen Energy, 910, 2025, https://doi.org/10.1016/j.ijhydene.2024.12.286

6.1. INTRODUCTION

When H_2 is burnt in systems designed for conventional carbon-based fuels, its substantially different combustion properties can have an adverse effect on the combustion process and on the reliability of the combustor. Higher adiabatic flame temperatures at the same equivalence ratio increase nitric oxide (NO_x) emission. Moreover, the high reactivity and flame speed of H_2 can alter the position of the flame in the combustion chamber. This can affect the mixing of oxidizer and fuel, potentially leading to flashback under unfavourable conditions [10, 11]. Partially premixed combustion, achieved by injecting the fuel as late as possible upstream of the combustion chamber, while still allowing some mixing length, is a widely used approach to keep NO_x emissions low while minimizing the risk of damage due to flashback. Adapting conventional swirl-stabilized injector geometries for fuel flexibility could allow operation for the full range of fuel mixtures, from entirely conventional carbon-based gaseous fuels to entirely H_2. However, the low-velocity region in the core of the swirling flows increases the propensity to flashback, particularly for highly reactive fuels like H_2. Axial air injection (AAI), where a part of the combustion air is injected non-swirling on the centreline of the flow has shown promise in reducing flashback risk [85]. By mitigating the centreline velocity deficit and shifting the stagnation point of the recirculation zone further downstream, AAI allows stabilization of high hydrogen-content flames [85]. Several studies on hydrogen enrichment showed that increasing the hydrogen content in the fuel lowers the lean blow-off and flashback limits, and makes the flames more compact, due to higher reaction rates and flame speeds [94, 166, 167]. Flame shape studies showed [98, 101] that hydrogen addition triggers a flame shape transition from M-flame to Π-flame, where the flame front on the centreline lifts off the injector. This changes the flashback mode from flashback due to combustion induced vortex breakdown to boundary layer flashback. In the study of Guo et al. [168] it has been shown that H_2 addition increases the OH-radical concentration and the overall reaction rate in the reaction zone. This is expected to reduce the strength of CRZ [44, 105] due to a high acceleration of the flow, leading to increased temperatures in the reaction zone. Consequently, this leads to rising NO_x emission values for increasing hydrogen contents, despite decreasing adiabatic flame temperatures and decreasing residence times in the reaction zone. It also has been shown numerically that hydrogen addition can largely increase the NO formation via the NHH pathway [106], which can contribute significantly to the overall NO emissions [107].

However, there remains a significant gap in the literature regarding the key parameters governing flame stability and emissions in fuel-flexible burners operating across the full range of fuel mixtures within a fixed geometry. Existing studies on H_2-enriched CH_4/air swirling flames have rarely explored hydrogen concentrations beyond 80 % by volume [21]. However, the transition from 80 % to 100 % H_2 involves substantial changes in both energy content and flow characteristics due to the low molecular weight of hydrogen. These changes have a significant impact on both the flow field and the chemical behaviour of the mixture, influencing parameters such as flame speed, quenching distance, and mixing characteristics, and therefore present major challenges for combustor design. Therefore, addressing the challenges associated with burning in the whole range from methane to hydrogen in conventional swirl stabilized geometries remains an open research area. This chapter aims to advance the understanding of the feasibility

and challenges of dual-fuel combustion for CH_4/H_2 mixtures in a swirl-stabilized combustor, by experimentally examining the operational range and flame/flow interactions for various CH_4/H_2 mixtures. The investigated burner operates at atmospheric conditions and employs fuel injection in Jet in Cross-flow (JICF) configuration, as discussed in Chapter 5. JICF, where fuel is injected perpendicular to the airflow, has emerged as one of the most promising solutions to mix two fluids in a limited space [169].

This study uses AAI to stabilize flames up to 100 % H_2 flames, and examines its effectiveness for mixtures with lower hydrogen content. This chapter is structured as follows: Section 6.2 presents an overview of the experimental set-up and the measurement techniques. Section 6.3 discusses the effect of H_2 enrichment and AAI on the operational range, flame/flow interactions, and emissions. Finally, Section 6.4 summarizes the most important findings of this study.

6.2. CONFIGURATION SPECIFICATIONS

GEOMETRY & OPERATING CONDITIONS

Experiments were conducted in the partially premixed, swirl-stabilized dual-fuel combustor located in the Sustainable Aircraft Propulsion Laboratory at TU Delft. The set-up comprises an axial swirler with a swirl number of $Sw = 0.7$ or $Sw = 1.1$. Downstream of the swirler exit, fuel is injected into the swirling flow via a jet in cross-flow configuration through four injection ports, each with a diameter of $d_{fuel} = 3.5$ mm. The exact dimensions of the combustor geometry can be found in Chapter 3. A schematic of the set-up can be seen in Figure 6.1.

A range of fuel mixtures is tested, from 100 % CH_4 to 100 % H_2, while maintaining constant thermal power and a fixed air mass flow rate of $\dot{m}_{air} = 5.1 \cdot 10^{-3}$ kg/s. The set points are designed according to the procedure described in Chapter 3. Operating conditions for the design point at $P = 12$ kW are summarized in Table 6.1, while the remaining conditions are provided in Appendix B. The adiabatic flame temperature and the thermal expansion ratio are calculated with CANTERA for a premixed freely propagating flame. Six fuel compositions are tested, corresponding to hydrogen molar fractions XH_2 = 0, 0.25, 0.4, 0.6, 0.8, and 1. These are denoted as cases A to F throughout this chapter.

Design points at $P = 12$ kW and $\dot{m}_{air} = 5.1 \times 10^{-3}$ kg/s							
Tag	XH_2	U_{MT} [m/s]	U_{fuel} [m/s]	φ	T_{ad} [K]	J_{swirl}	ρ_{react}/ρ_{prod}
A	0	10.45	9.92	0.75	1942	0.09	6.40
B	0.25	10.62	10.69	0.74	1930	0.09	6.33
C	0.4	10.75	12.76	0.73	1921	0.11	6.26
D	0.6	11.01	15.82	0.71	1908	0.12	6.13
E	0.8	11.44	20.96	0.68	1895	0.13	5.94
F	1	12.26	30.42	0.62	1858	0.12	5.60

Table 6.1: Operating conditions for the design points at constant air flow rate, H_2 fraction XH_2, the bulk velocity in the mixing tube U_{MT}, equivalence ratio φ, adiabatic flame temperature T_{ad}, momentum flux ratio J_{swirl} for $Sw = 1.1$ and thermal expansion ratio ρ_{react}/ρ_{prod}.

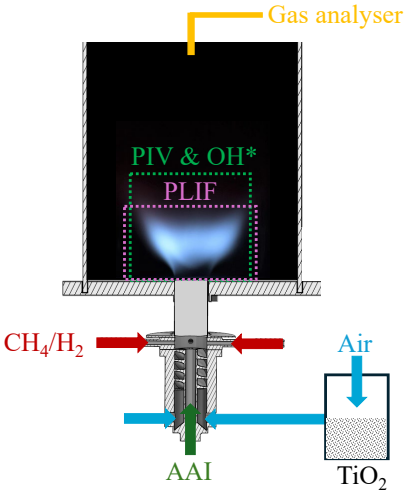

Figure 6.1: Set-up with the measurement locations for the laser-based diagnostics and location of the probe for the gas analyser.

MEASUREMENT TECHNIQUES

PARTICLE IMAGING VELOCIMETRY

Flow fields in the centre plane under reacting conditions were obtained using 2D2C PIV. The PIV settings are summarized in Table 6.2.

Laser	Nd:YAG Quantronix Darwin Duo 527-80-M
Camera	1 x LaVision Imager pro HS4M
Lens	180 mm
Sensor size	2016 × 2016 px
Final interrogation window	32 × 32 px, 50 % overlap
Spatial resolution	24.35 px/mm
Acquisition frequency	850 Hz
Seeding particles	TiO_2 ($d \approx 0.5$–$1\,\mu m$)
δt	37 µs

Table 6.2: Specifications PIV set-up reacting experiments.

The camera was equipped with a bandpass filter 532±10 mm, to avoid capturing the luminescence of the flame during acquisition. The raw images were scaled using a calibration image and then background-corrected by applying a minimum sliding background subtraction over nine images. The velocity fields were computed with the cross-correlation algorithm (LaVision, Davis 10 software). The data was filtered for outliers (Davis 10 universal outlier detection with median filter) and interpolated from adjacent interrogation areas. The velocity fields are averaged over 2000 images and normalized by the bulk velocity in the mixing tube U_{MT}.

The systematic error of PIV was examined by correlation statistics method (LaVision,

Davis 10 software) and the results indicate that the estimated uncertainties of velocities are lower than 5.0 %.

OH* CHEMILUMINESCENCE

The OH* signal was captured with a Tucsen CMOS camera, equipped with a UV lens and an optical filter with a width of 50 nm, centred at 325 nm. The images were acquired at a frequency of 10 Hz. The inverse Abel transform [129] was applied to time-averaged OH* results (over 100 single shot images) so that the distribution of OH* signal on the symmetric plane of the flame was obtained. This OH* distribution can be used as an indicator of the location of heat release [170]. For the Abel transform, each image is first normalized by the maximum pixel value of the image. After the Abel transform, the signal is again normalized by its maximum value, and a smoothing filter with a filter size of 25 × 25 px is applied. This reduces the noise caused by the Abel transform but does not distort the shape of the flame.

OH-PLIF

Pump Laser	Nd:YAG laser (Q-Smart 850 from Quantel)
Dye Laser	Sirah Cobra Stretch
Dye	Rhodamine 590
Camera	LaVision Imager M-lite 5M
Intensifier	LaVision IRO X , Gain 60 %, gate time 100 ns
Lens	85 nm
Filter	LaVision 1108760 VZ (75 % transmissivity at 308 nm)
Sensor size	1216× 1024 px
Spatial resolution	9.6 px/mm
Acquisition frequency	10 Hz
Excitation wavelength	283.55 nm, $Q_1(8)$ transition

Table 6.3: Specifications OH-PLIF set-up.

The specifications of the OH-PLIF set-up can be seen in Table 6.3. A more detailed description of the OH-PLIF set-up and the selection of the excitation wavelength is provided in Section 3.2.4. A laser sheet, approximately 100 mm high and 1.5 mm thick was formed by steering the laser beam into a collimator. For each operating condition, 500 single-shot PLIF images were collected. The images were corrected for variations in laser sheet intensity using the flat field function in Davis. Variations in the laser sheet within the combustion chamber were mapped by filling the chamber with acetone vapour.

GAS ANALYSER

Emission measurements were acquired with the ABB AO2000 gas analyser at 3 Hz. The exhaust gas was sampled in the centre of the outlet plane of the combustion chamber. The emission values were averaged over a time span of at least 30 s, once stationary conditions for the set point were reached. The averaged values were normalized by a volumetric fraction of 15 % O_2 in the flue gases. CO and CH_4 values were measured below

4 ppm and 15 ppm, respectively, which are the detection limits of the gas analyser. Due to their low values, these emission values are not discussed, and it is assumed that complete combustion took place. NO_2 for all points was below 2 ppm. In some cases, the values of NO_2 are not representative, because the dew temperature increased with increasing concentrations of water vapour in the products. For high hydrogen content fuels, this temperature exceeded the product temperature in the gas analyser (80°C). This most likely led the water to condensate, creating significant uncertainties due to NO_2 dissolving in water. Additionally, NO_2 is well known to react with liquid water to form nitric acid and nitrous acid [171]. NO on the other hand remains largely inert and has a limited solubility in water. Given that, for 100 % CH_4 the NO_2 value is an order of magnitude lower than NO, it is assumed that NO is the primary contributor to NO_x emissions. Consequently, it was decided to compare combustion performance by focusing on NO emissions.

6.3. RESULTS

The results chapter first explores the operational range of the proposed lean partially premixed set-up, focusing on the flashback and blowout limits across various equivalence ratios φ and hydrogen contents at different levels of AAI. Following this, flow fields obtained by PIV are discussed, highlighting the effects of H_2 enrichment on the average flow fields within the combustion chamber. Next, OH* chemiluminescence and OH-PLIF images illustrate the different flame stabilization mechanisms and the location of the flame in the flow field. Finally, the combustor performance is evaluated under different operating conditions by analysing the measured emissions

6.3.1. OPERATIONAL RANGE

In this section, the operational range of the combustor is discussed. Only lean conditions have been tested, as this is the intended operational regime for this set-up. The selected operating conditions (between 8 kW and 12 kW) to allow exploration of a broad equivalence ratio range for multiple hydrogen contents. Figure 6.2 presents the stability map of $Sw = 1.1$ at a constant air flow rate of $\dot{m}_{air} = 5.1 \times 10^{-3}$ kg/s, examining the cases with $\chi = 0$ % and $\chi = 20$ %. The stability map indicates the stable region, the Lean Blowout (LBO) limits, and the Flashback (FB) limits. The stability analysis in this chapter focuses on static stability, thus excluding consideration of thermoacoustic instabilities in the analysis. Therefore, even if a flame is classified as statically stable, it could still manifest thermoacoustic instabilities. Static stable flames stabilize downstream of the mixing tube exit. Flashback is typically defined as the uncontrolled upstream propagation of the flame front, caused by an imbalance of local burning velocity and local flow speed [172]. In the current set-up, the short distance from the fuel injection location to the combustion chamber prevents flames from travelling far upstream. Therefore, in this study, flames exhibiting flashback are identified by the presence of an upstream flame front within the mixing tube. The flame burning in the mixing tube is undesired, as it can impose high thermal loads on the combustor components, potentially leading to material failure.

The images above the stability map display the average natural emissions of the

flame, captured with a Nikon 7500 DSLR camera fitted with an AF-S DX NIKKOR 18-140 mm telephoto lens. Each image represents an average of 30 snapshots. An example of a stable flame at $\chi = 0\,\%$ is marked with a ⋆. An example of a flame in flashback mode can be seen marked with the red triangle Δ for the $\chi = 0\,\%$ case.

For $\chi = 0\,\%$, only a narrow operational range of stable combustion can be identified. It is observed that increasing the hydrogen content reduces the critical φ for the LBO limit. This decrease results from the increase in reaction rate, the increase in diffusivity and burning velocity for H_2-enriched flames. This can be seen as an advantage, as a lower LBO allows the combustor to be operated at leaner conditions, thus lowering the formation of thermal NO_x. However, due to a higher flame speed, it also decreases the equivalence ratio for the flashback limits, as shown in Figure 6.2. Flames above XH_2 = 0.8 can not be stabilized without AAI, even at very lean conditions(φ = 0.38). When the overall equivalence ratio is increased to φ = 0.65, flames can only be stabilized up to XH_2 = 0.4.

The introduction of AAI, instead, allows full operational range from 100 % CH_4 to 100 % H_2 (Figure 6.2). When a high level of AAI is introduced ($\chi = 20\,\%$), flashback does not occur within the investigated range of XH_2 and φ. However, blowout occurs at lean conditions for lower H_2 contents, which limits the operable range to higher φ values where stable combustion can be sustained for all fuel mixtures. For the case with XH_2 = 0.4 (⋆), the flame is significantly lifted off the injector. With at least $\chi = 20\,\%$, flames can even be stabilized reliably up to XH_2 = 1 across the entire range of investigated φ. Lower levels of AAI have resulted in flashback when φ reached a critical value.

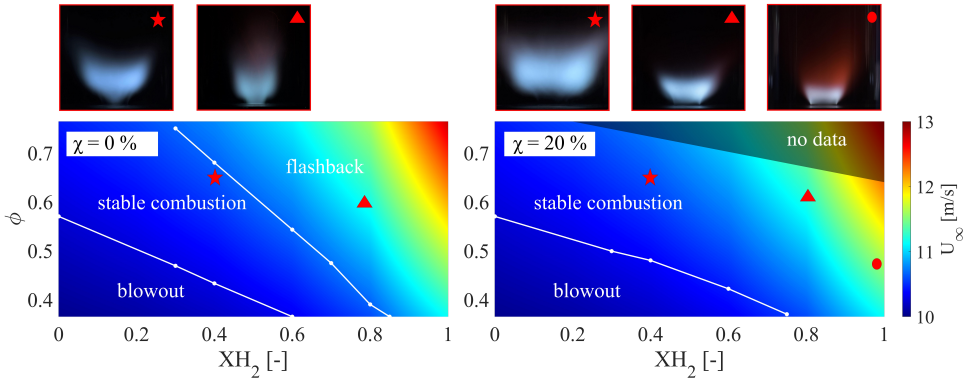

Figure 6.2: Stability maps for Sw = 1.1 at $\chi = 0\,\%$ and $\chi = 20\,\%$ at a constant air mass flow rate with average images of natural emissions of example static stable and unstable flames.

Figure 6.3 illustrates the average images of the natural emissions of the flame for Sw = 1.1 and $\chi = 20\,\%$ with varying hydrogen content. As the hydrogen content in the fuel increases, the flame becomes compact and is located closer to the injector, due to the higher flame speed and reactivity of hydrogen-rich fuels. Noticeably the reddish colour resulting from H_2O^* Chemiluminescence [173] is more intense with increased hydrogen content, due to the greater amount of water vapour in the products. The colour of the reaction zone transitions from blue, for fuels with high methane content (CH^* Chemi-

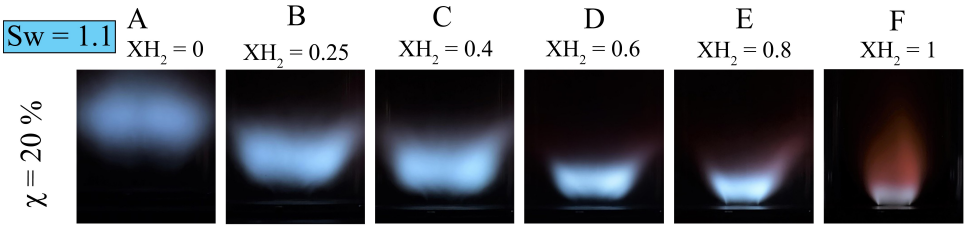

Figure 6.3: Effect of H_2 enrichment on the flame shape for at P = 12 kW, Sw = 1.1, AAI = 20 %. Natural emission in the visible spectrum.

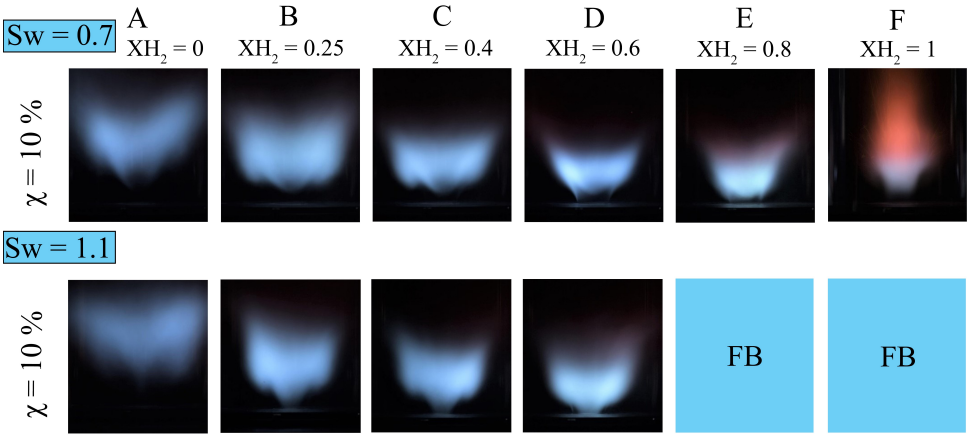

Figure 6.4: Effect of the swirl number on the flame shape for at P = 12 kW and varying XH_2. Average image of natural emission in the visible spectrum. FB = flames exhibiting flashback.

luminescence) to grey for 100 % H_2 (presumably a result of H_2O_2* Chemiluminescence [174]).

For the lower geometric swirl number of Sw = 0.7, less AAI is required to stabilize the flame at high hydrogen contents. This is expected, as the swirl induces a radial pressure gradient that balances the centrifugal force. As a consequence, a higher swirl number also introduces a higher adverse axial pressure gradient, resulting in an upstream location of the stagnation point. This behaviour is illustrated in Figure 6.4, which compares flame shapes for Sw = 0.7 and Sw = 1.1 at a moderate AAI level of χ = 10 % and varying hydrogen fractions (XH_2). The intermediate AAI level was selected because, at χ = 20 % for Sw = 0.7, the flame lifts significantly from the injector, leading to unstable conditions close to blowout for the fuel mixtures with low hydrogen content. High AAI levels are known to suppress the CRZ by reducing the effective swirl number below the critical threshold for vortex breakdown (Sw = 0.6) [31]. For the lower swirl number, the burner can be operated across the entire range of hydrogen contents, while for the higher swirl number, the flame experiences flashback above XH_2 = 0.6.

Notably, at the lower swirl number, the flame is attached to the outer radius of the

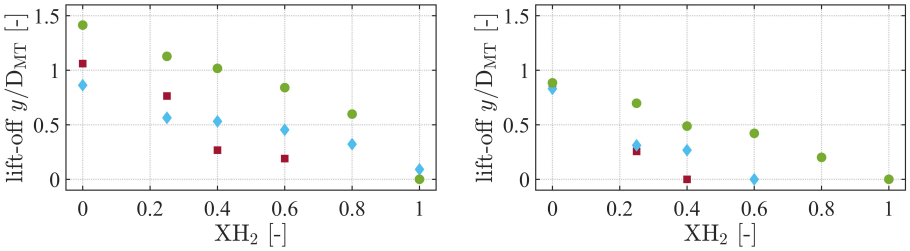

a) Lift-off heights for $Sw = 0.7$ **b)** Lift-off heights for $Sw = 1.1$

Figure 6.5: Lift-off heights in y/D_{MT} of the injector for two different swirl numbers, at $\chi = 0\,\%$ (■), $\chi = 10\,\%$ (◆) and $\chi = 20\,\%$ (●).

mixing tube, suggesting stabilization of the flame in the boundary layer of the mixing tube. This is especially pronounced for $XH_2 > 0.4$. Conversely, at the higher swirl number, the flame stabilizes more towards the centre of the swirling flow. This suggests more fuel-rich conditions close to the periphery of the mixing tube for lower swirl numbers due to decreased mixing quality. This observation aligns with findings discussed in Chapter 5, which showed that lower swirl numbers result in less effective mixing, causing the fuel to remain closer to the mixing tube periphery. Figure 6.5 shows the lift-off heights for varying levels of XH_2 at different levels of AAI and the two different swirl numbers. The lift-off height is obtained from the OH* images, while assuming that the flame front is at 20 % of the maximum OH*signal. For the same level of AAI, the lift-off height from the injector is increased for the lower swirl number in all cases. This is due to the lower adverse pressure gradient for lower swirl numbers, which results in a more downstream stagnation point. Overall, the lift-off heights for $Sw = 1.1$ at $\chi = 20\,\%$ are comparable to those for $Sw = 0.7$ at $\chi = 10\,\%$. However, the flame shapes differ significantly between the two swirl numbers. As shown in Figure 6.3 and Figure 6.4 ($Sw = 0.7$, $\chi = 10\,\%$), the flame significantly protrudes into the OSL. For $XH_2 > 0.4$, the flame attaches to the injector rim within the OSL, while along the centreline it remains lifted off the injector. In contrast, for $Sw = 1.1$, the flame stabilizes at a more uniform distance from the injector across both the centre and outer regions. As previously discussed in Chapter 5, the degree of fuel-air mixing near the mixing tube outlet is higher for all $Sw = 1.1$ cases compared to $Sw = 0.7$, even when the level of AAI is high. This improved mixing is reflected in the flame images by the more uniform stabilization of the flame for the higher swirl cases. However, for cases with $XH_2 = 0.8$ and $XH_2 = 1$, the flame also shows significant stabilization within the boundary layer of the mixing tube. This may be attributed to the reduced velocity gradient near the wall at higher swirl numbers, which can increase the risk of flame stabilization in the shear layer and boundary layer flashback, especially for higher hydrogen content fuels [175].

6.3.2. FLOW FIELD ANALYSIS

In Figure 6.6 the average streamwise velocity plots are shown for $Sw = 1.1$ and $\chi = 20\,\%$ at various hydrogen contents at the design conditions presented in Table 6.1. The scale of the coloured background indicates the normalized streamwise velocity, with superim-

posed streamlines calculated from the x - and y-component of the velocity. In a swirl-stabilized burner with a high swirl number ($Sw > 0.6$), the flow field is usually characterized by a CRZ, which forms as a consequence of vortex breakdown, as shown previously in Chapter 4. The CRZ serves as an aerodynamic flame holder, allowing flames to stabilize away from the solid components of the combustor. The figure illustrates a notable alteration in flow field shape with increasing hydrogen content. The case with $X\mathrm{H_2} = 0$ (case A) exhibits a flow field featuring a CRZ, which can be seen as the area of negative axial velocities in Figure 6.6. This feature fully disappears for the case with $X\mathrm{H_2} = 1$ (case F). For the cases with $\mathrm{CH_4}/\mathrm{H_2}$ mixtures, the strength of the CRZ diminishes with increasing hydrogen content. The drastic change in flow field structure from case E to case F results from the way fuel composition was defined. In case E, the fuel was specified by a hydrogen volume of $X\mathrm{H_2} = 0.8$, which corresponds to a mass fraction of only $Y\mathrm{H_2} = 0.33$. This leads to a significantly lower hydrogen content than in the pure hydrogen case (case F), causing substantial differences in fuel properties and consequently in the flow field.

Additionally, the flow fields illustrate that increasing hydrogen content in the fuel increases the maximum axial velocity magnitude. For case A, the maximum axial velocity is around 1.3 $U_{\mathrm{MT,CH4}}$, while it reaches around 2 $U_{\mathrm{MT,H2}}$ for case F. Firstly, this is due to the increased bulk velocities in the mixing tube, which also have shown increased peak velocities in the non-reacting case, as discussed in Chapter 4. However, the even stronger acceleration downstream of $y/D_{\mathrm{MT}} = 0.5$ in case F indicates more pronounced thermal expansion due to heat release compared to the cases with lower $X\mathrm{H_2}$. This is consistent with the observed reduction in size and strength of the CRZ in the reacting case as the hydrogen content increases.

Increasing the hydrogen content can be seen to induce a strong axial feature to the flow emerging from the mixing tube, as seen in Figure 6.6 from the streamlines ($-0.5 \leq x/D_{\mathrm{MT}} \leq 0.5$). For case A, this feature looks very similar to the one discussed in the non-reacting flow field in Chapter 4, as a result of the AAI jet. For cases E and F the axial jet-like structure at the mixing tube outlet becomes significantly stronger and suppresses the CRZ seen prominently in the other cases.

When transitioning from $\mathrm{CH_4}$ to $\mathrm{H_2}$ as fuel, several factors influence the flow field. First, the momentum flux ratio J_{swirl} between the fuel and the swirling air changes. As shown in Chapter 4, radial fuel injection reduces the effective swirl number. The results of the non-reacting study further indicate that increasing $X\mathrm{H_2}$ leads to a reduction in the effective swirl number, which notably influences the flow field, particularly in the high-hydrogen cases. In addition, the thermal expansion associated with combustion has been shown to reduce the swirl number, as it accelerates the flow more strongly in the axial direction [176]. A similar behaviour also has been observed in the work of Shoji et al. [177], where increasing the equivalence ratio φ of a low-swirl $\mathrm{H_2}$ flame resulted in the formation of widespread high-velocity regions. This is attributed to an increased thermal expansion ratio due to an increase in φ and due to a reduced lift-off height of the flame, which causes an intense thermal expansion of the gas very close to the injector. Table 6.1 summarizes the ratios for J_{swirl} and the thermal expansion ratios calculated for perfectly premixed conditions for the operating conditions at $P = 12\,\mathrm{kW}$. The thermal expansion ratio decreases for increasing hydrogen content. However, as shown in Chapter 5, the

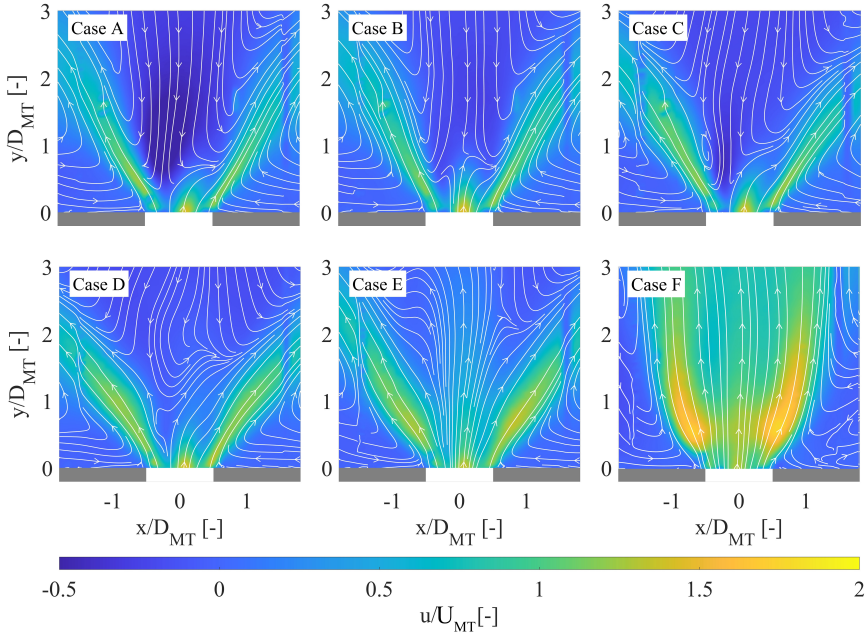

Figure 6.6: Average streamwise velocity fields in reacting conditions with superimposed streamlines, obtained from PIV at with $Sw = 1.1$, $P = 12\,\text{kW}$ for different XH_2 at $\chi = 20\,\%$.

mixture enters the combustion chamber under partially premixed conditions. Consequently, the location of the flame front determines significantly the equivalence ratio at which the reaction takes place. A flame front positioned upstream or even attached to the rim, as in case F, is expected to burn in some regions under conditions much richer than the nominal equivalence ratio. In a lifted flame configuration, such as in case A, the additional distance between the injector and the flame front allows more time for mixing between fuel and oxidizer before combustion occurs. As a result, the flame tends to burn at an equivalence ratio closer to the nominal value. Additionally, the location in the flow field determines the magnitude of the local flow speed perpendicular to the flame front. A flame located close to the mixing tube outlet will consequently accelerate the flow to higher axial velocities downstream of the flame compared to a lifted flame. The flow field for case F is that of the low-swirl flame discussed in [177]. This similarity suggests that the increased thermal expansion in case F reduces the swirl number to a level typical of a low-swirl flame, resulting in the absence of a CRZ.

Figure 6.7 presents the average streamwise velocity fields for the same fuel compositions as shown in Figure 6.6, but at a lower swirl number, $Sw = 0.7$, and $\chi = 10\,\%$. No data is shown for case A, as the flame was highly unstable and close to lean blowout. At this level of AAI, the axial jet is no longer visible along the centreline, in contrast to the flow fields shown in Figure 6.6. This absence supports the interpretation that the strong axial feature observed for the cases $Sw = 1.1$ at $\chi = 20\,\%$ is a result of the interaction between the flame and the axial jet. This interaction leads to flow acceleration through

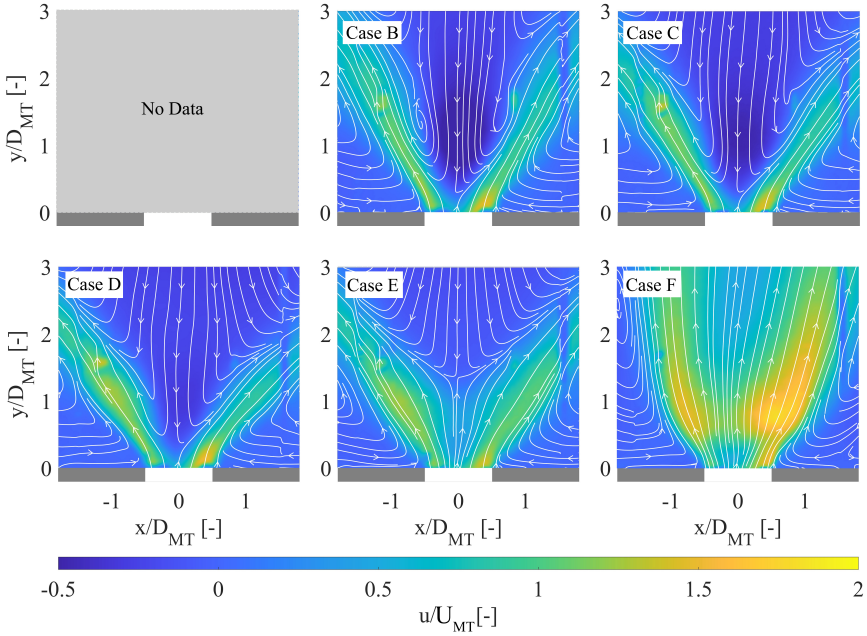

Figure 6.7: Average streamwise velocity fields in reacting conditions with superimposed streamlines, obtained from PIV at with $Sw = 0.7$, $P = 12\,\text{kW}$ for different XH_2 at $\chi = 10\,\%$

thermal expansion, particularly at higher XH_2, where the flame stabilizes further upstream. The absence of the AAI jet on the centreline also results in higher negative axial velocities within the CRZ for the lower swirl number. As a result, a CRZ persists up to $XH_2 = 0.8$ (case E), although the stagnation point moves progressively downstream with increasing XH_2. The opening angle of the high-velocity jets as well as the axial velocity magnitudes remain similar to the ones observed for $Sw = 1.1$ and $\chi = 20\,\%$ (Figure 6.6), for cases up to $XH_2 = 0.8$. For case F, the overall flow field structure is similar for both swirl numbers, with suppression of the CRZ and significant acceleration within the jet. The velocity magnitudes are similar in both cases, though slightly higher axial velocities are observed in the lower swirl configuration, likely due to the higher axial momentum associated with a lower swirl number.

To investigate the role of heat release in the disappearance of the CRZ, a 100 % hydrogen flame was studied at $Sw = 1.1$ and $\chi = 20\,\%$, for two different equivalence ratios while keeping the air mass flow rate constant. The first case, with $\varphi = 0.62$, corresponds to a thermal power P_{th} of 12 kW, and the second, with $\varphi = 0.4$, to $P_{\text{th}} = 7.5\,\text{kW}$. Figure 6.8 presents instantaneous OH-PLIF images of the flame (top row) and the average flow field (bottom row) for both equivalence ratios. At the higher equivalence ratio ($\varphi = 0.62$), the flame exhibits a jet-like flow field without a CRZ, with flame branches aligned more parallel to the main flow and not spreading radially. Additionally, the flame is attached to the injector in the OSL. In contrast, for the lower equivalence ratio, the axial velocities of the AAI jet can clearly been seen on the centre line, but the flow field still features a

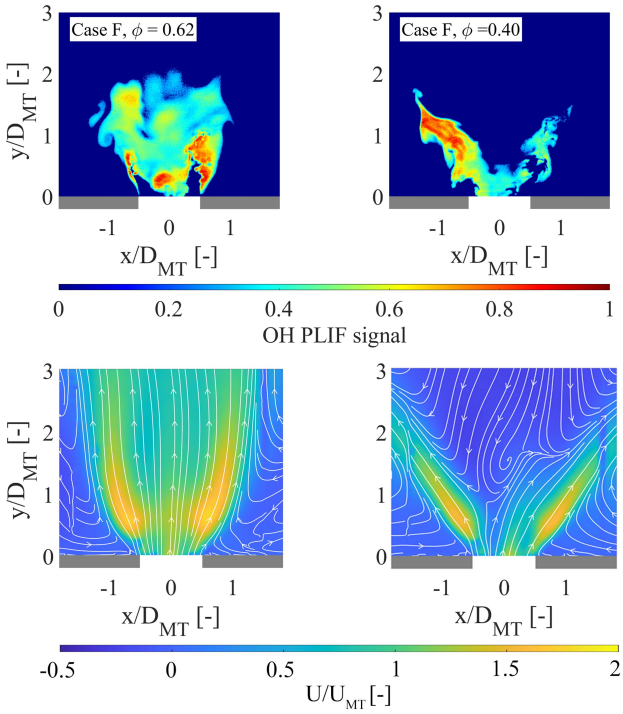

Figure 6.8: Instantaneous OH-PLIF images (top row) and average flow field (bottom row) for Sw = 1.1, χ = 20 % at two different equivalence ratios φ.

CRZ. This is also reflected the OH-PLIF distribution, where the flame brushes follow the opening angle of the swirling flow.

Some variations in the non-reacting flow field are expected with changes in equivalence ratio, due to variations in J_{swirl} and the total mass flow rate in the mixing tube, as discussed in Chapter 4. However, the results presented in Chapter 4 indicate that the non-reacting flow field is only moderately sensitive to these changes, and no disappearance of the CRZ was observed under any of the investigated conditions. Therefore, it is concluded that the disappearance of the CRZ is primarily driven by thermal expansion effects.

6.3.3. FLAME STABILIZATION

FLAME TYPES

Figure 6.9 shows the instantaneous OH-PLIF images of the different flame shapes observed in the experiment. The flame shapes are identified through single-shot OH-PLIF images, providing clear insights into the mechanisms responsible for flame stabilization. OH* Chemiluminescence images offer a less detailed, line-of-sight averaged perspective, making it more difficult to distinguish specific flame features. The V-flame shape (XH_2 = 0.25, χ = 0 %) is similar to the ones in literature. For a V-flame shape, the flame is stabilized in the ISL and the flame trailing edge tip is pointing towards the exit of the com-

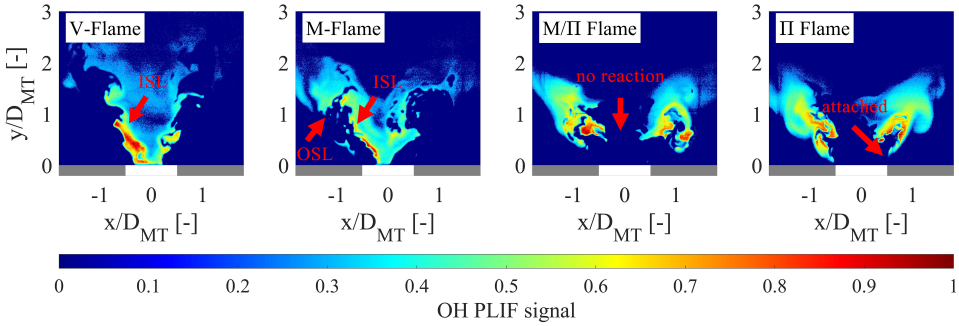

Figure 6.9: Instantaneous OH-PLIF images of flame types observed in this study with $Sw = 1.1$ at $P = 12\,\mathrm{kW}$, **V-Flame**: $XH_2 = 0.25$, $\chi = 0\,\%$ | **M-Flame**: $XH_2 = 0.4$, $\chi = 10\,\%$ | **M/Π-Flame**: $XH_2 = 0.4$, $\chi = 20\,\%$ | **Π-Flame**: $XH_2 = 0.8$, $\chi = 20\,\%$.

bustion chamber [99]. Additionally, the flame is attached to the rim in the ISL. For an M-flame ($XH_2 = 0.4$, $\chi = 10\,\%$), the flame trailing-edge tip protrudes in the outer shear layer (OSL), pointing towards the combustion chamber dump plane. When the fuel contains a high amount of H_2 or when the mixing is reduced due to an increased accumulation of fuel close to the periphery of the mixing tube, the flame can stabilize in the OSL, due to lower chemical time scales τ_{chem}. The flames in the OSL are strongly affected by heat losses, which quenches the reactions for low hydrogen contents or lean conditions. In contrast to the definition in literature, the flame in the outer shear layer is not attached to the injector, presumably due to heat losses to the steel baseplate [178]. Nevertheless, the flame will be classified as M-flame, as it is attached to the injector in the ISL, and is clearly protruding into the outer shear layer. For a Π-Flame ($XH_2 = 0.8$, $\chi = 20\,\%$), the flame front in the centre is pushed downstream, while the flame is attached to the outer rim. This type of flame has been observed and described in Liu et al. [98]. In comparison to their work, however, for the Π-flame presented here no reaction takes place on the centreline of the swirling flow. Both, high axial velocities due to AAI and lean quenching due to a fuel lean core of the swirling flow (as discussed in Chapter 5) on the centreline partly contribute to this effect. This will be discussed later in this section. Since the flame is attached to the outer rim of the injector, the risk of boundary layer flashback is significantly higher compared to an M-flame. A flame, where the flame front on the centreline is pushed downstream, but the flame is not attached to the outer radius will be called M/Π Flame ($XH_2 = 0.4$, $\chi = 20\,\%$).

EFFECT OF AXIAL AIR INJECTION

The flame structure is initially investigated for a fixed hydrogen content to analyse the effect of AAI. Images were taken in the emissions band $\lambda = 320 \pm 25\,\mathrm{nm}$, centred at the OH* Chemiluminescence signal to study the reaction zone. The Abel deconvoluted images can be considered as a good indication of the location of a heat release zone in the axial plane of the burner, and are therefore used to determine the location of the flame in the flow field [170].

Figure 6.10 shows the Abel deconvoluted OH* images with superimposed stream-

lines obtained from PIV measurements for different levels of AAI at $XH_2 = 0.4$. The apparent high signal along the centreline in Abel-transformed chemiluminescence images is an artifact caused by the inversion. The flame in Figure 6.10 represents a V-flame shape for $\chi = 0\,\%$. Throughout the investigated range, for $\chi = 0\,\%$, only V-flames occurred. The stagnation point being inside the mixing tube and the low velocities on the centreline of the swirling flow allowed the flame burn attached to the injector, even in the case with no hydrogen in the fuel mixture. For the intermediate level of AAI ($\chi = 10\,\%$), the flame burns in the ISL but develops small branches in the OSL. The flame classification presented in Chapter 2 shows that this is an M-flame. This outcome is anticipated due to reduced mixing, causing increased accumulation of fuel close to the periphery of the mixing tube, thereby facilitating stabilization of the flame in the OSL. For $\chi = 20\,\%$, the flame is lifted off the injector and partially burns in the ISL and OSL, transitioning to an M/Π-flame.

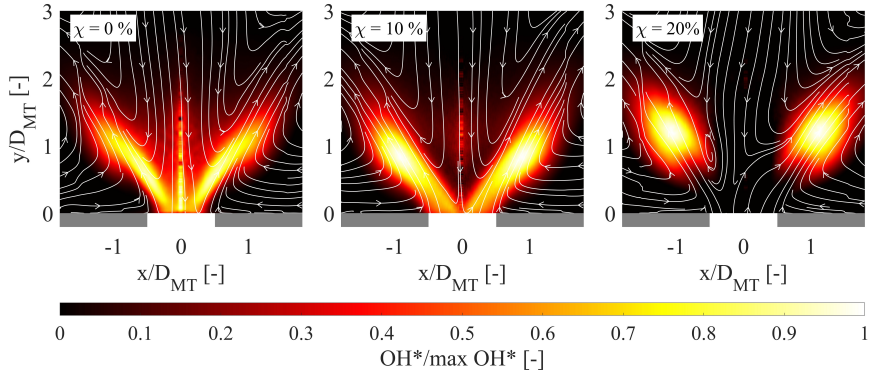

Figure 6.10: Abel deconvoluted OH* images for $Sw = 1.1$ at for case C at $P = 12$ kW for $XH_2 = 0.4$ with different levels of χ, with superimposed streamlines.

As it has been thoroughly discussed in [85] and shown in Chapter 4, increasing the level of AAI shifts the location of vortex breakdown further downstream and reduces the negative axial velocity on the centreline. For $\chi = 20\,\%$ in Figure 6.10, the flow field even exhibits a region of positive axial velocity around the injector outlet section between -0.5 $\leq x/D_{MT} \leq 0.5$. The significant change in the flow field between $\chi = 10\,\%$ to $\chi = 20\,\%$ can be explained by the non-linear effect of AAI on the swirl number. For lower levels of AAI, the effect on the swirl number for increasing AAI is smaller than for high levels of AAI, as confirmed in [53]. Additionally, it can be seen that the flame up to $\chi = 10\,\%$ is burning on the centreline, while for $\chi = 20\,\%$ no reaction takes place on the centreline, despite low velocities being present. As previously discussed in the mixing study in Chapter 5, the cases for the fuel injector diameter $d_{fuel} = 3.5$ mm results in a lean core region, with most of the fuel concentrated near the periphery of the mixing tube. Although unmixedness values near the outlet of the mixing tube appear similar across cases, it is assumed that increasing AAI reduces the local fuel concentration on the centreline. This is likely due to the insufficient mixing length, which prevents complete mixing between the fuel and the high-momentum AAI jet.

The absence of reaction along the centreline at higher AAI levels suggests local flame

extinction in that region, likely due to deteriorated mixing quality. However, since the streamlines exiting the mixing tube reach the reaction zone indicated by high OH* signal and no CO or CH_4 is detected in the exhaust gas, complete combustion still occurs. Additionally, flames at higher AAI levels are observed to burn more in the outer shear layer (OSL), further supporting the notion that increased AAI leads to a more fuel-rich region near the mixing tube wall.

EFFECT OF HYDROGEN CONTENT

Figure 6.11 shows the Abel deconvoluted images for different hydrogen contents. Due to the high level of AAI (χ = 20 %) the flames are lifted off the injector for almost all the cases, except for 100 % H_2 (Case F). When no H_2 is present in the fuel (Case A), the flame stabilizes at a location of y/D_{MT} = 1 and stretches until y/D_{MT} = 3. Since it is burning in the inner and the outer shear layer, the flame is classified as a lifted M-flame. As it has been discussed before, the flame is not burning on the centreline, close to the stagnation point. Since a low-velocity region is present, this suggests that the flow features a core with the mixture below the lean flammability limit.

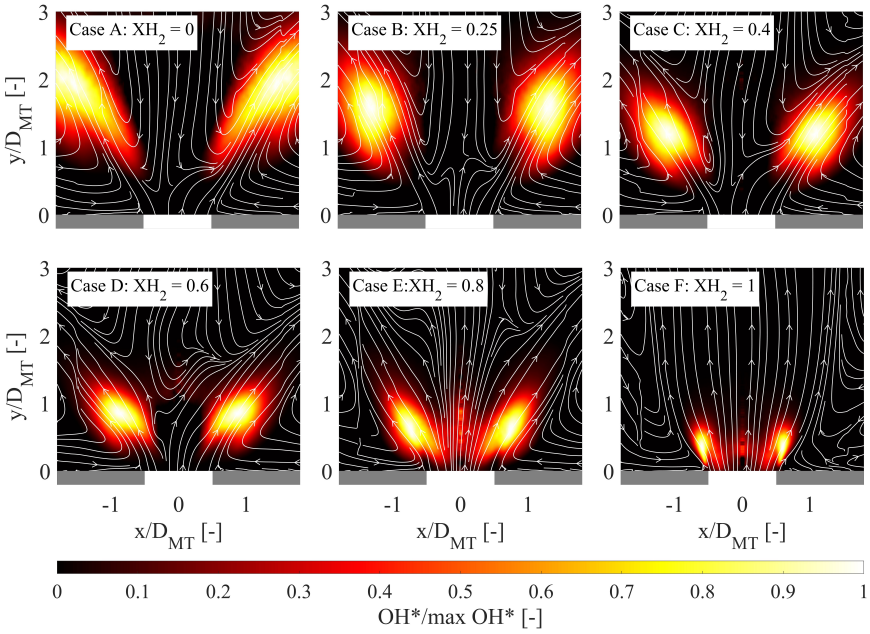

Figure 6.11: Abel deconvoluted OH* images for Sw = 1.1 at P = 12 kW for different XH_2 with χ = 20 %, with superimposed streamlines.

When enriching the fuel with a small amount of H_2 (XH_2 = 0.25), the flame trailing edge in the outer shear layer moves closer to the combustor dump plane, while the tip in the inner shear layer moves further away. When the hydrogen content is increased even more up to 80 %, both the inner tip and the outer tip of the flame move closer to the combustor dump, while still featuring the shape of an M-flame. For 100 % H_2 (Case F),

the flame is a Π-flame attached to the outer rim of the injector. The flame for case F is similar to the low swirl flame observed in the work of Cheng et al. [179], which together with the flow field shown in Figure 6.6 suggests that the swirl number is significantly decreased compared to the low H_2 cases.

6.3.4. EMISSION ANALYSIS

Figure 6.12 shows the CO_2 emissions for $Sw = 1.1$ at different XH_2 and different power settings P. As expected, CO_2 emissions exhibit a reverse exponential trend with increasing hydrogen content. This occurs because CO_2 emissions (in vol%) are directly proportional to the mass fraction of CH_4 in the fuel. When the hydrogen content is expressed in volume fraction, the mass fraction of CH_4 decreases exponentially.

Additionally, lower values of P result in reduced CO_2 emissions. This is because, in this configuration, the flame burns overall leaner at lower P, leading to a lower concentration of carbon atoms in the fuel mixture.

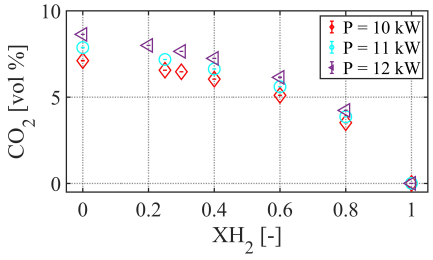

Figure 6.12: Average CO_2 emissions and standard deviations at $Sw = 1.1$ for different P and XH_2.

Figure 6.13 shows the NO emissions under various operating conditions for the two different swirl numbers. The average NO values, including the standard deviation, are plotted against the adiabatic flame temperature of the perfectly premixed case. The measurements are presented for increasing power levels, keeping the air flow rate constant, which increases the equivalence ratio φ. This results in increased NO emissions due to increased NO formation via the thermal pathway. As flame shapes are strongly influenced by the levels of AAI and XH_2, no relation between the flame shape and emissions can be established.

Increasing hydrogen content generally leads to increased NO emissions, contradictory to what is expected from calculated adiabatic flame temperatures for the premixed case, as shown in Table 6.1. As it has been shown in Chapter 5, the fuel-air mixing is expected to be higher for increasing XH_2 in the fuel. This would further decrease the NO emissions for increasing levels of XH_2, contrary to what is observed.

The trend of increasing NO emissions for increasing hydrogen content is particularly evident in the $Sw = 0.7$, $\chi = 20$ % case. Two plausible explanations which combined can explain this trend are proposed. Due to the partially premixed operational mode, flames with a higher flame speed are attached to the injector (Case F), and have therefore less time available for mixing. As a result, the local fuel-air mixture is expected to be richer than the nominal equivalence ratio φ shown in Table 6.1. This leads to locally high flame temperatures, and consequently an increased formation of thermal NO.

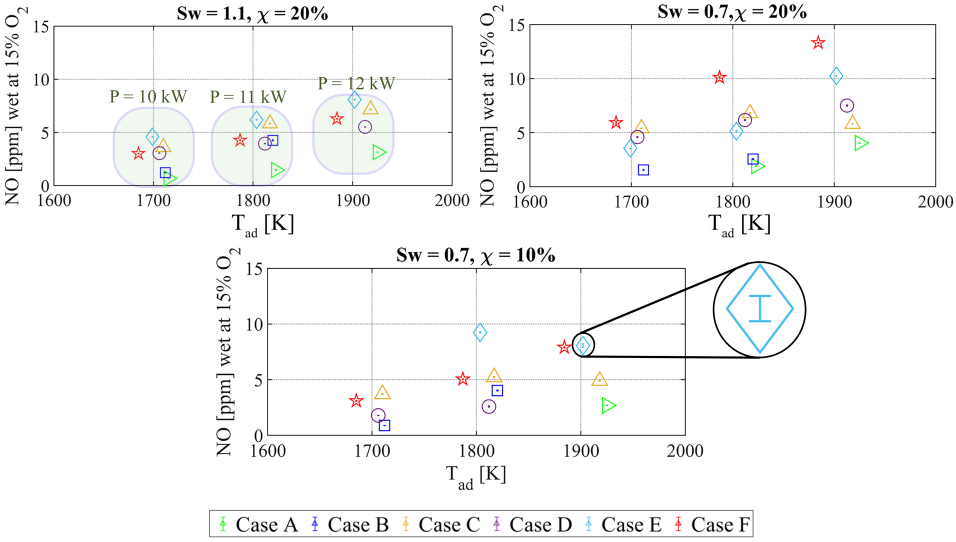

Figure 6.13: Average NO emissions and standard deviations for Sw = 0.7 and Sw = 1.1 at different levels of AAI, P and XH_2.

6

In contrast, flames with lower flame speed are lifted further from the injector (case A), and benefit from an additional length of y/D_{MT} = 1 downstream of the mixing tube exit, where mixing can take place. This allows for a more uniform flame temperature and a fuel-air mixture closer to the nominal φ, thereby limiting the formation of thermal NO. This means that due to the substantial increase in flame speed, the change in flame position appears to have a greater influence on the NO emissions than the improvement in mixing quality for increasing XH_2. Additionally, as observed in other studies [44, 105], a weakened CRZ for increasing hydrogen contents can increase the actual flame temperature. This happens due to less or no recirculation of colder products into the reaction zone. Consequently, more thermal NO can form. This can outweigh the effect of a lower residence time in the reaction zone for increasing hydrogen contents [105].

Overall, for the same level of AAI, the higher swirl number results in lower NO values compared to the lower swirl number (Figure 6.13 top row), a trend observed in other studies as well [180]. Higher swirl numbers facilitate better mixing, thereby reducing the locally rich zones. When comparing the plot with Sw = 1.1, χ = 20 % with the one of Sw = 0.7, χ = 10 %, it can be observed that for the high hydrogen content cases (Case E and Case F), the higher swirl number performs slightly better. Since the location of the flame is similar for all flames for cases E and F (see Figure 6.3 and Figure 6.4) it is assumed that the high swirl number with a higher level of AAI still ensures a better mixing of fuel and air. This has also been confirmed in the results of the mixing study in Chapter 5. For lower hydrogen content fuels, the change in swirl number does not show any significant difference in NO emissions, supporting the assumption that a considerable degree of mixing still takes place within the combustion chamber. Since low hydrogen content flames are lifted off the injector, (see Figure 6.4), the equivalence ratio at which the re-

action takes place is less affected by the flow field and the level of mixing in the mixing tube.

6.4. CONCLUSIONS

This chapter explored the fuel flexibility (CH_4/H_2) of a laboratory-scale swirl stabilized combustor. The concept of AAI is utilized to stabilize flames with high hydrogen content. Various optical diagnostic techniques and emission gas analysis were employed to investigate the flow field, flame stabilization, and emission performance. The operational range of the combustor was examined for different equivalence ratios (φ) and H_2 fractions (XH_2) at two different swirl numbers. AAI significantly increases both the lean blowout limit and the flashback limit. As expected, the low swirl number results in flames that stabilize further downstream in the combustion chamber compared to the high swirl number, thus requiring less AAI to prevent flashback. High levels of AAI (20 % for Sw = 1.1) are necessary to stabilize 100 % H_2 flames. A small operational window is identified, covering the full range from 100 % of CH_4 to 100 % of H_2.

The flow field analysis revealed significant changes in the overall flow field structure when changing the fuel from CH_4 to H_2 at χ = 20 %. While CH_4 flames exhibit a CRZ, which anchors the flame, the CRZ is completely suppressed for the H_2 flame at the design point of P_{th} =12 kW.

In terms of flame stabilization, introducing a high level of AAI changes the flame from a V-flame to an M/Π-flame, which leads to local flame extinction on the centreline, and consequently richer conditions in the reaction zone. This behaviour was observed for all hydrogen contents investigated. The low momentum flux ratio between the fuel jet and the air jet forces the fuel to remain near the periphery of the mixing tube. Additionally, the introduction of AAI further impairs mixing, leading to a mixture in the core of swirling flow below flammability limit.

Furthermore, switching from CH_4 to H_2 results in greater NO emissions, despite lower theoretical adiabatic flame temperatures for perfectly premixed configurations. This is expected, as the CH_4 flame anchors further downstream in the combustion chamber, providing more time for fuel and air to mix. In contrast, combustion in high-H_2 flames occurs under less premixed conditions, resulting in regions with equivalence ratios exceeding the nominal φ. The main findings of this chapter summarized are:

- AAI allows stabilizing flames throughout the full range of 100 % CH_4 to 100 % H_2.
- Despite allowing for fuel-flexibility, the current configuration does not achieve good mixing. This results in higher NO emissions when compared to a perfectly premixed system, but also in a high risk of boundary layer flashback, since fuel is located close to the periphery of the mixing tube.
- Changing the fuel from 100 % CH_4 to 100 % H_2 significantly alters the flow field structure. For 100 % H_2, the inner recirculation zone is not established in the current configuration.

It is concluded that AAI presents a promising approach for fuel-flexible combustion chambers. However, for high hydrogen content fuels, the fuel injection strategy requires

further optimization to ensure improved fuel-air mixing and to stabilize the flame away from the mixing tube boundary layer. The NO emissions exhibit a non-linear trend with increasing hydrogen content, generally rising as the H_2 fraction increases. This highlights the importance of local fuel-air mixing, which is influenced by the flame lift-off height as well as potential changes in the NO formation mechanism. Therefore, Chapter 7 provides a more detailed investigation into the NO emission characteristics of the swirl-stabilized burner. To address the challenges related to limited fuel-air premixing and flame stabilization near the boundary layer, Chapter 8 evaluates the combustor performance using reduced fuel injector diameters, to increase the momentum flux ratio J_{swirl}. Based on the findings in Chapter 5, these configurations are expected to enhance mixing and thereby mitigate the aforementioned issues.

7

NO Emissions of swirl-stabilized CH_4/H_2 flames

One of the main challenges in fuel-flexible combustion systems is achieving low NO_x emissions while maintaining flashback-free operation, particularly for fuels with high hydrogen content. AAI, despite being an effective strategy to stabilize H_2 flames, significantly alters the flow field and can reduce the degree of fuel-air mixing, which in turn increases the NO formation due to locally high flame temperatures. Higher flame speeds, associated with increased hydrogen content, shift the flame position closer to the injector within the flow field. In a partially premixed configuration, this reduces the available mixing length, resulting in spots with higher local equivalence ratios compared to flames that stabilize further downstream. To effectively minimize NO emissions, it is therefore crucial to understand how both the fuel composition and the level of AAI influence NO emissions. This chapter investigates the NO emission characteristics of a partially premixed swirl-stabilized burner for different fuel compositions and different levels of AAI. The NO distribution within the combustion chamber is measured using NO-PLIF and validated against NO concentrations in the exhaust gas. These measurements are complemented by OH-PLIF, OH* chemiluminescence images and PIV measurements to provide detailed insights into the flame structure, flow field characteristics, and the link between flame location and NO formation.

Parts of this chapter have been published as **S.Link et. al.** Proceedings of the Combustion institute, 41, 2025, 10.1016/j.proci.2025.105964

7.1. INTRODUCTION

Chapter 6 successfully demonstrated the feasibility of flashback-free operation in a partially premixed swirl-stabilized set-up for flames up to 100 % H_2, when using AAI. However, NO emissions increase with increasing hydrogen content in the fuel, a trend not expected when looking at the theoretical adiabatic flame temperatures for the perfectly premixed case. As discussed in detail in Chapter 2, formation of NO_x is a complex mechanism involving multiple pathways, and it is highly influenced by the fuel composition and local flame temperatures. Therefore, a detailed investigation of the NO_x emission performance of the injector is essential to assess its suitability for fuel flexibility. Many studies have been carried out to experimentally examine the effect of H_2 enrichment on NO_x emissions in CH_4/H_2 swirl-stabilized flames. In fully premixed flames, studies have shown that adding hydrogen to the fuel can either increase or decrease NO_x emissions, depending on the swirl number. This happens despite an increase in adiabatic flame temperature for increasing hydrogen contents XH_2 [44, 105]. In partially premixed burners, such as the HYLON burner [108] and the SGT-700/800 Burner [102], increasing the hydrogen content in the fuel has been associated with an increase in NO_x emissions. The authors suggested that H_2 enrichment can result in locally elevated flame temperatures due to increased flame speeds for higher XH_2. These studies also highlighted the significant influence of geometrical features on NO_x emissions, attributing these differences to changes in fuel-oxidizer mixing [108]. For non-premixed swirl stabilized flames, it has been observed that NO_x emissions increase linearly up to 80 % hydrogen content in volume, and then decrease again when the volume flow rate of air and gas remain constant [181].

It should be pointed out that, although NO_x emissions are composed of NO and NO_2, for flame studies, NO_2 is often disregarded as it is typically produced via NO in post-combustion regions [104]. Furthermore, when present within a flame, NO_2 decomposes into NO due to the high temperatures. Therefore, many studies [106, 107, 182] consider only the NO formation mechanisms. Due to changes in flame characteristics, the temperature distribution within the flame is altered, resulting in different NO formation pathways for various fuel mixtures. For an approach at constant power, increasing hydrogen content up to $XH_2 = 0.6$ has been shown to increase the NO formation via the thermal, the NNH and the N_2O mechanism due to increasing flame temperatures and the increasing availability of H-radicals. The prompt NO pathway is almost unaffected, but slightly decreases due to the lack of CH_i radicals [107]. Chemical kinetics models have shown that, for perfectly premixed laminar flames at the same flame temperature and equivalence ratio (φ), achieved by dilution with an inert gas, the addition of H_2 decreases NO formation [106, 183]. This is explained by a weakening of the thermal NO pathway, presumably due to a decrease in O radical concentration. [106, 184].

Most experimental studies rely primarily on point-wise exhaust gas analysis to establish emission trends, which can be challenging given the various time scales and temperature sensitivity involved in NO formation. Laser-induced fluorescence (LIF) of the NO molecule can provide valuable insights into the spatial distribution of NO within the combustion chamber. This provides a deeper understanding of the causes behind varying emission levels in the exhaust for different fuel compositions and changing geometric features. This chapter investigates the NO emission characteristics of a fuel-flexible

combustor with a jet in cross-flow fuel injection. The combustor is designed to operate with fuel compositions ranging from 100 % CH_4 to 100 % H_2, using the concept of AAI [85]. Through exhaust gas analysis, OH & NO PLIF measurements, and PIV, the chapter investigates the relationship between the flow field, flame location, and emissions. Additionally, the chapter assesses the effects of varying hydrogen content and AAI on emissions.

This chapter is structured as follows: Section 7.2 presents an overview of the experimental setup and the measurement techniques. Section 7.3 first discusses the suitability of NO-PLIF to describe NO emission trends. After that, it evaluates the effect of H_2 enrichment and AAI on the NO emissions in the burner. Finally, Section 7.4 summarizes the most important findings of this chapter.

7.2. CONFIGURATION SPECIFICATIONS

GEOMETRY & OPERATING CONDITIONS

Experiments were performed in the TU Delft partially premixed swirl-stabilized burner. A schematic of the burner can be seen in Figure 7.1. Details on the design and the working principle are provided in Chapter 3. Experiments were performed with a swirl number of Sw = 1.1. Downstream of the swirler, fuel is injected into the swirling flow via a jet in cross-flow configuration through four injection ports, each with a diameter of d_{fuel} = 3.5 mm. The set-up operates with different fuel mixtures, ranging from 100 % CH_4 to 100 % H_2. The optically accessible quartz combustion chamber (diameter d_{cc} = 148 mm mm and length l_{cc} = 400 mm) is made from ilmasil® PN with a transmissivity of around 80 % at 226nm, which corresponds to the laser exciting wavelength for NO-PLIF.

Design points at P = 12 kW and $\dot{m}_{\text{air}} = 5.1 \times 10^{-3}$ kg/s							
Tag	XH_2	U_{MT} [m/s]	U_{fuel} [m/s]	φ	T_{ad} [K]	J_{swirl}	$\rho_{\text{react}}/\rho_{\text{prod}}$
A	0	10.45	9.92	0.75	1942	0.09	6.40
B	0.25	10.62	10.69	0.74	1930	0.09	6.33
C	0.4	10.75	12.76	0.73	1921	0.11	6.26
D	0.6	11.01	15.82	0.71	1908	0.12	6.13
E	0.8	11.44	20.96	0.68	1895	0.13	5.94
F	1	12.26	30.42	0.62	1858	0.12	5.60

Table 7.1: Operating conditions for the design points at constant air flow rate, H_2 fraction XH_2, the bulk velocity in the mixing tube U_{MT}, equivalence ratio φ, adiabatic flame temperature T_{ad}, momentum flux ratio J_{swirl} for Sw = 1.1 and thermal expansion ratio $\rho_{\text{react}}/\rho_{\text{prod}}$.

The mass flow rates for both fuel and air were controlled by Bronkhorst digital mass flow meters with an accuracy of ± 0.5 % RD plus ± 0.1 % FS. Experiments were performed at the reference point of P = 12 kW. For a constant air mass flow rate of $\dot{m}_{\text{air}} = 5.1 \times 10^{-3}$ kg/s, the combustor operates for 100 % CH_4 at φ = 0.75 (which corresponds to a total fuel flow $\dot{m}_{CH_4} = 2.2 \times 10^{-4}$ kg/s) and for 100 % H_2 at φ = 0.62 (corresponds to a fuel flow $\dot{m}_{H_2} = 1.0 \times 10^{-4}$ kg/s). The operating conditions are summarized in Table 7.1. The value for the momentum flux ratio J_{swirl} is calculated with Equation 2.22. The adiabatic

flame temperature and the thermal expansion ratio are calculated with CANTERA for a premixed freely propagating flame. However, it is worth noting that heat losses as well as non-perfect mixedness of the fuel and air are expected to generate local flame temperatures which differ from the adiabatic flame temperatures.

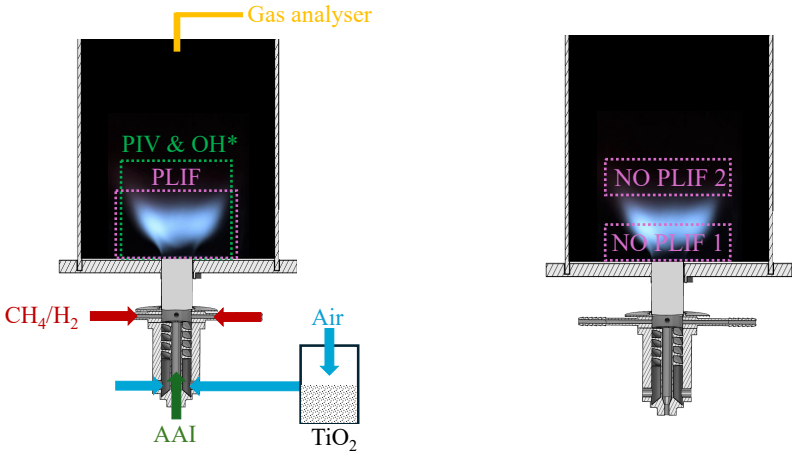

Figure 7.1: (a) Set-up with the measurement locations for the laser-based diagnostics, location of the probe for the gas analyser and the seeding location (b) NO-PLIF measurement locations.

7

MEASUREMENT TECHNIQUES

The PIV images where reused from Chapter 6, and not acquired separately. For completeness, a summary of the PIV setup is provided again in Table 7.2.

Laser	Nd:YAG Quantronix Darwin Duo 527-80-M
Camera	1 x LaVision Imager pro HS4M
Lens	180 mm
Sensor size	2016 × 2016 px
Final interrogation window	32 × 32 px, 50 % overlap
Spatial resolution	24.35 px/mm
Acquisition frequency	1 kHz
Seeding particles	TiO_2 ($d \approx 0.5$–$1\,\mu m$)
δt	37 µs

Table 7.2: Specifications PIV set-up.

The spatial distributions of the minor species OH and NO within the swirl-stabilised flame were obtained using planar-laser induced fluorescence (PLIF). The set-up specifications of the PLIF set-up can be found in Table 7.3. A detailed description of the camera and laser set-up as well as the selection of the excitation wavelength can be found in Section 3.2.4 in Chapter 3.

Pump Laser	Nd:YAG laser (Q-Smart 850 from Quantel)
Dye Laser	Sirah Cobra Stretch
Dye	Rhodamine 590 (OH), Coumarine (NO)
Camera	LaVision Imager M-lite 5M
Intensifier	IRO X, gate 100 ns, Gain - 55 % (OH), 85 % (NO)
Lens	85 mm
Filter OH	LaVision 1108760 VZ (75 % transmissivity at 308 nm)
Filter NO	LaVision 1108619 VZ (92 % transmissivity at > 250 nm)
Sensor size	1216× 1024 px
Spatial resolution	9.6 px/mm
Acquisition frequency	10 Hz
Excitation wavelength	OH = 283.55 nm - $Q_1(8)$, NO = 226.033 nm - $Q_2(20)$

Table 7.3: Specifications OH & NO-PLIF set-up

The scaling factor of the acquired images is around 0.11 mm/px for both species, providing a field of view (FoV) as shown in Figure 7.1a. For each operating condition and both species, 200 single-shot PLIF images were collected. For OH-PLIF, the laser sheet was mapped by introducing acetone into the combustion chamber, which absorbs light at the same wavelength as OH and emits light at a wavelength similar to that of CH. To image the sheet, the camera was equipped with a bandpass filter with a width of 15 nm and centred around 435 nm (LaVision 1108566 VZ-Image), with an average transmissivity of 40 %. For NO-PLIF, the laser sheet was corrected in vertical direction by estimating a uniform NO distribution in the ORZ, far away from the reaction zone. Since the Field of View (FoV) of the camera is much larger than the height of the laser, two separate locations within the FoV were mapped (see Figure 7.1b) by manually lifting the laser sheet and repeating the measurements. OH* chemiluminescence was recorded using the LaVision Imager in combination with the IRO X intensifier and an OH filter, as shown in Table 7.3. The exposure time was set to 8 ms and the acq settings for the intensifier were a gate time of 100 µs and a gain setting of 65 %.

NO exhaust gas emissions were measured in the exhaust with an ABB AO2000 gas analyser. To detect NO and O_2, the gas analyser is equipped with the modules Limas21 (HW) (NO and NO_2, accuracy 0.1 ppm) and Magnos 28 (O_2, accuracy 0.1 %vol). The NO emissions were averaged over a time span of at least 30 s, and then normalized by a volumetric fraction of 15 % O_2 in the flue gases. The measurement planes within the combustion chamber can be seen in Figure 7.1a.

7.3. RESULTS AND DISCUSSION

This section begins with a discussion on the interpretation of the NO-PLIF results. The section first explores how the spatial distribution of NO relates to other measurements, such as the flame front location within the flow field. This provides a reference framework for interpreting the results presented in the following sections. Furthermore, the section includes a comparison between the NO-PLIF signal and the NO emissions measured in the exhaust, to evaluate the suitability of NO-PLIF to predict the NO emis-

sions in the exhaust gas. As outlined in Chapter 3, the selected excitation wavelength (226.033 nm) yields a stronger signal intensity than other excitation wavelengths, but this comes at the cost of slightly higher temperature sensitivity. In the first part, the correlation between the integrated NO signal downstream of the flame and the NO concentration measured in the exhaust gas is analysed. Additionally, the relationship between NO levels in the ORZ and those in the exhaust is examined. In the second part, the influence of AAI on both the total NO emissions and their spatial distribution within the combustion chamber is evaluated. Lastly, it is investigated how varying the hydrogen mole fraction (XH_2) affects the NO distribution, considering both cases, with and without AAI.

7.3.1. INTERPRETATION OF THE PLIF RESULTS

To analyse the subsequent results, the procedure and interpretation of the different measurement techniques are discussed for a single representative case in this section (XH_2 = 0.6, χ = 20 %). The OH-PLIF signal, unlike OH* chemiluminescence, does not provide a direct visualization of the reaction zone, as the presence of OH radicals extends beyond the short duration of heat-releasing reactions. As a result, OH is also present in the high-temperature post-flame region, making it an unreliable marker for the exact flame location. However, flame fronts can still be estimated using OH-PLIF data. Previous studies have shown that regions with strong gradients in the OH-PLIF signal correspond to the reaction zone in premixed flames, enabling indirect identification of the flame front [185].

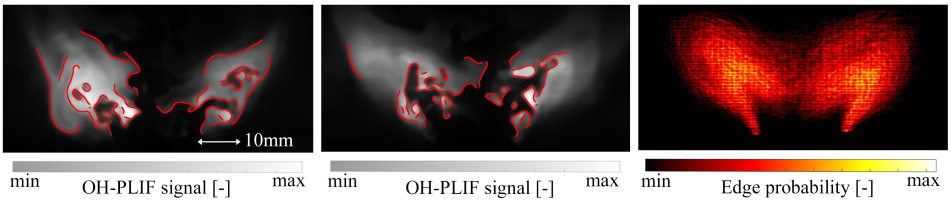

Figure 7.2: Instantaneous OH-PLIF images for XH_2 = 0.6, χ = 20 % (left and middle image). Edge detection by Canny edge detection algorithm (red lines). Edge probability (right image).

Figure 7.2 presents two instantaneous OH-PLIF images (left and middle). The gradients which exceed 17 % (number optimized based on trial and error) of the maximum gradient where identified using a Canny detection algorithm and are indicated in the figures by the red lines. Prior to edge detection, images were processed with [3 × 3] pixel binning and a median filter to reduce noise. Among the detected edges, only the upstream edge is representative of the instantaneous flame front. The downstream edge, although weaker, is occasionally detected by the algorithm in certain frames. However, the edge is not representative of the flame front, but is a result of the OH gradient in the post-flame region, where OH radicals are still present. The right side in Figure 7.2 shows the edge probability map, obtained by averaging the detected edges over all 200 individual frames. These edge lines were converted into a density distribution, providing a statistical representation of where edges are most likely to occur. Due to the highly

wrinkled and dynamic nature of the flame, the flame front in the edge probability map does not appear as a single line, but rather as a broad region of high edge probability.

Figure 7.3 presents, on the left side, the NO-PLIF signal overlaid with streamlines obtained from the PIV measurements. The right side shows the OH-PLIF distribution. Several reference lines are included in the left-hand image to facilitate the interpretation. The green dashed line indicates the contour of the OH-PLIF signal, while the purple dashed line shows the contour line of 20 % of the maximum of the OH* chemiluminescence signal, included for comparison. This value was chosen to suppress the background noises, and is in line with values previously reported in literature [186]. The blue dashed line connects the turning points of the streamlines, which mark the locations where the flow direction changes from predominantly radial to predominantly axial. In addition, the red line shows the approximate average flame front, derived from the gradient-based detection method described in Figure 7.2. Although the instantaneous flame front is highly unsteady and wrinkled, resulting in a broad region of high edge probability in the average image rather than a distinct line, it is shown here as a single averaged line for clarity. This line aligns well with the location of the OH* contour shown in the figure.

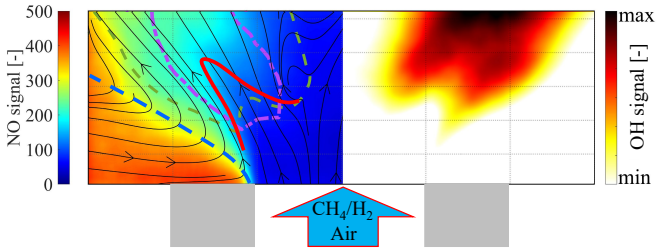

Figure 7.3: Case XH_2 = 0.6, χ = 20 %. Left side: NO-PLIF with superimposed streamlines from PIV, lines indicate: turning points of the streamlines (▪▪▪▪), OH* signal (▪ ▪), OHPLIF signal (▪▪▪▪), estimated flame front (▬). Right side OH-PLIF image.

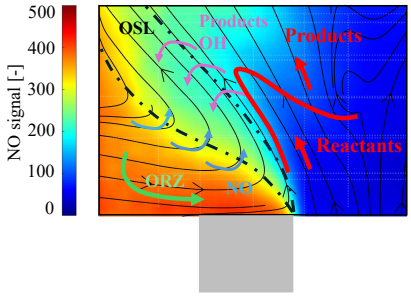

Figure 7.4: Case XH_2 = 0.6, χ = 20 %. NO-PLIF with superimposed streamlines from PIV, illustration of the mixing process in the OSL, located between the high velocity jet and the ORZ.

Discrepancies between the OH* and OH-PLIF contours are evident and expected. As previously mentioned, OH* emissions are present in the reaction zone, making it a

reliable indicator of heat release. In contrast, the OH-PLIF signal persists beyond the reaction zone due to the longer lifetime of OH radicals in high-temperature post-flame regions, resulting in a broader spatial distribution. Most of the NO appears downstream of the flame front, consistent with its formation as a slow-forming species when produced through the thermal NO pathway. Near the centreline, no NO signal is observed within the field of view. This is attributed to the absence of reaction along the centreline, as indicated by the OH-PLIF and OH* contour showing no signal in that region. The highest NO concentrations are observed in the ORZ, primarily because the flame stabilizes in the OSL, causing most of the NO to be recirculated into the ORZ. Furthermore, the recirculation of combustion products within the ORZ contributes to an accumulation of NO in this region. Interestingly, the regions with high NO-PLIF intensity extend radially up to the line which connects the turning points of the streamlines, the point where the direction of the streamline changes. Moving horizontally from these turning points toward the centreline, the NO signal gradually decreases, forming a gradient between the high NO levels in the CRZ and the lower NO concentrations characteristic of the reactant stream or the region just downstream of the reaction zone. This is likely caused by the OSL that forms between the swirling jet and the ORZ. As shown in Figure 7.4, which presents the NO distribution overlaid with streamlines for the case XH_2 = 0.6 and χ = 20 %, the shear layer promotes mixing between the ORZ gases and the incoming reactants or combustion products, particularly downstream of the flame front. Since thermal NO forms relatively slowly, a significant portion is expected to form outside the field of view, resulting in higher NO concentrations within the ORZ compared to the region immediately downstream of the flame. As those two regions mix in the OSL, the NO number density decreases radially from the ORZ toward the swirling jet centreline, resulting in a corresponding drop in LIF signal intensity. This mixing process also explains the presence of OH radicals at radial positions beyond the flame front, as OH is partially transported into the shear layer. In addition to mixing, NO can be removed in carbon-free fuels through reactions such as $HO_2 + NO \leftrightarrow NO_2 + OH$ and $NO + OH + M \leftrightarrow HONO + M$ [187]. Since OH is observed in regions with lower NO concentrations, it is likely that part of the NO is consumed through these reactions. However, since NO_2 could not be measured in the current analysis, the impact of the NO reburning mechanism cannot be estimated. Although the relative contribution of mixing versus NO removal by recombination to the NO distribution remains uncertain, this is not critical to the present analysis.

7.3.2. SUITABILITY OF NO-PLIF TO DESCRIBE NO EMISSION TRENDS

In order to assess the suitability of the NO-PLIF measurements to predict the measured NO emission in the exhaust, Figure 7.5a compares the measured NO concentration, normalized at 15 % O_2 in the exhaust with the integrated values of the NO-PLIF signal in the post-flame zone for different cases. For each case, the NO signal was horizontally integrated at the edge of the field of view of the camera (62 mm < y < 68 mm), located downstream of the flame zone, as indicated by the red box in the inset of Figure 7.5a. Since the NO distribution is largely uniform at this point, this location was chosen to correlate measured NO exhaust gas emissions with NO PLIF intensity. Additionally, the NO PLIF signal is expected to plateau in the final millimetres of the field of view as the curve of

the integrated NO signal flattens, a trend previously demonstrated in [182], where the NO signal sharply rises in the reaction zone before levelling off at a height of around 0.5 d_{CC}. Furthermore, it is important to consider the temperature dependence of the NO-PLIF signal. As noted in Section 3.2.4, the excitation wavelength used for NO-PLIF shows a temperature dependence of approximately 10 % within the expected temperature range of the combustor (1300–1800 %). As a result, regions with significantly different temperatures will exhibit deviations in NO-PLIF signals for the same NO number density. However, because the integration window for this comparison is limited to areas with similar temperature ranges, just downstream of the reaction zone, the temperature dependence is not expected to significantly influence the analysis.

Figure 7.5a shows a positive correlation between the measured NO values and the integrated NO-PLIF intensities for the investigated cases. These cases include variations in AAI, as well as cases with varying hydrogen content (XH_2) where AAI is held constant, either no AAI or 20 % AAI. Although the exact impact of heat loss on NO formation or consumption in this burner is difficult to quantify, the trends observed downstream of the reaction zone align with the measured NO values in the exhaust. The substantial heat losses associated with the quartz tube are expected to suppress thermal NO formation, which is the dominant yet slowest NO pathway [184], to negligible levels further downstream. Therefore, it is assumed that NO concentrations are comparably affected under all tested conditions. This supports the use of the NO-PLIF signal for a qualitative comparison of NO distributions across cases.

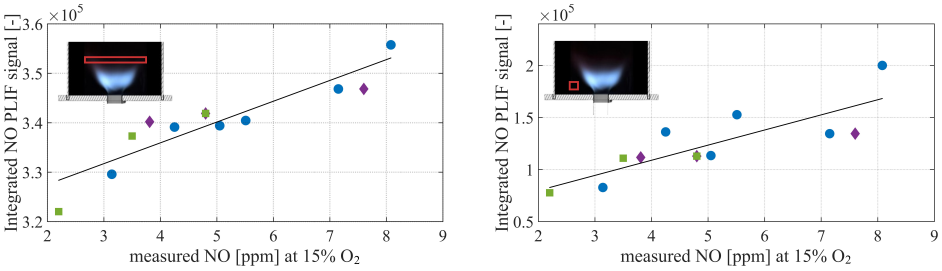

a) Integrated NO-PLIF signal downstream of the flame vs. measured NO values

b) Integrated NO-PLIF signal in ORZ vs. measured NO values

Figure 7.5: Integrated NO-PLIF signal at two different measurement locations for different scenarios (χ = 0 % & varying XH_2 (■), varying χ & XH_2 = 0.4 (◆) and χ = 20 % & varying XH_2 (●)) vs. measured NO values in the exhaust, in ppm at 15 ms O_2.

Figure 7.5b presents the integrated NO-PLIF signal within a defined integration window in the ORZ (as indicated in the figure inset) plotted against the measured NO emissions in the exhaust. While the temperature range is likely wider than in the region just downstream of the reaction zone due to significantly different stabilization mechanisms, the differences in the NO-PLIF signal within the ORZ across different cases significantly exceed 10 %, as shown in the following sections. Therefore, these differences cannot be attributed solely to temperature variations within the expected temperature range. This confirms that the NO-PLIF measurements are valid and reliably reflect variations in NO concentration.

Overall, a positive correlation is observed between the local NO-PLIF signal and the exhaust NO levels. However, the scatter around the trend line is significantly higher compared to Figure 7.5a, indicating that the NO concentration in the ORZ alone is not sufficient to reliably predict the total NO emissions in the exhaust. This discrepancy is likely due to the shift in relative contribution of NO formation in the CRZ with respect to the one in the ORZ, driven by the significant changes in the flow field when either the fuel composition or the level of AAI is varied. This aspect will be further discussed in the following sections. It is important to note that the NO-PLIF signal is influenced by collisional quenching with species such as N_2, O_2, H_2, and H_2O, which can be estimated using the approach described in [188]. Variations in fuel composition, equivalence ratio, and product species can therefore affect the NO-PLIF signal. However, due to the partially premixed nature of the flame, it is difficult to accurately determine the local composition of the mixture. As a result, collisional quenching effects are not accounted for in the present analysis, and the results are instead compared quantitatively based on the linear trends observed in Figure 7.5.

7.3.3. EFFECT OF AAI

In this section, the effect of AAI on the flame shape and NO formation is investigated. The burner is operated at the design point for $XH_2 = 0.4$ for three different levels of AAI (0, 10 and 20 %). Average OH-PLIF with superimposed streamlines are shown in Figure 7.6 to assess the flame stabilization mechanism and the OH distribution for varying levels of AAI. The OH signal rises sharply within the reaction zone and decreases exponentially in the post-flame zone, where initially elevated OH concentrations due to super-equilibrium gradually relax toward equilibrium. The OH-PLIF images show that with increasing levels of AAI, the flame lifts off from the injector. As previously discussed, this is due to an increase in centreline velocity due to AAI, which alters the flow field and leads to a noticeable shift in flame shape. At $\chi = 0$ %, the flame exhibits a classic V-shape, stabilized primarily in the inner shear layer [99]. When χ increases to 20 %, the flame transitions to an M-shape, with its centre pushed downstream while remaining attached to the injector rim in the outer shear layer [98]. The OH distribution within the flow field also changes significantly with increasing AAI. Without AAI, the OH concentration increases steeply in the CRZ, forming a narrow band of high intensity before declining. At $\chi = 10$ %, the maximum OH concentration is lower but more evenly distributed, with a more gradual increase and decrease downstream of the flame front. This suggests a lower temperature increase across the inner shear layer flame front compared to the $\chi = 0$ % case, likely resulting in fewer H radicals and a suppression of O/H chain-branching reactions. This is in line with a decrease in fuel-air mixing for increasing AAI observed in the previous chapters, which reduces the local equivalence ratio of the flame close to the centreline. Additionally, the lower and more distributed OH signal may result from the lifted flame being significantly more unsteady than the V-flame, due to a weaker recirculation zone.

As discussed in Chapter 5, AAI reduces the amount of fuel reaching the centreline of the swirling flow. Consequently, the flame burns leaner in the ISL and richer in the OSL as AAI increases. This is reflected in the change in flame shapes from a V-flame to an M-flame. While the flame is primarily stabilized in the ISL at $\chi = 0$ %, it stabilizes

predominantly in the OSL at $\chi = 20\,\%$. The absence of OH signal along the centreline at $\chi = 20\,\%$ supports the conclusion that the core mixture is below the lean flammability limit. In contrast, the presence of OH at $\chi = 10\,\%$ indicates that the mixture, though lean, remains within flammable limits.

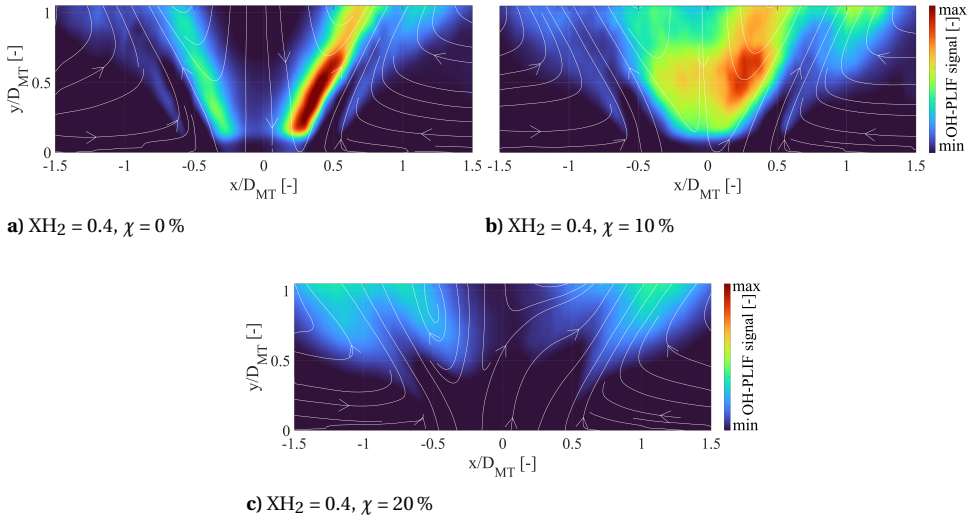

a) $XH_2 = 0.4$, $\chi = 0\,\%$ **b)** $XH_2 = 0.4$, $\chi = 10\,\%$

c) $XH_2 = 0.4$, $\chi = 20\,\%$

Figure 7.6: Average OH-PLIF images with superimposed streamlines obtained from PIV for $XH_2 = 0.4$ at different levels of χ.

Figure 7.7 presents the averaged NO PLIF signal, with superimposed streamlines (left) alongside the Abel deconvoluted OH* images (right) for $XH_2 = 0.4$ at varying levels of AAI. The OH* images are used for comparison since, as previously discussed, the OH PLIF signal is more spatially distributed than the actual reaction zone, making it less suitable for visualizing the flame shape. The NO PLIF images show that as AAI increases, the region of highest NO concentration shifts from a uniform distribution between CRZ and ORZ to most of the NO located in the ORZ. At $\chi = 0\,\%$, where the flame features a V-shape, the NO signal is evenly distributed between the CRZ and the ORZ. At $\chi = 10\,\%$, the OH* image shows the flame lifting off the injector. The NO distribution clearly highlights regions with absent or low NO signal corresponding to the reactant stream and the reaction zone, followed by a sharp increase in NO levels just downstream of the reaction zone. While NO is still present in the CRZ, its intensity is notably reduced compared to the $\chi = 0\,\%$ case, whereas the signal in the ORZ remains roughly constant. This indicates that although increasing the level of AAI decreases local fuel-air mixing, the additional distance between the injector and the flame allows more time for premixing, resulting in lower NO production in the CRZ. Additionally, increasing the level of AAI reduces the strength of the CRZ. This leads to a reduced residence time of the gases in the CRZ, which is expected to decrease thermal NO formation. At $\chi = 20\,\%$, the flame is clearly lifted and primarily stabilized in the OSL. With the stagnation point located outside the mixing tube, there is no NO signal close to the injector outlet. Instead, NO is observed

almost exclusively in the ORZ, with only a negligible amount remaining in the CRZ. This is attributed to flame being extinct near the centreline at this high level of AAI, previously discussed in Chapter 6, which suppresses NO formation close to the centreline. Additionally, the lower NO levels in the CRZ are partially due to a reduced axial velocity deficit along the centreline, decreasing residence times and thereby limiting thermal NO formation.

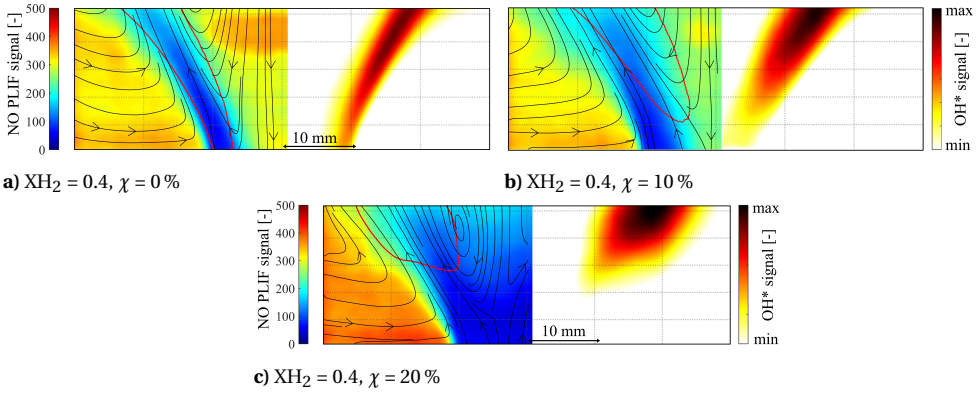

Figure 7.7: NO-PLIF signal with superimposed streamlines obtained from PIV (left side in each graph) and Abel deconvoluted OH* signal (right side) for XH_2 = 0.4 at different levels of χ.

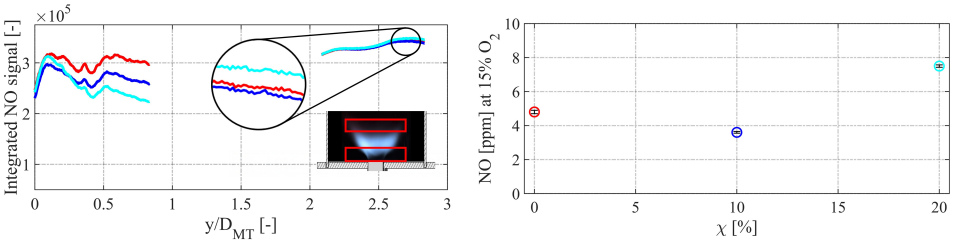

Figure 7.8: Left: Horizontally integrated NO-PLIF signal for XH_2 = 0.4 at different y/D_{MT}, inset shows the measurement locations with respect to the flame. χ = 0 % (—), χ = 10 % (—), χ = 20 % (—). Right: Corresponding measured NO exhaust values with error bars in ppm at 15 ms O_2.

In Figure 7.8 (left side) the horizontally integrated emissions are shown for the first and the last y/D_{MT} = 0.8 of the field of view of the camera. As mentioned earlier, due to the limited sheet height of only 30 mm, the laser sheet had to be raised in order to illuminate the last part of the FoV ($2.1 < y/D_{MT} < 2.9$). The inset shows the laser sheet planes with respect to the flame location. Notably, as it was evident from the quartz reflections, this adjustment of the laser sheet to capture the final millimetres resulted in a change of the intensity distribution in the sheet, which prevents direct quantitative comparison with the intensity of the signals in the upstream measurements. However, the trends

observed within each measurement window remain valid. Interestingly, between 0.5 < y/D_{MT} < 0.8 the case with no AAI shows the highest integrated NO emissions, while the case with χ = 20 % shows the lowest value. This appears despite the significantly higher NO concentration in the ORZ for the case with χ = 20 %. Further downstream, in the region 2.1 < y/D_{MT} < 2.8 at the end of the field of view, the trend aligns with the measured NO emissions in the exhaust shown in Figure 7.8 (right side). As AAI increases from χ = 0 % to 10 %, NO emissions initially decrease, then rise again for χ = 20 %, where they reach a maximum. Although AAI generally reduces mixing efficiency, the flame is lifted off the injector at χ = 10 %, creating additional length for fuel-air mixing upstream of the reaction zone. This is expected to create locally more premixed conditions and, consequently, lower NO emissions compared to the case with χ = 0 %. At χ = 20 %, the reduced mixing appears to be the dominant factor, leading to the highest NO emissions measured across all cases.

7.3.4. EFFECT OF HYDROGEN CONTENT

In this section, first the effect of hydrogen addition on NO distribution in flames without AAI is analysed. Chapter 6 showed that, in the absence of AAI, flashback occurs when the hydrogen content exceeds XH_2 = 0.4. This results in the absence of data for hydrogen content higher than XH_2 = 0.4. Figure 7.9 shows the change in NO distribution and the OH* chemiluminescence when increasing the hydrogen content in the fuel up to XH_2 = 0.4 at χ = 0 %. Across all cases without AAI, the overall flow structure remains largely unchanged, consistently exhibiting a CRZ. The OH* images reveal that the flame maintains a V-flame shape but shifts progressively closer to the injector as XH_2 increases, ultimately attaching to the injector for XH_2 = 0.4.

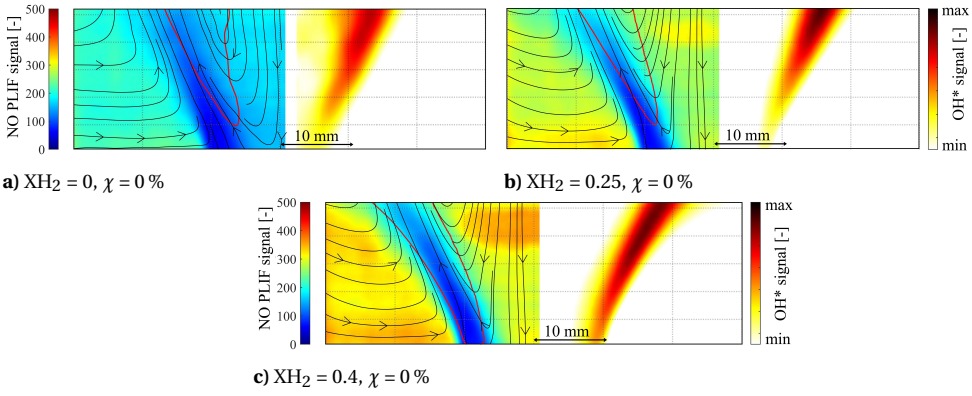

Figure 7.9: NO-PLIF signal with superimposed streamlines obtained from PIV (left side in each graph) and Abel deconvoluted OH* signal (right side) for different XH_2 at χ = 0 %.

The NO distribution is uniformly distributed between the CRZ and the ORZ, with a clear increase in NO intensity in both regions as the hydrogen content increases, leading to a higher integrated NO signal for higher hydrogen content, as shown in Figure 7.10

(left side). This trend continues throughout the field of view and is confirmed by measured NO emissions in the exhaust, as seen in Figure 7.10 (right side). This suggests that higher hydrogen content leads to more NO formation, despite similar adiabatic flame temperatures for the perfectly premixed cases (see Table 3.1 in Chapter 3).

For higher hydrogen content, the flame stabilizes more upstream, which is expected to result in locally richer flame conditions and consequently more NO formation through the thermal pathway. However, it is also assumed that NO formation pathway changes with increasing XH_2. As discussed in Chapter 2, increasing the hydrogen content in the CH_4/H_2 mixture at a constant adiabatic flame temperature significantly increases the NO formation rate through the NNH pathway [107], which has a significant contribution to the overall NO levels for fuels with high hydrogen content.

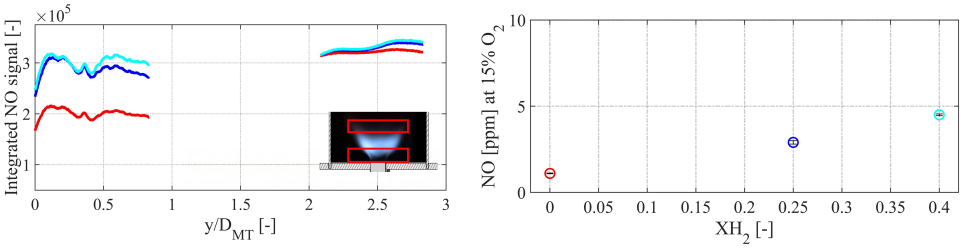

Figure 7.10: Left: Horizontally integrated NO-PLIF signal at $\chi = 0\,\%$ at different y/D_{MT}, inset shows the measurement locations with respect to the flame. $XH_2 = 0$ (—), $XH_2 = 0.25$ (—), $XH_2 = 0.4$ (—). Right: Corresponding measured NO exhaust values with error bars in ppm at 15 ms O_2.

Stabilization of the flame above $XH_2 = 0.6$ requires high levels of AAI, as lower AAI levels result in flashback. Figure 7.11 shows the average OH-PLIF images for different XH_2 at $\chi = 20\,\%$, with superimposed streamlines. It can be seen that for increasing XH_2, the flame front shifts closer to the injector outlet due to the higher flame speed and becomes notably shorter. The flame transitions from a M/Π flame for lower hydrogen contents to a Π-shape for $XH_2 = 1$, with attachment to the boundary layer of the mixing tube. Additionally, the intensity of the OH signal increases significantly with increasing XH_2, which is attributed to the higher concentration of hydrogen atoms in the fuel mixture and is consistent with the enhanced reactivity of hydrogen-rich flames [181]. In all cases, little to no OH is detected along the centreline of the combustion chamber. As the hydrogen content increases, the horizontal OH gradient decreases, suggesting that more fuel is burning near the centreline. As shown in Chapter 5, the higher diffusivity of hydrogen and lower density ratio enhance mixing in a jet in cross-flow configuration compared to higher-density fuels. Additionally, higher hydrogen content fuels have a lower lean extinction limit, allowing reaction to take place at leaner conditions.

Figure 7.12 shows the effect of increasing XH_2 at $\chi = 20\,\%$ on the NO and Abel deconvoluted OH* distribution. The NO concentration in the ORZ increases up to $XH_2 = 0.8$ but decreases again at $XH_2 = 1$. For $XH_2 > 0.4$, no NO is observed along the of the combustion chamber, likely due to the AAI jet suppressing reactions in this region, as confirmed by the OH-PLIF data, and the high velocity jet, which significantly reduces the residence time in the hot region. At $XH_2 = 0.4$, a small amount of NO appears along the centreline, possibly due to the presence of a CRZ which increases residence time in

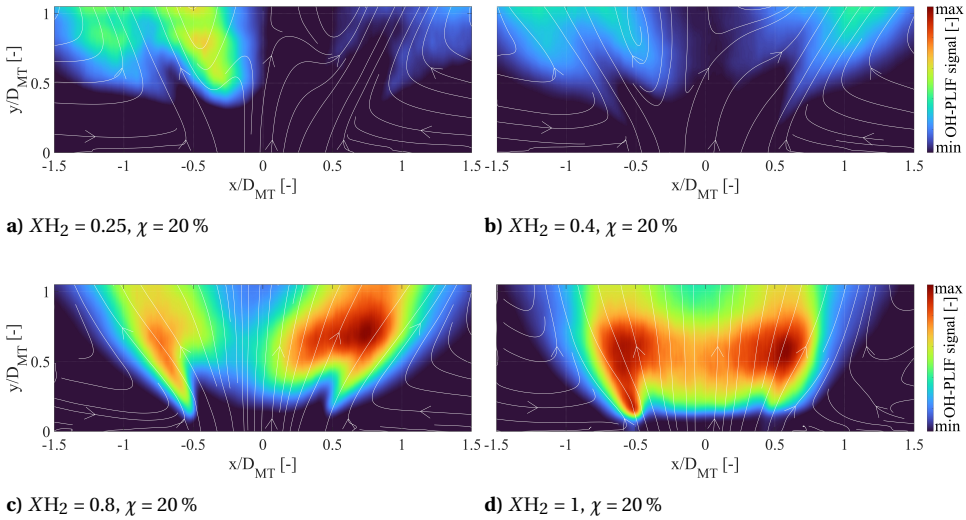

Figure 7.11: Average OH-PLIF images with superimposed streamlines obtained from PIV for different XH_2 at $\chi = 20\,\%$.

the high-temperature zone. Across all cases, most of the NO formation occurs significantly downstream of the OH* signal, indicating that NO is primarily produced via the thermal pathway, which dominates in the post-flame zone.

Figure 7.13 (left side) shows the integrated NO-PLIF signal at different positions in the field of view. Unlike the case at $\chi = 0\,\%$ (see Figure 7.10), no consistent trend between integrated NO-PLIF signal and XH_2 is observed. Additionally, the trends vary between the upstream and downstream integration windows. In the range $2.1 < y/D_{MT} < 2.8$, the highest NO signal is seen for $XH_2 = 0.8$, followed by $XH_2 = 0.4$. The case with $XH_2 = 1$ exhibits similar values to $XH_2 = 0.25$. This trend matches with the measured NO emissions in the exhaust (Figure 7.13 right side). In contrast, in the near-injector region ($0 < y/D_{MT} < 0.8$), the integrated NO signal for $XH_2 = 1$ is almost equal to that of $XH_2 = 0.8$ and significantly higher than for $XH_2 = 0.4$. This suggests that for $XH_2 = 1$, more NO is formed close to the injector outlet, while for $XH_2 = 0.4$, NO production primarily occurs further downstream. This trend is reflected in the spatial distributions shown in Figure 7.12, where higher NO concentrations appear just downstream of the flame front for $XH_2 = 1$ compared to $XH_2 = 0.4$. This is likely due to the upstream shift of the flame front at higher hydrogen contents, which alters the location of heat release and thereby the location of NO formation. Additionally, as suggested by Wang et al. [107], hydrogen-rich flames promote NO formation via the NNH mechanism within the reaction zone, leading to elevated NO levels closer to the flame front compared to cases dominated by the slower thermal NO pathway. When methane is present in the fuel (e.g., $XH_2 = 0.8$), prompt NO formation near the injector becomes more pronounced due to lower levels of premixing. This is supported by the NO concentration observed just downstream of the flame front in this case. As XH_2 increases, the upstream flame front shifts closer to the injector, modifying the heat release location and thereby affecting downstream NO

production.

In summary, the observed non-linear trend in NO production, with peaks at XH_2 = 0.8 and XH_2 = 0.4, is driven by shifts in NO formation pathways, changes in flame location, and differences in fuel-oxidizer mixing prior to combustion.

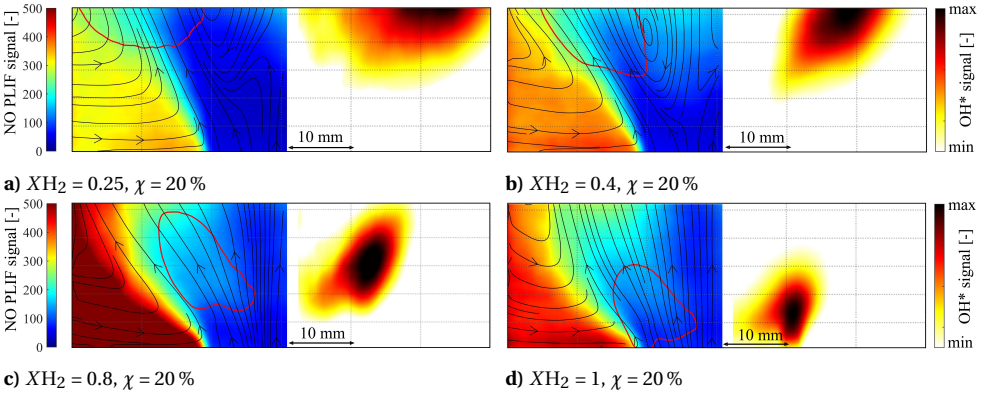

Figure 7.12: NO-PLIF signal with superimposed streamlines obtained from PIV (left side in each graph) and Abel deconvoluted OH* signal (right side) for different XH_2 at χ = 20 %.

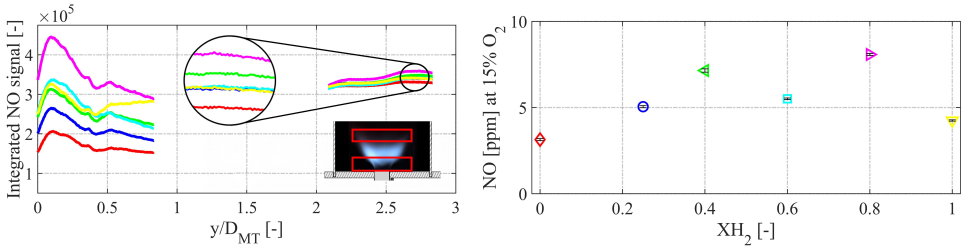

Figure 7.13: Left: Horizontally integrated NO-PLIF signal at different y/D_{MT}, inset shows the measurement locations with respect to the flame. XH_2 = 0 (—), XH_2 (—), XH_2 = 0.4 (—), XH_2 = 0.6 (—), XH_2 = 0.8 (—), XH_2 = 1 (—). Right: Corresponding measured NO exhaust values with error bars in ppm at 15 ms O_2.

7.4. CONCLUSIONS

This chapter examined the NO emission characteristics of a partially premixed swirl-stabilized dual-fuel CH_4/H_2 combustor. Flame stabilization was achieved through injecting axial air (AAI). The chapter analyses the impact of varying AAI level and hydrogen fraction (XH_2) on NO emissions. Exhaust gas measurements of NO were combined with NO-PLIF imaging to investigate the correlation between NO emissions in the exhaust and its spatial distribution within the flame. Complementary OH-PLIF and PIV measurements provided further insights into NO distribution and the flame location with respect to the flow field. The analysis demonstrated that introducing AAI significantly

alters the NO distribution within combustion chamber. In the absence of AAI, where the flow field exhibits a CRZ, NO is evenly distributed between CRZ and ORZ. However, at high levels of AAI, a substantially higher amount of NO can be found in the ORZ. This is attributed to a decrease in mixing quality, which allows the flame to stabilize in the OSL at conditions above the nominal φ.

Without AAI, increasing the $X\mathrm{H}_2$ in the fuel up to $X\mathrm{H}_2 = 0.4$ leads to higher NO emissions. This trend is likely caused by the flame stabilizing further upstream at higher $X\mathrm{H}_2$, which reduces local fuel-air mixing, leading to a less uniform equivalence ratio distribution and consequently locally high temperatures. For the cases with $\chi = 20\,\%$, no linear trend is observed between $X\mathrm{H}_2$ and NO emissions. When hydrogen content in the fuel is increased, the flow field transitions from the one featuring a CRZ to resembling the one of a low swirl flame. This is expected to influence residence time in the high-temperature regions, thus limiting the time available for thermal NO production. Moreover, as previously mentioned, the fuel composition influences the flame lift-off height, which in turn affects local fuel-air mixing and consequently the flame temperature distribution.Together with the anticipated changes in NO formation pathways with increasing $X\mathrm{H}_2$, it is expected that the change in produced NO emissions is the result of a complex interplay between mixing, change in flame temperatures, and a change in NO formation mechanism. The main finding of this can be summarized as follows

- Axial air injection increases the overall NO emissions by decreasing mixing. This changes the flame shape to a flame stabilized in the OSL, which promotes long residence times of products in the ORZ
- In cases without AAI, increasing $X\mathrm{H}_2$ leads to an increase in overall NO emissions, since the flame shifts upstream for increasing $X\mathrm{H}_2$, which decreases the local fuel-air mixing and consequently affects local flame temperatures.
- For cases with high levels of AAI ($\chi = 20\,\%$), the NO emissions are expected to be an interplay between local fuel-air mixing and NO formation pathway, which is non-trivial to predict.

Overall, the results indicate that the degree of mixing alone does not directly correlate with NO emissions. While it can serve as a useful indicator when the fuel composition is kept constant, flame location plays a critical role in determining where and how much NO forms. Changes in flame position affect the local fuel-air mixing at which the flame stabilizes, which may deviate significantly from the predicted overall mixing quality. Moreover, changes in the dominant NO formation pathways must be taken into account. Although local fuel-air mixing provides insight into thermal NO production, variations in the underlying mechanisms can substantially influence the relative contributions of different pathways. A comprehensive assessment of these effects would require detailed kinetic modelling, which is beyond the scope of this thesis.

Nonetheless, the findings suggest that enhancing fuel-air mixing, particularly at high levels of AAI, offers potential for reducing NO emissions. This hypothesis will be further examined in the following chapter.

8

EFFECT OF MOMENTUM FLUX RATIO ON COMBUSTOR PERFORMANCE

Effective fuel-air mixing is essential for reducing NO_x emissions by creating a more uniform equivalence ratio distribution, thereby limiting thermal NO_x formation. As demonstrated in Chapter 5, increasing the momentum flux ratio J_{swirl} notably improves fuel-air mixing in the investigated swirl-stabilized configuration with jet in cross-flow fuel injection. This improvement is directly connected to the flow field changes induced by J_{swirl}, including modifications to velocity profiles and turbulence intensity, as detailed in Chapter 4. Changes in both fuel-air mixing and flow field can influence flame stabilization within the combustor. This chapter investigates the impact of varying J_{swirl} on NO emissions and flame stability across different CH_4/H_2 mixtures in the already introduced partially premixed, swirl-stabilized combustor. To gain a comprehensive understanding of the emissions, NO-PLIF measurements are employed to map the spatial distribution of NO, complemented by exhaust gas analysis to accurately quantify NO levels across various operating conditions. Furthermore, OH-PLIF and OH* chemiluminescence imaging are employed to investigate flame structure, lift-off height, and stabilization behaviour. Together, these diagnostic techniques offer complementary insights into the relationship between flame topology and NO emissions across various fuel compositions.

8.1. INTRODUCTION

NO emissions in the examined burner geometry are strongly influenced by both the fuel composition and the level of AAI, as demonstrated in Chapter 7. This is partly attributed to variations in fuel-air mixing, as explored in the mixing study in Chapter 5. A greater fraction of H_2 in the fuel mixture initially improves fuel-air mixing; however, increased levels of AAI are required to achieve stable combustion. These increased AAI levels significantly reduce mixing, causing the mixture in the core of the swirling flow to become significantly leaner than the nominal equivalence ratio. This leads to a higher amount of fuel accumulating near the mixing tube wall compared to cases without AAI, resulting in a different flame stabilization mechanism, the formation of locally richer zones, and consequently higher NO emissions. Maughan et al. [189] investigated how the initial distribution of gaseous fuel in the injection plane and the length of the premixing section affect NO_x emissions. Their results indicate that NO_x emissions decreases with longer premixing lengths and increased turbulence intensity. Additionally, optimizing the fuel distribution at the upstream end of the premixing section reduces the requirements for the subsequent mixing process. Zajadatz et al. [190] found a strong correlation between the spatial unmixedness, measured using LIF in a water test rig representative of the burner, and the NO_x emissions observed in the reacting conditions at atmospheric conditions. This finding was further supported by Lacerelle et al. [191], who observed that unmixedness values obtained in cold-flow investigations correlated well with NOx emissions in the corresponding reacting cases. However, other studies have concluded that spatial unmixedness alone is insufficient to explain NO_x emissions, as temporal unmixedness (i.e., temporal concentration fluctuations) also plays a significant role in increasing emissions [48]. According to the authors, if both the spatial and temporal unmixedness, defined as time-dependent variation in the composition or concentration of species are known prior to combustion, NO_x trends can be predicted.

Incomplete fuel-air mixing has been shown to reduce flame stability by increasing the lean blowout limit and risk of combustion oscillations, thereby narrowing the stable operating range [192]. However, other studies have found no direct correlation between changes to the temporal unmixedness parameter, and the flame instabilities observed under reacting conditions [191].

When a fuel jet is injected into the air in cross-flow configuration, the momentum flux ratio J between fuel and the cross-flow has been identified as the key parameter governing mixing behaviour [69]. As demonstrated in Chapter 5, this also holds for swirling cross-flows, where increasing J_{swirl} leads to reduced unmixedness across various fuel compositions. A logical step forward is to modify the fuel injection strategy by adjusting the fuel inlet diameter of the combustor investigated in Chapter 6 and Chapter 7. This chapter investigates how decreasing J_{swirl} affects NO emissions and flame stability in the TU Delft swirl stabilized burner. A change in J_{swirl} has a significant impact on the mixing quality and the flow field, thereby affecting the flame position and NO emissions. The chapter is structured as follows: Section 8.2 describes the experimental set-up and the measurement techniques. Section 8.3 presents the results of the experiments, including the effect of J_{swirl} on the flame stabilization, operational range and NO emissions. Finally, Section 8.4 summarizes the main findings and conclusions of this chapter.

8.2. CONFIGURATION SPECIFICATIONS

GEOMETRY & OPERATING CONDITIONS

The experiments were performed in the TU Delft swirl-stabilized burner. For a detailed description of the set-up description the reader is referred back to Section 3.1.1. Experiments were performed with a swirl number of $Sw = 1.1$. Measurements were taken for different fuel compositions at a constant air flow rate of $\dot{m}_{air} = 5.1 \times 10^{-3}$ kg/s. All measurements were performed for the design point of $P = 12$ kW. The operating conditions are summarized in Table 8.1. To investigate the effect of the momentum flux ratio, the fuel inlet diameter was varied between 2 mm and 3.5 mm, which results in values for the momentum flux ratio J_{high} and J_{low} in Table 8.1, respectively. The selected diameters were based on the baseline case of $d_{fuel} = 3.5$ mm and the second-largest diameter d_{fuel} listed in Table 3.2. Due to manufacturing tolerances, a diameter of $d_{fuel} = 2$ mm was the closest achievable to the $d_{fuel} = 1.96$ mm used in the non-reacting studies. Although a diameter of $d_{fuel} = 1.6$ mm was also considered, it was excluded from testing because the 2 mm case already significantly restricted the operational range, as discussed in the results chapter. The choice of $d_{fuel} = 2$ mm leads to lower J_{swirl} values compared to those investigated in Chapter 5, but still increases the momentum flux ratio by approximately an order of magnitude relative to the baseline case. Figure 8.1 shows the schematic of the experimental set-up with the locations of the different measurement techniques.

Design points at $P = 12$ kW and $\dot{m}_{air} = 5.1 \times 10^{-3}$ kg/s							
Tag	XH_2	φ	J_{low}	U_{J-low} [m/s]	J_{high}	U_{J-high} [m/s]	T_{ad} [K]
A	0	0.75	0.09	9.92	0.80	28.20	1942
B	0.25	0.74	0.09	10.69	0.89	32.76	1930
C	0.4	0.73	0.11	12.76	0.99	39.10	1921
D	0.6	0.71	0.12	15.82	1.12	48.47	1908
E	0.8	0.68	0.13	20.96	1.22	63.73	1895
F	1	0.62	0.12	30.42	1.10	93.17	1858

Table 8.1: Operating conditions for the design points at constant air flow rate, H_2 fraction XH_2, equivalence ratio φ, adiabatic flame temperature T_{ad}, momentum flux ratios J_{swirl} for $Sw = 1.1$ and the corresponding velocities in the fuel nozzles U_{fuel}.

MEASUREMENT TECHNIQUES

The spatial distributions of the minor species OH and NO within the swirl-stabilized flame were measured using PLIF. The specifications of the PLIF set-up are provided in Table 8.2.

For each operating condition and both species, 200 single-shot PLIF images were acquired. For OH-PLIF, the laser sheet was characterized by introducing acetone into the combustion chamber, as acetone absorbs at the same wavelength as OH and fluoresces at a wavelength similar to that of CH. To image the sheet, the camera was equipped with a bandpass filter with a width of 15 nm and centred around 435 nm (LaVision 1108566 VZ-Image), with an average transmissivity of 40 %. The changes in laser sheet intensity were

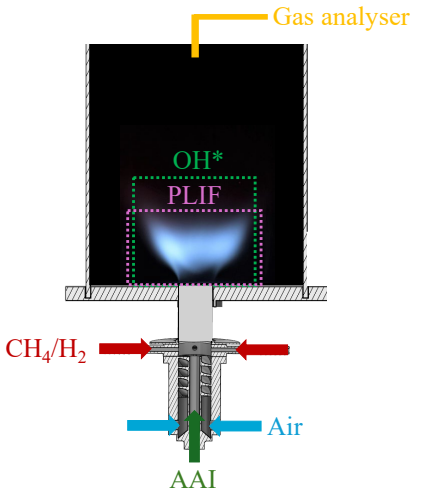

Figure 8.1: Set-up with the measurement locations for the laser-based diagnostics and location of the probe for the gas analyser.

corrected using the Davis flat field function. However, variations in pump laser power at different measurement points caused fluctuations in both the intensity and profile of the laser sheet. Since only one laser sheet image was available for correction, these fluctuations introduced artifacts in some of the corrected OH-PLIF images. Nevertheless, since the OH-PLIF images are primarily used to identify flame stabilization mechanisms and the location of OH-rich regions, the image quality is considered adequate for these purposes. For NO-PLIF, the laser sheet was corrected in the vertical direction by assuming a uniform NO distribution in the ORZ, far from the reaction zone. OH* chemiluminescence was recorded using the LaVision Imager in combination with the IRO X intensifier and an OH filter, as detailed in Table 8.2. The acquisition parameters were a gate time of 100 µs and a gain setting of 65 %.

NO exhaust gas emissions were measured with an ABB AO2000 gas analyser at 3 Hz. The NO emissions were averaged over a time span of at least 30 s, and then normalized by a volumetric fraction of 15 % O_2 in the flue gases. The measurement locations can be seen in Figure 8.1.

8.3. RESULTS

In Chapter 5, the fuel-air mixing behaviour for different values of J_{swirl} was investigated. It was concluded that increasing J_{swirl} enhances the degree of mixing at the outlet of the mixing tube. This improved mixing is expected to reduce NO emissions, as it helps to avoid the formation of local hot spots. Moreover, variations in fuel-air mixing are anticipated to affect flame stabilization: with increased J_{swirl}, more fuel tends to reach in the core of the swirling flow, leading to flame stabilization under locally richer conditions in the ISL compared to cases with lower J_{swirl}. Overall, since the hydrogen content has a stronger influence on the degree of mixing than J_{swirl} in the investigated cases, the effect

Pump Laser	Nd:YAG laser (Q-Smart 850 from Quantel)
Dye Laser	Sirah Cobra Stretch
Dye	Rhodamine 590 (OH), Coumarine 2 (NO)
Camera	LaVision Imager M-lite 5M
Intensifier	IRO X, gate 100 ns, Gain - 60 % (OH), 80 % (NO)
Lens	85 mm
Filter OH	LaVision 1108760 VZ (75 % transmissivity at 308 nm)
Filter NO	LaVision 1108619 VZ (92 % transmissivity at > 250 nm)
Sensor size	1216× 1024 px
Spatial resolution	11.1 px/mm
Acquisition frequency	10 Hz
Excitation wavelength	OH = 283.55 nm - $Q_1(8)$, NO = 226.033 nm - $Q_2(20)$

Table 8.2: Specifications OH & NO-PLIF set-up.

of J_{swirl} on NO emissions is expected to be less significant at higher hydrogen contents and more pronounced at lower hydrogen contents. Furthermore, as shown in Chapter 5, at the highest investigated value of J_{swirl} for the surrogate case $XH_2 = 1$, the core of the swirling flow was found to be slightly richer than the outer regions of the mixing tube. This stratification is expected to significantly affect flame stabilization and may also influence the stability limits of the combustor. In Chapter 4, it was shown that changes in J_{swirl} affect the non-reacting flow field. An increase in J_{swirl} leads to a larger opening angle of the swirling jets. This effect is observed across all levels of AAI, but becomes more pronounced as AAI increases. Moreover, the effect becomes more significant with increasing hydrogen content. The resulting changes in the flow field are expected to influence flame shape and potentially the stabilization location. These hypotheses will be examined and discussed in the following sections.

The results chapter begins by examining the effect of the momentum flux ratio J_{swirl} on flame stabilization. This includes identifying the stabilization mechanism by determining which flame type occurs, using both instantaneous and time-averaged OH-PLIF images. Additionally, the lift-off height of the flame relative to the injector is presented, to evaluate the effect on the operational range. The second part of the chapter explores how J_{swirl} impacts NO emissions. This analysis is based on emission measurements taken at the combustion chamber outlet for two different levels of J_{swirl} and fuel compositions. Through NO-PLIF imaging, the spatial distribution of NO is correlated with the flame position indicated by OH* chemiluminescence. Changes in overall NO emissions are then linked to shifts in flame location and the associated NO distribution.

8.3.1. EFFECT OF MOMENTUM FLUX RATIO J_{swirl} ON THE FLAME STABILIZATION

This section discusses the influence of J_{swirl} on the averaged OH distribution. Figure 8.2 presents the average OH-PLIF images for the two different momentum flux ratios J_{swirl}, at $XH_2 = 0.25$ and $\chi = 0\,\%$. In both cases, the flames exhibit similar stabilization behaviour, with the flame anchored in the ISL near the outlet of the mixing tube and the

flame tips predominantly oriented toward the combustor outlet. The configuration with J_{high} shows less OH concentration in the OSL, resulting in a flame shape more characteristic of a lifted M-flame. In contrast, for J_{low} the flame appears to protrude slightly more into the OSL, giving it a shape more characteristic of an attached M-flame. This shift in flame structure is likely related to differences in fuel-air mixing, where more fuel is located close to the mixing tube wall for the lower level of J_{swirl}. Additionally, the areas of high OH signal for J_{high} show an increased opening angle of around 40°, compared to 25° for the case with J_{low}. Since the flame stabilizes predominantly in the ISL, it adopts a shape that reflects the opening angle of the swirling jets. This observation aligns with the findings from Chapter 4, where higher values of J_{swirl} were associated with a broader opening angle of the high-velocity swirling jets within the combustion chamber. However, because only a slight change in opening angle is observed in the non-reacting (a decrease of the opening angle from 24° to 31° when J_{swirl} is increased from 0.1 to 3.5) compared to that of the flame, it is expected that the presence of heat release significantly amplifies this effect.

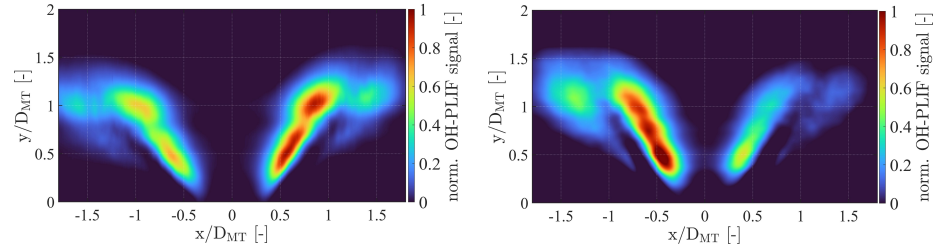

Figure 8.2: Average OH-PLIF images for two different momentum flux ratios J_{swirl} at $XH_2 = 0.25$, $\chi = 0\,\%$.

Figure 8.3 and Figure 8.4 show the average OH-PLIF images for the two different momentum flux ratios J_{swirl} for $XH_2 = 0.6$ and $XH_2 = 0.8$ at $\chi = 20\,\%$. For both J_{swirl}, the flames adopt an M/Π-flame shape as discussed in Chapter 6, characterized by a flame front that is lifted off the injector along the centreline and protrudes into the OSL without attachment to the injector rim. The stabilization location in the OSL is not significantly affected by a change in J_{swirl}. However, the flame with J_{high} stabilizes significantly closer to the baseplate of the combustion chamber within the ISL, especially for the case $XH_2 = 0.6$, as indicated by the red arrows in Figure 8.3. For $XH_2 = 0.8$ the change in stabilization location is less significant, but still present. This upstream shift of the flame centre is expected, as a higher level of J_{swirl} promotes better fuel-air mixing. As a result, more fuel reaches the core of the swirling flow, leading to a more uniform equivalence ratio distribution and a locally richer mixture in the core compared to configurations with lower J_{swirl}. Because more fuel reaches the centre of the flow, the mixture in the ISL becomes richer and consequently exhibits a higher flame speed, which promotes flame stabilization in the ISL closer to the injector. Similar to the observation in Figure 8.2, but more pronounced, the opening angle of the flame lobes is also larger for J_{high}. As previously discussed in Chapter 4, J_{swirl} has a strong influence on the non-reacting flow field, particularly in configurations with AAI. Generally, it was observed that an increase in J_{swirl}

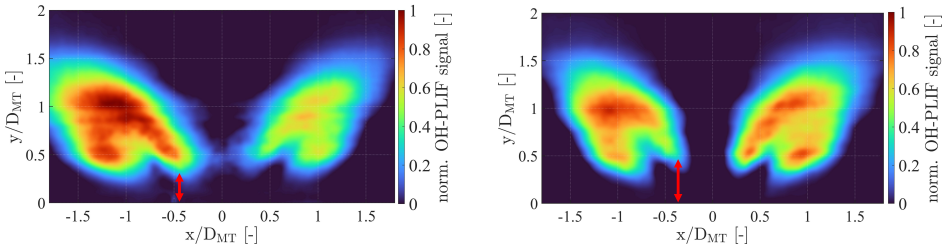

a) J_{high} **b)** J_{low}

Figure 8.3: Average OH-PLIF images for two different momentum flux ratios J_{swirl} at $XH_2 = 0.6$ and $\chi = 20\,\%$.

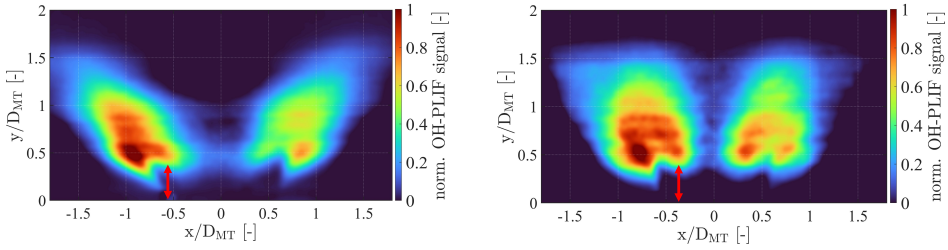

a) J_{high} **b)** J_{low}

Figure 8.4: Average OH-PLIF images for two different momentum flux ratios J_{swirl} at $XH_2 = 0.8$ and $\chi = 20\,\%$.

increases the transverse velocity component, which is reflected in a wider opening angle of the swirling flow. This is in line with the wider opening angle of the flame. This effect is even more pronounced for the case XH_2 =0.8, which is also consistent with the findings in Chapter 4, where the flow field of the case with higher hydrogen content is more affected by the level of J_{swirl} compared to lower hydrogen content fuels.

Figure 8.5 presents instantaneous OH-PLIF images for the two different momentum flux ratios J_{swirl} at $XH_2 = 0.6$ and $\chi = 20\,\%$. This allows for a closer assessment of the OH distribution on the centreline, which might not be clearly visible in the average OH image. Notably, differences in OH intensity near the centreline are evident, as highlighted by the red arrows in the figures. For the higher J_{swirl}, at $x/D_{\text{MT}} = 0$, all instantaneous images display a significantly stronger OH signal along the centreline compared to the cases with lower J_{swirl}, where the OH signal is near zero. The positive gradient of OH signal along the centreline indicates heat release in this region. As already discussed in Chapter 7, for J_{low} and $\chi = 20\,\%$, no reaction is observed along the centreline, evidenced the lack of OH radicals in this region. This is attributed to a fuel-lean core of the swirling flow, which, according to the mixing study in Chapter 5, locally drives the mixture below the lean flammability limit, especially for cases with high levels of AAI. The increased OH concentration along the centreline at higher J_{swirl} is consistent with the expected improvement in mixing as the momentum flux ratio increases, as shown in Chapter 5. Nonetheless, certain instantaneous frames reveal pockets near the centreline with little or no OH concentration. Where OH is detected, its intensity is generally lower than in the

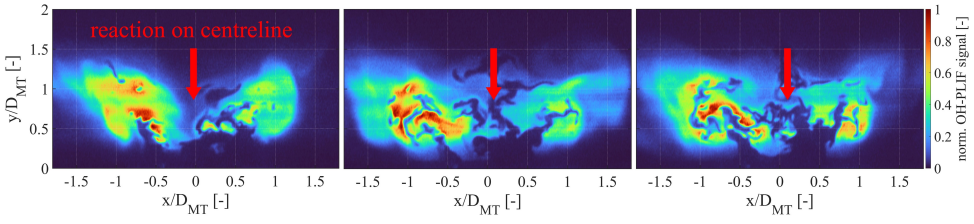

a) J_{high}

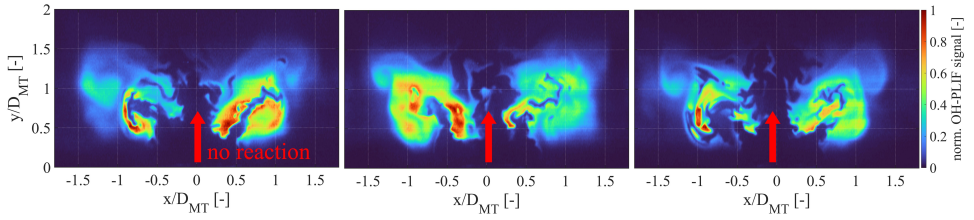

b) J_{low}

Figure 8.5: Instantaneous OH-PLIF images for two different momentum flux ratios J_{swirl} at XH_2 = 0.6, χ = 20 %.

outer flame branches, suggesting reduced heat release along the centreline compared to the OSL. Although higher J_{swirl} values increase the local equivalence ratio along the centreline, fuel stratification remains, leading to leaner conditions there than near the outer periphery of the mixing tube.

8.3.2. EFFECT OF MOMENTUM FLUX RATIO J_{swirl} ON THE OPERATIONAL RANGE

The effect of varying J_{swirl} on the operational range, which is defined as the range of stable operation without flashback or blowout, is assessed based on the flame lift-off height. Figure 8.6 presents the lift-off heights for the two momentum flux ratios J_{swirl} and hydrogen volume fractions at χ = 20 %. The lift-off height is defined as the distance

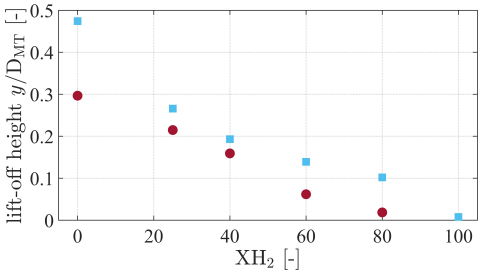

Figure 8.6: Lift-off height of the flames in y/D_{MT} for two different momentum flux ratios J_{swirl} (● - J_{high} and ■ - J_{low}) for different XH_2 at χ = 20 %.

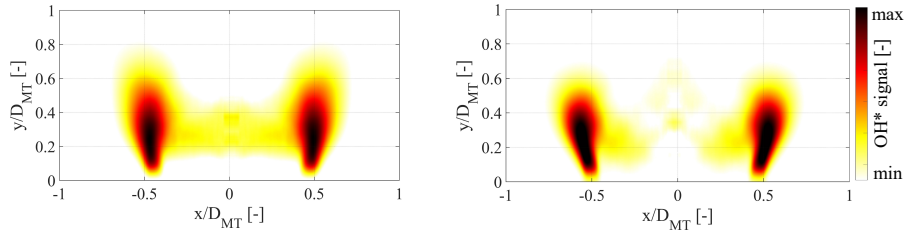

a) J_{high} at $\chi = 25\,\%$ **b)** J_{low} at $\chi = 20\,\%$

Figure 8.7: OH* images for $XH_2 = 1$ for (a) J_{high} at $\chi = 25\,\%$ and (b) J_{low} at $\chi = 20\,\%$.

from the mixing tube outlet to the nearest point of the flame. The flame front is identified from Abel-deconvoluted OH* images, where it is assumed to correspond to 20 % of the maximum OH* signal. As shown in the figure, the lift-off height decreases with increasing XH_2 for both J_{swirl}, which is expected due to the higher laminar flame speeds of hydrogen-rich mixtures. Additionally, for all tested conditions, the case with higher J_{swirl} leads to a lower lift-off height. At $XH_2 = 1$, stable flame operation was only achieved with the lower J_{swirl}; with the higher J_{swirl}, the flame consistently stabilized upstream of the mixing tube outlet, which is considered flashback. As shown in Chapter 5, an increase in J_{swirl} results in a more uniform fuel distribution within the mixing tube. Thus, the core of the swirling flow is richer compared to the cases with lower J_{swirl}. This interpretation aligns with previous observations at lower hydrogen contents (see Figure 8.3), where the flame moves closer to the injector near the centreline of the mixing tube as J_{swirl} decreases. For the case with $XH_2 = 1$, assuming $u_{rms} = 0.2\times\ u_{\text{bulk}} = 2.4\,\text{m/s}$ and a worst-case laminar flame speed for H_2 flames of $s_l = 2.5\,\text{m/s}$, the resulting ratio $s_l/u_{rms} = 2.1$ remains below the critical flashback threshold of 5 in the core flow, as defined in Equation 2.23. This excludes flashback through the core flow as the responsible mechanism. It is possible that the flame, which stabilizes closer to the mixing tube outlet, undergoes flashback via the CIVB mechanism. As more fuel reaches the centreline, resulting in increased heat release, greater negative azimuthal vorticity is generated. This can induce negative axial velocities, potentially leading to flashback, as described in Section 2.5.1. Alternatively, as observed in the lower hydrogen content cases (e.g. Figure 8.3), the flame may still stabilize in the OSL near the outlet. Changes in boundary layer velocity profiles could also contribute to flashback. However, due to the lack of time-resolved measurements, a detailed analysis of the mechanism responsible for flashback cannot be performed.

Figure 8.7 shows OH* images for $XH_2 = 1$ at both J_{swirl}. For J_{high}, flame stabilization required AAI levels as high as $\chi = 25\,\%$. The image shows that under these conditions, the flame for J_{high} with $\chi = 25\,\%$ (Figure 8.7a) closely resembles the flame at $\chi = 20\,\%$ for J_{low} (Figure 8.7b). Both flames stabilize attached to the injector, with the central region of the flame lifted off or showing no reaction along the centreline, resembling the Π-flame structure described in Chapter 6. Stabilizing a 100 % H_2 flame with a higher level of J_{swirl} requires higher levels of AAI. This increase in AAI makes the core fuel lean again and helps reproduce conditions similar to those at a lower J_{swirl} and a lower level of AAI.

8.3.3. EFFECT OF MOMENTUM FLUX RATIO J_{swirl} ON THE NO EMISSIONS

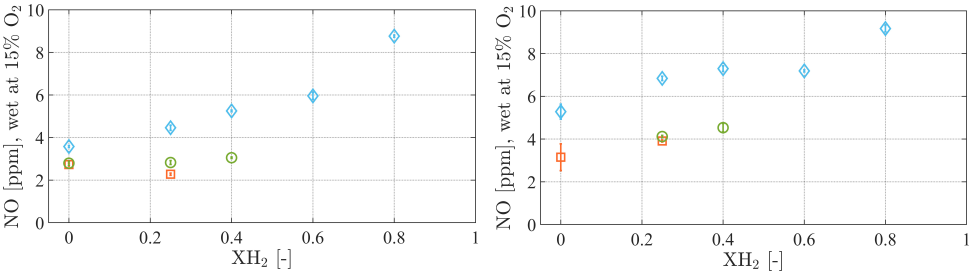

a) J_{high} **b)** J_{low}

Figure 8.8: NO emissions in ppm with standard deviations for two different momentum flux ratios J_{swirl}, varying XH_2 and χ, χ = 0 % (□), χ = 10 % (○) and χ = 20 % (◇).

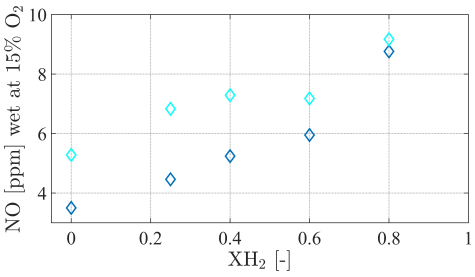

Figure 8.9: NO emissions in ppm at χ = 20 % for J_{high} (◇) and J_{low} (◇).

This section evaluates the effect of J_{swirl} on NO emissions by analysing both exhaust gas measurements and the spatial distribution of NO within the combustion chamber. Figure 8.8 shows the NO emissions in ppm measured with the exhaust gas analyser, normalized to 15 % O_2, for the two different J_{swirl} across varying hydrogen fractions (XH_2) and AAI levels. For χ = 0 % and χ = 10 %, the maximum investigated hydrogen mole fractions are XH_2 = 0.25 and XH_2 = 0.4, respectively, as higher hydrogen contents lead to flame stabilization upstream of the mixing tube outlet. Generally, increasing the hydrogen content leads to an increase in NO emissions. This observation contrasts with the spatial unmixedness trends presented in Chapter 5, but can be explained by variations in the lift-off heights of the flame. Lift-off height significantly influences local fuel-air mixing, where a lifted flame burns closer to perfectly premixed conditions compared to an attached flame, due to a longer mixing length. In all cases, J_{high} (Figure 8.8a) leads to higher NO emissions than cases with J_{low} (Figure 8.8b). This difference is attributed to the reduced spatial unmixedness associated with the increased J_{swirl}, as discussed in Chapter 5, which results in a more uniform temperature field and reduced thermal NO formation. The effect is particularly pronounced at lower XH_2 levels, as it can be seen in Figure 8.9, which compared the NO emissions for the two different J_{swirl} at χ = 20 %. At XH_2 = 0.8, the difference in NO emissions between the two levels of J_{swirl} is minimal, only a 0.4 ppm reduction is observed when increasing the level of J_{swirl} from 0.13 to 1.22.

This aligns with the OH-PLIF results in Figure 8.4, which show that for XH_2 = 0.8, both levels of J_{swirl} exhibit OH signal along the centreline of the combustion chamber. In contrast, at lower hydrogen contents (e.g., XH_2 = 0.6 in Figure 8.5), no centreline reaction is observed for J_{low}, while the case with J_{high} still shows heat release in that region. This indicates that at XH_2 = 0.8, the mixing quality for J_{low} is already sufficient to sustain reaction on the centreline, which explains the negligible reduction in NO emissions when increasing the level of J_{swirl}. This is in line with the findings in Chapter 5, where it was shown that at higher hydrogen the fuel-air mixing was already high, even for the lowest investigated J_{swirl} values.

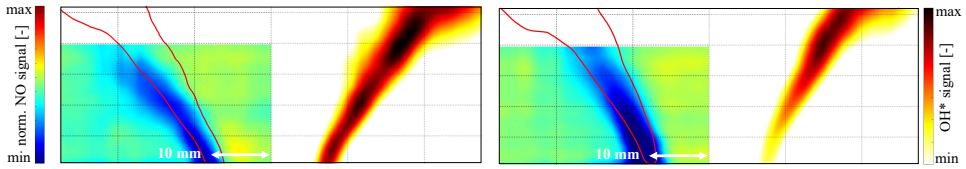

a) J_{high} **b)** J_{low}

Figure 8.10: NO-PLIF signal (left) and OH* signal (right) for two different momentum flux ratios J_{swirl} at XH_2 = 0.25, χ = 0 %.

To further investigate the observed differences in NO emissions, the spatial NO distribution within the combustion chamber is analysed for a V-flame and an M/Π-flame. Figure 8.10 shows the NO-PLIF and Abel-deconvoluted OH* images at X_{H_2} = 0.25 and χ = 0 %, for two different J_{swirl}. The red contour indicates 20 % of the maximum OH* signal, serving as a reference for the flame front. Due to laser power fluctuations over the course of the measurements, the absolute NO concentrations cannot be directly compared; rather, the focus is on differences in the spatial distribution. Regarding the measured NO emissions in the exhaust, increasing the level of J_{swirl} results in a decrease in the emissions from 4.2 ppm to 3.0 ppm, as shown in Figure 8.8. The OH* images in Figure 8.10 show that the flame for the configuration with a larger J_{swirl} has a wider opening angle, which is also reflected in the wider opening angle of the region with no NO concentration (dark blue area). Additionally, while the case with J_{low} produces a more uniform NO distribution across the outer and central recirculation regions (ORZ and CRZ), the case with J_{high} leads to higher NO concentration in the CRZ compared to the ORZ. This confirms that increasing J_{swirl} enhances mixing, leading to a more uniform equivalence ratio distribution for J_{high}. As a result, NO production increases in the ISL, which is then recirculated into the CRZ. In contrast, for the case with J_{low}, the flame partially stabilizes in the OSL, as shown previously by the higher OH concentration in the OSL (see Figure 8.2). This stabilization promotes more NO formation in the OSL, contributing to the higher overall NO emissions measured in this configuration. Figure 8.11 shows the NO and OH* distributions for XH_2 = 0.6 and χ = 20 %. At this high hydrogen content, a noticeable shift in the NO distribution is observed as J_{swirl} varies. For the case with J_{high}, the flame stabilizes further upstream as previously shown with the lift-off height in Figure 8.6. This shifts the region where NO concentration occurs closer to the injector. This is reflected in the reduced height of the NO region without any NO concentration (dark blue region). Additionally, the NO distribution becomes more radially uniform as J_{swirl}

decreases. Whereas the case with J_{low} configuration exhibits peak NO concentrations in the ORZ, the case with J_{high} leads to increased NO formation along the centreline. The region associated with the AAI jet, which typically exhibits low NO concentrations at the centre (see Chapter 7), shows a detectable NO signal in the case of J_{high}. In contrast, no NO signal is observed along the centreline for J_{low}. This aligns with the expected increase in fuel concentration along the centreline of the swirling flow, which enhances reaction near the centreline and leads to increased local NO formation.

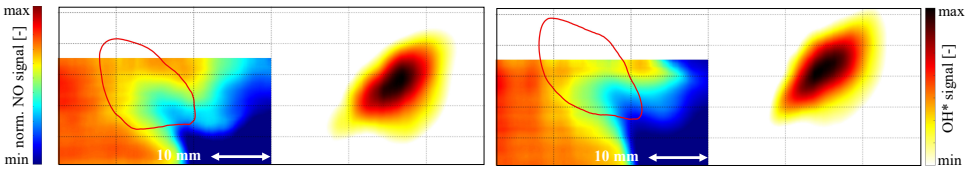

a) J_{high} **b)** J_{low}

Figure 8.11: NO-PLIF signal (left) and OH* signal (right) for two different momentum flux ratios J_{swirl} at XH_2 = 0.6, χ = 20 %.

8.4. CONCLUSIONS

This chapter investigated the effect of the momentum flux ratio (J_{swirl}) between fuel and air on flame stability and NO emissions in swirl-stabilized CH_4/H_2 flames with jet in cross-flow fuel injection. Increasing J_{swirl} was achieved by decreasing the fuel injection diameter, based on the analysis presented in Chapter 5. Flame stabilization mechanisms and lift-off heights were examined using OH-PLIF and OH* chemiluminescence imaging, while NO-PLIF measurements and exhaust gas analysis were employed to investigate the overall and spatial NO concentration and relate it to the flame location. The results show that increasing J_{swirl} leads to an increase in flame lift-off height across all cases, as the flame moves closer to the injector along the centreline. More OH signal is observed on the flame centreline as the level of J_{swirl} increases, indicating a more uniform equivalence ratio distribution, as a result of improved fuel-air mixing. This enhanced reactivity on the centreline contributes to the observed reduction in flashback resistance at higher J_{swirl} values. NO emissions decrease with increasing J_{swirl}, primarily due to the improved mixing quality, which promotes a more uniform temperature distribution in the flame and thus reduces thermal NO formation. The reduction in NO is more pronounced at lower hydrogen contents. This is because a higher hydrogen content in the fuel significantly enhances mixing, and therefore even cases with low J_{swirl} exhibit a high degree of mixing. The NO-PLIF results further confirm that for higher J_{swirl}, more NO is present along the centreline of the combustion chamber, consistent with the expected improvement in mixing quality. The key findings of this chapter are summarized as follows:

- Increasing J_{swirl} leads to a reduction in NO emissions, attributed to enhanced fuel-air mixing. This effect is more pronounced at lower hydrogen fractions, where mixing quality is more sensitive to changes in J_{swirl}

- An increase in J_{swirl} leads to a reduction in flame lift-off height, particularly near the centreline of the mixing tube, due to improved mixing quality. However, this enhanced mixing also lowers the flashback limits of the combustor, as more fuel reaches the centreline and promotes upstream flame propagation.
- The requirement to increase the AAI level at higher J_{swirl} values in order to achieve stable combustion, to levels exceeding those used at lower J_{swirl}, counteracts the benefits of enhanced mixing.

III

Conclusions & Recommendations

9

Conclusions & Recommendations

This dissertation explored emissions and flame stability in a partially premixed fuel-flexible (CH_4/H_2) swirl-stabilized burner. The main objective was to identify the governing parameters influencing flame stability and emissions in a partially premixed burner with axial air injection. To achieve this, the study began by examining the influence of key operational and geometric parameters, such as fuel composition and the swirl number on the non-reacting flow field. This allowed a distinguishing of the aerodynamic effects of geometrical features from those resulting from combustion on flame stability. The fuel-air mixing process governs the equivalence ratio distribution and, consequently, the flame temperature, which directly influences NO_x formation. Therefore, the mixing behaviour of a jet in a swirling cross-flow configuration was analysed, and the dominant parameters governing the mixing process were identified. These included the fuel composition and the momentum flux ratio J_{swirl}. The investigation then progressed to reacting cases, focusing on the flow field, flame stabilization mechanisms, and emission characteristics across different fuel compositions. A detailed assessment of NO emissions was conducted to link observed variations in NO levels to changes in mixing, the flow field and flame structure. Finally, the influence of J_{swirl}, identified as a key factor affecting fuel-air mixing, was investigated in detail. This analysis aimed to understand its impact on flame stability and emissions, thereby linking insights from the non-reacting studies to potential design improvement strategies for the reacting cases. This chapter summarizes the key findings by addressing the research questions presented in Chapter 1 and brings the answers of the research questions into perspective of the main research goal. The limitations of this work are then discussed. Finally, the chapter presents recommendations for future work.

Fuel flexibility (CH_4/H_2) is a key enabler for the transition toward more sustainable power generation. Using H_2 in gas turbines offers a promising solution to reduce CO_2 emissions. However, the uncertainty about its availability due to ongoing challenges in production and storage require fuel-flexible combustion systems. The markedly different combustion characteristics of H_2 compared to CH_4 complicate efforts to accommodate both fuels in the same combustion chamber, while maintaining stable flames with low emissions. Specifically, the addition of H_2 to the fuel mixture in gas turbines designed for CH_4 can lead to increased NO_x emissions due to high adiabatic flame temperatures and flame stability issues due to high flame speeds, creating significant challenges on the combustor design.

The present dissertation aims to identify the key design and operating parameters, such as the swirl number and fuel composition, that govern stability and NO_x emissions in a partially premixed, fuel-flexible, swirl-stabilized combustor with axial air injection. This study was carried out experimentally using a laboratory-scale set-up and included both non-reacting and reacting experiments. The fuel was radially injected into a swirling cross-flow of air just downstream of the swirler outlet, resulting in partially premixed conditions at the combustion chamber entrance. Throughout this work, multiple aspects of the combustor were investigated, each chapter aiming to answer one of the research questions presented in Chapter 1. Figure 9.1 summarizes the overall contributions of this dissertation, categorized into three types: Type I (Methodology), Type II (Mechanism), and Type III (Dataset). Type I - Methodology refers to the development of new methods for investigating the flow field and mixing characteristics. Type II - Mechanism involves identifying the underlying mechanisms driving the observed trends, which are helpful for future designs of fuel-flexible combustion chambers. Type III - Dataset encompasses the generation of new datasets, which are suitable for and have been used in the validation of numerical models.

Chapter 4 presents an extensive dataset of non-reacting flow fields, providing a comprehensive baseline characterization of the aerodynamic behaviour of the combustor geometry. The chapter also provides insights in how both geometric factors such as combustion chamber and swirler design and operational parameters including momentum flux ratio, surrogate fuel composition, and AAI influence the time-averaged and unsteady flow dynamics. Chapter 5 introduces a framework for experimentally studying the mixing characteristics of H_2 and air. By validating a tracer method using helium seeded with DEHS droplets, it establishes a versatile measurement approach applicable to fuel-air mixing investigations in various combustor configurations. Furthermore, it explores fuel-air mixing in a jet in cross-flow configuration and identifies the dominant parameters controlling the degree of fuel-air mixing. Chapter 6 provides an extensive dataset of reacting flow fields across a range of fuel compositions, AAI levels, and swirl numbers. It also demonstrates the effectiveness of AAI as a control parameter for CH_4/H_2 flames, highlighting the trade-offs concerning operational range and emissions. Chapter 7 identifies how variations in fuel composition and AAI influence the spatial distribution of NO within the combustion chamber and relates these findings to the flow field, flame position, and overall NO emissions. Chapter 8 reveals how changes in mixing driven by increasing the momentum flux ratio between fuel and air affect flame stabilization and emissions across different fuel compositions.

The Type II contributions (Revealing Mechanism) are discussed in greater detail in the following section, where the research questions introduced in Chapter 1 are addressed.

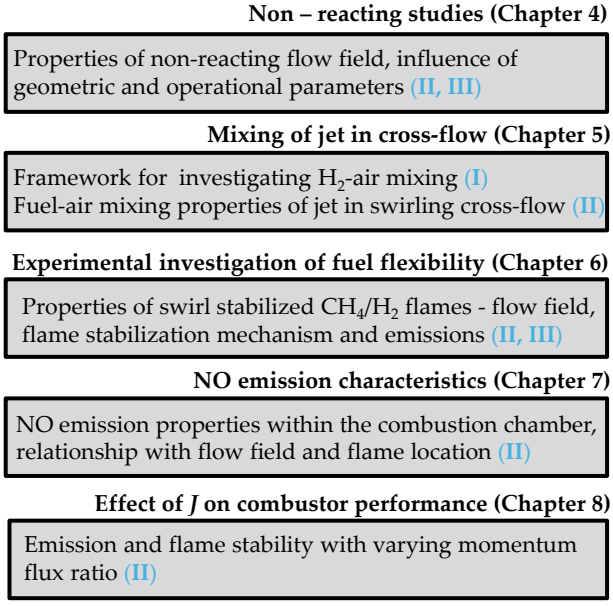

Figure 9.1: Contributions of this dissertations, shown for each chapter. Type I: Methodology, Type II: Mechanism, Type III: Dataset.

9.1. NEW FINDINGS

This section aims to clarify the key mechanisms governing flame stability and emissions identified in this dissertation by addressing the research questions presented in Chapter 1. In Chapter 4, this work first addressed the primary parameters governing the non-reacting flow field through detailed analysis of flow field behaviour within the mixing tube and combustion chamber. The parameters investigated included geometric features such as confinement ratio and outlet contraction, as well as operational factors like the level of AAI, fuel composition, and momentum flux ratio (J_{swirl}). Understanding how a change in these parameters affects the flow field is critical to distinguish flow-field driven phenomena from those caused by combustion. Helium/air mixtures were used as surrogates to isolate density effects. This chapter focused on answering the following research question:

Subquestion 1

What are the effects of the geometric parameters and the operating conditions on the non-reacting flow field in a swirl-stabilized combustor with AAI and jet in cross-flow

fuel injection?

Variations in combustion chamber geometry, including changes in the confinement ratio and the introduction of a nozzle at the outlet, have a significant impact on the flow field, especially on the size and strength of the recirculation zones. Increasing AAI weakens the CRZ and alters PVC dynamics in the non-reacting flow field by affecting the effective swirl number. If the effective swirl number drops below a critical level, vortex breakdown shifts from bubble to cone type, suppressing the PVC. Changing the surrogate fuel composition does not alter the overall flow structure, but it does affect the absolute velocities due to an increased volumetric flow rate with higher hydrogen content. The unsteady flow field is also influenced by increasing the hydrogen content. The observed PVC frequency is lower than expected based on Strouhal number scaling, demonstrating that fuel composition may influence the effective swirl number. The momentum flux ratio J_{swirl} significantly affects the non-reacting flow field, both with and without AAI. Higher values of J_{swirl} generally reduce the maximum axial velocity in the swirling jets while they increase the radial velocity, resulting in a broader centreline recirculation zone. However, the unsteady flow field remains largely unchanged, as indicated by the nearly constant PVC frequency. Several features of the non-reacting flow field, including velocity magnitudes and the opening angle of the swirling jets, can help explain the observed trends in emissions and flame stability in the reacting cases. Since certain parameters, such as the level of AAI, the swirl number, and the momentum flux ratio, already have a strong influence on the flow field without combustion, this enables a distinction between changes already present in the non-reacting flow field and those resulting from the combustion process.

Since fuel-air mixing strongly influences thermal NO_x formation by influencing the equivalence ratio distribution and consequently the temperature distribution, achieving a high degree of mixing is crucial—particularly in partially premixed configurations where mixing must occur rapidly. A major focus of this thesis was thus to investigate mixing behaviour in the partially premixed burner and to identify the key parameters governing it. In Chapter 5, the influence of fuel composition, J_{swirl}, AAI level, and swirl number on mixing in a jet in swirling cross-flow configuration was examined. A methodology was developed to assess mixing by tracking the spatial distribution of a seeded surrogate fuel with DEHS droplets through Mie scattering imaging. The chapter evaluated how the spatial unmixedness value and fuel distribution vary within the mixing tube as operating conditions change. The following research question was answered in this chapter:

Subquestion 2

How do the momentum flux ratio, the density ratio, and AAI affect fuel-air mixing in a jet in swirling cross-flow configuration?

The degree of fuel-air mixing in a jet in swirling cross-flow is strongly governed by

the interplay of J_{swirl}, density ratio, and AAI. The fuel density appeared as the dominant factor: lighter fuels experience less centrifugal forces, therefore they penetrate deeper into the cross-flow. Heavier fuels convect towards the mixing tube wall. Additionally, lighter fuels exhibit a wider fuel jet spreading angle at the fuel injection points, which also contributes to enhanced mixing. As J_{swirl} increases, mixing improves up to a critical point, beyond which, further increase provide no additional benefit at a fixed mixing tube length. High levels of AAI hinder mixing near the fuel injection plane due to the high-momentum axial jet, which prevents the fuel from entering the core of the flow, resulting in greater local unmixedness compared to cases without AAI. If the swirl number is high (for example Sw = 1.1), increased turbulence downstream partially compensates for the initial decrease of unmixedness with AAI, leading to unmixedness levels at the outlet of the mixing tube comparable to the case without AAI. In contrast, for lower swirl numbers (for example Sw = 0.7), AAI leads to a consistent significant reduction in fuel-air mixing throughout the mixing tube.

In Chapter 6, the partially premixed burner was evaluated under reacting conditions at varying fuel compositions, AAI levels, and swirl numbers. Flame stability and emission characteristics were analysed and correlated to the results of the non-reacting studies. Also, the stability limits of the combustor were identified. The results highlighted the complex interplay between flow dynamics, mixing, flame behaviour, and emissions performance. The central question investigated in this chapter was:

Subquestion 3

What is the effect of AAI on the emissions and operational range of CH_4/H_2 swirl-stabilized flames?

Axial air injection (AAI) has been identified as an effective approach to achieve stable, fuel-flexible combustion across the full range from methane to hydrogen under lean partially premixed conditions. At sufficiently high AAI levels (χ = 20 % for Sw = 1.1, χ = 10 % for Sw = 0.7), the flame is stable even with high hydrogen content, while lower AAI stabilizes methane flames but does not prevent flashback in hydrogen-rich cases. These results show that flame stability depends on the interplay between AAI and swirl number, with higher swirl requiring higher AAI levels to stabilize hydrogen-rich flames. However, increased AAI also raises the lean blowout limit for methane flames. Flashback-free operation for hydrogen flames results from shifting the flame stabilization mode from attached V-flames to lifted flame structures, including newly identified M/Π shapes, where the flame front near the centreline is pushed downstream of the injector. These changes relate to the AAI-induced flow modifications that increase centreline axial velocity. The impact of AAI on the flow field varies strongly with the fuel composition and φ: methane flames and very lean hydrogen flames keep a swirl-stabilized flow field with a CRZ, while hydrogen flames at a higher φ values resemble low-swirl flames without a CRZ. This is due an upstream shift of the flame, caused by higher flame speeds, resulting in a strong

axial acceleration of the flow. Although AAI generally increases NO emissions due to a decrease in fuel-air mixing, it also strongly influences the lift-off height of the flame. A higher lift-off height can provide additional mixing length in the combustion chamber, lowering peak temperatures and reducing NO formation compared to an attached flame. Overall, the use of AAI in fuel-flexible systems presents a trade-off. While high levels of AAI extend the operational range at high H_2 contents, they also reduce mixing quality, leading to increased NO emissions across all fuel compositions. Moreover, they slightly raise the blowout limits for fuels with low hydrogen content. These findings highlight the need for careful optimization of AAI levels to balance flame stability and emissions performance in fuel-flexible combustors.

NO emissions in partially premixed combustion are strongly influenced by the degree of local fuel-air mixing, making accurate prediction challenging. This complexity increases in dual-fuel combustion, where mixing quality and dominant NO formation pathways vary significantly between fuels. Chapter 7 investigated the NO emission characteristics of the partially premixed swirl-stabilized burner. Detailed NO measurements combined with flow and flame location analysis provided valuable insights into the mechanisms driving variations in NO emissions and their spatial distribution within the combustion chamber. The following question served as the basis for the analysis in this chapter:

Subquestion 4

What is the effect of the flow field (AAI, fuel injection, recirculation zones) on the NO emissions?

AAI significantly influences the NO distribution within the combustion chamber. As AAI levels increase, the NO distribution shifts from a relatively uniform distribution between the CRZ and ORZ to being concentrated mainly in the ORZ. This shift is directly tied to the change in flame shape caused by the different distribution of equivalence ratio. AAI generally causes fuel to remain near the mixing tube periphery, stabilizing the flame primarily in the OSL, which results in most of the NO being produced in the OSL and then being recirculated into the ORZ. Notably, increasing AAI at a constant hydrogen content does not always increase NO emissions, as an increased flame lift-off height results in additional mixing length, compensating for the decrease in fuel-air mixing in the mixing tube. Thus, NO emissions depend critically on local fuel-air mixing, influenced by both by the degree of fuel-air mixing achieved in the mixing tube and flame lift-off height. This trade-off suggests the existence of an optimal level of AAI to minimize emissions. While NO emissions increase with rising hydrogen content at 0 % AAI, the emission trend becomes less predictable for the CH_4/H_2 flames with AAI. Although the low density of hydrogen enhances fuel-air mixing, this benefit is offset by a significantly reduced flame lift-off height, creating locally richer conditions compared to lifted flames. Thermal NO is expected to be the dominant formation pathway downstream of the reaction zone; however, the non-monotonic trends observed suggest a shift in the relative

contributions of different NO formation pathways to the overall NO emissions. This is supported by findings in the literature. Overall, when the hydrogen content in the fuel varies at a constant level of AAI, NO emissions are a result of a complex interplay of mixing, flame stabilization location, and changes in NO formation mechanisms.

Building on earlier findings that increasing the momentum flux ratio (J_{swirl}) effectively reduces fuel-air unmixedness, the final part of this study applied this strategy under reacting conditions by reducing the fuel inlet diameter to increase J_{swirl}. Results from emissions measurements and flame stabilization observations provided valuable insights into how the combustor performs under more premixed conditions compared to the baseline case. This chapter investigated the central question:

Subquestion 5

What is the effect of the fuel momentum on the emissions and operational range of CH_4/H_2 swirl-stabilized flames?

Increasing the momentum flux ratio J_{swirl} enhances fuel-air mixing, leading to a reduction in NO emissions. This effect is most pronounced for flames with low hydrogen content and reduces as the hydrogen concentration increases. This reduction is consistent with mixing experiments showing that higher hydrogen content achieves a high degree of mixing even at lower J_{swirl} values, which reflects in a small change in emissions across different fuel inlet diameters. An increase in J_{swirl}, which enhances mixing, results in a more pronounced NO signal along the flame centreline. Although the flame stabilization mechanism (e.g., V-flame or M-flame) remains the same, higher J_{swirl} values cause the flame to move closer to the mixing tube outlet. This shift is most prominent along the centreline and is consistent with mixing studies that show increased fuel concentration in this region for higher J_{swirl}. Additionally, the opening angle of the flame widens significantly with increasing J_{swirl}, consistent with flow field behaviour in non-reacting cases. The reduced lift-off height at higher J_{swirl} also lowers the flashback limit if the bulk velocities are not sufficiently high, thereby constraining the operational range with respect to φ and hydrogen content.

9.2. COMMENTS ON THE MAIN RESEARCH GOAL

The answers to the sub-research questions directly support the main research goal: identifying the governing parameters for flame stability and emissions in partially premixed, swirl-stabilized CH_4/H_2 flames with AAI. These identified mechanisms can form the basis for establishing design and operational considerations in the development of fuel-flexible combustion systems that ensure low emissions and stable operation. There are several main takeaways from this study.

The non-reacting flow field shows sensitivity to several of the investigated parameters, and clear correlations have been identified between the flow field structure and the flame shape and stabilization mechanisms observed in the reacting case. While the mag-

nitude of changes in the non-reacting conditions may not directly reflect those in the reacting conditions, the non-reacting flow field still offers valuable insight for predicting key features of the reacting flow field. Additionally, non-reacting mixing studies have proven valuable for identifying the key parameters that govern mixing, making them a critical part of the injector design and characterization process. Therefore, a comprehensive investigation of the non-reacting flow field and mixing characteristics should be considered an essential first step in assessing any new combustor geometry prior to examining reacting conditions.

In jet in cross-flow configurations, increasing the value of J_{swirl} enhances mixing for both fuels CH_4 and H_2 up to a critical threshold, beyond which no further improvement is observed. This threshold depends on several factors, including the fuel composition, swirl number and Re numbers in the mixing tube and must therefore be determined for each specific geometry and fuel blend to ensure optimal mixing. While H_2 typically mixes more effectively than CH_4 due to its lower density and high diffusivity, excessively high J_{swirl} values can lead to H_2 accumulation in the core of the swirling flow, underscoring the need to carefully identify the optimal J_{swirl} range.

However, the results showed that unmixedness values measured in the mixing tube during non-reacting studies are not sufficient indicators of NO emissions in the reacting cases. Flames with high hydrogen content have a lower lift-off height compared to methane flames, which significantly reduces the mixing length within the combustion chamber. As a result, attached flames burn at locally higher equivalence ratios than lifted flames. Therefore, for operation with high hydrogen content or pure hydrogen mixtures, achieving a high degree of premixing in the mixing tube is essential. Methane flames, with their larger lift-off height, allow for more downstream mixing even when the fuel-air mixing level in the mixing tube is lower than that for hydrogen. Consequently, flame lift-off height emerges as a key parameter linking fuel-air mixing, flame stabilization, and NO emissions. Since lift-off height is influenced by both AAI and fuel composition, it plays a critical role in designing fuel-flexible systems. However, because this parameter can only be determined through experimental testing in the reacting conditions and no predictive method is provided here, its consideration remains dependent on direct measurements.

To summarize, AAI can be incorporated into the design of fuel-flexible injector geometries, as it shows strong potential for stabilizing flames across a wide range of fuel mixtures. However, its effect on flame stability and emissions is complex. On one hand, AAI can lift the flame off the injector rim, which reduces the risk of flashback, prevents high temperatures near the injector, and increases the effective mixing length. On the other hand, excessive levels of AAI reduce the degree of premixing in the mixing tube, decrease the effective swirl number and can lead to higher emissions. There is a critical level of AAI at which the benefits of flame lift-off are outweighed by the negative effects on premixing. It is therefore essential to identify this threshold for each configuration.

Increasing J_{swirl} remains an effective strategy for enhancing mixing and reducing emissions for a given fuel composition and level of AAI. However, a change in fuel distribution can change the flame stabilization location, which can increase the risk of flashback, especially if the local flow velocities near the injector are not sufficient to anchor the flame downstream of the mixing tube outlet. While flames with different swirl num-

bers and AAI combinations may exhibit similar lift-off heights and operational ranges, their emission characteristics can vary significantly. These factors highlight the complexity of burner design and optimization for both emissions and flame stability. Overall, balancing flame stability and emissions requires careful adjustment of swirl number, AAI, and J_{swirl}.

Together, the findings in this work lead to several important design insights. For each new combustor geometry, a non-reacting analysis should be performed to characterize the influence of geometry and operating conditions on the flow field. Additionally, for partially premixed combustion, this involves analysing the mixing process. The optimal J_{swirl} should be determined through a mixing analysis tailored to the specific fuel blend, since further increase of J_{swirl} offers no additional benefit. In the reacting case, the degree of AAI should be optimized to ensure the flame is lifted off the injector while maintaining a high degree of fuel-air premixing. Particular attention must be paid to the operation with full hydrogen, which requires a high degree of fuel-air premixing and careful control of flame stabilization to avoid flashback or increased emissions.

This dissertation makes a significant contribution to the understanding of flame stability and emissions in partially premixed, swirl-stabilized CH_4/H_2 flames with AAI. Through detailed experimental analysis, it identifies the key mechanisms and governing parameters that influence flame stability and emissions. The findings offer valuable insights into how fuel composition, injector design, and flow field characteristics interact to affect stability limits, emissions, and overall combustor performance. A major strength of this work is its systematic investigation within a well-characterized combustor geometry and under a controlled range of operating conditions. This focused approach enables a clear identification of trends and underlying mechanisms, providing a solid foundation for the future design and optimization of fuel-flexible combustors. While some of the results are specific to the tested configuration, they offer a robust baseline and a conceptual framework for understanding more complex systems. Additionally, due to the limited availability of data in fuel-flexible configurations, these results can serve as valuable references for improving the knowledge of fundamental concepts and for validating computational models. It is recognized, however, that changes to the combustion chamber geometry or operating conditions, such as thermal power or injector design, can significantly alter flow structures, turbulence levels, and mixing behaviour. Many trends observed in this study are non-linear, which is expected to complicate scaling to different geometries or operating conditions. Therefore, any such modifications must be carefully analysed, as they may affect the extent to which the relationships identified in this study remain valid. Nonetheless, the insights gained from this study are broadly applicable and highly relevant to the development of next-generation combustion systems. They emphasize the need for configuration-specific investigations, particularly when targeting low-emission, hydrogen-enriched combustion across different scales.

9.3. RECOMMENDATIONS FOR FUTURE WORK

This dissertation establishes a strong foundation for understanding dual-fuel combustion in a swirl-stabilized configuration. The inherent complexity and numerous interacting processes in partially premixed combustion present additional opportunities for

research directions. These topics lie beyond the scope of the present work but offer valuable directions for future research. The following section presents recommendations for further investigation based on the insights gained in this study. The main recommendations are as follows:

- **Increase of thermal power output** The thermal power output of the combustor was constrained by infrastructure limitations, which in turn restricted the operational window—particularly for fuels with a high hydrogen content. In these cases, the burning velocity exceeded the flow velocity, leading to flashback. The combustor design resulted in relatively low bulk velocities of approximately 11 m/s, which is about one-tenth of the velocities typically found in conventional combustors. The Mach numbers at the air and fuel inlets are 0.06 and 0.02, respectively, both significantly lower than the values commonly encountered in conventional configurations. Increasing the bulk velocity would likely raise the flashback threshold, enabling the exploration of a broader range of equivalence ratios to better assess how emissions and flame stability evolve in a fuel-flexible system.

- **Changes in the confinement ratio:** Some of the results presented in this dissertation are highly specific to the chosen geometry, such as the confinement ratio. As demonstrated in Chapter 4, the confinement ratio has a notable impact on the flow field in the combustion chamber, particularly influencing the size and strength of the recirculation zones. In this study, a large confinement ratio was selected to ensure full optical access and minimize wall heat losses. However, future research should explore the effects of a smaller confinement ratio on the flow field and flame stabilization to assess the broader applicability of these findings across different geometries.

- **Further investigation of the influence of the momentum flux ratio on emissions:** The results of this thesis highlight the momentum flux ratio as a key parameter for enhancing mixing and reducing emissions. However, its effect on emissions was examined only within a limited range of swirl numbers and momentum flux ratios, allowing only indicative trends to be identified. Future research should extend this investigation across a broader range of swirl numbers and fuel mixtures to gain a more comprehensive understanding of how to optimize the momentum flux ratio under varying operating conditions.

- **Determining the local equivalence ratio:** While the mixing study provided insights of the local fuel mixing close to the mixing tube outlet, the subsequent chapters have shown that it is not sufficient to only look at the fuel-air mixing at the mixing tube to predict NO emissions. Since the location of the flame stabilization is highly dependent on the fuel composition, it is crucial to determine the local equivalence ratio at the flame stabilization location. This would allow for a more accurate assessment of the combustion conditions and their impact on emissions. Future work should focus on developing experimental methods, like Raman scattering or numerical models to estimate the local equivalence ratio at the flame anchoring location in partially premixed configurations.

- **Mixing analysis with Lagrangian Particle Tracking:** Since DEHS droplets have a significantly different density than helium, their presence is expected to influence the observed mixing behaviour. Although the overall trends of helium and air mixing from LES and from the experiments, where the air stream is seeded with DEHS droplets, appear similar, a more accurate assessment of the experimental mixing could be obtained by validating the use of DEHS particles through Lagrangian Particle Tracking in LES. This approach would allow quantification of particle inertia effects on the mixing behaviour and provide correction factors if needed.

- **Adjustments to measure NO_2 emissions:** Although NO_2 concentrations are often small, including its contribution is necessary to accurately quantify total NO_x emissions. Due to the gas analyser maximum temperature limit of 80°C, water condensation cannot always be prevented in some test cases. Condensed water can cause NO_2 to dissolve, but more importantly, it can lead to a significant overestimation of NO_2 measurements. This happens because condensation changes the refractive index of the sample gas, reducing the transmitted light through the measurement cuvette. The only way to prevent condensation is by diluting the exhaust gas with an inert gas, such as nitrogen, and correcting the measured concentrations based on the dilution ratio. This method allows for more accurate measurement of NO_x emissions as the sum of NO and NO_2 concentrations. Additionally, this would provide more insight into the strength of the NO reburning effect, that is, the oxidation of NO to NO_2, and would help in interpreting the observed NO emission trends.

A

COMBUSTOR P & ID

A

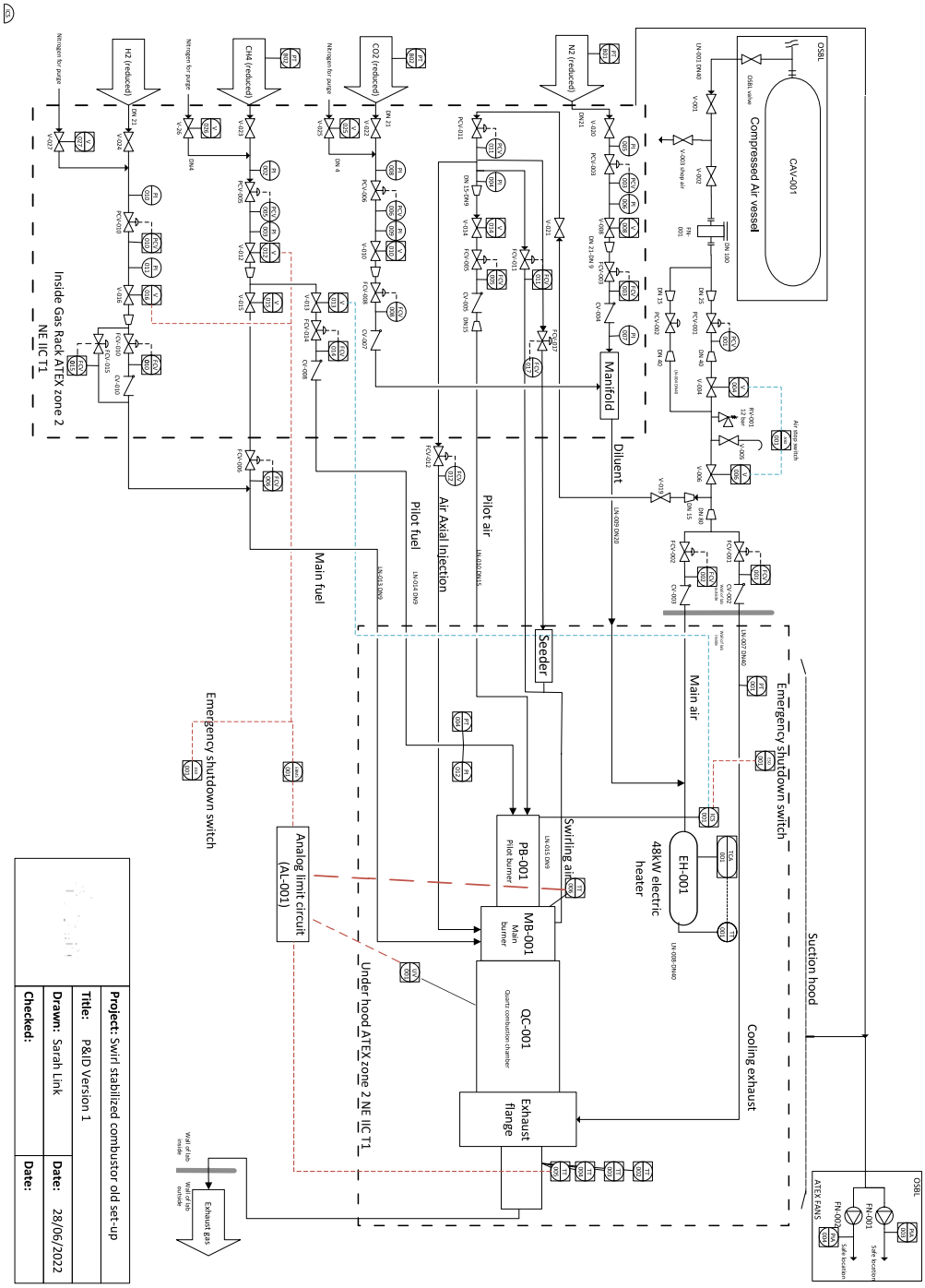
CAV-001
Compressed Air vessel
Manifold
Diluent
Pilot air
Air Axial Injection
Pilot fuel
Main fuel
Main air
Seeder
Swirling air
PB-001
Pilot burner
MB-001
Main burner
QC-001
Quartz combustor chamber
Exhaust flange
EH-001
48KW electric heater
Analog limit circuit (AL-001)
Emergency shutdown switch
Emergency Shutdown switch
Suction hood
Cooling exhaust
Under hood ATEX zone 2 NE IIC T1
Inside Gas Rack ATEX zone 2 NE IIC T1
FN-001
FN-002
ATEX FANS
N2 (reduced)
CO2 (reduced)
CH4 (reduced)
H2 (reduced)
Exhaust gas
Project: Swirl stabilized combustor old set-up
Title: P&ID Version 1
Drawn: Sarah Link
Date: 28/06/2022
Checked:
Date:

B

Operating conditions overview

B

Operating points at $\dot{m}_{air}$ = 5.1 ·10^{-3} kg/s					
P_{th} [kW]	XH_2[-]	$\dot{Q}_{CH_4}$ [L/min]	$\dot{Q}_{H_2}$ [L/min]	U_{MT} [m/s]	φ
8	0	14.1	0	10.23	0.51
	0.25	12.85	4.28	10.24	0.50
	0.4	11.78	7.85	10.43	0.49
	0.6	9.75	14.61	10.61	0.48
	0.8	6.42	25.68	10.89	0.46
	1	0	44.03	11.44	0.42
9	0	15.91	0	10.29	0.58
	0.25	14.46	4.82	10.42	0.57
	0.4	13.25	8.84	10.53	0.56
	0.6	10.96	16.45	10.72	0.54
	0.8	7.22	28.89	10.89	0.52
	1	0	52.91	11.66	0.48
10	0	17.68	0	10.36	0.64
	0.25	16.07	5.36	10.50	0.63
	0.4	24.54	9.81	10.61	0.62
	0.6	12.18	18.27	10.83	0.60
	0.8	8.03	32.10	11.18	0.58
	1	0	58.79	11.88	0.53
11	0	19.45	0	10.42	0.70
	0.25	17.67	5.89	10.58	0.69
	0.4	16.20	10.80	10.71	0.68
	0.6	13.40	20.10	10.94	0.67
	0.8	8.83	35.31	11.33	0.64
	1	0	64.67	12.09	0.58
12	0	21.21	0	10.49	0.77
	0.25	19.28	6.43	10.66	0.76
	0.4	16.67	11.17	10.80	0.75
	0.6	14.62	21.93	11.06	0.73
	0.8	9.13	39.21	11.49	0.70
	1	0	71.8	12.31	0.64

Table B.1: Operating conditions for the design points at constant air flow rate, H_2 fraction XH_2, the CH_4 and H_2 volumetric flow rates at T = 288.15 K and p = 1 atm, the bulk velocity in the mixing tube U_{MT} and equivalence ratio φ

C

STOKES NUMBER CALCULATION

The Stokes number determines how well the particle follows the flow, and is defined as the ratio of the particle response time to the characteristic timescale of the flow

$$St = \frac{\tau_p}{\tau_f} \tag{C.1}$$

where the particle response time τ_p is given by

$$\tau_p = \frac{\rho_p d_p^2}{18\mu} \tag{C.2}$$

and the characteristic timescale of the flow τ_f is given by

$$\tau_f = \frac{\delta}{U_\infty} \tag{C.3}$$

For the cases where the DEHS droplet are seeded into the fuel stream, the fuel inlet diameter and the fuel inlet velocity are used to calculate the flow timescale. For the particle timescale, a droplet diameter of 0.9 µm is assumed and a density of 912 kg/m^3. The viscosity of the fuel mixture is calculated with the equation of Herning and Zipperer [193]:

$$\mu_{mix} = \frac{\sum(\mu_i \cdot X_i \cdot \sqrt{W_i})}{\sum(X_i \cdot \sqrt{W_i})} \tag{C.4}$$

where μ_i is the dynamic viscosity, X_i the mole fraction and W_i the molar mass of the component i. The resulting Stokes numbers for different surrogate cases are presented in Figure C.1, with flow rates defined in Table 3.2 in Appendix 3. It should be noted that not all surrogate cases were experimentally tested for every diameter, but the values are provided here for completeness. The smallest investigated fuel diameter for XH_2 is $d_{fuel} = 1.64$, corresponding to a Stokes number of approximately $St = 0.18$. Similarly, the

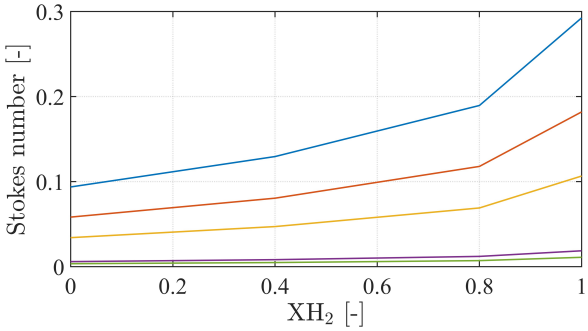

Figure C.1: Stokes numbers for surrogate XH_2 cases at different fuel diameters d_{fuel}: d_{fuel} = 1.4 mm (—), d_{fuel} = 1.64 mm (—), d_{fuel} = 1.94 mm (—), d_{fuel} = 3.5 mm (—) and d_{fuel} = 4.17 mm (—)

case with XH_2 = 0.8 at d_{fuel} = 1.4 shows comparable values. Since these Stokes numbers remain well below St = 1, it is expected that the particles closely follow the flow, particularly the large-scale structures, which are the primary focus of this study.

For the reacting cases, TiO_2 is used as a tracer and is introduced via the swirling air stream. Assuming a droplet diameter of 1 µm and a density of 4000 kg/m^3, the particle timescale is calculated. Using the bulk velocity and diameter of the mixing tube, this results in a Stokes number of $St = 8.5 \cdot 10^{-5}$, based solely on the air flow rate in the mixing tube. Since this value is significantly below 1, it is assumed that the particles closely follow the flow, even in regions of higher shear or velocity.

D

NON REACTING FLOW FIELDS

Complementary to the results presented in Appendix 4, this appendix provides additional information on the non-reacting flow fields, which include the contour plots for both axial and transverse velocity.

EFFECT OF FUEL COMPOSITION

Figure D.1 and Figure D.2 show the streamwise and transverse velocity fields for surrogate cases A_s-D_s at $\chi = \chi = 0\,\%$, respectively for J_{low}. It can be seen that the overall flow field structure is not affected, all flow fields have a CRZ of similar size and shape. The main difference is the change in velocity magnitudes of both components, which increases with increasing X_{H2}, as expected due to the higher flow rates.

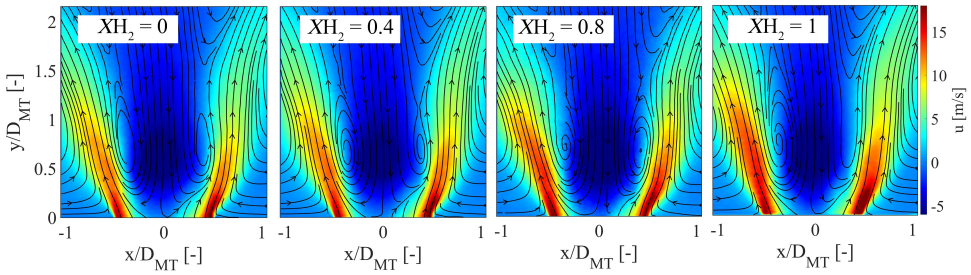

Figure D.1: Streamwise velocity fields for surrogate cases A_s-D_s at $\chi = 10\,\%$

EFFECT OF J_{swirl}

Figure D.3 shows the streamwise velocity fields for surrogate cases A_s ($XH_2 = 0$) and D_s ($XH_2 = 1$) at $\chi = 0\,\%$ for varying J_{swirl}. While the overall flow structure stays similar, the changes are more pronounced compared to Figure D.1. The CRZ is wider for higher

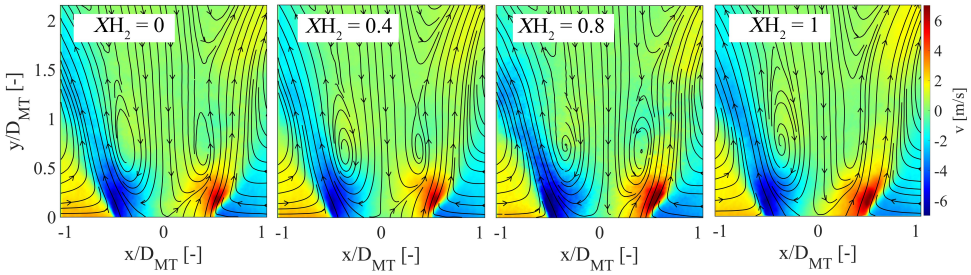

Figure D.2: Transverse velocity fields for surrogate cases A_s-D_s at $\chi = 0\,\%$

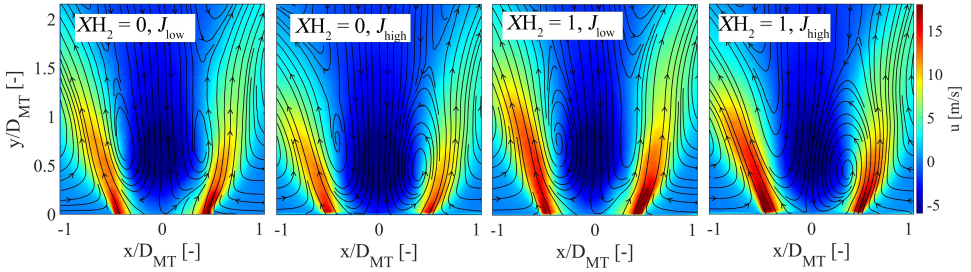

Figure D.3: Streamwise velocity fields for surrogate cases A_s ($XH_2 = 0$) and D_s ($XH_2 = 1$) for varying J_{swirl} at $\chi = 0\,\%$

J_{swirl}, which is in line with the wider opening angle of the swirling jets, and also reflected in the transverse velocity plots shown in Figure D.4.

Figure D.5 and Figure D.6 show the streamwise and transverse velocity fields for surrogate cases C_s ($XH_2 = 0.8$) and D_s ($XH_2 = 1$) at $\chi = 20\,\%$ for varying J_{swirl}. It can be seen that the overall flow field structure is significantly more affected compared to the previously investigated cases. For both surrogate cases, the spreading of the CRZ is delayed in streamwise direction as J_{swirl} increases, which is reflected in the transverse velocity fields. Further downstream, however, the CRZ for the cases with higher J_{swirl} is significantly wider.

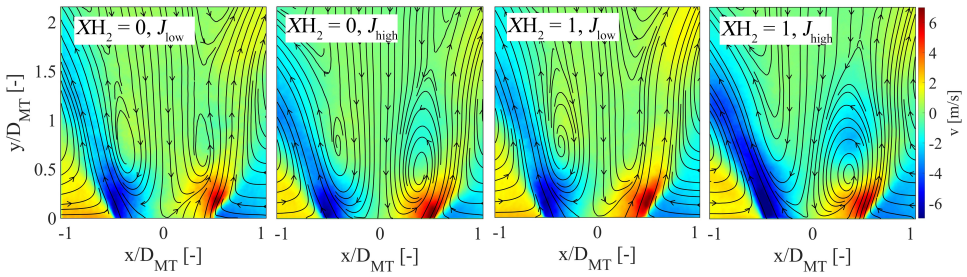

Figure D.4: Transverse velocity fields for surrogate cases A_s ($XH_2 = 0$) and D_s ($XH_2 = 1$) for varying J_{swirl} at $\chi = 0\,\%$

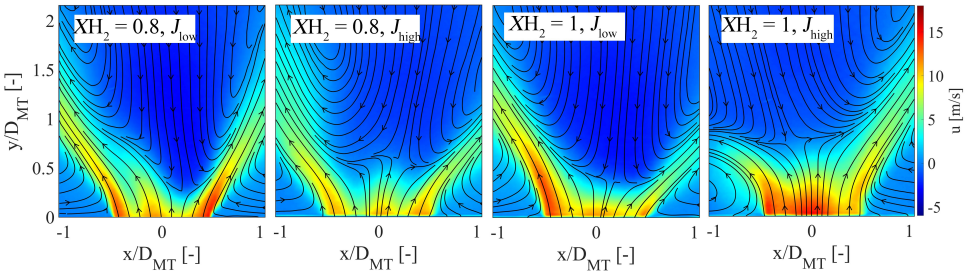

Figure D.5: Streamwise velocity fields for surrogate cases C_s ($XH_2 = 0.8$) and D_s ($XH_2 = 1$) for varying J_{swirl} at $\chi = 20\,\%$

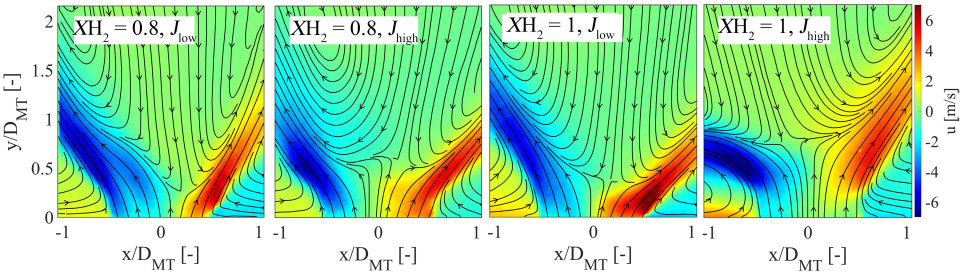

Figure D.6: Transverse velocity fields for surrogate cases C_s ($XH_2 = 0.8$) and D_s ($XH_2 = 1$) for varying J_{swirl} at $\chi = 20\,\%$

BIBLIOGRAPHY

[1] C. A. Horowitz. “Paris Agreement”. In: *International Legal Materials* 55.4 (2016), pp. 740–755. DOI: 10.1017/S0020782900004253.

[2] I. P. on Climate Change (IPCC). *Climate Change 2021 - The Physical Science Basis: Working Group I Contribution to the Sixth Assessment Report of the Intergovernmental Panel on Climate Change*. Cambridge University Press, 2023.

[3] International Civil Aviation Organization. *Joint ACI World-ICAO Passenger Traffic Report, Trends, and Outlook*. 2025. URL: https://aci.aero/2025/01/28/joint-aci-world-icao-passenger-traffic-report-trends-and-outlook/.

[4] International Energy Agency. *Energy and AI*. Accessed: 2025-07-30. Paris: IEA, 2025. URL: https://www.iea.org/reports/energy-and-ai.

[5] N. A. of Sciences, Medicine, D. on Engineering, et al. *Advanced technologies for gas turbines*. National Academies Press, 2020. ISBN: 978-0-309-66425-7. DOI: 10.17226/25630.

[6] A. Tuluhong, Q. Chang, L. Xie, et al. “Current Status of Green Hydrogen Production Technology: A Review”. In: *Sustainability* 16 (Oct. 2024), p. 9070. DOI: 10.3390/su16209070.

[7] N. Ma, W. Zhao, W. Wang, et al. “Large scale of green hydrogen storage: Opportunities and challenges”. In: *International Journal of Hydrogen Energy* 50 (2024), pp. 379–396. DOI: 10.1016/j.ijhydene.2023.09.021.

[8] M. Tao, J. A. Azzolini, E. B. Stechel, et al. “Review—Engineering Challenges in Green Hydrogen Production Systems”. In: *Journal of The Electrochemical Society* 169.5 (May 2022), p. 054503. DOI: 10.1149/1945-7111/ac6983.

[9] J. A. Lasek and R. Lajnert. “On the issues of NOx as greenhouse gases: an ongoing discussion…” In: *Applied Sciences* 12.20 (2022), p. 10429. DOI: 10.3390/app122010429.

[10] O. Tuncer, S. Acharya, and J. Uhm. “Dynamics, NOx and flashback characteristics of confined premixed hydrogen-enriched methane flames”. In: *International Journal of Hydrogen Energy* 34.1 (2009), pp. 496–506. DOI: 10.1016/j.ijhydene.2008.09.075.

[11] S. Taamallah, K. Vogiatzaki, F. M. Alzahrani, et al. “Fuel flexibility, stability and emissions in premixed hydrogen-rich gas turbine combustion: Technology, fundamentals, and numerical simulations”. In: *Applied Energy* 154 (2015), pp. 1020–1047. DOI: 10.1016/j.apenergy.2015.04.044.

[12] H. H.-W. Funke, N. Beckmann, J. Keinz, et al. “30 Years of Dry-Low-NOx Micromix Combustor Research for Hydrogen-Rich Fuels: An Overview of Past and Present Activities”. In: *Journal of Engineering for Gas Turbines and Power* 143.7 (Mar. 2021), p. 071002. DOI: 10.1115/1.4049764.

[13] T. O. Lucca-Negro. “Vortex Breakdown: a review”. In: *Progress in Energy and combustion Science* 27 (2001), pp. 431–481. DOI: 10.1016/S0360-1285(00)00022-8.

[14] GE Vernova (GE Gas Power). *Hydrogen Overview (GEA35685)*. PDF fact sheet. Jan. 2025. URL: https://www.gevernova.com/content/dam/gepower-new/global/en_US/downloads/gas-new-site/future-of-energy/GEA35685-GEV-Hydrogen-Overview_8.5x11_RGB_R4.pdf.

[15] Ansaldo Energia S.p.A. *GT36 Sequential Combustion Technology Achieves 100% Hydrogen*. Press release. Feb. 2024.

[16] GE Vernova. *9HA Gas Turbine*. https://www.gevernova.com/gas-power/products/gas-turbines/9ha. Accessed: 2025-08-01. n.d.

[17] Siemens Energy. *HL-class Gas Turbines*. Accessed: 2025-08-01. 2025. URL: https://www.siemens-energy.com/global/en/home/products-services/product-offerings/gas-turbines/hl-class.html.

[18] *CAVENDISH Project*. https://cordis.europa.eu/project/id/101102000. Accessed: 14 April 2025.

[19] *APPU project*. https://www.tudelft.nl/lr/appu. Accessed: 14 April 2025.

[20] *HOPE HORIZON project*. https://hope-eu-project.eu/. Accessed: 14 April 2025.

[21] R. Mao, J. Wang, W. Lin, et al. "Effects of flow-flame interactions on the stabilization of ultra-lean swirling CH4/H2/air flames". In: *Fuel* 319 (2022), p. 123619. DOI: 10.1016/j.fuel.2022.123619.

[22] T. Reichel. "Flashback Prevention in Lean-Premixed Hydrogen Combustion". PhD thesis. July 2017. DOI: 10.14279/depositonce-6530.

[23] H. Kutkan, A. Amato, G. Campa, et al. "Modeling of Turbulent Premixed CH4/H2/Air Flames Including the Influence of Stretch and Heat Losses". In: *Journal of Engineering for Gas Turbines and Power* 144 (Aug. 2021). DOI: 10.1115/1.4051989.

[24] G. Ferrante, L. Doodeman, A. G. Rao, et al. "LES of Hydrogen-Enriched Methane Flames in a Lean-Burn Combustor With Axial Air Injection". In: vol. Volume 3B: Combustion, Fuels, and Emissions. Turbo Expo: Power for Land, Sea, and Air. June 2023, V03BT04A015. DOI: 10.1115/GT2023-103006.

[25] S. Link, K. Dave, F. de Domenico, et al. "Experimental analysis of dual-fuel (CH4/H2) capability in a partially-premixed swirl stabilized combustor". In: *International Journal of Hydrogen Energy* 101 (2025), pp. 427–437. DOI: 10.1016/j.ijhydene.2024.12.286.

[26] C. Cardenas, J. Denev, R. Suntz, et al. "Study of parameters and entrainment of a jet in cross-flow arrangement with transition at two low Reynolds numbers". In: *Experiments in Fluids* 53 (Oct. 2012). DOI: 10.1007/s00348-012-1333-1.

[27] A. R. Karagozian. "Transverse jets and their control". In: *Progress in Energy and Combustion Science* 36.5 (2010), pp. 531–553. DOI: 10.1016/j.pecs.2010.01.001.

[28] D. Crabb, D. F. G. Durão, and J. H. Whitelaw. "A Round Jet Normal to a Crossflow". In: *Journal of Fluids Engineering-transactions of The Asme* 103 (1981), pp. 142–153. DOI: 10.1115/1.3240764.

[29] J. Beér and N. Chigier. *Combustion Aerodynamics [by] J.M. Beér and N.A. Chigier*. Fuel and energy science series. Applied Science Publishers Limited, 1972. URL: https://books.google.nl/books?id=LQ3JtAEACAAJ.

[30] T. Lieuwen, V. Mcdonell, D. Santavicca, et al. "Burner Development and Operability Issues Associated with Steady Flowing Syngas Fired Combustors". In: *Combustion Science and Technology* 180 (May 2008), pp. 1169–1192. DOI: 10.1080/00102200801963375.

[31] P. Billant, J.-M. Chomaz, and P. Huerre. "Experimental study of vortex breakdown in swirling jets". In: *Journal of Fluid Mechanics* 376 (Dec. 1998), pp. 183–219. DOI: 10.1017/S0022112098002870.

[32] H. Sheen, W. Chen, S. Jeng, et al. "Correlation of swirl number for a radial-type swirl generator". In: *Experimental Thermal and Fluid Science* 12.4 (1996), pp. 444–451. DOI: 10.1016/0894-1777(95)00135-2.

[33] M. P. Escudier and J. J. Keller. "Recirculation in swirling flow - A manifestation of vortex breakdown". In: *AIAA Journal* 23.1 (1985), pp. 111–116. DOI: 10.2514/3.8878.

[34] P. K. Kundu, I. M. Cohen, and D. R. Dowling. "Chapter 5 - Vorticity Dynamics". In: *Fluid Mechanics (Sixth Edition)*. Ed. by P. K. Kundu, I. M. Cohen, and D. R. Dowling. Sixth Edition. Boston: Academic Press, 2016, pp. 195–226. ISBN: 978-0-12-405935-1. DOI: https://doi.org/10.1016/B978-0-12-405935-1.00005-8.

[35] R. L. Panton. *Incompressible flow*. John Wiley & Sons, 2024. ISBN: 9781118013434. DOI: 10.1002/9781118713075.

[36] N. Syred and J. Beér. "Combustion in swirling flows: A review". In: *Combustion and Flame* 23.2 (1974), pp. 143–201. DOI: 10.1016/0010-2180(74)90057-1.

[37] Y. Huang and V. Yang. "Dynamics and stability of lean-premixed swirl-stabilized combustion". In: *Progress in Energy and Combustion Science* 35.4 (2009), pp. 293–364. DOI: 10.1016/j.pecs.2009.01.002.

[38] R. Weber and J. Dugué. "Combustion accelerated swirling flows in high confinements". In: *Progress in Energy and Combustion Science* 18.4 (1992), pp. 349–367. DOI: 10.1016/0360-1285(92)90005-L.

[39] V. TANGIRALA, R. H. CHEN, and J. F. DRISCOLL. “Effect of Heat Release and Swirl on the Recirculation within Swirl-Stabilized Flames”. In: *Combustion Science and Technology* 51.1-3 (1987), pp. 75–95. DOI: 10.1080/00102208708960316.

[40] M. Choi, K. W. Choi, D. W. Kang, et al. “Experimental investigation of combustion characteristics of a CH4/O2 premixed flame: Effect of swirl intensity on flame structure, flame stability, and emissions”. In: *Case Studies in Thermal Engineering* 55 (2024), p. 104069. DOI: 10.1016/j.csite.2024.104069.

[41] Z. Tiezheng, L. Xiao, Z. Zhang, et al. “The effects of swirl number on the combustion characteristics in an internally-staged combustor”. In: *Proceedings of the Institution of Mechanical Engineers, Part C: Journal of Mechanical Engineering Science* 236 (Aug. 2021), p. 095440622110373. DOI: 10.1177/09544062211037360.

[42] D. S. de Almeida and P. T. Lacava. “Analysis of Pollutant Emissions in Double-stage Swirl Chamber for Gas Turbine Application”. In: *Energy Procedia* 66 (2015). The 12th International Conference on Combustion & Energy Utilisation, pp. 117–120. DOI: 10.1016/j.egypro.2015.02.067.

[43] R. Jarpala, N. Burle, M. Voleti, et al. “Effect of Swirl on the Flame Dynamics and Pollutant Emissions in an Ultra-lean Non-premixed Model GT Burner”. In: *Combustion Science and Technology* 189 (May 2017). DOI: 10.1080/00102202.2017.1333500.

[44] H. Kim, V. Arghode, and A. Gupta. “Flame characteristics of hydrogen-enriched methane–air premixed swirling flames”. In: *International Journal of Hydrogen Energy* 34.2 (2009), pp. 1063–1073. DOI: 10.1016/j.ijhydene.2008.10.035.

[45] H. Liang and T. Maxworthy. “An experimental investigation of swirling jets”. In: *Journal of Fluid Mechanics* 525 (2005), pp. 115–159. DOI: 10.1017/S0022112004002629.

[46] M. Stöhr, I. Boxx, C. Carter, et al. “Experimental study of vortex-flame interaction in a gas turbine model combustor”. In: *Combustion and Flame* 159 (Aug. 2012), pp. 2636–2649. DOI: 10.1016/j.combustflame.2012.03.020.

[47] T. Claypole and N. Syred. “The effect of swirl burner aerodynamics on NOx formation”. In: *Symposium (International) on Combustion* 18.1 (1981). Eighteenth Symposium (International) on Combustion, pp. 81–89. DOI: 10.1016/S0082-0784(81)80013-6.

[48] T. F. Fric. “Effects of fuel-air unmixedness on NOx emissions”. In: *Journal of Propulsion and Power* 9.5 (1993), pp. 708–713.

[49] F. Lueckoff, M. Sieber, C. O. Paschereit, et al. “Impact of the Precessing Vortex Core on NOx Emissions in Premixed Swirl-Stabilized Flames - An Experimental Study”. In: *Journal of Engineering for Gas Turbines and Power* 142.11 (Oct. 2020). 111010. DOI: 10.1115/1.4048603.

[50] K. Oberleithner, M. Stöhr, S. H. Im, et al. “Formation and flame-induced suppression of the precessing vortex core in a swirl combustor: Experiments and linear stability analysis”. In: *Combustion and Flame* 162.8 (2015), pp. 3100–3114. DOI: 10.1016/J.COMBUSTFLAME.2015.02.015.

[51] N. Syred. “A review of oscillation mechanisms and the role of the precessing vortex core (PVC) in swirl combustion systems”. In: *Progress in Energy and Combustion Science* 32.2 (2006), pp. 93–161. DOI: 10.1016/j.pecs.2005.10.002.

[52] I. V. Litvinov, S. I. Shtork, P. A. Kuibin, et al. “Experimental study and analytical reconstruction of precessing vortex in a tangential swirler”. In: *International Journal of Heat and Fluid Flow* 42 (2013), pp. 251–264. DOI: 10.1016/j.ijheatfluidflow.2013.02.009.

[53] S. Terhaar, T. Reichel, C. Schrodinger, et al. “Vortex Breakdown and Global Modes in Swirling Combustor Flows with Axial Air Injection”. In: 43rd Fluid Dynamics Conference. June 2013. ISBN: 978-1-62410-214-1. DOI: 10.2514/6.2013-2602.

[54] A. P.M, E. Fernandes, H. M.V, et al. “Swirl flow structure and flame characteristics in a model lean premixed combustor”. In: *Combustion Science and Technology* 175 (Aug. 2003), pp. 1369–1388. DOI: 10.1080/00102200302354.

[55] T. Boningari and P. G. Smirniotis. “Impact of nitrogen oxides on the environment and human health: Mn-based materials for the NOx abatement”. In: *Current Opinion in Chemical Engineering* 13 (2016). Energy and Environmental Engineering / Reaction engineering and catalysis, pp. 133–141. DOI: 10.1016/j.coche.2016.09.004.

[56] Y. B. Zeldvich. “The oxidation of nitrogen in combustion and explosions”. In: *J. Acta Physicochimica* 21 (1946), p. 577. DOI: 10.1515/9781400862979.404.

[57] J. A. Miller and C. T. Bowman. “Mechanism and modeling of nitrogen chemistry in combustion”. In: *Progress in Energy and Combustion Science* 15.4 (1989), pp. 287–338. DOI: 10.1016/0360-1285(89)90017-8.

[58] C. P. Fenimore. “Formation of nitric oxide in premixed hydrocarbon flames”. In: *Symposium (international) on combustion*. Vol. 13. 1. Elsevier. 1971, pp. 373–380. DOI: 10.1016/S0082-0784(71)80040-1.

[59] Q. Cui, K. Morokuma, J. Bowman, et al. “The spin-forbidden reaction CHÑ 2PÖ1N2ðHCN1NÑ 4SÖ revisited. II. Nonadiabatic transition state theory and application”. In: *The Journal of Chemical Physics* 110 (May 1999), pp. 9469–9482. DOI: 10.1063/1.478949.

[60] J. Xu, D. Wang, and H. Meng. “Quantitative analyses of NO formations from different reaction pathways in methane-air combustion at various pressures and temperatures”. In: *Fuel* 337 (2023), p. 126856. DOI: 10.1016/j.fuel.2022.126856.

[61] J. Bozzelli and A. Dean. “O + NNH: A possible new route for NOX formation in flames”. In: *Int. J. Chem. Kinet.* 27 (Nov. 1995), pp. 1097–109. DOI: 10.1002/kin.550271107.

[62] A. Hayhurst and E. Hutchinson. “Evidence for a New Way of Producing NO via NNH in Fuel-Rich Flames at Atmospheric Pressure”. In: *Combustion and Flame* 114.1 (1998), pp. 274–279. DOI: 10.1016/S0010-2180(97)00328-3.

[63] J. P. Bons, R. Sondergaard, and R. B. Rivir. “The fluid dynamics of LPT blade separation control using pulsed jets”. In: *J. Turbomach.* 124.1 (2002), pp. 77–85. DOI: 10.1115/1.1425392.

[64] L. Gevorkyan, T. Shoji, D. R. Getsinger, et al. “Transverse jet mixing characteristics”. In: *Journal of Fluid Mechanics* 790 (2016), pp. 237–274. DOI: 10.1017/jfm.2016.5.

[65] J. D. Holdeman. “Mixing of multiple jets with a confined subsonic crossflow”. In: *Progress in Energy and Combustion Science* 19.1 (1993), pp. 31–70. DOI: 10.1016/0360-1285(93)90021-6.

[66] A. R. Karagozian. “The jet in crossflow”. In: *Physics of Fluids* 26.10 (2014). DOI: 10.1063/1.4895900.

[67] T. Tan, W. Fan, and R. Zhang. “A numerical and experimental investigation into the mixing mechanism of hydrogen transverse jets into an air swirl flow”. In: *Physics of Fluids* 36.3 (Mar. 2024), p. 037147. DOI: 10.1063/5.0198960.

[68] S. Ahmed and R. So. “Characteristics of air jets discharging normally into a swirling crossflow”. In: *AIAA Journal* 25 (Feb. 1987), pp. 429–435. DOI: 10.2514/3.9641.

[69] R. M. C. So and S. A. Ahmed. “Helium jets discharging normally into a swirling air flow”. In: *Experiments in Fluids* 5 (1987), pp. 255–262. DOI: 10.1007/BF00279739.

[70] S. Link, G. Ferrante, K. Dave, et al. “Experimental and numerical investigation of mixing in a partially premixed CH4/H2 combustor”. In: *International Journal of Hydrogen Energy* 141 (2025), pp. 176–192. DOI: 10.1016/j.ijhydene.2025.05.070.

[71] B. T. Zinn and T. C. Lieuwen. “Combustion instabilities: basic concepts”. In: *Progress in Astronautics and Aeronautics* 210 (2005), p. 3.

[72] A. C. Benim and K. Syed. *Flashback Mechanisms in Lean Premixed Gas Turbine Combustion*. Academic Press, Jan. 2015, pp. 1–123. ISBN: 978-0-12-800755-6.

[73] T. Lieuwen, V. Mcdonell, E. Petersen, et al. “Fuel Flexibility Influences on Premixed Combustor Blowout, Flashback, Autoignition, and Stability”. In: *Journal of Engineering for Gas Turbines and Power* 130 (Jan. 2008). DOI: 10.1115/1.2771243.

[74] B. Lewis and G. Von Elbe. “Stability and structure of burner flames”. In: *The Journal of Chemical Physics* 11.2 (1943), pp. 75–97. DOI: 10.1063/1.1723808.

[75] O. Scha¨fer, R. Koch, and S. Wittig. “Flashback in Lean Prevaporized Premixed Combustion: Non-swirling Turbulent Pipe Flow Study”. In: *Journal of Engineering for Gas Turbines and Power* 125.3 (Aug. 2003), pp. 670–676. ISSN: 0742-4795. DOI: 10.1115/1.1581897. URL: 10.1115/1.1581897.

[76] B. Su, M. Papp, P. Zhang, et al. “Dependence of ignition delay time on its definition - A case study on methane ignition”. In: *Combustion and Flame* 262 (2024), p. 113364. DOI: 10.1016/j.combustflame.2024.113364.

[77] P.-A. Glaude, R. Fournet, R. Bounaceur, et al. “Kinetic study of the combustion of hydrogen under pressure”. In: *Conference at ENSIC*. Oct. 2022. DOI: 10.13140/RG.2.2.26190.95040.

[78] S. Panigrahy, A. A. E.-S. Mohamed, P. Wang, et al. “When hydrogen is slower than methane to ignite”. In: *Proceedings of the Combustion Institute* 39.1 (2023), pp. 253–263. DOI: 10.1016/j.proci.2022.08.025.

[79] Y. Zhang, Z. Huang, L. Wei, et al. “Experimental and modeling study on ignition delays of lean mixtures of methane, hydrogen, oxygen, and argon at elevated pressures”. In: *Combustion and Flame* 159.3 (2012), pp. 918–931. DOI: 10.1016/j.combustflame.2011.09.010.

[80] R. Cheng and A. Oppenheim. “Autoignition in methane-hydrogen mixtures”. In: *Combustion and Flame* 58.2 (1984), pp. 125–139. DOI: 10.1016/0010-2180(84)90088-9.

[81] C. Fotache, T. Kreutz, and C. Law. “Ignition of hydrogen-enriched methane by heated air”. In: *Combustion and Flame* 110.4 (1997), pp. 429–440. DOI: 10.1016/S0010-2180(97)00084-9.

[82] F. Kiesewetter, M. Konle, and T. Sattelmayer. “Analysis of Combustion Induced Vortex Breakdown Driven Flame Flashback in a Premix Burner With Cylindrical Mixing Zone”. In: *Journal of Engineering for Gas Turbines and Power* 129.4 (Apr. 2007), pp. 929–936. DOI: 10.1115/1.2747259.

[83] S. Burmberger and T. Sattelmayer. “Optimization of the Aerodynamic Flame Stabilization for Fuel Flexible Gas Turbine Premix Burners”. In: *Journal of Engineering for Gas Turbines and Power* 133.10 (2011). DOI: 10.1115/1.4003164.

[84] S. Burmberger, C. Hirsch, and T. Sattelmayer. “Designing a Radial Swirler Vortex Breakdown Burner”. In: *Turbo Expo: Power for Land, Sea, and Air*. Vol. Volume 1: Combustion and Fuels, Education. May 2006, pp. 423–431. DOI: 10.1115/GT2006-90497.

[85] T. G. Reichel, S. Terhaar, and O. Paschereit. “Increasing Flashback Resistance in Lean Premixed Swirl-Stabilized Hydrogen Combustion by Axial Air Injection”. In: *Journal of Engineering for Gas Turbines and Power* 137.7 (July 2015). 071503. DOI: 10.1115/1.4029119.

[86] A. A. Putnam and R. A. Jensen. “Application of dimensionless numbers to flash-back and other combustion phenomena”. In: *Symposium on Combustion and Flame, and Explosion Phenomena* 3.1 (1948). Third Symposium on Combustion and Flame and Explosion Phenomena, pp. 89–98. DOI: 10.1016/S1062-2896(49)80011-0.

[87] S. Plee and A. Mellor. “Characteristic time correlation for lean blowoff of bluff-body-stabilized flames”. In: *Combustion and Flame* 35 (1979), pp. 61–80. DOI: 10.1016/0010-2180(79)90007-5.

[88] K. Radhakrishnan, J. B. Heywood, and R. J. Tabaczynski. “Premixed turbulent flame blowoff velocity correlation based on coherent structures in turbulent flows”. In: *Combustion and flame* 42 (1981), pp. 19–33. DOI: 10.1016/0010-2180(81)90139-5.

[89] D. Noble, Q. Zhang, A. Shareef, et al. “Syngas Mixture Composition Effects Upon Flashback and Blowout”. In: *Proceedings of the ASME Turbo Expo* 1 (Jan. 2006). DOI: 10.1115/GT2006-90470.

[90] I. Wierzba and V. Kilchyk. “Flammability limits of hydrogen-carbon monoxide mixtures at moderately elevated temperatures”. In: *International Journal of Hydrogen Energy* 26.6 (2001), pp. 639–643. DOI: 10.1016/S0360-3199(00)00114-2.

[91] T. Vezirgŭ and F. Barbir. “Hydrogen: the wonder fuel”. In: *International Journal of Hydrogen Energy* 17.6 (1992), pp. 391–404. DOI: 10.1016/0360-3199(92)90183-W.

[92] F. A. Williams. *Combustion theory*. CRC Press, 2018. ISBN: 9780429494055. DOI: 10.1201/9780429494055.

[93] D. G. Goodwin, H. K. Moffat, I. Schoegl, et al. *Cantera: An Object-oriented Software Toolkit for Chemical Kinetics, Thermodynamics, and Transport Processes*. https://www.cantera.org. Version 3.0.0. 2023. DOI: 10.5281/zenodo.8137090.

[94] R. W. Schefer, D. M. Wicksall, and A. K. Agrawal. “Combustion of hydrogen-enriched methane in a lean premixed swirl-stabilized burner”. In: *Proceedings of the Combustion Institute* 29.1 (2002), pp. 843–851. DOI: 10.1016/S1540-7489(02)80108-0.

[95] P. Strakey, T. Sidwell, and J. Ontko. "Investigation of the effects of hydrogen addition on lean extinction in a swirl stabilized combustor". In: *Proceedings of the Combustion Institute* 31.2 (2007), pp. 3173–3180. DOI: https://doi.org/10.1016/j.proci.2006.07.077.

[96] B. Dam, N. Love, and A. Choudhuri. "Flashback propensity of syngas fuels". In: *Fuel* 90.2 (2011), pp. 618–625. DOI: 10.1016/j.fuel.2010.10.021.

[97] B. Dam, G. Corona, M. Hayder, et al. "Effects of syngas composition on combustion induced vortex breakdown (CIVB) flashback in a swirl stabilized combustor". In: *Fuel* 90.11 (2011), pp. 3274–3284. DOI: 10.1016/j.fuel.2011.06.024.

[98] X. Liu, M. Bertsch, A. A. Subash, et al. "Investigation of turbulent premixed methane/air and hydrogen-enriched methane/air flames in a laboratory-scale gas turbine model combustor". In: *International Journal of Hydrogen Energy* 46.24 (2021), pp. 13377–13388. DOI: 10.1016/j.ijhydene.2021.01.087.

[99] T. F. Guiberti, D. Durox, L. Zimmer, et al. "Analysis of topology transitions of swirl flames interacting with the combustor side wall". In: *Combustion and Flame* 162.11 (2015), pp. 4342–4357. DOI: 10.1016/j.combustflame.2015.07.001.

[100] T. G. Reichel and C. O. Paschereit. "Interaction mechanisms of fuel momentum with flashback limits in lean-premixed combustion of hydrogen". In: *International Journal of Hydrogen Energy* 42.7 (2017), pp. 4518–4529. DOI: 10.1016/j.ijhydene.2016.11.018.

[101] Q. An, S. Kheirkhah, J. Bergthorson, et al. "Flame stabilization mechanisms and shape transitions in a 3D printed, hydrogen enriched, methane/air low-swirl burner". In: *International Journal of Hydrogen Energy* 46.27 (2021), pp. 14764–14779. DOI: 10.1016/j.ijhydene.2021.01.112.

[102] A. Lantz, R. Collin, M. Aldén, et al. "Investigation of Hydrogen Enriched Natural Gas Flames in a SGT-700/800 Burner Using OH PLIF and Chemiluminescence Imaging". In: *Journal of Engineering for Gas Turbines and Power* 137.3 (Oct. 2014), p. 031505. DOI: 10.1115/1.4028462.

[103] T. Reichel, S. Terhaar, and C. Paschereit. "Flashback Resistance and Fuel-Air Mixing in Lean Premixed Hydrogen Combustion". In: *Journal of Propulsion and Power* 34 (May 2018), pp. 670–701. DOI: 10.2514/1.B36646.

[104] S. R. Turns and L. L. Pauley. *Thermodynamics: concepts and applications*. Cambridge University Press, 2020. ISBN: 978-0-521-85042-1.

[105] H. Kim, V. Arghode, M. Linck, et al. "Hydrogen addition effects in a confined swirl-stabilized methane-air flame". In: *International Journal of Hydrogen Energy* 34.2 (2009), pp. 1054–1062. DOI: 10.1016/j.ijhydene.2008.10.034.

[106] S. Park. "Hydrogen addition effect on NO formation in methane/air lean-premixed flames at elevated pressure". In: *International Journal of Hydrogen Energy* 46.50 (2021), pp. 25712–25725. DOI: 10.1016/j.ijhydene.2021.05.101.

[107] D. Wang, Z. Tan, J. Xu, et al. "Quantitative studies of NO emissions from various reaction pathways in swirling combustion of hydrogen-enriched methane". In: *International Journal of Hydrogen Energy* 53 (2024), pp. 409–421. DOI: 10.1016/j.ijhydene.2023.12.001.

[108] S. Marragou, H. Magnes, T. Poinsot, et al. "Stabilization regimes and pollutant emissions from a dual fuel CH4/H2 and dual swirl low NOx burner". In: *International Journal of Hydrogen Energy* 47.44 (2022), pp. 19275–19288. DOI: 10.1016/j.ijhydene.2022.04.033.

[109] J. Sangl, C. Mayer, and T. Sattelmayer. "Dynamic Adaptation of Aerodynamic Flame Stabilization of a Premix Swirl Burner to Fuel Reactivity Using Fuel Momentum". In: *Journal of Engineering for Gas Turbines and Power* 133.7 (2011). DOI: 10.1115/1.4002659.

[110] S. Marragou, H. Magnes, A. Aniello, et al. "Experimental analysis and theoretical lift-off criterion for H2/air flames stabilized on a dual swirl injector". In: *Proceedings of the Combustion Institute* 39.4 (2023), pp. 4345–4354. DOI: 10.1016/j.proci.2022.07.255.

[111] M. Leroy, C. Mirat, A. Renaud, et al. "Stabilization of Low-NOx Hydrogen Flames on a Dual-Swirl Coaxial Injector". In: *Journal of Engineering for Gas Turbines and Power* 145.2 (Nov. 2022), p. 021021. DOI: 10.1115/1.4055711.

[112] C. Mayer, J. Sangl, T. Sattelmayer, et al. “Study on the Operational Window of a Swirl Stabilized Syngas Burner Under Atmospheric and High Pressure Conditions”. In: *Journal of Engineering for Gas Turbines and Power* 134.3 (2012). DOI: 10.1115/1.4004255.

[113] C. Martin. “Aspects of the design of swirlers as used in fuel injectors for gas turbine combustors”. In: *2. international gas turbine conference and exhibition*. American Society of Mechanical Engineers, New York, NY, 1987. DOI: 10.1115/87-GT-139.

[114] A. Carmack, S. Ekkad, Y. Kim, et al. “Comparison of Flow and Heat Transfer Distributions in a Can Combustor for Radial and Axial Swirlers Under Cold Flow Conditions”. In: *Journal of Thermal Science and Engineering Applications* 5 (July 2012). DOI: 10.1115/HT2012-58550.

[115] S. Link, K. Dave, G. Eitelberg, et al. “The Influence of the Confinement Ratio on the Precessing Vortex Core Dynamics in a Counter-Rotating Dual Swirler”. In: vol. Volume 3B: Combustion, Fuels, and Emissions. Turbo Expo: Power for Land, Sea, and Air. June 2023, V03BT04A001. DOI: 10.1115/GT2023-101678.

[116] “Suitability of helium gas as surrogate fuel for hydrogen in H2-Air non-reactive supersonic mixing studies”. In: *International Journal of Hydrogen Energy* 47.15 (2022), pp. 9408–9421. DOI: 10.1016/j.ijhydene.2022.01.022.

[117] J. A. Schetz and P. T. Harsha. “Injection and Mixing in Turbulent Flow (Progress in Aeronautics and Astronautics, Vol. 68)”. In: *Journal of Fluids Engineering* 102.4 (Dec. 1980), pp. 525–525. DOI: 10.1115/1.3240750.

[118] C. Tropea, A. Yarin, and J. Foss. *Springer Handbook of Experimental Fluid Mechanics*. Springer, Jan. 2007. ISBN: 9783540251415. DOI: 10.1007/978-3-540-30299-5.

[119] J. L. Lumey. *Stochastic tools in turbulence*. Elsevier, 2012. ISBN: 978-0486462707.

[120] M. Sieber, C. O. Paschereit, and K. Oberleithner. “Spectral proper orthogonal decomposition”. In: *Journal of Fluid Mechanics* 792 (2016), pp. 798–828. DOI: 10.1017/jfm.2016.103.

[121] O. T. Schmidt. “Spectral proper orthogonal decomposition using multitaper estimates”. In: *Theoretical and Computational Fluid Dynamics* (2022), pp. 1–14. URL: https://rdcu.be/cUtP3.

[122] S. Karami and J. Soria. “Analysis of Coherent Structures in an Under-Expanded Supersonic Impinging Jet Using Spectral Proper Orthogonal Decomposition (SPOD)”. In: *Aerospace* 5 (July 2018), p. 73. DOI: 10.3390/aerospace5030073.

[123] A. Towne, O. T. Schmidt, and T. Colonius. “Spectral proper orthogonal decomposition and its relationship to dynamic mode decomposition and resolvent analysis”. In: *Journal of Fluid Mechanics* 847 (2018), pp. 821–867. DOI: 10.1017/jfm.2018.283.

[124] J. Hall and E. Petersen. “An optimized kinetics model for OH chemiluminescence at high temperatures and atmospheric pressures”. In: *International Journal of Chemical Kinetics* 38 (Dec. 2006). DOI: 10.1002/kin.20196.

[125] T. Kathrotia, M. Fikri, M. Bozkurt, et al. “Study of the H+O+M reaction forming OH*: Kinetics of OH* chemiluminescence in hydrogen combustion systems”. In: *Combustion and Flame* 157.7 (2010), pp. 1261–1273. DOI: 10.1016/j.combustflame.2010.04.003.

[126] H. N. Najm, P. H. Paul, C. J. Mueller, et al. “On the Adequacy of Certain Experimental Observables as Measurements of Flame Burning Rate”. In: *Combustion and Flame* 113.3 (1998), pp. 312–332. DOI: 10.1016/S0010-2180(97)00209-5.

[127] Y. Hardalupas and M. Orain. “Local measurements of the time-dependent heat release rate and equivalence ratio using chemiluminescent emission from a flame”. In: *Combustion and Flame* 139.3 (2004), pp. 188–207. DOI: 10.1016/j.combustflame.2004.08.003.

[128] M. Lauer and T. Sattelmayer. “On the Adequacy of Chemiluminescence as a Measure for Heat Release in Turbulent Flames With Mixture Gradients”. In: *Journal of Engineering for Gas Turbines and Power* 6 (Mar. 2010). 061502. DOI: 10.1115/1.4000126.

[129] S. Simons and Z.-G. Yuan. “The Filtered Abel Transform and Its Application in Combustion Diagnostics”. In: *NASA/CR—2003-212121* (Apr. 2003).

[130] J. Runyon. “Gas Turbine Fuel Flexibility: Pressurized Swirl Flame Stability, Thermoacoustics, and Emissions”. PhD thesis. May 2017.

[131] C. Killer. *Abel Inversion Algorithm*. https://www.mathworks.com/matlabcentral/fileexchange/43639-abel-inversion-algorithm. MATLAB Central File Exchange, Retrieved March 17, 2025. 2025.

[132] M. Lauer and T. Sattelmayer. “Heat release calculation in a turbulent swirl flame from laser and chemiluminescence measurements”. In: *14th Int Symp on Applications of Laser Techniques to Fluid Mechanics*. Jan. 2008.

[133] A. C. Eckbreth. *Laser diagnostics for combustion temperature and species*. CRC press, 2022. ISBN: 9781003077251. DOI: 10.1201/9781003077251.

[134] J. H. Bechtel and R. E. Teets. “Hydroxyl and its concentration profile in methane–air flames”. In: *Appl. Opt.* 18.24 (Dec. 1979), pp. 4138–4144. DOI: 10.1364/AO.18.004138.

[135] R.Sadanandan, M.Stoehr, W.Meier. “Simultaneous OH-PLIF and PIV measurements in a gas turbine model combustor”. In: *Applied Physics B* 90 (2008), pp. 609–618. DOI: 10.1007/s00340-007-2928-8.

[136] R. Mével, D. Davidenko, J. Austin, et al. In: *Int. J. Hydrogen Energy* 39.11 (2014), pp. 6044–6060.

[137] A. Silva Correia. *LIFTempDependence*. 10.4121/dd222007-8c0f-4cde-a642-5e4580324af6. Version 1. 2025.

[138] M. A. Linne. *Spectroscopic measurement: an introduction to the fundamentals*. Academic Press, 2024. ISBN: 978-0124510715.

[139] K. P. Huber and G. H. Herzberg. *Constants of Diatomic Molecules*. in NIST Chemistry WebBook, NIST Standard Reference Database Number 69, Eds. P.J. Linstrom and W.G. Mallard, National Institute of Standards and Technology, Gaithersburg MD, 20899. Data prepared by Jean W. Gallagher and Russell D. Johnson, III. 2024. URL: 10.18434/T4D303 (visited on 10/30/2024).

[140] X. Tu, L. Wang, X. Qi, et al. “Effects of temperature and pressure on OH laser-induced fluorescence exciting the A-X (1,0) transition at high pressures”. In: *Chinese Physics B* 29 (Aug. 2020). DOI: 10.1088/1674-1056/aba5ff.

[141] A. M. Steinberg, C. M. Arndt, and W. Meier. “Parametric study of vortex structures and their dynamics in swirl-stabilized combustion”. In: *Proceedings of the Combustion Institute* 34.2 (2013), pp. 3117–3125. DOI: 10.1016/j.proci.2012.05.015.

[142] A. Karmarkar, S. Gupta, I. Boxx, et al. “Impact of precessing vortex core dynamics on the thermoacoustic instabilities in a swirl-stabilized combustor”. In: *Journal of Fluid Mechanics* 946 (2022). DOI: 10.1017/jfm.2022.610.

[143] F. Lückoff and K. Oberleithner. “Excitation of the precessing vortex core by active flow control to suppress thermoacoustic instabilities in swirl flames”. In: *International Journal of Spray and Combustion Dynamics* 11 (2019), p. 175682771985623. DOI: 10.1177/1756827719856237.

[144] M. Stöhr, C. M. Arndt, and W. Meier. “Transient effects of fuel–air mixing in a partially-premixed turbulent swirl flame”. In: *Proceedings of the Combustion Institute* 35.3 (2015), pp. 3327–3335. DOI: 10.1016/j.proci.2014.06.095.

[145] S. Terhaar, O. Krueger, and C. O. Paschereit. “Flow Field and Flame Dynamics of Swirling Methane and Hydrogen Flames at Dry and Steam Diluted Conditions”. In: *Journal of Engineering for Gas Turbines and Power* 137.4 (Oct. 2014). 041503. DOI: 10.1115/1.4028392.

[146] B. Ćosić, B. C. Bobusch, J. P. Moeck, et al. “Open-Loop Control of Combustion Instabilities and the Role of the Flame Response to Two-Frequency Forcing”. In: *Journal of Engineering for Gas Turbines and Power* 134.6 (Apr. 2012), p. 061502. DOI: 10.1115/1.4005986.

[147] D. W. Bechert. “Sound absorption caused by vorticity shedding, demonstrated with a jet flow”. In: *Journal of Sound and Vibration* 70.3 (1980), pp. 389–405. DOI: 10.1016/0022-460X(80)90307-7.

[148] G. Li and E. J. Gutmark. “Effect of exhaust nozzle geometry on combustor flow field and combustion characteristics”. In: *Proceedings of the Combustion Institute* 30.2 (2005), pp. 2893–2901. DOI: 10.1016/j.proci.2004.08.189.

[149] S. Terhaar, B. C. Bobusch, and C. O. Paschereit. “Effects of Outlet Boundary Conditions on the Reacting Flow Field in a Swirl-Stabilized Burner at Dry and Humid Conditions”. In: *Volume 2: Combustion, Fuels and Emissions, Parts A and B*. American Society of Mechanical Engineers, 2012, pp. 1295–1306. ISBN: 978-0-7918-4468-7. DOI: 10.1115/GT2012-69753.

[150] Y. Fu, S. Jeng, and R. Tacina. “Confinement Effects on the Swirling Flow Generated by a Helical Axial Swirler”. In: vol. 9. Collection of Technical Papers - 44th AIAA Aerospace Sciences Meeting. Jan. 2006. ISBN: 978-1-62410-039-0. DOI: 10.2514/6.2006-545.

[151] L. Ji, J. Wang, W. Zhang, et al. “Effect of confinement ratio on flame structure and blow-off characteristics of swirl flames”. In: *Experimental Thermal and Fluid Science* 135 (2022), p. 110630. DOI: 10.1016/j.expthermflusci.2022.110630.

[152] A. E. Khalil, J. M. Brooks, and A. K. Gupta. “Impact of confinement on flowfield of swirl flow burners”. In: *Fuel* 184 (2016), pp. 1–9. DOI: 10.1016/J.FUEL.2016.06.098.

[153] K. Oberleitner, M. Sieber, C. N. Nayeri, et al. “Three-dimensional coherent structures in a swirling jet undergoing vortex breakdown: stability analysis and empirical mode construction”. In: *Journal of Fluid Mechanics* 679 (2011), pp. 383–414. DOI: 10.1017/jfm.2011.141.

[154] S. Terhaar, B. Ćosić, C. O. Paschereit, et al. “Suppression and excitation of the precessing vortex core by acoustic velocity fluctuations: An experimental and analytical study”. In: *Combustion and Flame* 172 (2016), pp. 234–251. DOI: 10.1016/j.combustflame.2016.06.013.

[155] J. Weiss. “A Tutorial on the Proper Orthogonal Decomposition”. In: *AIAA Aviation 2019 Forum*. Reston, Virginia: American Institute of Aeronautics and Astronautics, 2019. ISBN: 978-1-62410-589-0. DOI: 10.2514/6.2019-3333.

[156] O. Schmidt and T. Colonius. “Guide to Spectral Proper Orthogonal Decomposition”. In: *AIAA Journal* 58 (Jan. 2020), pp. 1–11. DOI: 10.2514/1.J058809.

[157] A. Favrel, Z. Liu, and K. Miyagawa. “Enhancing effect of an open pipe exit on the precessing vortex core occurring in confined swirling flows”. In: *Experiments in Fluids* 61 (Sept. 2020), p. 211. DOI: 10.1007/s00348-020-03042-1.

[158] I. V. Litvinov, S. I. Shtork, P. A. Kuibin, et al. “Experimental study and analytical reconstruction of precessing vortex in a tangential swirler”. In: *International Journal of Heat and Fluid Flow* 42 (2013), pp. 251–264. DOI: 10.1016/j.ijheatfluidflow.2013.02.009.

[159] J. D. Holdeman. “Mixing of multiple jets with a confined subsonic crossflow”. In: *Progress in Energy and Combustion Science* 19.1 (1993), pp. 31–70. DOI: 10.1016/0360-1285(93)90021-6.

[160] M. T. Kandakure, V. C. Patkar, A. W. Patwardhan, et al. “Mixing with Jets in Cross-Flow”. In: *Industrial & Engineering Chemistry Research* 48.14 (2009), pp. 6820–6829. DOI: 10.1021/ie801863a.

[161] Z. Li, S. Murugappan, E. Gutmark, et al. “Numerical Simulation and Experiments of Jets in Cross Flow”. In: vol. 6. Jan. 2006. ISBN: 978-1-62410-039-0. DOI: 10.2514/6.2006-307.

[162] J. P. Bons, R. Sondergaard, and R. B. Rivir. “The Fluid Dynamics of LPT Blade Separation Control Using Pulsed Jets ”. In: *Journal of Turbomachinery* 124.1 (Feb. 2001), pp. 77–85. DOI: 10.1115/1.1425392.

[163] T. Demayo, M. Leong, G. Samuelsen, et al. “Assessing jet-induced spatial mixing in a rich, reacting crossflow”. In: *Journal of propulsion and power* 19.1 (2003), pp. 14–21. DOI: 10.2514/2.6098.

[164] P. E. Dimotakis. “Turbulent mixing”. In: *Annu. Rev. Fluid Mech.* 37.1 (2005), pp. 329–356. DOI: 10.1146/annurev.fluid.36.050802.122015.

[165] S. V. Alekseenko, V. M. Dulin, Y. S. Kozorezov, et al. “Effect of axisymmetric forcing on the structure of a swirling turbulent jet”. In: *International Journal of Heat and Fluid Flow* 29.6 (2008), pp. 1699–1715. DOI: 10.1016/j.ijheatfluidflow.2008.07.005.

[166] S. Abdelwahid, M. Nemitallah, B. Imteyaz, et al. “On the effects of H2-enrichment and inlet velocity on stability limits and shape of CH4/H2-O2/CO2 flames in a premixed swirl combustor”. In: *Energy and Fuels* 32 (Aug. 2018). DOI: 10.1021/acs.energyfuels.8b01958.

[167] C. Liu, Z. Cao, F. Li, et al. “Flame monitoring of a model swirl injector using one-dimensional tunable diode laser absorption spectroscopy tomography”. In: *Measurement Science and Technology* 28 (Mar. 2017). DOI: 10.1088/1361-6501/aa5aee.

[168] S. Guo, J. Wang, W. Zhang, et al. “Effect of hydrogen enrichment on swirl/bluff-body lean premixed flame stabilization”. In: *International Journal of Hydrogen Energy* 45.18 (2020), pp. 10906–10919. DOI: 10.1016/j.ijhydene.2020.02.020.

[169] J. Broadwell and R. Breidenthal. “Structure and Mixing of a Transverse Jet in Incompressible Flow”. In: *Journal of Fluid Mechanics* 148 (Nov. 1984), pp. 405–412. DOI: 10.1017/S0022112084002408.

[170] S. Sardeshmukh, M. Bedard, and W. Anderson. “The use of OH and CH as heat release markers in combustion dynamics”. In: *International Journal of Spray and Combustion Dynamics* 9.4 (2017), pp. 409–423. DOI: 10.1177/1756827717718483.

[171] D. Baulch, C. Cobos, R. Cox, et al. “Evaluated Kinetic Data for Combustion Modeling. Supplement I”. In: *Journal of Physical and Chemical Reference Data - J PHYS CHEM REF DATA* 23 (Nov. 1994), pp. 847–848. DOI: 10.1063/1.555953.

[172] A. Benim and K. Syed. *Flashback Mechanisms in Lean Premixed Gas Turbine Combustion*. Elsevier Science, 2014. ISBN: 9780128008263. URL: https://books.google.nl/books?id=o3ODBAAAQBAJ.

[173] R. Schefer, W. Kulatilaka, B. Patterson, et al. “Visible emission of hydrogen flames”. In: *Combustion and Flame* 156.6 (2009), pp. 1234–1241. DOI: 10.1016/j.combustflame.2009.01.011.

[174] T. Fiala and T. Sattelmayer. “Heat release and UV-Vis radiation in non-premixed hydrogen–oxygen flames”. In: *Experiments in Fluids* 56 (June 2015), p. 144. DOI: 10.1007/s00348-015-2013-8.

[175] J. Bertsch, T. Poinsot, and N. Bertier. “Boundary layer flashback of H2/Air premixed flames in a swirling flow around a central body”. In: *Combustion and Flame* 276 (2025), p. 114123. DOI: 10.1016/j.combustflame.2025.114123.

[176] N. Syred, N. A. Chigier, and J. M. Beér. “Flame stabilization in recirculation zones of jets with swirl”. In: *Symposium (International) on Combustion* 13.1 (1971), pp. 617–624. DOI: 10.1016/S0082-0784(71)80063-2.

[177] T. Shoji, Y. Iwasaki, K. Kodai, et al. “Effects of Flame Behaviors on Combustion Noise from Lean-Premixed Hydrogen Low-Swirl Flames”. In: *AIAA Journal* 58 (Aug. 2020), pp. 1–17. DOI: 10.2514/1.J059049.

[178] R. Mercier, T. Guiberti, A. Chatelier, et al. “Experimental and numerical investigation of the influence of thermal boundary conditions on premixed swirling flame stabilization”. In: *Combustion and Flame* 171 (2016), pp. 42–58. DOI: 10.1016/j.combustflame.2016.05.006.

[179] R. Cheng, D. Littlejohn, P. Strakey, et al. “Laboratory investigations of a low-swirl injector with H2 and CH4 at gas turbine conditions”. In: *Proceedings of the Combustion Institute* 32.2 (2009), pp. 3001–3009. DOI: 10.1016/j.proci.2008.06.141.

[180] P. Schmittel, B. Günther, B. Lenze, et al. “Turbulent swirling flames: Experimental investigation of the flow field and formation of nitrogen oxide”. In: *Proceedings of the Combustion Institute* 28.1 (2000), pp. 303–309. DOI: 10.1016/S0082-0784(00)80224-6.

[181] H. Pan, S. Geng, H. Yang, et al. “Influence of H2 blending on NOx production in natural gas combustion: Mechanism comparison and reaction routes”. In: *International Journal of Hydrogen Energy* 48.2 (2023), pp. 784–797. DOI: 10.1016/j.ijhydene.2022.09.251.

[182] G. Wang, T. Guiberti, and W. Roberts. “Exploring the Effects of Swirl Intensity on NO Emission in Ammonia-Methane-Air Premixed Swirling Flames”. In: *Journal of Ammonia Energy* 1 (July 2023). DOI: 10.18573/jae.14.

[183] J. Wang, Z. Huang, C. Tang, et al. “Numerical study of the effect of hydrogen addition on methane-air mixtures combustion”. In: *International Journal of Hydrogen Energy* 34.2 (2009), pp. 1084–1096. DOI: 10.1016/j.ijhydene.2008.11.010.

[184] H. Pan, S. Geng, H. Yang, et al. “Influence of H2 blending on NOx production in natural gas combustion: Mechanism comparison and reaction routes”. In: *International Journal of Hydrogen Energy* 48.2 (2023), pp. 784–797. DOI: 10.1016/j.ijhydene.2022.09.251.

[185] R. Sadanandan, M. Stöhr, and W. Meier. “Simultaneous OH-PLIF and PIV measurements in a gas turbine model combustor”. In: *Applied Physics B* 90 (Jan. 2007), pp. 609–618. DOI: 10.1007/s00340-007-2928-8.

[186] Y. Liu, J. Tan, M. Wan, et al. “OH * and CH * chemiluminescence characteristics in low swirl methane-air flames”. In: *AIP Advances* 10 (May 2020), p. 055318. DOI: 10.1063/5.0002660.

[187] D. Knyazkov, A. Shmakov, I. Dyakov, et al. “Formation and destruction of nitric oxide in methane flames doped with NO at atmospheric pressure”. In: *Proceedings of the Combustion Institute* 32.1 (2009), pp. 327–334. DOI: 10.1016/j.proci.2008.06.037.

[188] P. Paul, J. Gray, J. Durant Jr, et al. “Collisional quenching corrections for laser-induced fluorescence measurements of NO A2Sigma (+)”. In: *AIAA journal* 32.8 (1994), pp. 1670–1675. DOI: 10.2514/3.12158.

[189] J. Maughan, R. Warren, A. Tolpadi, et al. “Effect of initial fuel distribution and subsequent mixing on emissions from lean, premixed flames”. In: *Turbo Expo: Power for Land, Sea, and Air*. Vol. 78958. American Society of Mechanical Engineers. 1992, V003T06A018. DOI: 10.1115/92-GT-121.

[190] M. Zajadatz, R. Lachner, S. Bernero, et al. “Development and Design of Alstom’s Staged Fuel Gas Injection EV Burner for NOx Reduction”. In: vol. Volume 2: Turbo Expo 2007. Turbo Expo. May 2007, pp. 559–567. DOI: 10.1115/GT2007-27730.

[191] A. Lacarelle, J. Moeck, H. Konle, et al. “Effect of fuel/air mixing on NOx emissions and stability in a gas premixed combustion system”. In: *45th AIAA Aerospace Sciences Meeting and Exhibit*. 2007, p. 1417. DOI: 10.2514/6.2007-1417.

[192] W.-P. Shih, J. G. Lee, and D. A. Santavicca. “Stability and emissions characteristics of a lean premixed gas turbine combustor”. In: *Symposium (International) on Combustion* 26.2 (1996), pp. 2771–2778. DOI: 10.1016/S0082-0784(96)80115-9.

[193] F. Herning and L. Zipperer. “Calculation of the viscosity of technical gas mixtures from the viscosity of the individual gases”. In: *Gas u. Wasserfach* 79.39 (1936), p. 69.

ACKNOWLEDGEMENTS

These four years of work have truly been a rollercoaster of emotions, challenges, and growth. The PhD journey has tested my perseverance, strengthened my curiosity, and allowed me to grow both as a researcher and as a person. I would like to express my deepest gratitude to all those who have supported me throughout this journey and contributed in various ways to the completion of this thesis.

First and foremost, I would like to thank my promotors, Georg and Arvind. Thank you for trusting me with this challenging and ambitious project and for your continuous guidance over the past four years. Our discussions were always insightful and thought-provoking, and your advice helped me to keep a clear focus on the broader picture, even when I became absorbed in the details. A very special acknowledgement goes to my daily supervisor, Francesca. Your excellent guidance, patience, and encouragement have been fundamental to my development as a researcher. You have an incredible ability to bring clarity to complex problems, and your thoughtful feedback, which is always detailed, timely, and constructive, has pushed me to continuously improve the quality of my work. Beyond the scientific guidance, your empathy and support have made this journey far more enjoyable and rewarding. I am very grateful for the time and care you dedicated to supporting me navigate the challenges of my research.

I would also like to sincerely thank my two closest colleagues, Kaushal and Gioele, for the excellent collaboration and support we shared throughout these four years. Navigating the complexities of this project, from vague initial goals to intricate lab safety regulations, would not have been possible without your ideas, encouragement, and guidance. Thank you both for always having an open ear, whether for technical challenges or personal discussions, and for making the journey much more enjoyable along the way.

A special thanks goes to Kaushal for the countless hours we spent together in the lab, troubleshooting experiments and equipment, and celebrating successful measurement campaigns—even when they ran late into the night. Your dedication, energy, and enthusiasm for research were truly contagious and kept me motivated even during the most challenging moments. It is incredibly rewarding to reflect on how far we came, from the early days of combustor exhaust mishaps to the peak of our work which is reflected in several collaborative publications.

I would like to extend my heartfelt thanks to André, who spent countless hours in the lab mastering the PLIF technique and dealing with the frustrations of a temperamental laser and tricky dyes. Thanks to your commitment and determination to learn the technique quickly, we were able to obtain high-quality images for my thesis during the first LIF campaign ever conducted in the group.

A heartfelt thank you goes to all the lab and DEMO technicians, who went above and beyond on multiple occasions to ensure the timely execution of my experiments. Your problem-solving skills and willingness to help, even on short notice, were invaluable to the success of my research.

Additionally, I am grateful to the entire *Combustion Research Young Crew*. Your support, whether helping me meet the "two eyes" safety requirement for the experiment or contributing ideas during group discussions and meetings, has been invaluable. Being part of such a motivated, collaborative, and inspiring group has significantly contributed to both my personal and academic growth, and I feel very fortunate to have shared this experience with all of you.

I would also like to thank the students I have directly supervised: Vlad, Aydin, Jelle, Johannes, Willem, and Giulia. Working together in the lab is not always easy, and through our collaborations I learned a great deal, not only about research, but also about patience, communication, and teamwork. I hope you have learned just as much from me as I have learned from you.

On a more personal note, I would like to thank all the amazing PhD colleagues within FPP who accompanied me throughout these years. A special thanks goes to my office mates from office 7.15 (Pieter-Jan, Anne-Liza, Alam, Rúben, Emre and Abdel), who turned everyday challenges into shared laughter and motivation. Thank you for always having an open ear, for the countless coffee breaks that helped clear our minds, and for celebrating both the small victories and the bigger milestones together. It truly made a difference to go through the ups and downs of the PhD alongside you.

I am also very grateful for the PhD community within FPP, that was so strong and connected. Beyond our scientific discussions, we created memorable moments outside the office, whether over drinks, during our trips to Tenerife and Braunschweig, or in our board game evenings. These moments allowed us to unwind, build genuine friendships, and transform from colleagues into a close-knit group of friends. Looking back, those shared experiences are among the best memories of my PhD years.

In order to be a successful PhD candidate, maintaining a healthy balance between work and personal life is essential. I feel incredibly fortunate to have such wonderful friends outside of work who made this possible and who have contributed enormously to making the Netherlands feel like home. To my Girls group — Chiara, Charlotte, Betzy, Isabel, and Vivien — thank you for the countless memories we have created together over the past years. From dinners and weekend getaways to long conversations over coffee or wine, you have been a constant source of laughter, energy, and perspective. Thank you for listening to my endless PhD stories, celebrating milestones with me, and for offering valuable advice and encouragement from outside the academic bubble. Your friendship has been a true anchor throughout this journey. A heartfelt thank you also goes to Delphine, for always being there for me as a good friend. Your ability to listen, share your thoughts, and offer comfort in both good and difficult times has meant more than words can express.

One of my biggest thanks goes to my family. Even though we live far apart, the support and love I receive from you has been unwavering. To my parents, thank you for teaching me the values of hard work, curiosity, and resilience, and for always believing in me and giving me the opportunity to find my own path, even if it meant being far from home. Your confidence in my abilities has been a constant source of motivation throughout my life. To my brother, thank you for the fun and enjoyable moments we share whenever we see each other, those times always brighten my life.

Last, and most importantly, I want to say thank you to my partner, Carmine. Your

tireless support, patience, and love have been my rock throughout this entire journey. Thank you for believing in me even when I doubted myself, for celebrating every achievement with genuine joy, and for offering comfort during the difficult moments. I am incredibly grateful to have you. Without you, none of this would have been possible.

CURRICULUM VITÆ

Sarah Jacqueline LINK

13-11-1995 Born in Tuttlingen, Germany.

EDUCATION

2021–2025 Doctoral Education Programme
Delft University of Technology, Delft, The Netherlands

2018–2021 M.Sc. Aerospace Engineering
University of Stuttgart, Stuttgart, Germany
Thesis: *Experimental investigation of leading edge serrations as noise mitigation techniques in a linear cascade*

Erasmus exchange programme
Instituto Superior Técnico, Lisbon, Portugal

2014–2018 B.Sc. Aerospace Engineering
University of Stuttgart, Stuttgart, Germany

RESEARCH & WORK EXPERIENCE

2025–now **R&D Engineer**
Netherlands Aerospace Centre, Amsterdam, The Netherlands

2021–2025 **PhD candidate**
Delft University of Technology, Delft, The Netherlands
Dissertation: *"Flame stability and emissions for methane-hydrogen combustion: Designing for fuel flexibility"*

Promotors: Prof. dr. Georg Eitelberg, Prof. dr. Arvind Gangoli Rao
Co-promotor: Dr. Francesca de Domenico

2018–2020 **Student Research Assistant**
German Aerospace Center (DLR), Institute of Combustion Technology Stuttgart, Germany

2018–2018 **Internship**
Rolls Royce Power Systems (MTU), Friedrichshafen, Germany

LIST OF PUBLICATIONS

JOURNAL PAPERS

1. **S.Link**, K.Dave, F.de Domenico, G.Eitelberg and A. Gangoli Rao "Experimental analysis of dual-fuel (CH_4/H_2) capability in a partially premixed swirl-stabilized combustor", *International Journal of Hydrogen Energy*, 2025, 10.1016/j.ijhydene.2024.12.286.

2. K.Dave, **S.Link**, F.de Domenico, F. Schrijer, F. Scarano and A. Gangoli Rao "Kerosene-H_2 blending effects on flame properties in a multi-fuel combustor", *Fuel Communications*, 2025, 10.1016/j.jfueco.2025.100139.

3. **S.Link**, G.Ferrante, K.Dave, G.Monti, G.Eitelberg and F.de Domenico "Experimental and numerical investigation of mixing in a partially premixed CH_4/H_2 combustor", *International Journal of Hydrogen Energy*, 2025, 10.1016/j.ijhydene.2025.05.070.

4. **S.Link**, André Silva Correia, A. Gangoli Rao and F. de Domenico "Experimental investigation of the NO emission characteristics in swirl stabilized technically premixed CH_4/H_2 flames", *Proceedings of the Combustion Institute*, 2025, 10.1016/j.proci.2025.105964

CONFERENCE PAPERS

1. **S.Link**, K.Dave, G.Eitelberg and A. Gangoli Rao "TOWARDS "ENERGY MIX" IN AVIATION", *Towards Sustainable Aviation Summit*, 2022.

2. **S.Link**, K.Dave, G.Eitelberg, F.de Domenico and A. Gangoli Rao "The influence of the confinement ratio on the precessing vortex core dynamics in a counter-rotating dual swirler", *Proceedings of the ASME Turbo Expo*, 2023, 10.1115/GT2023-101678.

3. L.Palanti, L.Mazzei, C.Bianchini, **S.Link**, K. Dave, F.de Domenico and A. Gangoli Rao "CFD-based scouting for the design of a multi-fuel kerosene/hydrogen atmospheric burner", *34th Congress of the International Council of the Aeronautical Sciences*, 2024

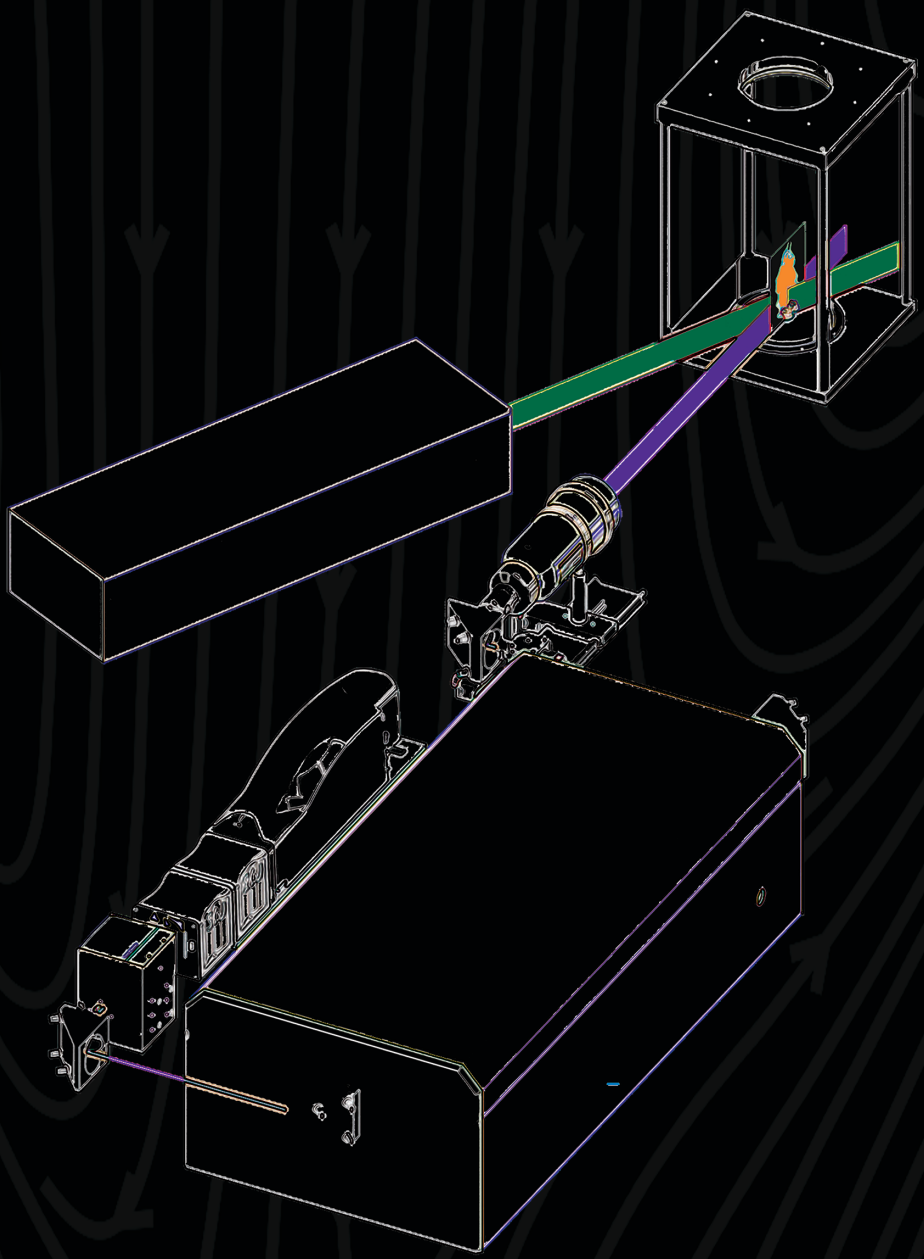

TU Delft